Photophysical studies of triarylamine dyes and an investigation into polyelectrolyte-DNA interactions.

Davies, Matthew Lloyd

How to cite:

Davies, Matthew Lloyd (2010) *Photophysical studies of triarylamine dyes and an investigation into polyelectrolyte-DNA interactions..* thesis, Swansea University.
http://cronfa.swan.ac.uk/Record/cronfa42510

Swansea University
Prifysgol Abertawe

Photophysical Studies of Triarylamine Dyes and an Investigation Into Polyelectrolyte-DNA Interactions

Matthew Lloyd Davies

A thesis submitted in fulfilment of the requirements for the degree of Doctor of Philosophy in Swansea University

Chemistry Group
Multidisciplinary Nanotechnology Centre
Swansea University
2010

ProQuest LLC.
789 East Eisenhower Parkway
P.O. Box 1346
Ann Arbor, MI 48106 – 1346

For my Mam

Acknowledgements

My PhD studies have been filled with an abundance of memorable experiences that have been due to, in part, all the fantastic people that I have been lucky enough to work and socialise with.

My thanks go first and foremost to Dr Peter Douglas who it has been an absolute privilege and pleasure to work with. His guidance, enthusiasm, humour, patience, encouragement, helpfulness and friendship have been a constant throughout my studies. I will never forget the research trip through Portugal nor will I ever forget driving around Ireland with the demo lecture and having to paint fluorescent paint on Peter's body! All in the name of science of course! For everything you have done Peter, thank you. I would also like to thank Dr Stefan Doerr for assuming the role of second supervisor and for all his help and support.

I would like to thank Swansea University for financial support. Many thanks go to all my friends from the Chemistry Department in Swansea, past and present, that made Swansea such a great place to work, in particular; Karen, Steve, Rach, Vic, Jeremie, Des, Hans and Souad. Karen and Rachel your unique sense of humour (usually aimed at my expense!) always made me laugh! Thank you to Dr Rod Mason and Dr Bill Bentley for always being available for a cup of tea and a chat. Thanks also go to Dr Mike Garley for advice on all things computer-related, along with Stan, John Tregembo and Ian Matthews for their willingness to help whenever it was needed.

I have been fortunate enough to carry out a great deal of research at the University of Coimbra, Portugal, which would not have been possible without the financial support of the CIPSNAC training network. A special thank you must go to Prof. Hugh Burrows for his guidance, enthusiastic manner and all his research ideas during my time in Portugal, and to Prof. Maria da Graça Miguel who has been incredibly supportive of my studies and a constant source of help and advice. I would like to thank Prof. Sérgio Seixas de Melo, Fernando Dias, João Pina and Carlos Serpa for help with, and a great deal of time on, all the photophysical equipment. Thank you to Ricardo Castro for assistance with the hot stage microscopy experiments. I would like to thank the many special people that made me feel so at home in Coimbra and made my time there so fun, namely; Elsa, Medronho, Carmen, Sérgio, Andre, Fatinha, Sylwia, Andreia, Rui, Dan and Fafe. I would like to thank Elsa, in particular, for all her help and support with.....well with everything in my life!! A special thank you must also go to Rachel for her friendship, advice and willingness to share a beer both in Swansea and Coimbra! Coimbra terá sempre um lugar especial no meu coração. E isso deve-se às pessoas maravilhosas que lá encontrei, e que hoje são amigos fantásticos. Obrigado a todos!

To all the people at the University of Kwa-Zulu Natal I would like to thank you for welcoming me with such open arms. In particular Prof. Bice Martincigh, Prof. Andy Kindness and Dr Vincent Nyamori I would like to thank you for making the trip really successful and providing me with an experience that was truly fantastic.

I must say a massive thank you to all my family for their unwavering support, help and love whenever I needed it. To my Mam, without whom none of this would have been possible, I would like to thank her for everything; her unbelievable level of pride in me constantly drives me when it would be so much easier to stop! I would like to thank my Nana for providing a cup of tea and her famous bacon sandwich whenever it was needed. A special mention should go to Grandad, Dean, Angela, Steve, Suzanne, Natalie and Brian, who have all helped me enormously in their own ways. I would like to thank Kayleigh for always brightening up my day by making me laugh and smile!

To my extremely special group of friends the 'Neath boys' I have to thank you for always being up for a beer and a curry and for the constant source of banter that has provided me with many hours of laughter. To Mark, Ian and Ross, my housemates during my PhD studies, I thank you for your help and support, all the micky-taking and light hearted fun but most of all for your fantastic friendship. I would also like to thank all the boys that regularly pop in to watch the sport, have a beer, or just see how things are going, especially; Cookie, Foz, Oatway and Radders. I would like to thank Laura for always making me laugh when I need it most; just thinking of a space-hopper makes me break out in laughter!! To everyone that has helped me though this time, in both a social and professional capacity, I wholeheartedly thank you.

Abbreviations and Symbols

Abs	Absorbance
A	Acceptor ion
A	Adenine
AFM	Atomic force microscopy
Å	Angstrom
bp	Base pair
CC	(Manning) Counterion condensation theory
CCP	Cationic conjugated polyelectrolyte
CPE	Conjugated polyelectrolyte
CT	Charge transfer
C	Cytosine
1D	One dimensional
DAPI	4,6-diamidino-2- phenylindole
DIDP	Diisodecyl phthalate
DMSO	Dimethyl sulfoxide
DNA	Deoxyribonucleic acid
dsDNA	Double stranded DNA
ssDNA	Single stranded DNA
D	Donor ion
ε_{dielec}	Dielectric constant
ε	Molar absorption coefficient
ε_{max}	Maximum molar absorption coefficient
FM	Fluorescence microscopy
FRET	Förster resonance energy transfer
fwhm	Full width at half-maximum

G	Guanine
HOMO	Highest occupied molecular orbital
HTL	Hole transport layer
I	Intensity of fluorescence
I_0	Intensity of fluorescence in the absence of quencher
IRF	Instrument response function
IC	Internal conversion
ISC	Inter system crossing
IPECs	Interpolyelectrolyte complexes
J	Spectral overlap integral
k^2	Orientation factor
k	Rate constant for emission
k_T	Rate constant for energy transfer
k_{PC}	Rate constant for energy transfer calculated from ProgClusters
K_a	Association constant
K_{SV}	Stern Volmer constant
LED	Light emitting diode
LCD	Liquid crystal display
LUMO	Lowest unoccupied molecular orbital
L	Lumophore
ME	Mercaptoethanol
$\overline{M_n}$	Number average molecular weight
MW	Molecular weight
ns	Nanosecond

n	Solvent refractive index
n*	number of excited molecules
η_{int}	Internal quantum efficiency
ηs	Singlet excitation efficiency
OLED	Organic light emitting diode
PLED	Polymer light emitting diode
PB	Poisson-Boltzmann
PEG	Polyethylene glycol
PF	Polyfluorene
PFP	Phenylene- fluorene polymer
PNA	Peptide nucleic acid
ps	Picosecond
Φ_f	Fluorescence quantum yield
Q	Quencher
[Q]	Quencher concentration
r	Measured anisotropy
r_0	Fundamental anisotropy
R_0	Förster radius
S_n	Singlet state
S	Spin quantum number
ST DNA	Salmon testes DNA
σ	Standard deviation
T_n	Triplet state
T_m	DNA melting temperature
TAA	Triarylamine
T	Thymine

TS_f	Fast transient species
TS_s	Slow transient species
τ	Lifetime of luminescence
τ_0	Lifetime of luminescence in the absence of quencher
τ_{rad}	Radiative lifetime
τ_{nat}	Natural lifetime
UV	Ultraviolet
μs	Microsecond
V	Volts
v/v	Volume to volume ratio
γ	Charge balance factor
Ψ	Wavefunction
W_R	Depolarization factor due to rotations
W_T	Depolarization factor related to FRET
λ	Wavelength
λ_{ex}	Wavelength of excitation
λ_{em}	Wavelength of emission
λ_{max}	Wavelength of maximum absorbance
λ_{emax}	Wavelength of maximum emission
ξ	Charge density

Summary

The photophysics and thermal properties of a series of seven novel triarylamine (TAA) dyes are described. Fluorescence characteristics have been studied in solvents of various polarities at room temperature and at 77 K. High molar extinction coefficients of the magnitude of $3.0\text{-}4.0(\pm0.50)\times10^4\ M^{-1}cm^{-1}$ were obtained for most compounds, and relatively short radiative lifetimes were observed. Fluorescence quantum yields of the dyes at room temperature in cyclohexane were found to be between 0.34-0.57 increasing to 0.67-0.95 at 77 K. It has been shown that while at room temperature, solvent shell relaxation around the excited state can occur, and emission is from an equilibrium excited state to a twisted ground state, at 77 K in a rigid matrix environment solvent shell relaxation cannot occur and emission is from a Franck-Condon excited state to a planar ground state. The TAAs studied have excellent thermal properties for possible use in devices with thermal decomposition temperatures of greater than 300 °C, they also do not crystallise readily.

Three poly {9,9-bis[N,N-(trimethylammonium)hexyl] fluorene-co-1,4-phenylene}, fluorescent cationic conjugated polymers (CCP), of average chain lengths ≈ 6, 12 and 100 repeat units, and their interaction with DNA and guanine are reported. Fluorescence microscopy and atomic force microscopy have been utilised to visualise the interaction between the polymers and DNA. Results show both efficient compaction of DNA induced by the polymer and linking and bridging of DNA/polymer aggregates. CCPs are known to aggregate in water, and for the CCPs studied here this is reflected in a decrease in fluorescence. These aggregates can be broken up by mixtures of solvents, e.g. acetonitrile/water. Steady state and ps time resolved techniques have been used to study: (i) aggregation of CCPs in various acetonitrile/water mixtures, and (ii) fluorescence quenching by single and double strand DNA, and guanine. All CCPs are extremely sensitive to quenching by DNA or guanine, with sensitivity increasing with chain length of both the CCP and DNA. Stern-Volmer plots are sigmoidal and have initial quenching rates constants far in excess of the diffusion controlled limit. The results have been analysed in terms of energy migration and trapping within and between polymer chains. Quenching seems best analysed in terms of an equilibrium in which a CCP/DNA aggregate complex is formed which brings polymer chains into close enough proximity to allow interchain excitation energy migration and quenching at aggregate or DNA base traps. We also report preliminary results of modelling time resolved data, of both the aggregation and quenching, using a kinetic model in which energy migration and trapping are represented as a series of energy transfer steps between neighbours.

Contents

Chapter 1: *Introduction*

Chapter 2: *Experimental Details*

Chapter 3: *Photophysics of Some Dehydroabietic Acid Based Triarylamine Dyes*

Chapter 4: ***Cationic Conjugated Polyelectrolytes: Aggregation, Energy Transfer and Photophysical Properties***

Chapter 5: *Imaging and Statistical Image Analysis of CCP-DNA Interactions in Solution and at Surfaces*

5.3 Results

Chapter 6: ***The Interaction of Cationic Conjugated Polyelectrolytes with DNA***

Chapter 7: *Flash Photolysis Study of CCP/DNA and CCP/Guanine Interactions*

Chapter 8: *Conclusions*

Chapter 1

Introduction

1.1 Photochemistry and photophysics

The work presented here falls into two main areas of research: (i) a study of the photophysical properties of a series of triarylamine (TAA) dyes for use in organic light emitting diodes OLEDs and device applications and (ii) a study of the photophysics of a series of cationic conjugated polyelectrolytes (CCPs) and their interaction with DNA. The CCPs studied have potential use as sensors for the detection and identification of DNA. For both the TAAs and CCPs a good understanding of their photophysics is essential for evaluating and fine-tuning their properties for use in any possible devices.

In this chapter a short introduction to photochemistry and photophysics is given along with important considerations for both the polymer and TAA systems. Potential applications of CCPs rely on efficient fluorescence energy transfer and quenching processes and thus particular emphasis is placed on these phenomena in this introduction.

1.1.1 Photochemical principles

Photochemistry deals with those processes by which light interacts with matter so as to induce chemical reactions. By contrast, photophysics is the science of the absorption, transfer, localization, and emission of electromagnetic energy, with no chemical reactions occurring.[1] The fact that radiation can only induce a chemical reaction if it is first absorbed was discovered by von Grotthuss in 1819 and verified John William Draper in 1841. Thus the first principle of photochemistry: '*only the light absorbed by a molecule can produce photochemical change in the molecule*', is known as the Grotthuss-Draper law. Photochemistry, however, was still not well understood until the development of the quantum theory in 1912. Einstein applied the concepts of quantum theory to photochemical reactions and developed the second principle of photochemistry known as Einstein's law of photochemical equivalence, which states that "*each quantum of radiation absorbed by a molecule activates one molecule in the primary step of a photochemical process*". However, under intense laser irradiation multiphoton absorption can take place.

1.2 Excitation

When a molecule absorbs light the process is referred to as excitation. The molecule is raised from its ground state of minimum energy to an excited state of higher energy.[2] Light incident upon a system can be transmitted, scattered, or absorbed. How the energy interacts with the system depends on the wavelength of the incident light. Low energy/long wavelength energy in the infrared region usually only results in rotational and vibrational excitation; however, ultraviolet (UV) and visible light is able to induce transitions between the electronic energy levels of a chemical species leading to electronic excitation.

In general the excited states of organic molecules can be classified as singlet, doublet, triplet, quartet *etc.* where these terms define the multiplicity of the molecular spin state. The multiplicity of a state is given by $(2S + 1)$, where S is the total spin of the state. In the singlet (S_n) state, the electrons are paired with antiparallel spins (i.e. (↑↓)) and there is no resultant spin magnetic moment ($S = 0$). In the triplet state (T_n), there are two unpaired electrons with parallel spins (↑↑) with a resultant spin given by $S=1$. The triplet state is composed of three states which are degenerate in the absence of a magnetic or electric field ($2S+1 = 3$). The photochemistry of most organic molecules is dominated by singlet and triplet states.

1.2.1 Selection rules for electronic transitions

Whether the particular mechanism for excitation and relaxation of electronic energy states is allowed is governed primarily by the spin selection rule. This selection rule arises due to the necessity that angular momentum must be conserved during a transition and that a photon of light has a spin of one. The spin-selection rule states that the spin quantum number (S) must not change during a transition ($\Delta S = 0$). This means that all transfers, radiative or non-radiative, between states that differ in multiplicity in the zero order approximation, in which there are no interactions between states i.e. they are "pure", are forbidden. This begs the question why do "forbidden" transitions such as phosphorescence occur? The answer is due to a breakdown of these selection rules because of interactions between spin angular momentum and orbital angular momentum resulting in spin-orbit coupling which allows the occurrence of "forbidden" transitions.

1.2.2 Light absorption

A molecule can be excited from the ground state into an excited state by the absorption of a photon of light, i.e.

$$A + h\nu \rightleftharpoons A^{*} \qquad [1.1]$$

where A is the molecule to be excited, A^* represents the excited state, and $h\nu$ represents the photon of electromagnetic energy absorbed. A photon can be absorbed only if its energy corresponds to the difference in energy between two stationary states of the molecule. Experimentally, the efficiency of light absorption at a wavelength λ by an absorbing medium is characterized by the absorbance, Abs(λ), defined by the Beer-Lambert law (Equation 1.2).

$$\mathrm{Abs}=\log_{10}\frac{\mathrm{I}_0}{\mathrm{I}} = \varepsilon \mathrm{cl} \qquad [1.2]$$

where I_0 and I are the intensity of the incident and transmitted light, respectively; ε is the molar absorption coefficient, c is the concentration of the absorbing species and l is the absorption path length.

Absorption of ultraviolet and/or visible radiation in organic molecules is restricted to certain functional groups (*chromophores*) that contain valence electrons of low excitation energy. The spectrum of a molecule containing these chromophores is complex due to the fact that the superposition of rotational and vibrational transitions on the electronic transitions gives a combination of overlapping lines. While for relatively simple molecules in the gas phase these may be capable of resolution, in the solution phase, with which all of the work in this thesis is concerned, this results in broad absorption "bands". Possible electronic transitions of π, σ, and n electrons are given in Figure 1.1.

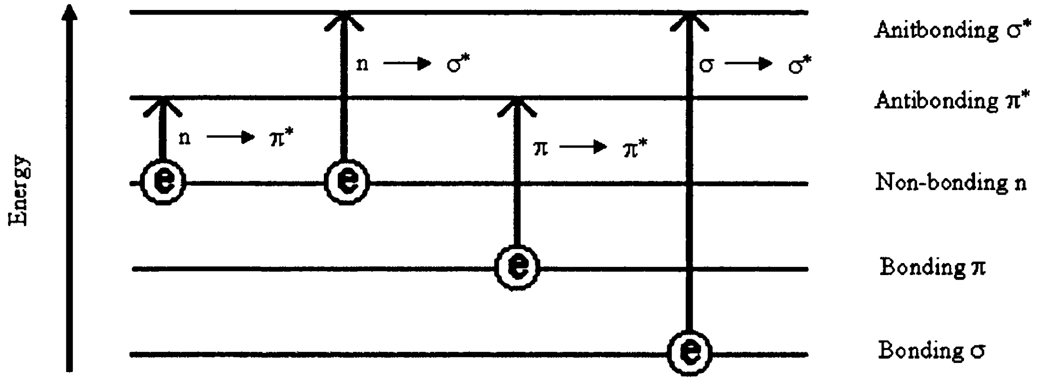

Figure 1.1 Possible electronic transitions of π, σ, and *n* electrons.

Most absorption spectroscopy of organic compounds is based on transitions of *n* or π electrons to the π^* excited state. This is because the absorption peaks for these transitions fall in an experimentally convenient region of the spectrum (200 - 700 nm). These transitions need an unsaturated group in the molecule to provide the π electrons. The solvent in which the absorbing species is dissolved also has an effect on the spectrum of the species. This is discussed further in Section 1.4 along with the Franck-Condon principle.

1.3 Deactivation of excited states

Once a molecule has become electronically excited it contains excess electronic and vibrational energy, and this is lost via a number of relaxation processes and the molecule returns to the ground state. Relaxation occurs via radiative or non-radiative mechanisms. The absorption of light and the resulting processes of decay/relaxation are conveniently represented in the Jablonski diagram (Figure 1.2).

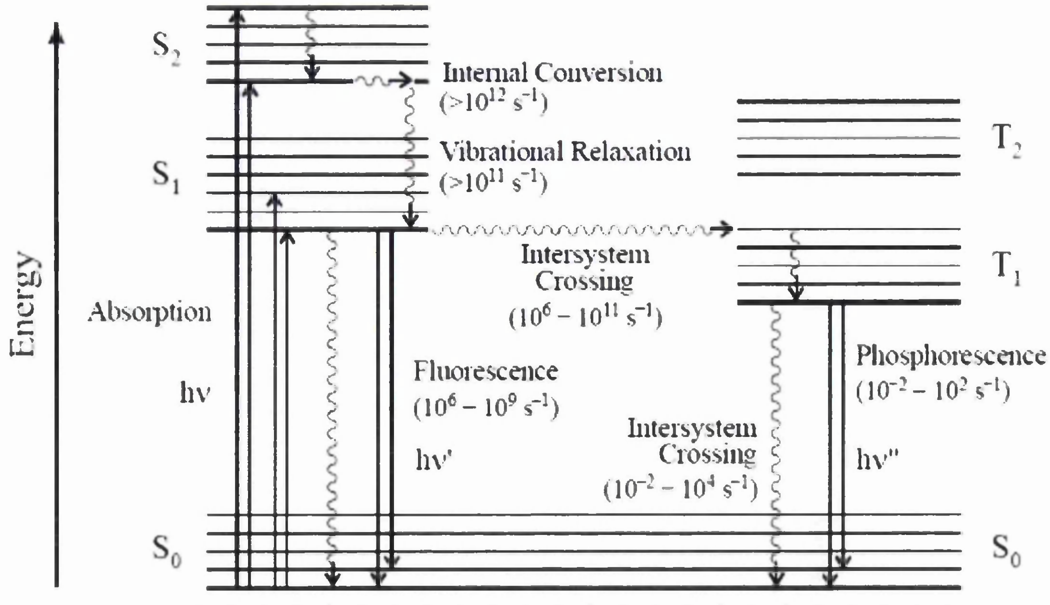

Figure 1.2 The Jablonski Diagram. Radiative transitions are indicated by straight line arrows whereas non-radiative transitions are represented by wavy line arrows. The range of rate constants generally observed is given in parentheses.

1.3.1 Radiative decay

The loss of excess energy via radiative decay, characterised by the emission of a photon of light, is broadly referred to as luminescence. Radiative decay occurs either via fluorescence or phosphorescence. Fluorescence is the term used to describe the radiative decay when the emission of a photon occurs between states of the same spin multiplicity, e.g. singlet-singlet (S_1-S_0) emission.[3] Phosphorescence is the term used to describe radiative decay when the spin states of the initial and final energy levels are different, e.g. triplet-singlet emission ($T_1 \rightarrow S_0$). Phosphorescence is a "forbidden" radiative transition since it is between states of differing multiplicity[4], conversely fluorescence is an "allowed" transition since it occurs between states of the same multiplicity.

1.3.2 non-radiative decay

There are three mechanisms by which non-radiative decay can occur; these are internal conversion (IC), intersystem crossing (ISC), and vibrational relaxation. Internal conversion is the internal transfer of energy between vibronic levels of the same multiplicity (*cf.* fluorescence). Intersystem crossing is internal energy transfer between vibronic levels in states of differing multiplicity (*cf.* phosphorescence). Vibrational relaxation within a state occurs very quickly ($<1\times10^{-12}$ sec) and is enhanced by physical contact of an excited molecule with other particles to which energy, in the form of vibrations and rotations, can be transferred through collisions.

1.4 The Franck-Condon principle

The effects of size, shape, and energy of the molecule on its photophysical properties in its different electronic states can all be rationalized in terms of the Franck-Condon principle.[5,6] The Franck-Condon principle is a consequence of the Born-Oppenheimer approximation[7], which assumes that electronic, vibrational and rotational energy are entirely independent because of the great differences in frequency between the three types of motion. The Born-Oppenheimer approximation can be expressed as;

$$\Psi(r,R) \approx \Psi_{i}(r,R)^{*}\chi_{n(i)}(R) \qquad [1.3]$$

where Ψ is the total wavefunction, r and R are position vectors of the electron and nuclei respectively, Ψ_i is the electronic wavefunction and $\chi_{n(i)}$ is the nuclear wavefunction i.e. the total wavefunction, Ψ, can be expressed in terms of separate electronic, ($\Psi_i(r,R)$), and nuclear, ($\chi_{n(i)}(R)$), wavefunctions. Transitions from the vibrational levels of one electronic state to the vibrational levels of another take place so rapidly (about 10^{-15} sec) that the positions of the nuclei do not change.[3] The potential function of a vibrational mode of a molecule will depend upon the electronic state of the molecule, and the internuclear distances in the electronic excited state will therefore differ from the ground-state value. For an electronic transition to occur there must be a net positive overlap of the vibrational wavefunctions of the initial and final states of the transition, and the degree of this overlap is an indication of transition intensity. Therefore the most intense, and most probable, transition occurs between states with the maximum degree of overlap of vibrational wavefunctions.

Franck-Condon principles can be applied to the interactions between the fluorophore and the surrounding solvent. If we consider a case where a fluorophore has a different dipole moment in the excited state then upon excitation the molecule is excited to a higher electronic energy level in a far shorter timeframe than it takes for the fluorophore and solvent molecules to re-orientate themselves within the solvent-solute interactive environment.[9] As a result, there is a time delay between the excitation event and the re-ordering of solvent molecules around the solvated fluorophore, which generally has a much larger dipole moment in the excited state than in the ground state.[9]

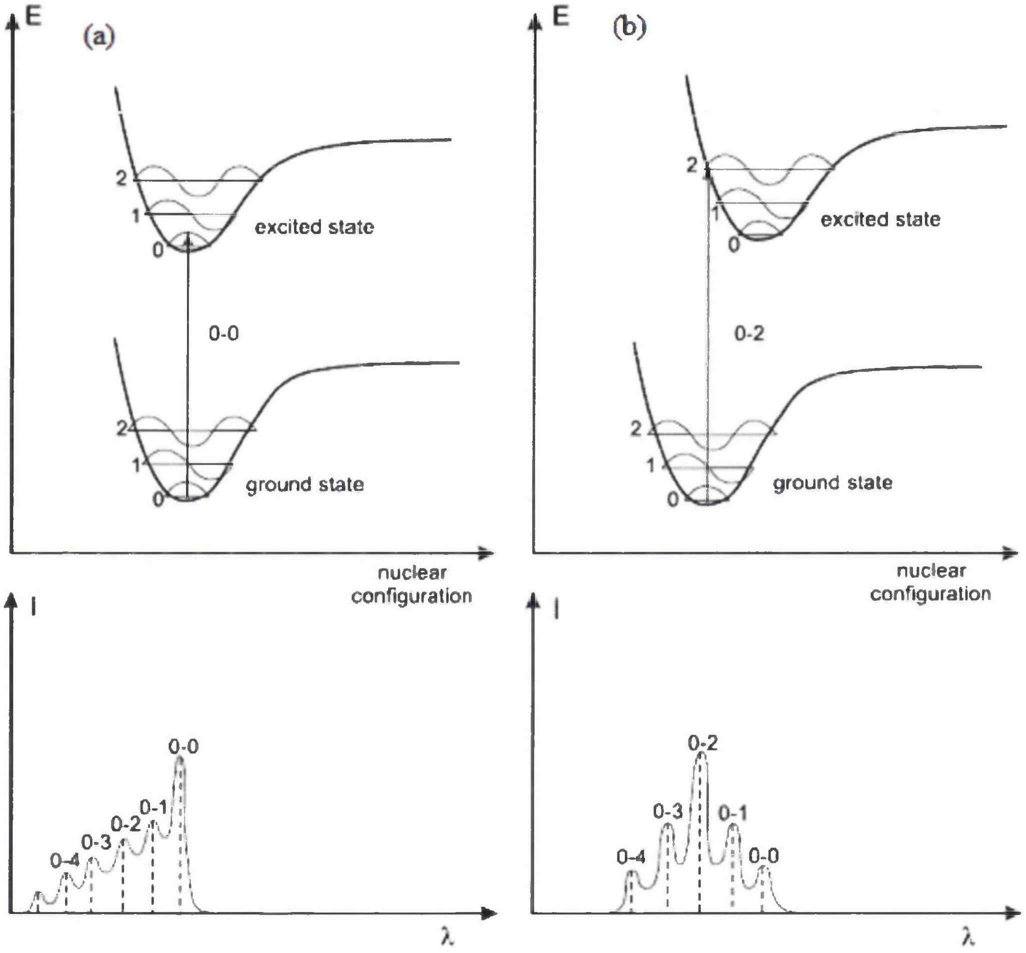

Figure 1.3 Top: Electronic radiative transitions of greatest probability from the lowest vibrational levels between states of a) the same nuclear geometry and b) different nuclear geometry. Bottom: shape of the absorption bands; the vertical broken lines represent the absorption lines that are observed for a vapour, whereas broadening of the spectra is expected in solution (solid line). Figure adapted from reference [8].

After the fluorophore has been excited to higher vibrational levels of the first excited singlet state (S_1), excess vibrational energy is rapidly lost to surrounding solvent molecules as the fluorophore relaxes over the ps timescale to the lowest vibrational energy level. The rate of solvent relaxation depends on the viscosity of the solvent. Assuming the solvent relaxation time is short compared with the lifetime of the electronic excited state, emission will be from the lowest solvent stabilised energy state of the excited electronic state. For $\pi \rightarrow \pi^*$ this usually has the effect of reducing the energy separation between the ground and excited states, and the magnitude of this reduction in energy separation generally increases with solvent polarity. This results in a red shift of fluorescence emission which increases with solvent polarity. By way of contrast the energy gap for $n \rightarrow \pi^*$ transitions are shifted to shorter wavelengths with increasing solvent polarity because of increased solvation of the lone pair, which lowers the energy of the n orbital.

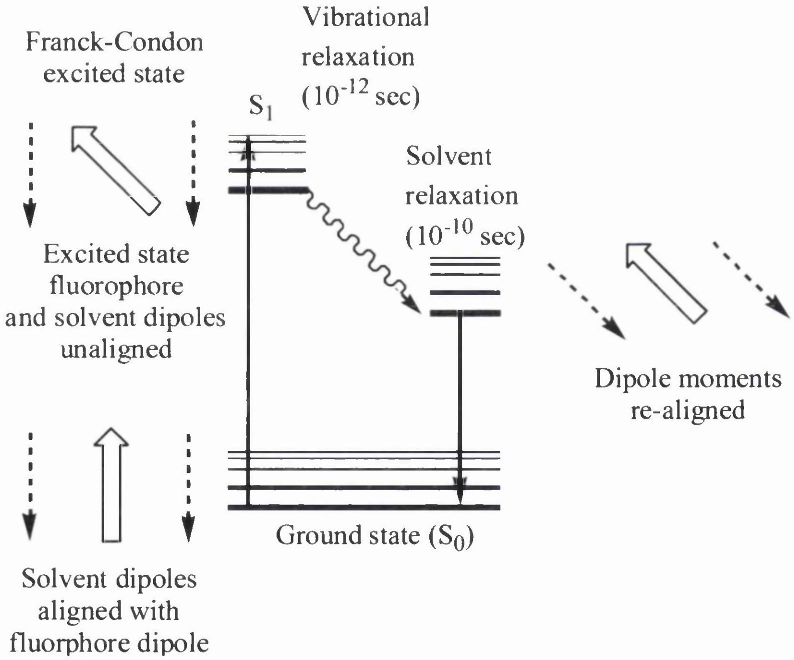

Figure 1.4 The Franck-Condon principle, showing fluorophore-solvent excited state interactions. The block arrows represent the dipole of the fluorophore and the dashed arrows represent the solvent dipoles.

1.5 Intermolecular energy transfer and types of exciton formation

There are three types of excitons: Mott-Wannier, Frenkel and charge transfer excitons.

1.5.1 Mott-Wannier excitons

Mott-Wannier excitons are typical of inorganic semiconductors and involve a Coulombic interaction over a relatively large distance (~100 Å),[10] i.e. they have an interacting radius which is much larger than the lattice spacing (Figure 1.5). The binding energy is usually much less than a hydrogen atom.[11]

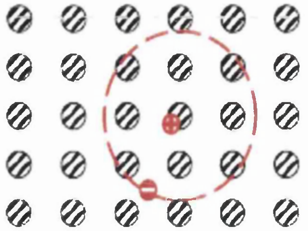

Figure 1.5 The Coulombic interaction in a Mott-Wannier exciton.

1.5.2 Frenkel excitons

Frenkel excitons are found in organic materials which have a small dielectric constant and thus the Coulombic interaction between the electron and the hole is relatively large and consequently over a much smaller distance (~10 Å).[12] The fact that the Coulombic interaction is over a much shorter distance results in a larger binding energy (~1 eV) than in the Mott-Wannier case.[13] The electron-hole pair is therefore localised on the same molecular site (Figure 1.6).[14]

Figure 1.6 The electron-hole pair in a Frenkel exciton.

1.5.3 Charge-transfer excitons

Charge-transfer excitons have a Coulombic interaction over a smaller distance than Mott-Wannier excitons. In charge transfer excitons an electron is in correlation with a hole on a neighbouring molecular site. In OLEDs the excitons formed in the emissive layer are Frenkel or charge-transfer excitons. In order to induce electroluminescence the excitons must transfer their energy non-radiatively to the excited states of the dopant molecules. This energy transfer may occur via charge trapping, or Förster or Dexter energy transfer.

1.5.4 Förster energy transfer

Förster energy transfer[15,16] (also known as dipole-dipole energy transfer, and Förster Resonance Energy Transfer, FRET) is a long range Coulombic interaction (~40-100Å). The energy transfer occurs via dipole-dipole coupling of donor (D) and acceptor (A) states. The interaction energy depends on both the distance between the molecules and their relative orientation. There is a need for the energy difference between states of the donor to match that for an absorption transition in the acceptor. Then, with sufficient coupling between these molecules (overlap of the emission spectrum of the donor and absorption spectrum of the acceptor), both processes may occur simultaneously, resulting in a transfer of excitation from the donor to the acceptor molecule.[17] Due to the need for an allowed transition in the acceptor, this mechanism transfers energy from the excited state in the donor exciton to the singlet state of the acceptor molecule (Equation 1.4), since in this case the spectral overlap integral is at its maximum, via : -

$$^1\mathrm{D}^* + {}^1A \rightarrow {}^1\mathrm{D} + {}^1A^* \qquad [1.4]$$

In most cases the donor exciton must be a singlet to participate in energy transfer; however, there is an exception for donor materials where a triplet-to-ground state transition is weakly allowed. Here the long donor lifetime compensates for a slow energy transfer rate. The energy transfer process culminating in Förster energy transfer is summarised in Figure 1.7. Förster showed that the rate of energy transfer between D* and A for a dipole-dipole interaction may be given by:[17]

$$k_{DA} = \frac{k^2 J \times 8.8 \times 10^{-28}}{n^4 \tau_{rad} R^6} \qquad [1.5]$$

where k^2 is an orientation factor which reflects that interaction between two dipoles in space, J is the spectral overlap integral of D* emission with *A* absorption, taking into account the molar absorption coefficient (ε) of the $A \rightarrow A^*$ transition, n is the refractive index of the medium, τ_{rad} is the radiative lifetime of the donor, D, and R is the distance between D and *A*.

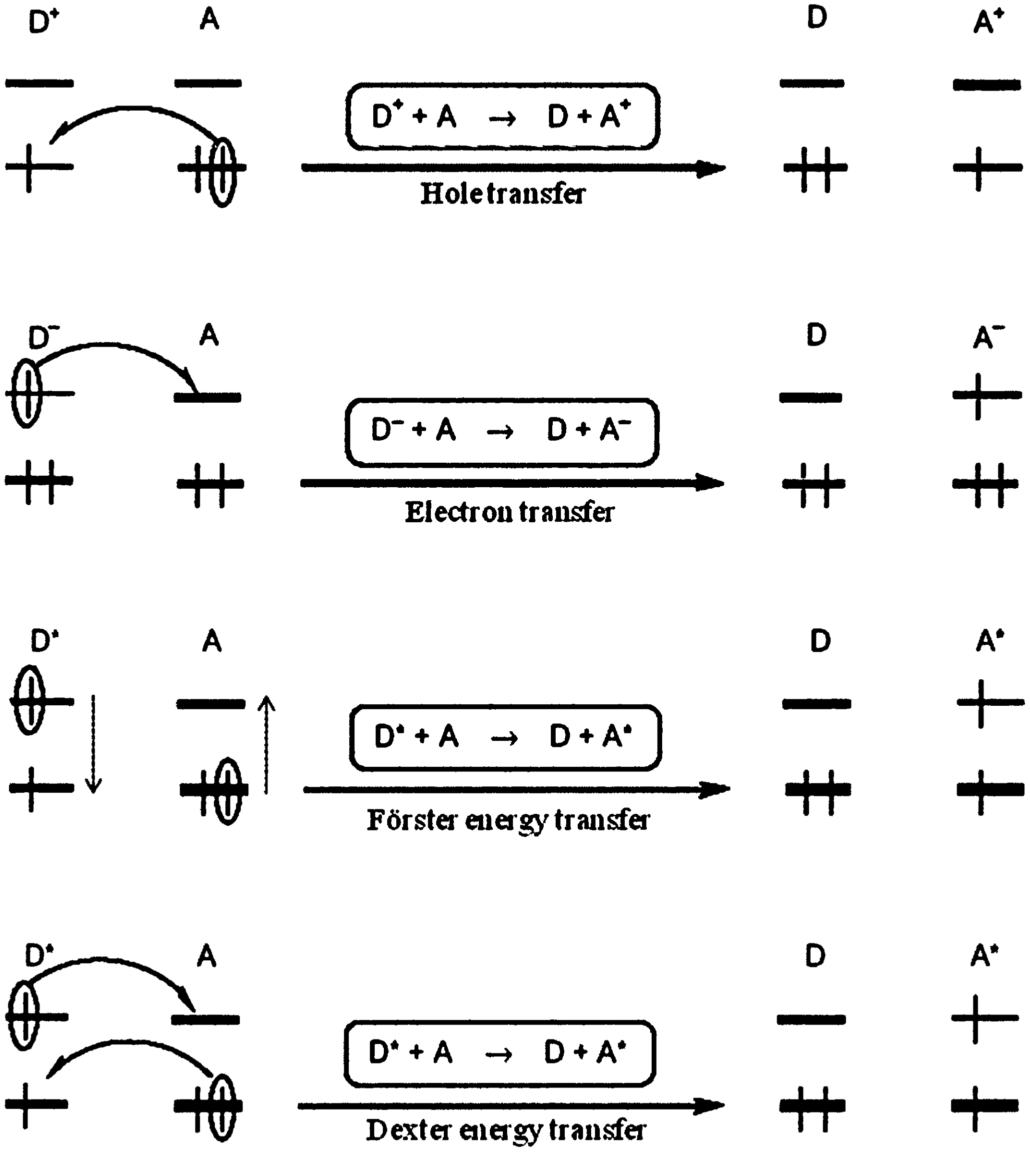

Figure 1.7 Hole and electron transfer and Förster and Dexter energy transfer.

To this point we have considered the donor and acceptor molecules to be different. However, if a fluorophore's excitation spectrum overlaps its emission spectrum, homo- transfer FRET can occur between identical molecules. Excitation transfer between like molecules can occur in repeated steps. This means that the excitation may migrate from the absorbing molecule over a considerable number of other ones before deactivation occurs by fluorescence or other process.[16] This is especially relevant to polyelectrolyte systems where it is possible for excitation energy to transfer along the polymer chain until an energy trap is reached.

1.5.5 Dexter energy transfer

Dexter energy transfer occurs over a shorter distance than Förster energy transfer typically ~10 Å. In this mechanism energy transfer occurs via intermolecular electron exchange (Figure 1.7). Since the only requirement is that the spin is conserved after the energy transfer occurs Dexter energy transfer process permits both singlet-singlet (Equation 1.6) and triplet-triplet transfer (Equation 1.7).

$$^{1}\mathrm{D}^{*} + {}^{1}A \rightarrow {}^{1}\mathrm{D} + {}^{1}A^{*} \qquad [1.6]$$

$$^{3}\mathrm{D}^{*} + {}^{1}A \rightarrow {}^{1}\mathrm{D} + {}^{3}A^{*} \qquad [1.7]$$

Dexter proposed that the rate constant for energy transfer by the electron exchange mechanism may be given by:[5,9]

$$k_{DA} = K'J\exp^{\left(\frac{-2R_{DA}}{L}\right)} \qquad [1.8]$$

where K′ is related to specific orbital interactions, J is the spectral overlap integral and R_{DA} is the donor-acceptor separation relative to their Van der Waals radii, L. Dexter processes are relatively slow except in the case of interactions between neighbouring molecules and thus Förster energy transfer usually dominates singlet-singlet transfer.

1.5.6 Charge-trapping

Due to the slow rates of Dexter energy transfer a third mechanism known as charge-trapping may successfully compete in triplet-triplet transfer. Charge-transport involves a guest molecule which traps the charge and then generates an exciton by recombination with an opposite charge on a neighbouring molecule. The type of energy transfer that occurs within OLEDs depends on the lifetime of the exciton, its mobility within the film, and the thickness of the emissive layer. The predominant energy sink for singlet excitons is Förster energy transfer.[19]

1.6 Quenching of fluorescence

A number of processes can lead to a reduction in fluorescence intensity, i.e., quenching. These processes can occur during the excited state lifetime, for example collisional quenching, energy transfer, charge transfer reactions, or they may occur due to formation of complexes in the ground state. There are two quenching processes usually encountered; namely collisional (dynamic) quenching and static (complex formation) quenching.[17] Fluorescence quenching, other than self-quenching, involves at least two chemical species, the fluorophore and the quencher.

1.6.1 Collisional quenching

Collisional quenching occurs when the excited fluorophore experiences contact with an atom or molecule that can facilitate non-radiative transitions to the ground state. In the simplest case of collisional quenching in homogeneous solution the quenching can be described by the SV relationship (Equation 1.9).

$$\frac{I_0}{I}=\frac{\tau_0}{\tau}=1+k_{SV}[Q] \qquad [1.9]$$

where I_0 and I are the fluorescence intensities, and τ_0 and τ are the fluorescence lifetimes, in the absence and presence of quencher respectively. In simple cases I_0/I and/or τ_0/τ are linearly related to the quencher concentration with a gradient of K_{sv}, the SV constant. The magnitude of K_{sv} can be used as a measure of the sensitivity of a given lumophore towards a quencher. The Stern-Volmer constant is given by:

$$k_{SV}=\frac{k_q}{k_r+k_{IC}+k_{ISC}}=k_q\tau_{nat} \qquad [1.10]$$

where τ_{nat} is the natural lifetime of the lumophore, i.e. the lifetime in the absence of the quencher.

1.6.2 Static quenching

In some cases, the fluorophore can form a stable complex with another molecule. If this complex is non-fluorescent, or even just less fluorescent that the free fluorophore, then we say that the fluorophore has been statically quenched. Over certain fluorophore and quencher concentration ranges the quenching process can again be described in terms of a SV relationship, however in this case the K_{SV} gives an indication of the strength of the association formed. In this case K_{SV} is sometimes referred to as an association constant K_a. Such cases of quenching via complex formation were first described by Weber.[18] In the case of static quenching the lifetime of the sample will not be reduced since those fluorophores which are not complexed n will have normal excited state properties.

1.6.3 A combination of static and dynamic quenching

It is possible, and indeed is quite common, that a fluorophore can be quenched by a combination of both static and dynamic quenching. This results in SV plots with an upward curvature as is shown in Figure 1.8. If both static and dynamic quenching are occurring then the SV equation can be modified to;

$$\frac{I_0}{I} = (1 + k_{\text{static}}[Q])(1 + k_{\text{dynamic}}[Q]) \qquad [1.11]$$

As can be seen the equation is second order in term of [Q] which accounts for the upward curvature of the graph. Since the lifetime is unaffected by the presence of quencher in cases of pure static quenching, a plot of I_0/I against [Q] would give a straight line. Therefore lifetime measurements are useful in identifying the dynamic and static components of quenching in systems where both types of quenching occur simultaneously.

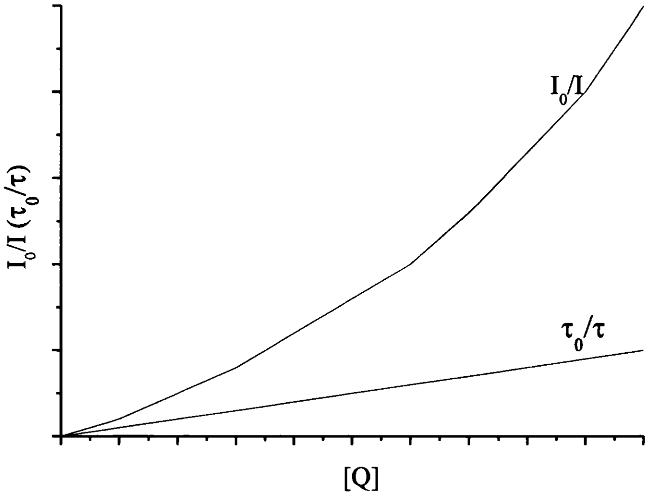

Figure 1.8 Typical SV plot for a combination of static and dynamic quenching.

1.6.4 Self-quenching

Self-quenching is the quenching of one fluorophore by another one of the same kind. It is a widespread phenomenon in fluorescence, but it requires high concentrations or labelling densities. The general physical description of the self-quenching processes involves a combination of trap-site formation, energy transfer among fluorophores, and trap-site migration, which results in quenching. Trap sites may be formal fluorophore complexes or aggregates, or they may result from sufficiently high concentrations of fluorophores leading to molecules in close proximity. Aggregation quenching is a common characteristic of the conjugated cationic polymers (CCPs) discussed in Chapters 4, 6 and 7.

1.6.5 Quenching by electron transfer

In an electron transfer reaction two neutral molecules, for example, will form an ion pair; if one of these neutrals is electronically excited it will be deactivated, and the overall process may appear as a quenching if the ion pair recombines to return to the neutral ground state partners as is shown by Figure 1.9.[18]

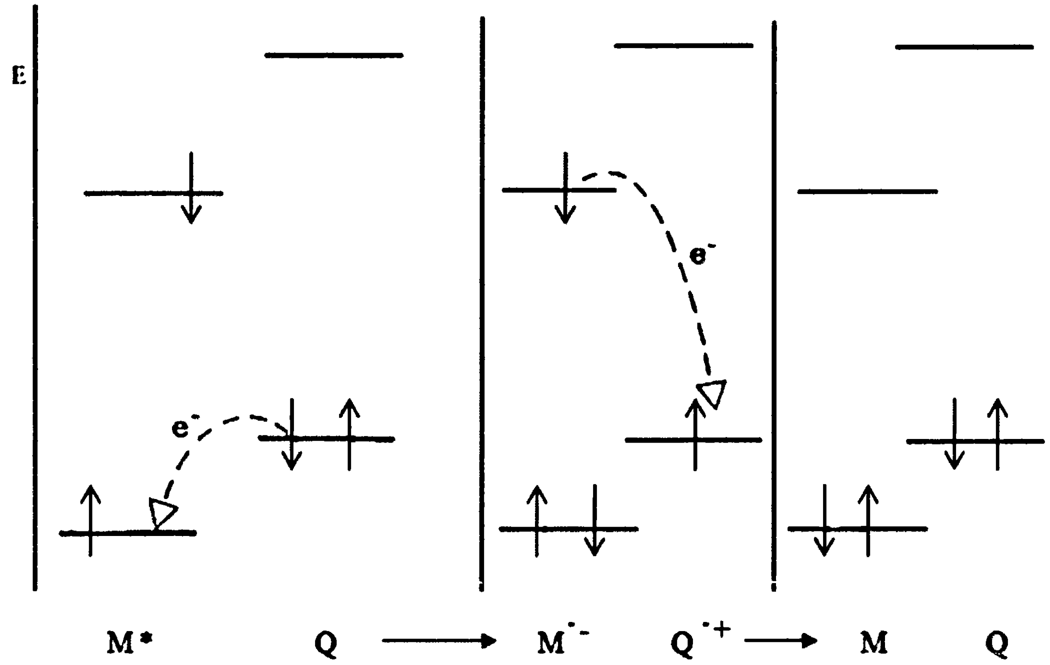

Figure 1.9 Quenching of an excited state molecule through electron transfer. An ion pair is formed initially within which back electron transfer leads to overall deactivation of the excited energy donor. Figure adapted from reference [19]

1.7 Fluorescence and molecular lifetimes

The properties of fluorophores are often described as if they are studied in isolation; however, such is not usually the case. Absorption and emission processes are almost always studied on populations of molecules and the properties of the supposed typical members of the population are deduced from the macroscopic properties of the process. In general, the behaviour of an excited population of fluorophores is described by the rate equation:

$$\frac{\Delta n^*}{\Delta t} = -n^*k+f(t) \qquad [1.12]$$

where n* is the number of excited molecules at time t, k is the rate constant of emission and f(t) is an arbitrary function of the time, describing the time course of the excitation.

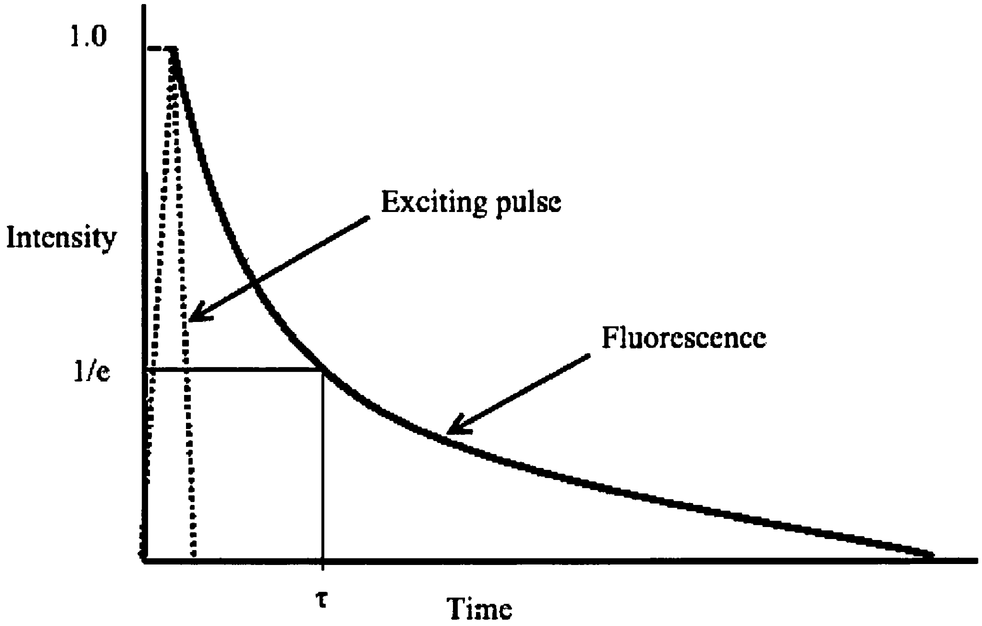

Figure 1.10 Typical time resolved fluorescence decay curve showing the exciting pulse and fluorescence decay.

In most cases of interest, it is virtually impossible to predict a priori the excited state lifetime of a fluorescent molecule. The radiative lifetime, i.e., the lifetime one expects in the absence of any excited state deactivation processes other than fluorescence can be approximated by the Strickler-Berg equation.[20]

$$(\tau)^{-1}=2.88\text{x}10^{-9}n^{2}\left[\langle\nu_f^{-3}\rangle\right]^{-1}\left[\int\left(\frac{\varepsilon(\nu_a)}{\nu_a}\right)d\nu\right] \qquad [1.13]$$

Where n is the solvent refractive index; ε is the molar absorption coefficient which, in the third term on the RHS, is integrated over the lowest energy absorption band with respect to ν, the frequency of the transition in cm^{-1}. The term ν_f^{-3} is given by the integral of the emission spectrum in units of quanta at each frequency, divided by the integral of the emission spectrum at ν^{-3} times this value (Equation 1.14).

$$\left[< \nu_f^{-3} >\right] = \frac{\int_{\Delta v_e} F(v)dv}{\int_{\Delta v_e} F(v)v^{-3}dv} \qquad [1.14]$$

Δv_e corresponds to the experimental limits of the emission band (S_0-S_1 transitions) and F(v) describes the spectral distribution of the emission in photons per wavelength interval.

Excited state lifetimes have traditionally been measured using either the impulse (or pulse) response or the harmonic response method. In principle both methods have the same information content. These methods are also referred to as either the "time domain" method or the "frequency domain" method. Here we describe the impulse (time domain) method as it is the method used throughout the work described in this thesis.

In the pulse method, the sample is excited with a short pulse of light and the intensity of the emission versus time is recorded. Originally the short light pulses were generated using flash-lamps which had widths on the order of several nanoseconds. Modern laser sources can now routinely generate pulses with widths on the order of picoseconds or shorter. As shown in Figure 1.10, the fluorescence lifetime, τ, is the time at which the intensity has decayed to 1/e of the original value. The decay of the intensity with time is given by Equation 1.15.

$$I_t = ae^{-t/\tau} \qquad [1.15]$$

Where I_t is the intensity at time t, a is a normalization term known as the pre-exponential factor and τ is the fluorescence lifetime. If the sample contains more than one fluorophore or the fluorophore is contained in a heterogeneous environment, the fluorescence decay can often be better described as a sum of exponential functions (Equation 1.16).

$$I_t = \sum_{i=1}^{n} ae^{-t/\tau} \qquad [1.16]$$

Where τ_i are fluorescence lifetimes of the various forms and a_i are the corresponding pre-exponential factors. The interpretation of a_i depends on the nature of the sample: if the emission comes from a single fluorophore in different conformational forms or environments, the a_i factors are proportional to respective populations. If multiple lifetimes result from the presence of several fluorophores in the sample, the a_i pre-exponential factors will depend not only on their populations, but also on radiative probability constants and molar extinction coefficients of respective fluorophores. In most cases the temporal width of the excitation pulse cannot be neglected and the observed decay ($I_{obs}(t)$) will be distorted by convolution with an instrument response function L(t) in accordance with Equation 1.17.

$$I_{obs}(t)=\int_0^t L(t-s)I(s)ds \qquad [1.17]$$

The instrument response function (IRF) L(t) is determined experimentally by using a scatter solution instead of a sample. The IRF accounts for the shape of the excitation pulse and for the temporal response of the detection system. Once $I_{obs}(t)$ and L(t) have been measured analysis software can perform the deconvolution and according to Equation 1.16 vary the fit parameters a_i and τ_i until the best fit to the experimental decay is obtained.

1.8 Thesis overview

The aim of this work is a photophysical characterisation of both; (i) a series of novel triarylamines and (ii) a series of cationic conjugated polyelectrolytes of varying chain length.

The potential uses of (i) and (ii) are very different. The triarylamines are thought to be good candidates for use in OLEDs, whereas the CCPs are thought to be valuable for probing DNA characteristics, and have potential use in DNA biosensors. The main aims were to ascertain the potential of triarylamines for OLED applications and develop an understanding of CCPs and CCP/DNA interactions and photophysics. Chapter 2 describes the experimental techniques used during the course of this study. Chapter 3 describes the photophysical and physical characteristics of a series of triarylamines with their potential application in OLED technology in mind. Chapters 4-7 are related to the study of three CCPs of varying chain length and their interaction with DNA. In Chapter 4 the photophysical properties of the CCPs are described: aggregation of CCPs and energy transfer in terms of energy transfer and trapping in CCP systems are reported and the use of a computer modelling program which is able to assist in the analysis of energy transfer kinetics in linear polymer systems is described. The application of various imaging techniques to CCPs and CCP/DNA interactions, with particular emphasis on the ability of CCP to compact DNA, are described in Chapter 5. In Chapter 6 the photophysical characteristics of CCP/DNA interactions and CCP/DNA base are described With emphasis on energy migration and fluorescence concentration quenching. Chapter 7 describes a flash photolysis study of CCP, and CCP/DNA, and CCP/guanine interactions. Chapter 8 provides some general conclusions.

1.9 References

1. J. Guillet, *Polymer Photophysics and Photochemistry*, Cambridge University Press, Cambridge, England, **1985**.
2. N. J. Turro, *Modern Molecular Photochemistry*, Univeristy Science Books, **1991**.
3. J. D. Winefordner, *Spectrochemical Methods of Analysis*, Wiley-Interscience, Toronto, Canada, **1971**.
4. C. E. Wayne and R. P. Wayne, *Photochemistry*, Oxford University Press, Oxford, **1997**.
5. J. Franck, *Trans. Faraday Soc.*, **1925**, *21*, 536.
6. E. U. Condon, *Phys. Rev.*, **1928**, *32*, 858.
7. M. Born and R. Oppenheimer, *Ann. Phys. (Leipzig),* **1920**, *84*, 457.
8. B. Valeur, *Molecular Fluorescence Principles and Applications*, Wiley Interscience, Weinheim, Germany, **2002**.
9. N. S. Bayliss and E. G. McRae, *J. Phys .Chem.*, **1954**, *58*, 1002.
10. J. M. Ziman, *Principles of the Theory of Solids*, 2nd edition, Cambridge University Press, London, **1969**.
11. Haskal, *Phys. Rev. B*, **1995**, *59*, 4449.
12. Ya. I. Frenkel, *Phys. Rev.,* **1931,** *37*, 17; *Phys. Rev.,* **1931**, *37*, 1276.
13. Q. Fang, B. Xu, B. Jiang', H. Fu, W. Zhu, X. Jiang and Z. Zhang, *Synthetic Metals,* **2005**, *155,* 206-210.
14. V. M. Agranovich, *Theory of Excitons*, Nauka, Moscow, **1968.**
15. T. Förster, *Ann. Physik.*, **1948**, *437*, 55-75.
16. T. Förster, *Disc. Farad. Soc.*, **1959**, *27*, 7-17.

17. J. R. Lakowicz, in *Principles of Fluorescence Spectroscopy*, 3rd edition, Plenum Press, New York, Springer, **2006**.
18. G. Weber, *Trans Faraday Soc.*, **1948**, *44*, 185-189.
19. P. Suppan, *Chemistry and Light*, Royal Society of Chemistry; 1st edition, **1994**.
20. Strickler-Berg, *J. Chem. Phys.,* **1962**, *37*, 814.

Chapter 2

Experimental Details

2.1 Materials

Chemical	**Supplier**	**Grade**
2-mercaptoethanol	Sigma-Aldrich	
4,6-diamidino-2- phenylindole (DAPI)	Sigma-Aldrich	
Acetone	Sigma-Aldrich	
Acetonitrile	Lab-Scan	Spectroscopic
Ammonium cerium (IV) nitrate	Sigma-Aldrich	99.99+%
Bacteriophage T4 DNA	Wako Nippon Gene	
Chloroform	Sigma-Aldrich	Spectroscopic
Cyclohexane	Sigma-Aldrich	Spectroscopic
Diisodecyl phthalate (DIDP)	Sigma-Aldrich	
Ethanol	Sigma-Aldrich	Spectroscopic
Guanine	Sigma-Aldrich	
Isopropanol	Sigma-Aldrich	Spectroscopic
Methylcyclohexane	Sigma-Aldrich	Spectroscopic
Polyethylene glycol 2000 (PEG)	Sigma-Aldrich	
Salmon testes DNA	Sigma-Aldrich	
Spermidine	Sigma-Aldrich	
Tris-HCl buffer	Sigma-Aldrich	
YOYO®-1 iodide	Invitrogen	

2.2 Reporting of experimental details

General experimental/instrumental techniques are reported here. Detailed descriptions of the materials and the instruments used for each specific application are given in the experimental section of the relevant chapter along with the appropriate sample preparation methods.

2.3 Steady-state measurements

2.3.1 UV/vis spectroscopy

Absorption spectra were recorded with a Hewlett Packard 8452A diode array spectrophotometer or a Shimadzu UV-2100 spectrophotometer. All UV-Vis absorption spectra were measured against the appropriate background reference. 77 K absorption spectra were obtained using a custom made quartz dewar containing liquid nitrogen which was held in the sample beam of the spectrophotometer using a specifically made attachment.

2.3.2 Fluorescence spectroscopy

Emission spectra were recorded using various spectrophotometers. The brief experimental section at the beginning of each chapter will specify which was used for the relevant investigation. A general schematic representation of a fluorometer is shown in Figure 2.1.

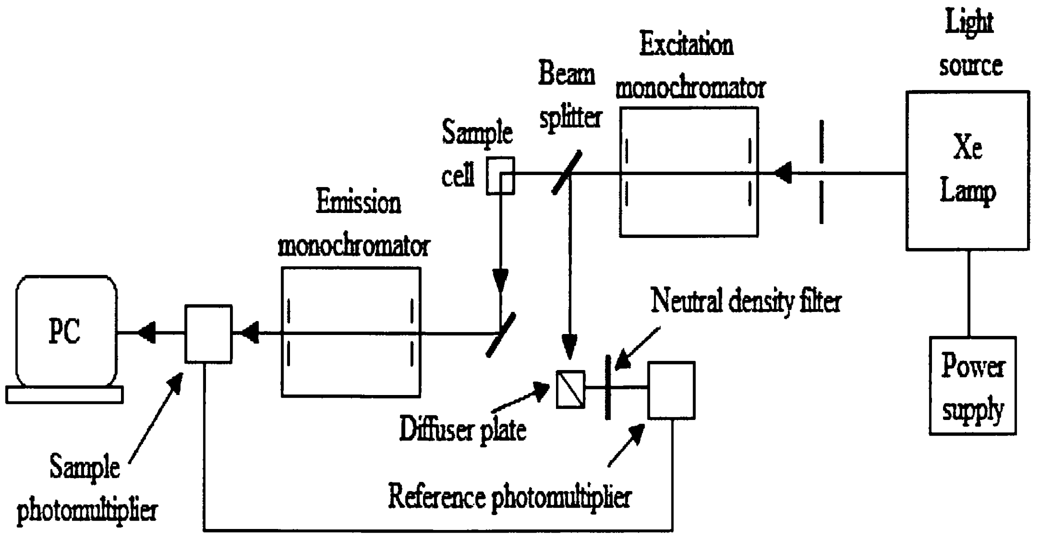

Figure 2.1 General schematic of a fluorimeter.

1) Most fluorescence spectra were measured in 1 cm quartz cuvettes using 90 degree geometry on a Jobin Yvon-Spex Fluorolog 3-22 instrument with 4.0 nm excitation and emission slits. Fluorescence spectra were automatically corrected for the spectral response of the light source (450 W xenon lamp, lamp profile given in Figure 2.2) and detector using the manufacturer's correction files.

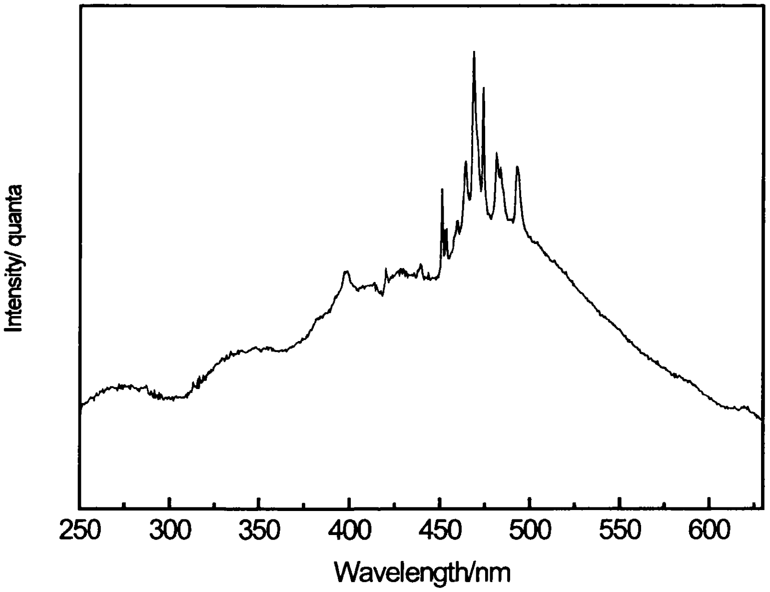

Figure 2.2 Lamp profile of a 450 W xenon arc lamp.

2) Some room temperature and all 77 K measurements were performed on a Perkin Elmer MPF-44E fluorescence spectrometer. The excitation source is a 150 W xenon arc lamp and the detector is a Hammamatsu R928 photomultiplier. The emission and excitation grating monochromators enable continuously variable bandpass selection from 0.2 to 20 nm. The wavelength accuracy of both the excitation and emission monochromator was checked by placing a diffusing plate in the cell holder so that it reflected the radiation from the excitation monochromator to the emission monochromator. To check the accuracy of the excitation monochromator the excitation wavelength was set to 430 nm with the excitation and emission slits set and 1 nm and 5 nm respectively, the spectrum was then recorded from 430 to 480 nm at a scan speed of 30 nm/min. To check the emission monochromator this procedure was repeated but the excitation wavelength was set to zero order with excitation and emission slits of 5 nm and 1 nm respectively. The wavelength accuracy was checked by comparison to the bright lines at 467.1 nm and 450.1 nm of the xenon lamp (see Figure 2.3). The instrument was accurate to ±0.30 nm which was not considered to be enough of an error to correct for.

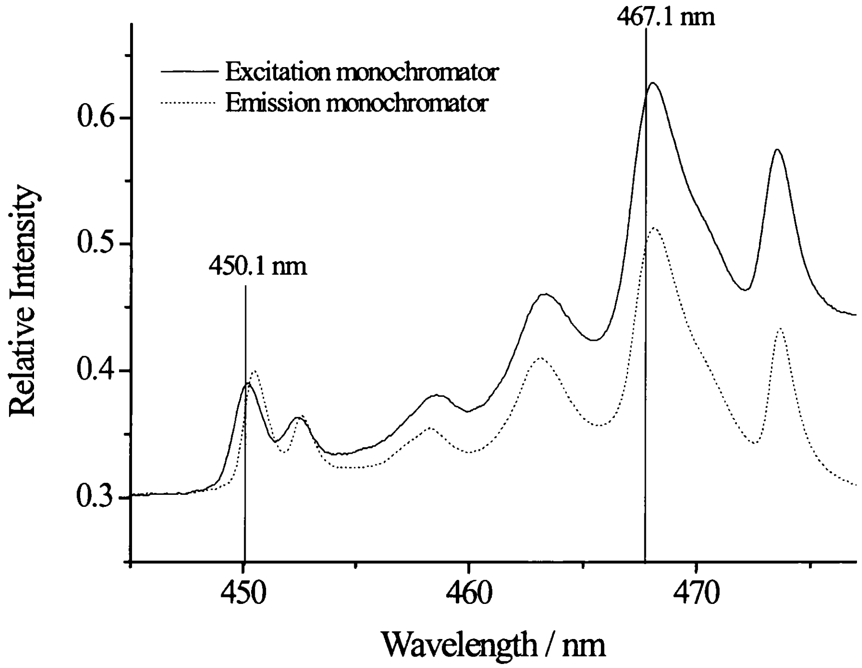

Figure 2.3 Emission of xenon lamp for determination of the wavelength accuracy of the instrument.

3) Some fluorescence anisotropy measurements we carried out with a Jobin-Yvon JY3 D spectrofluorometer with a 150 W xenon arc lamp and a Hammamatsu R928 photomultiplier.

4) Some room temperature measurements were performed on a Perkin Elmer LS 55 fluorescence spectrometer with a 150 W xenon arc lamp.

2.3.3 Fluorescence anisotropies

Steady-state fluorescence anisotropy experiments were carried out either using a Jobin-Yvon JY3 D spectrofluorometer or using a Jobin-Yvon Fluoromax-3 spectrometer with right angle geometry. Fluorescence anisotropies were measured using the single channel (L-format) method. This method must be used when fluorometers only have a single emission channel. To calculate the anisotropy four fluorescence spectra are recorded; one for every configuration of polarizers. The Jobin-Yvon Fluoromax-3 spectrometer has a complete PC controlled set-up with the position of the polarizers automatically changed between the four measurements needed. The Jobin-Yvon JY3 D spectrofluorometer was fitted with a polarizer accessory mount and Polaroid® polarizers (063-0571) which had to be manually changed to the required positions. Fluorescence anisotropy was calculated according to Equation 2.1.

$$r=\frac{I_{VV}-GI_{VH}}{I_{VV}+2GI_{VH}} \qquad [2.1]$$

where

$$G=\frac{I_{HV}}{I_{HH}} \qquad [2.2]$$

Here r is the fluorescence anisotropy, I is the intensity of the emission corrected for instrument response, V and H refer to the alignment of the excitation and emission polarizers respectively, and G is the instrumental correction factor for the wavelength response to polarization of the detection system. This correction must be included to correct for the wavelength response to polarization of the emission optics and detector.

2.4 Time-resolved emission measurements

2.4.1 Nanosecond lifetimes

Nanosecond fluorescent decays (fluorescence lifetimes) were measured using a home built time-correlated single photon counting apparatus with nitrogen filled IBH 5000 coaxial flashlamp as excitation source, Jobin-Yvon monochromator, Phillips XP2020Q photomultiplier, and Canberra Instruments time-to-amplitude converter and multichannel analyser. Alternate measurements (1000 counts per cycle), controlled by Decay® software (Biodinâmica Portugal), of the pulse profile at the excitation wavelength and the sample emission were performed until 1-2×10^4 counts at the maximum were reached.[1] All samples were held in 1 cm square cells and had an absorption of ~ 0.2 at the excitation wavelength. The fluorescence decays were analysed using the modulating functions method of Striker with automatic correction for the photomultiplier "wavelength shift".[2]

2.4.2 Picosecond lifetimes

Fluorescence decay times with picosecond time resolution were obtained by using a home-built picosecond time correlated single photon counting (TCSPC) apparatus.[3] The excitation source consists of a picosecond Spectra Physics mode-lock Tsunami laser (Ti: sapphire) model 3950 (repetition rate of about 82 MHz, tuning range 700-1000 nm), pumped by a Millennia Pro-10s, frequency-doubled continuous wave (CW), diode-pumped, solid-state laser (λ_{em} 532 nm). A harmonic generator, model GWU-23PS (Spectra-Physics), is used to produce the second and third harmonic from the Ti:sapphire laser exciting beam frequency output. The samples were measured with excitation at 395 nm and the horizontally polarized output beam from the GWU (second harmonic) was first passed through a ThorLabs depolarizer (WDPOL-A) and then through a Glan-Thompson polarizer (Newport 10GT04) with vertical polarization. Emission at 90° geometry collected at magic angle polarization was detected through a double subtractive Oriel Cornerstone 260 monochromator by a Hamamatsu microchannel plate photomultiplier (R3809U-50). Signal acquisition and data processing was performed employing a Becker & Hickl SPC-630 TCSPC module. Fluorescence decays and the instrumental response function (IRF) were collected using 4096 channels in a 0.814 ps/ channel scale, until 1×10^4 counts at maximum were reached. The full width at half-maximum (fwhw) of the IRF was about 22 ps and was highly reproducible for identical system parameters.

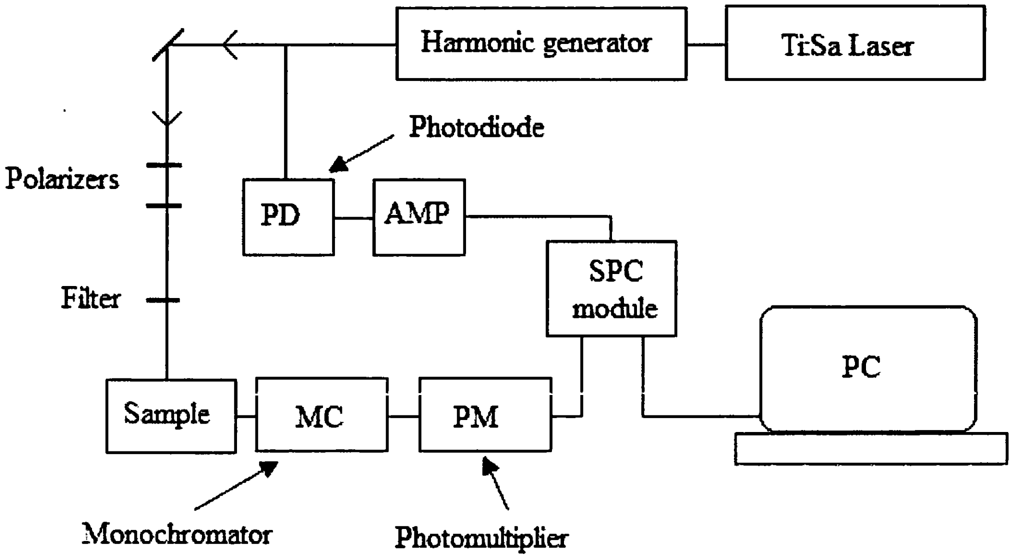

Figure 2.4 Schematic representation of ps-TCSPC set up.

2.4.3 Nanosecond flash photolysis

Flash photolysis experiments were performed with an Applied Photophysics LKS.60 flash photolysis spectrometer pumped by the third harmonic (355 nm) of a Nd:YAG laser (Spectra Physics). Signals were detected with Hamamatsu IP28 and R928 photomultipliers detection and the Tektronix DPO 7254 (2.5 GHz, 40 GSa/s) oscilloscope. The unfocussed excitation beam was ~0.5 cm in diameter with a pulse duration of ~5-6 ns. Samples were contained in 1 cm quartz cells and the transmission was monitored at 90 degrees to the excitation pulse. Transient spectra were obtained by monitoring the optical density change at 5-10 nm intervals over the 250- 700 nm range, averaging at least 4 decays at each wavelength. The photomultiplier signal voltage was kept between 200 and 600 mV in order to ensure linearity.

2.5 Imaging techniques

2.5.1 Fluorescence microscopy

Samples were illuminated with a UV-mercury lamp (100W Ushio Olympus). The fluorescence images of isolated DNA molecules were observed using a Olympus BX51M microscope, equipped with a UplanFL N 100x/1.30 oil-immersed objective lens (∞/0.17/FN 26.5) and a filter set type U-MNU2 (360-370 nm excitation and 400 nm dichromatic mirror). Images were digitized on a computer through a video camera (Olympus digital camera DP70) and were analyzed with an image processor (Olympus DP Controller 2.1.1.176, Olympus DP Manager 2.1.1.158). All observations were carried out at 25 °C. Special care was taken to clean the glass microscope slides (Marienfeld) and cover-slips with ethanol thoroughly before each observation to prevent DNA degradation and precipitation onto the glass surface. The apparent long-axis length of the DNA molecules, L, was defined as a longest distance in the outline of the fluorescence image of single DNA. The blurring effect of fluorescence light due to the diffraction limit causes the images of the DNA molecules to be slightly larger, ca. 0.3 μm, than the molecules. In order to evaluate changes in shape and conformation, 5 s (ca. 22 frames) movies were recorded. For each sample a minimum of twelve movies were recorded at points on the slide chosen by scanning the surface in a four-by-four grid pattern so as not to record the same area twice. From these movies a minimum of 200 DNA molecules were counted and measured

2.5.2 Atomic force microscopy

Samples were imaged in air (20 °C, RH 40.0±5.0 %)), using a Dimension 3100 scanning probe microscope in tapping mode (Digital Instrument Inc. Santa Barbara, CA). Tapping mode probes (Olympus, Japan) with a spring constant of 42 N/m and a nominal tip radius of 5 nm were used throughout. Images were obtained from areas of: 1 μm^2, 2.25 μm^2 and 25 μm^2, at a scan rate of 0.8 Hz and a typical image resolution of 512 x 512 pixels. All images were obtained with the same imaging parameters, amplitude set point, loading force and scan rate. Topographical (height) and phase images were captured simultaneously. At least ten different locations on each mica surface were imaged.

2.6 Image analysis

2.6.1 Analysis of fluorescence microscopy images

Analyses of the fluorescence microscopy images were performed using the public domain Image J 1.31v program (http://rsb.info.nih.gov/ij/) as described further in Chapter 6.

2.6.2 Analysis of AFM images

Analysis of the AFM images was performed using the computer programs Cellprofiler[4] and Nanoscope. Cellprofiler was used to calculate the lengths of the structures on the surface and Nanoscope was used to calculate widths and heights. Nanoscope is built-in AFM software and thus analysis using this program gives any measured values as real scale values, whereas Cellprofiler is an image analysis program that measures in pixels and a conversion factor is needed. Cellprofiler was used in preference to Nanoscope to calculate the lengths since it is better able to account for bending etc. of DNA strands. Cellprofiler works by converting the images to grayscale, with a threshold applied (set by the user) to exclude any artifacts; the program then identifies structures in the images based on contrast from background. DNA was identified from both the major axis length and the eccentricity. (The eccentricity is an indication of the shape; with values of close to one for rod-like structures and values close to zero for spheres). All measured DNA had an eccentricity of greater than 0.90. Average DNA lengths and associated standard deviations were calculated from more than 50 measurements.

2.7 Thermal characterisation

2.7.1 Hot stage microscopy

Hot stage microscopy (HSM) was carried out with a Leica DMRB microscope connected to a Sony HAD CCD-IRIS/RGB colour video camera linked to a Sony multiscan E400 PC monitor and PC. The thermal assembly used a Mettler Toledo FP900, consisting of a FP90 central processor unit and FP84 specimen holder. A five gold–nickel thermocouple arrangement provides the evaluation of the temperature difference between the cell containing the sample and that of the reference. Thus, with this hot stage microscope in addition to image recording, DTA following heating and cooling processes were also obtained. The instrument used for optical observation consisted of a Leica DMRB polarising microscope connected to Sony image processing equipment composed of CCD video camera, video recorder, video monitor and colour video printer. The sample was observed through the microscope, and either projected on the screen or recorded in a videocassette for later detailed examination. Temperature readings of the central processor unit were checked by determining the melting point of benzophenone (calibration substance, Mettler–Toledo, t_{fus}=48.1±0.2 °C) and benzoic acid (certified reference material, LGC 2606, t_{fus}=122.35±0.03 °C). The values obtained for these standards were 48.1±0.2 °C and 122.3±0.2 °C, respectively. Reported uncertainties correspond to 95% confidence interval based on five determinations. Benzoic acid was also used for quality assurance of the DTA method. The heating rate could be controlled between 0 and 20 °C min^{-1}. The heating rate was usually 10 °C min^{-1} and the cooling rate, using cold airflow, was 4 °C min^{-1}. A small amount of the substance to be studied was placed in a glass crucible and covered with a glass lid. Care was taken in order to have the solid particles separated from each other. This procedure allows the user to follow what happens to each solid particle during heating and cooling, in successive thermal cycles. An empty glass crucible identical to that of the sample was used as the reference. Any sample was submitted to five heating/cooling cycles between room temperature and the melting point and for each substance five samples were taken. Samples were usually imaged by 200 × magnification.

2.7.2 Thermogravimetric analysis

Thermogravimetric analysis was carried out with a Rheometric Scientific Simultaneous Thermal Analyser (STA). All samples were run in a nitrogen atmosphere and were heated from 30-625 °C at a rate of 10 °C/min. Sample masses in the range of 0.5-1 mg were used. All samples were run under identical conditions.

2.8 Calculations and data analysis

The more common calculations and general photochemical characteristics that have been used in several areas throughout the work are described here. More specific calculations and data treatment is given in the appropriate chapter. e.g. calculation of radiative lifetimes in Chapter 3.

2.8.1 Molar extinction coefficients

Molar extinction coefficients (ε) were obtained, in most cases, using six solutions of increasing sample concentration. Solutions of varying concentrations were obtained from dilutions from a 'mother' solution. Typically the mother solution was ~ 1 mg of sample in 5ml of solvent. The sample masses of ~ 1 mg were recorded using a six figure accurate mass balance. The values of the molar extinction coefficients were determined from slopes of absorbance as a function of concentration according to the Beer-Lambert law (Equation 1.2 Chapter 1). The error associated with the molar extinction coefficient was calculated from the line of best fit to the Beer-Lambert plots using Origin software®.

2.8.2 Solution phase fluorescence quantum yields

The most reliable method for recording the fluorescence quantum yield (Φ_f) is the comparative method of Williams et al.[5] which involves the use of well characterised reference compounds with known Φ_f values. Essentially, solutions of the standard and samples with optically matched absorbance at the same excitation wavelength absorb the same number of photons. Hence, a simple ratio of the integrated fluorescence intensities of the two solutions (recorded under identical conditions) will yield the ratio of the quantum yields. In all cases α-4-oligothiophene ($\Phi_f = 0.16$ in acetonitrile

^{6}) was used as the reference compound.. Φ_f for the sample is calculated using Equation 2.3, below.[7]

$$\Phi_f=\frac{\int_{cp} I(\lambda)d\lambda}{\int_{ref} I(\lambda)d\lambda}.\frac{\eta_{cp}^2}{\eta_{ref}^2}.\Phi_{f(ref)} \qquad [2.3]$$

Where $\int_{cp} I(\lambda)\, d\lambda$ is the integrated area of the emission spectrum of the sample; $\int_{ref} I(\lambda)\, d\lambda$ is the integrated area of the emission spectrum of the reference (both corrected for the spectral response of the lamp as discussed in Section 2.3.2), η is the solvent refractive index, and $\Phi_{f\,(ref)}$ is the quantum yield of the reference compound.

2.8.3 Stern-Volmer analysis

Stern-Volmer quenching constants were calculated from Equation 2.4. Stern-Volmer values were obtained from either the integrated area of emission or from the maximum intensity of emission.

$$\frac{I_0}{I}=\frac{\tau_0}{\tau}=1+K_{SV}[Q] \qquad [2.4]$$

I_0 and I are the fluorescence intensities, and τ_0 and τ are the fluorescence lifetimes, in the absence and presence of quencher respectively, [Q] is quencher concentration, and K_{SV} is the Stern-Volmer constant.

2.8.4 Error analysis

In most cases throughout this work, the error estimates quoted are ± one standard deviation (σ), where standard deviation is the square root of the sample variance (σ^2) of *n* observations, $x_1, x_2 \ldots x_n$, given by:

$$\sigma=\sqrt{\sum_{i=1}^{n}\frac{(x_i.-\bar{x})^2}{n^{-1}}} \qquad [2.5]$$

where $\bar{x}$ is the mean value.

Where the reported error is associated with a calculated value, the appropriated propagated error is quoted. The propagated error takes into account all the uncertainties associated with the parameters involved in the calculation and is determined from Equation 2.6 for addition/subtraction and from Equation 2.7 for division/multiplication:

$$y=\sqrt{a^2+b^2} \qquad [2.6]$$

$$\frac{y}{Y}=\sqrt{\left(\frac{a}{A}\right)^2+\left(\frac{b}{B}\right)^2} \qquad [2.7]$$

where y is the error of the calculated value Y, and a and b are the errors of the variables A and B respectively.

2.9 References

1. J. Seixas de Melo, L. M. Silva and M. Kuroda, *J. Chem. Phys.*, **2001**, *115,* 5625.
2. G. Stricker, V. Subramanian, C. A. M. Seidel and A. Volkmer, *J. Phys. Chem. B,* **1999**, *103*, 8612.
3. J. Pina, S. Seixas de Melo, H. D. Burrows, A. L. Maçanita,F. Galbrecht, T. Bünnagel, U. Scherf, *Macromolecules,* **2009**, *42*, 1710.
4. M. R. Lamprecht, D. M. Sabatini, A. E. Carpenter, CellProfiler: free, versatile software for automated biological image analysis. *Biotechniques*. **2007,** *42*, 71-75.
5. T. R. Williams, S. A. Winfield and J. N. Miller, Relative fluorescence quantum yields using a computer controlled luminescence spectrometer, *Analyst*, **1983**, *108*, 1067.
6. R .S. Becker, J. Seixas de Melo, A. L. Macanita and F. Elisei, *J. Phys. Chem*, **1996**, *100*, 18683 - 18685.
7. J. N. Miller, Standards in Fluorescence Spectrometry, Chapman and Hall, New York, (**1981**) p.75.

Chapter 3

Photophysics of Some Dehydroabietic Acid Based Triarylamine Dyes

3.1 Introduction

The use of small organic molecules or polymers in molecular electronics has reached the stage where many of these materials are in the preproduction or production phase for use in areas as diverse as light-emitting diodes (LEDs), photovoltaic systems, field effect transistors and chemical and biological sensors.[1] For many of these applications, the organic or polymeric material is present as a thin layer between two electrodes. To facilitate charge injection, thin films of hole and electron transporting materials are deposited on the anode and cathode, respectively. Aromatic amines have been shown to be excellent materials for hole injection.[1] It has been shown that by introducing a dehydroabietic acid moiety in these amines it is possible both to improve the film forming characteristics of these materials by preventing crystallisation and to increase their solubility in common solvents used for solvent film deposition methods.[2] For applications in LEDs, and for the development of novel potential blue light emitters, a photophysical characterisation of these compounds is important.

To achieve organic materials offering high performance for various molecular electronic applications intensive research has been focused on the development of new compounds with significant improvements in non-crystallinity or amorphous film-forming ability, thermal stability, electrochemical reversibility, emission colour purity and lifetime. These have been accompanied by advances in device architecture, leading to tremendous progress in the design and synthetic strategies of triarylamines (TAAs).[3-7]

TAAs possess a wide range of applications due to their outstanding physical, photochemical and electrochemical properties.[8] Aromatic amines have been tested as blue emitters in organic light emitting diodes[9], and also find use in areas such as antioxidants[10]. They also have potential for use as two-photon probes for imaging and other applications.[11,12] One of the most important and widely studied applications of TAAs is as hole transport layers (HTLs)[1,13-20] in organic light emitting diodes (OLEDs).[3] Photovoltaic and LED applications require optimisation of the charge carrier separation and balance, and the use of multilayer structures is a common method to improve efficiency. HTLs, which may also act as electron-blocking layers, have been widely used for this.[21,22] Among the large number of new compounds being tested for these applications, TAAs offer many attractive properties such as high hole mobility and ease of sublimation, leading to a wide range of practical applications.[1,23-25] TAAs are being explored either as small molecules (for which thin films can be formed by vacuum sublimation or by solution processing), or inserted, as co-monomer units, in luminescent copolymers.[26,27] So that light-output can be maximized HTL materials should not absorb in the visible range nor lead to significant light scattering (for which they must be amorphous) To avoid crystallisation, various derivatives (including polymers) with high glass transition temperatures (T_g)[28-30] have been developed. One of the most extensively used materials for this purpose[28] is N,N'-diphenyl-N,N'-bis(3-methylphenyl)-[1,1'-biphenyl]-4,4'-diamine (TPD), with a Tg of 60 °C.[31] However, TPD films prepared by sublimation tend to crystallise over time, even at ambient temperature. To circumvent these problems, many efforts have been devoted to the synthesis of new HTL materials with better thermal and morphological stability, and there is strong interest in the development of amorphous molecular materials for these applications.[3-7] It has previously been shown that TAAs containing a bulky aryl-substituent (a dehydroabietic acid methyl ester moiety)[2,32] inhibit crystallisation and show good solubility characteristics. In addition, the potential of dehydroabietic acid based bipolar arylamine-quinoxalines for device applications has been reported.[33]

3.1.1 OLEDs

The first research carried out on OLEDs which showed efficient organic luminescence was made by Tang and Van Slyke at Eastman Kodak in 1987.[23,34] Since then research into OLEDs has been pursued extensively due to the possibilities of their use in many different technological areas and their inherent advantages over current technologies.[35] The main area of application of OLEDs is in information displays such as televisions, computer monitors, head-up displays (HUD) for aircraft, small screens for mobile phones, car radios and digital cameras and also in high resolution microdisplays for head-mounted displays.[35] OLEDs offer many advantages over both liquid crystal displays (LCDs) and light emitting diodes (LEDs). Their great advantage is that in an OLED display each OLED pixel emits light and so no backlight is needed. OLEDs can be formed into different shapes and can be much thinner than LCD devices.[36] If they are grown on a plastic substrate, they are flexible too. This gives possible OLED devices the extremely interesting property of not having any restriction on size and shape. Thus devices can be in the form of fibres, and woven to fabrics. They can be on bent or rolled films or constitute the surface of three dimensional objects. The low cost of materials and fabrication processes is also an important factor, especially when the aim is mass production. Polymer based OLEDs can be fabricated by the cheap spin coating technology.[23,37] While for those using small-molecular-weight compounds sublimation is an easy production method.[23,34,37] The major problem with OLEDs is the limited lifetime of organic materials, and in particular current materials used for blue OLEDs.[3] If full colour displays are to be successful the development of new blue light emitters is crucial.

An OLED is made up of a thin film of a lumophore sandwiched between electrodes of differing work functions. The typical structure of an OLED is shown in Figure 3.1. Electrons are injected into one side from a metal cathode, while holes are injected in the other from an anode. The electron and hole move into the emissive layer and can meet to form an exciton.

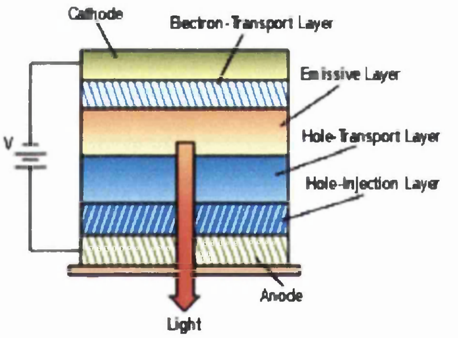

Figure 3.1 Typical structure of an OLED.

Initially the electron migrates from the cathode to the anode independently from the hole. However when the electron enters a region where there is a specific electron-hole separation the positively charged hole attracts the electron. This Coloumbic attraction causes electron-hole binding to occur.[38] The hole transport ability of the TAAs is based on the fact that they are easily oxidised to form stable radical cations. When considering electron hole recombination the spin of both the electron and the hole need to be taken into account. The spin of the electron and the hole can be coupled to produce four new combined states; one singlet state and one triplet state made up of three triplet sub states.[39,40] In a final step, the electron jumps in a very fast process directly to the emitter molecule which results in an excited emitter. Whether this occurs via a singlet or triplet path depends on the initial spin orientation of the electron-hole pair.[39,40] It is when the excited electron and hole combine that a photon can be emitted. The entire electroluminescence process that occurs within a device is summarised in Figure 3.2.

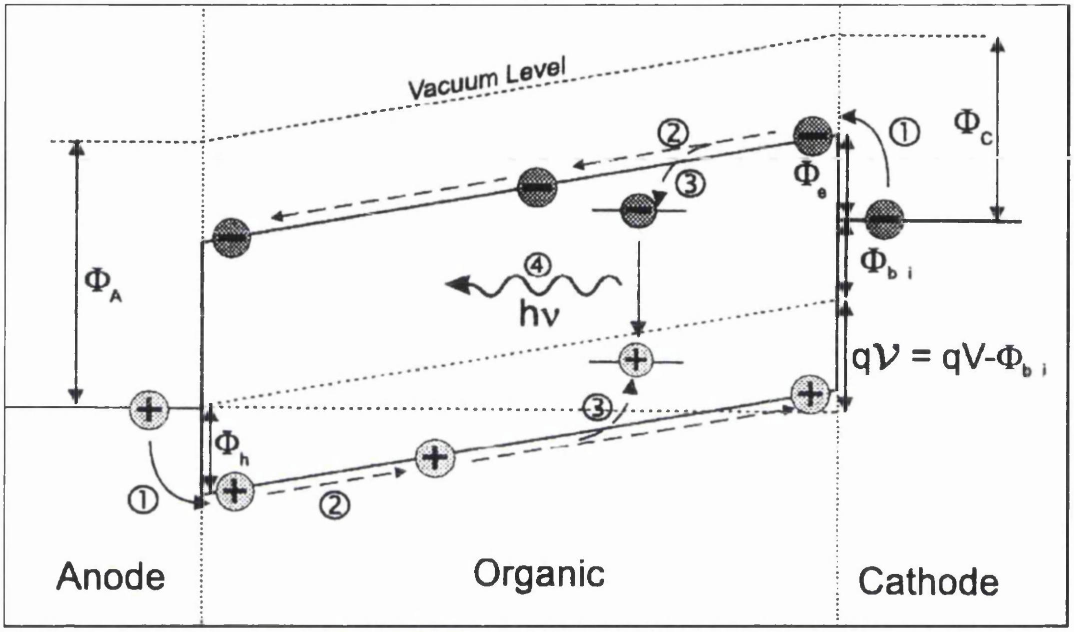

Figure 3.2 Diagram of the electroluminescent process that occurs within an OLED. Taken from BrÄutting et al. [41].

Figure 3.2 depicts four steps of electroluminescence these are:-

(1) Hole and electron injection from the anode and cathode respectively.

(2) Transport of both the hole and electron into the emissive layer.

(3) Attraction between the hole and the electron results in the formation of an exciton.

(4) Radiative exciton decay, i.e. a photon is emitted.

A major challenge in OLED manufacture is tuning the device such that an equal number of holes and electrons meet in the emissive layer. This is difficult because, in an organic compound, the mobility of a hole is much lower than that of an electron.

The materials currently employed in the emissive layer are typically fluorophores, which can only emit light when a singlet exciton forms, and since only one in four excitons is a singlet this reduces the OLEDs efficiency to a maximum of 25%. In order to overcome this problem there has been much research incorporating triplet emitters into OLEDs. In theory triplet emitters can be four times more efficient than singlet emitters, thus potentially 100% efficiency can be achieved.[42] However, this emission is always red-shifted compared to fluorescence, making blue light more difficult to achieve from triplet emitters. There are also other factors which affect the quantum efficiencies of OLED devices.

Internal quantum efficiency (η_{int} or IQE) is the number of photons generated inside the device per number of injected hole–electron pairs. The internal quantum efficiency is calculated as shown in Equation 3.1 below;

$$\eta_{int} = IQE = \gamma \, \eta s \, \Phi_f \qquad [3.1]$$

Where: -

η_{int} = internal quantum efficiency
γ = charge balance factor (fraction of injected charges that produce excitons)
ηs = singlet excitation efficiency (fraction of excitons that are formed as singlets)
Φ_f = Fluorescence quantum yield (quantum efficiency of fluorescence)

Equation 3.1 dictates that the internal quantum efficiency is directly proportional to the fluorescence quantum yield, thus it is essential that the fluorescence quantum yield is as high as possible in order to obtain maximum device efficiency. This highlights the fact that compounds which have high fluorescent quantum yields are extremely important in the fabrication of efficient OLED devices if high efficiency is to be obtained. Ideally the fluorescence quantum yield should approach unity, and as a general rule, in order to obtain a realistic level of device efficiency, quantum yields should be at least greater than 0.3.

The external quantum efficiency is always less than the internal quantum efficiency since a large fraction of generated photons stays trapped and absorbed inside the device.[43] There has been much recent work on the design of OLED surfaces to minimise this trapping by total internal reflection etc.[43]

3.1.2 Requirements of TAAs in OLED devices

In order to be used in practical OLED devices organic molecules need to have low ionisation potentials, high fluorescence quantum yields, high thermal stability, and should preferably form an amorphous glass upon melting.[3,13,17,44] TAAs currently being used in OLED devices have satisfactory ionisation potentials.[44] However there is a need for a significant improvement in thermal stability, ease of forming a glass and fluorescence quantum yields.[3] While aromatic amines have been shown to be good materials as hole transport layers (HTL)[1,17,45], problems exist in the long term stability of devices using these compounds due to effects such as chemical degradation and crystallisation. There is a clear demand for new materials for these applications.

Here results are given from a study on the effect of stilbene substituents on the chemistry, photophysics and device applications of the series of new compounds **3–8** shown in Figure 3.3. The TAA **9**, without the stilbene unit was also studied for comparison with **8**, in order to gain a greater understanding of its emission behaviour. They may also possess interesting photonic properties, since arylamines having electron accepting nitro groups are amongst the most important organic systems used in nonlinear optics.[17] Furthermore, the enhanced solubility of these compounds suggests that they may also be of interest as optical probes. Both the amorphous nature of these compounds and their good solubility characteristics favour many of these applications. The main characteristics of the compounds in this study include reversibility of oxidation reactions, chemical stability, high solubility, good film forming properties, and stability of amorphous films.[2] It has been shown that dehydroabietic acid based arylamines are excellent candidates for thin film device fabrication due to the fact that they form good amorphous layers which do not have a tendency to crystallise.[2] In addition, solvent based deposition techniques, such as spin coating[46] and inkjet printing[47] are attractive for film preparation, and the decrease in the degree of crystallinity in these compounds is also likely to increase their solubility, and hence their use in such applications. In the search for added value compounds from the renewable feed stock rosin, it has been shown that arylamines can be synthesised with a resin acid moiety by palladium catalysed cross-coupling reaction of aryl halides with either primary amines or diarylamines.[10]

3.1.3 Synthesis of TAA dyes

The TAAs were synthesised by our collaborators in the *INETI-DTIQ* group in Lisbon, Portugal, here is a summary of the synthetic route. The synthetic pathway for the new stilbene-based TAAs with dehydroabietic acid methyl ester moieties (**3**–**8**) is shown in Figure 3.4. Different *trans*-4-bromostilbenes (**1a**–**d**), prepared by a Horner-Wadsworth-Emmons procedure[48] were coupled to the diarylamines **2a** or **2b** using a suitable palladium-catalyzed route to aromatic carbon-nitrogen bond formation ($Pd(OAc)_2/P(t\text{-}Bu)_3/NaOt\text{-}Bu$)[49] to give the target compounds **3-8**. The starting stilbenes **1a-d**, the diarylamine intermediates **2a** and **2b**, as well as the new stilbene-TAAs **3-8** were purified by either repeated recrystallization or by column chromatography. The TAA **9,** without the stilbene moiety, was synthesised by reaction of **2a** with 1-bromo-4-nitrobenzene using the same palladium-catalyzed route.[49] The structures of the new compounds were confirmed by ^1H NMR spectroscopy, mass spectrometry and elemental analysis. All the TAAs are soluble in commonly used organic solvents.

3.1.4 Aims of this study

For application in OLEDs and as HTL there is the need for a complete photochemical, photophysical and physical characterisation, and this chapter describes the characterisation of compounds **3-9**, with emphasis on excited state characterisation and thermal properties. We have also compared the excited state behaviour of similar TAAs in order to ascertain the effect of the side groups on those properties which are key for their application in electronic devices.

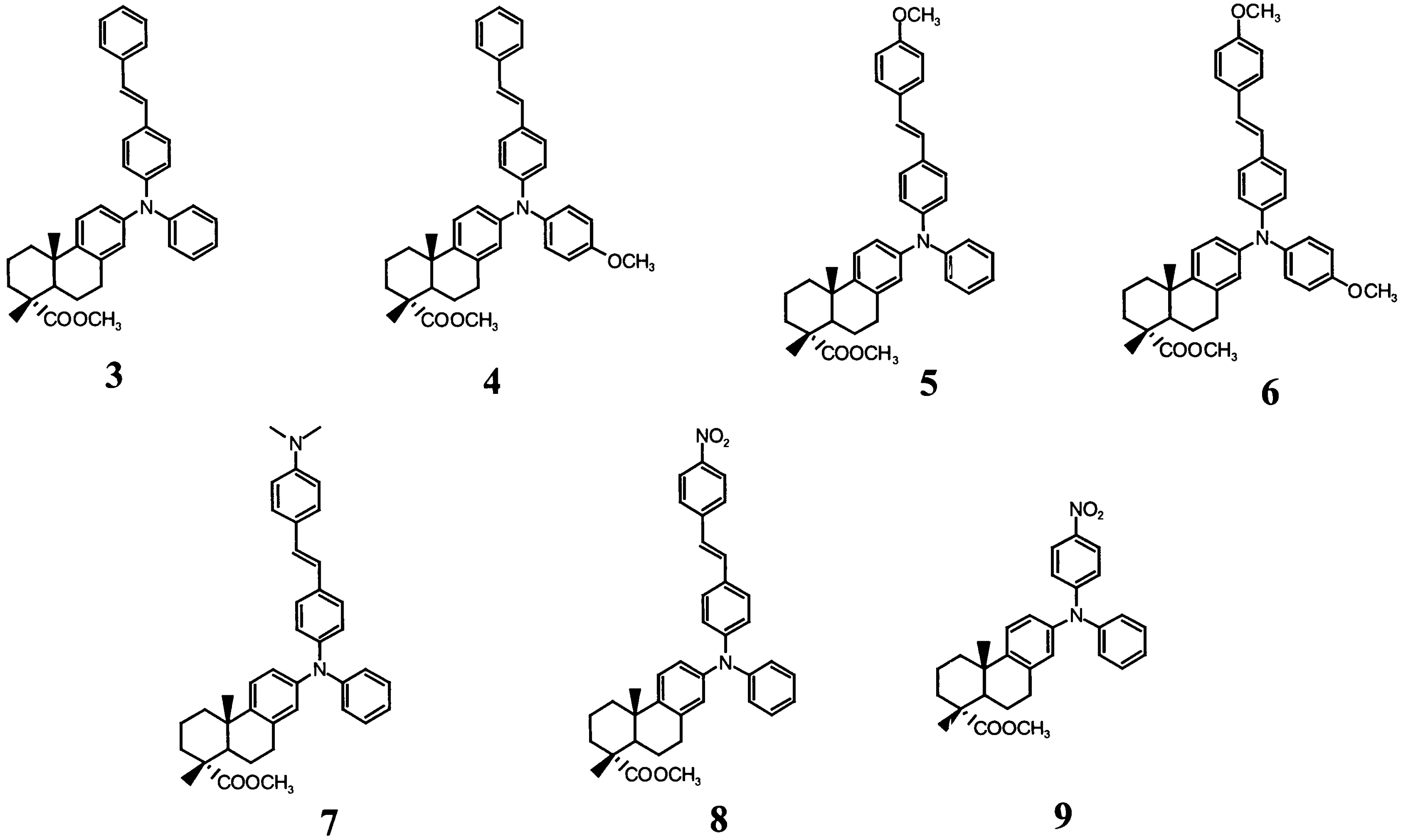

Figure 3.3 Structures of TAAs studied (**3**-**9**).

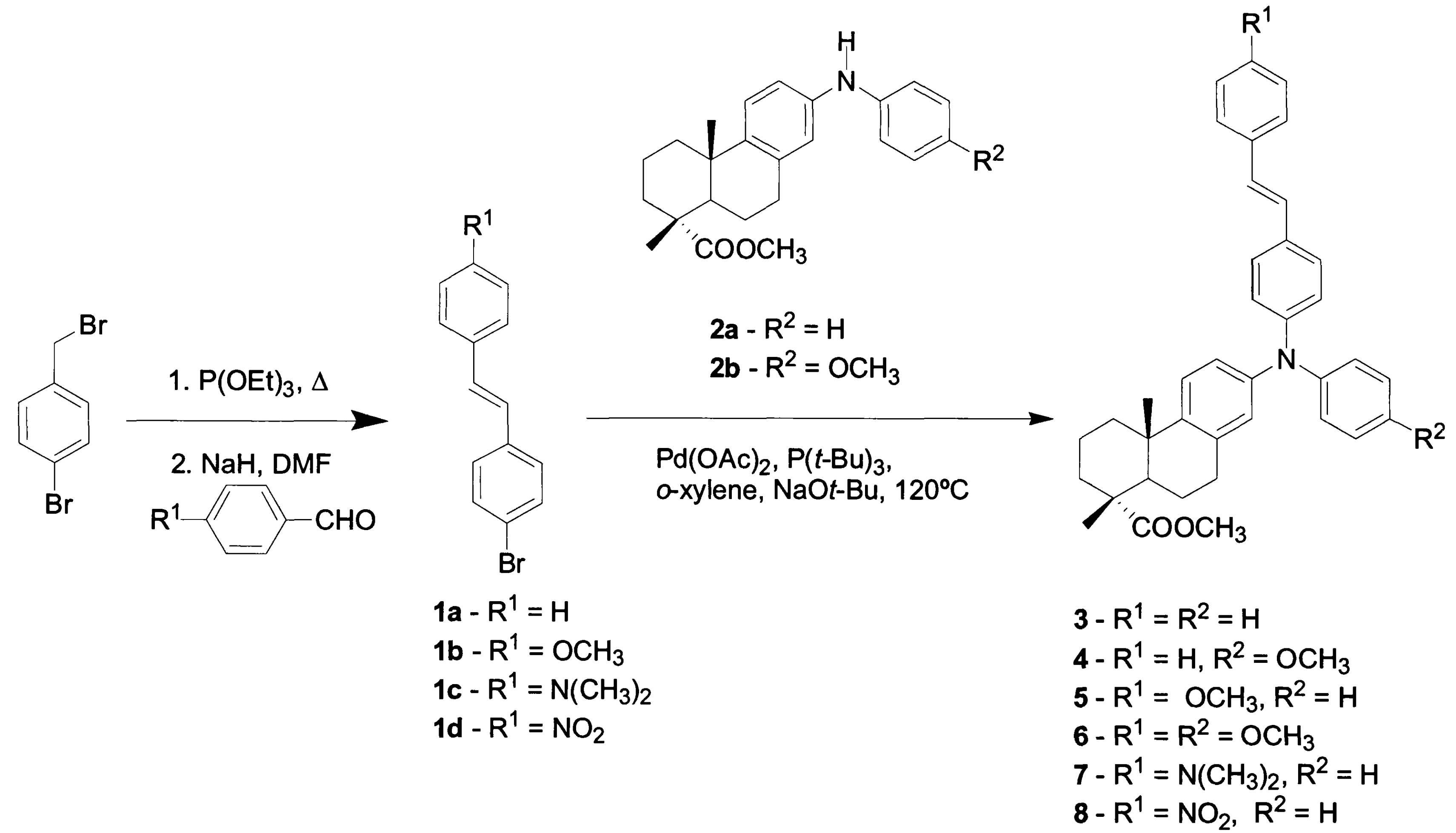

Figure 3.4 General synthetic pathway of all TAAs studied.

3.2 Experimental

3.2.1 Materials

3-9 were a gift from the INETI-DTIQ group in Lisbon and were used as received. All other chemicals were purchased from Sigma-Aldrich. Acetonitrile, isopropanol and methylcyclohexane were of spectroscopic or equivalent grade; cyclohexane was purified by fractional distillation.

3.2.2 Equipment and methods

3.2.2.1 Absorption measurements

Absorption measurements at 293 K were made on solutions in 1 cm quartz cuvettes on a Shimadzu UV-2100 spectrophotometer. Absorption measurements at 77 K were made with a Perkin-Elmer Lambda 5 UV/VIS spectrophotometer as described in Section 2. The molar extinction coefficients (ε) were obtained from Beer- Lambert plots from six solutions of different concentrations. Solutions of varying concentrations were obtained by dilution of a 'mother' solution. The mother solution for all samples was ~ 1 mg of TAA in 5ml of solvent. The sample masses of ~ 1 mg were recorded using a six figure balance. Molar extinction coefficients were obtained in three solvents of varying polarity namely: cyclohexane (solvent dielectric, ε, = 2.02), acetonitrile ($\varepsilon = 41.1$) and isopropanol ($\varepsilon = 19.9$).[50] The errors associated with the molar extinction coefficients were calculated from the line of best fit in the Beer-Lambert plots using Origin software®.

3.2.2.2 Excited state characterisation

Steady-state luminescence studies were carried out using the Jobin Yvon-Spex Fluorolog 3-22 spectrometer described in Section 2.3.1. Excitation and emission slits were 4.0 nm. Fluorescence spectra were corrected for the spectral response of the light source (450 W xenon lamp) and detector. Fluorescence spectra at liquid nitrogen temperatures were recorded with the Jobin Yvon JY3D spectrofluorimeter described in Section 2.3.2. Fluorescence quantum yields at 293 K were obtained using α-4-oligothiophene as a reference as described in Section 2.4 (Φ_f for α-4-oligothiophene is 0.18 in cyclohexane and ethanol, and 0.16 in acetonitrile)[51]. The fluorescence quantum yields at 77 K were obtained by comparison of 77 K and room temperature emission spectra of the same solution. The quantum yields at 77 K were obtained assuming 20% shrinkage of the solvent on going from 293 to 77 K. The 20% value was obtained from the differences in the absorption values of the low temperature samples compared to those at room temperature.

Time resolved fluorescence was measured using a home built Time-Correlated Single Photon Counting (TCSPC) apparatus with nitrogen filled IBH 5000 coaxial flashlamp as excitation source, Jobin-Yvon monochromator, Phillips XP2020Q photomultiplier, and Canberra instruments time-to-amplitude converter and multichannel analyser. Alternate measurements (1000 counts per cycle), controlled by Decay® software (Biodinâmica Portugal), of the pulse profile at 373 nm (430 nm in the case of **8**) and the sample emission, were performed until $1\text{-}2\times10^4$ counts at the maximum were reached.[52] All samples were held in 1 cm cuvettes and had an absorption value of ~ 0.2 at the excitation wavelength (373 nm for all samples, except **8** for which 430 nm was used). The fluorescence decays were analysed using the modulating functions method of Striker with automatic correction for the photomultiplier "wavelength shift".[53] Radiative lifetimes were calculated from experimental lifetimes and quantum yields, they were also determined from the lowest energy absorption band using the Strickler-Berg relationship as described in Section 3.4.4.

3.2.2.3 Chemical oxidation

TAAs were dissolved in chloroform ($\leq 10^{-4}$ M) and were oxidized with small quantities of a concentrated solution of cerium ammonium nitrate in acetonitrile dispensed from a micrometer syringe (the final solvent composition was always at least 98.5% chloroform). The resulting spectra, which appeared on mixing the reactants, were recorded immediately and their change with time was monitored. The change with time was comparatively slow, > 60 seconds, and a correction to zero time was applied from these decay kinetics for the interval between mixing and recording. The concentration of Ce (IV) was 6.6×10^{-6} to 4×10^{-5} M. Plots of optical density *ca.* 760 nm vs. Ce (IV) concentration yielded straight lines passing through the origin. Least-squares analysis yielded extinction data given in Section 3.4.7.

3.2.2.4 Thermal properties

3-9 were studied by hot stage microscopy (HSM) and thermogravimetric analysis (TGA). Details of the instruments used are given in Chapter 2. For TGA all samples were run in a nitrogen atmosphere and were heated from 30-625 °C at a rate of 10 °C/min. Sample masses were in the range of 0.5-1 mg, all samples were run under identical conditions.

3.3 Results

3.3.1 Absorption results

Absorption data for **3-9** in cyclohexane, acetonitrile and isopropanol solutions are given in Table 3.1. All TAAs studied show strong absorption bands,absorption maxima are in the 365–430 nm range with a weaker shoulder around 265–300 nm. . Figure 3.5 shows a typical Beer-Lambert plot.

As can be seen in Table 3.1 all compounds have high molar extinction coefficients, which are generally at their highest in cyclohexane or acetonitrile. This is important because high extinction coefficients means that the radiative lifetime is short, which is also an advantage as it means emission will compete very favourably with other processes (e.g. quenching by charged species). Only small red shifts (1-12 nm) were observed in the absorption maxima in the 360-430 nm region on going from cyclohexane to the polar solvents acetonitrile and isopropanol. **9** was the only compound to show a blue shift (9-10 nm) on going to the more polar solvents. The second wavelength band again only showed minor solvent effects, with all shifts being to the 'red' with increasing solvent polarity. The weak peak or shoulder around 300 nm can be assigned to the $S_0 \rightarrow S_1$ transition, the lowest energy band in TAAs is predominantly π,π^*, although there may be mixing involving some charge transfer from the nitrogen.

Table 3.1:- Absorption data for **3-9**.

Compound	Cyclohexane		Acetonitrile		Isopropanol	
	λ_{max} /nm	$\varepsilon/10^4$ M^{-1} cm^{-1}	λ_{max} /nm	$\varepsilon/10^4$ M^{-1} cm^{-1}	λ_{max} /nm	$\varepsilon/10^4$ M^{-1} cm^{-1}
3	296 371	2.26 3.64	293 367	3.79 2.81	292 367	2.06 2.93
4	291 375	2.50 3.77	289 369	2.50 3.70	284 371	2.45 3.52
5	298 367	2.90 3.90	294 365	2.96 4.05	298 366	2.79 3.79
6	300 371	2.90 3.90	292 367	2.94 4.02	296 370	2.71 3.56
7	309 379	2.64 4.82	302 373	3.31 4.15	290 377	2.65 4.24
8	301 432	3.17 3.29	301 428	3.31 2.96	289 430	2.84 2.83
9	287 388	1.35 1.90	264 398	1.60 2.14	283 397	1.04 1.43

ε values are precise to $\pm0.5\times10^4$ M^{-1} cm^{-1}

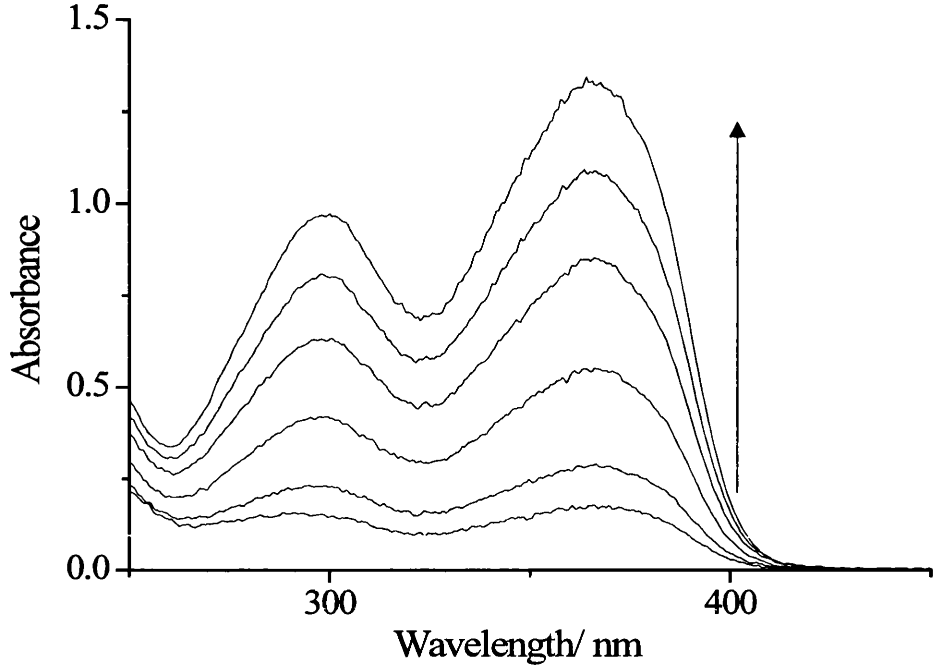

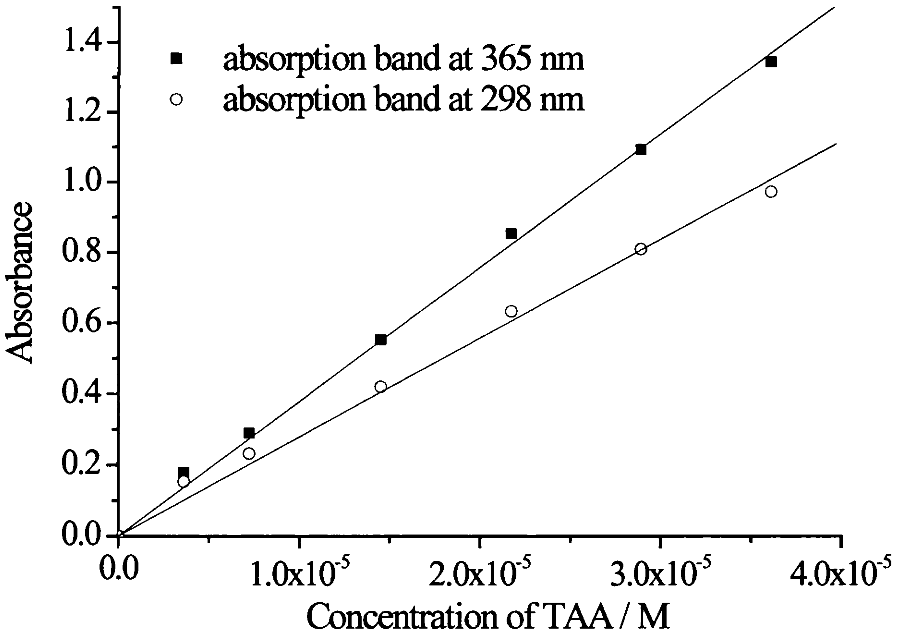

Figure 3.5 a) Absorption spectra of **5** in isopropanol with increasing concentration. b) The corresponding Beer-Lambert plots with absorption values at 365 nm (solid squares) and 298 nm (open circles).

3.3.2 Excited-state characterisation

All seven samples **3-9**, show broad band fluorescence in cyclohexane, acetonitrile or isopropanol. Typical spectra are shown in Figure 3.6, and data are collected in Table 3.2.

Table 3.2 Emission characteristics of **3-9**.

Compound	Cyclohexane		Acetonitrile		Isopropanol	
	λ_{emax}/nm	Φ_f^a	λ_{emax}/nm	Φ_f^a	λ_{emax}/nm	Φ_f^a
3	404	0.34	479	0.68	453	0.67
4	418	0.43	517	0.27	472	0.42
5	411	0.35	493	0.49	471	0.54
6	400	0.39	473	0.56	438	0.56
7	410	0.50	445	0.24	436	0.29
8	483	0.57	No emission	N/A	No emission	N/A
9	495	0.50	No emission	N/A	No emission	N/A

[a] The error in the quantum yields is ± 5%

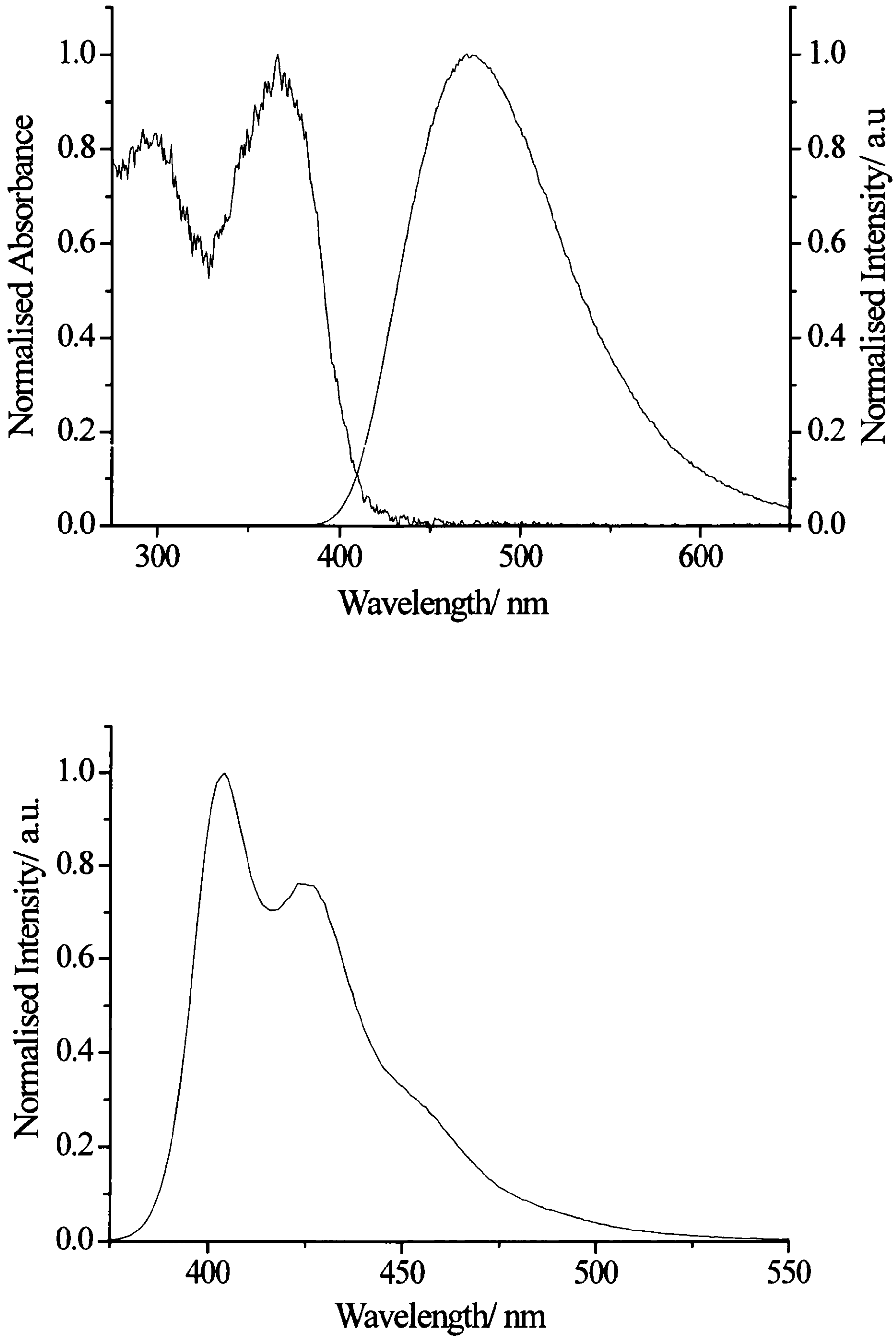

Figure 3.6. Typical fluorescence spectra. a) absorption (left) and emission (right) of **5** in acetonitrile. b) Fluorescence spectrum of **3** in cyclohexane.

As can be seen in Table 3.2 fluorescence quantum yields are markedly higher in cyclohexane than those of related dehydroabietic acid based diarylamines in the same solvent.[54] Although in part this may be due to the presence of the strongly fluorescent N-phenylaminostilbene group,[55] the fact that compound **9**, lacking this moiety, also has a relatively high fluorescence yield shows that this is not the only factor. The observation of high luminescent yields is relevant to the potential of these compounds either as probes or in light emitting devices. Solvent effects on all of the compounds are substantial. With the exceptions of **9** and **8** (which are quenched, discussed below) the compounds undergo a bathochromic shift on going to a polar solvent, with the shift increasing with an increase in polarity of the solvent (e.g. on going from isopropanol to acetonitrile). This is due to the fact that in solution, solvent molecules surrounding the compound in its ground state have dipole moments that can interact with the dipole moment of the compound to yield an ordered distribution of solvent molecules around the compound. Energy level differences between the ground and excited states in the given compound produce a change in the molecular dipole moment, which ultimately induces a rearrangement of surrounding solvent molecules. However, the Franck-Condon principle dictates that, upon excitation of a fluorophore, the molecule is excited to a higher electronic energy level in a far shorter timeframe than it takes for the fluorophore and solvent molecules to re-orientate themselves within the solvent-solute interactive environment.[56] As a result, there is a time delay between the excitation event and the re-ordering of solvent molecules around the solvated fluorophore, which generally has a much larger dipole moment in the excited state than in the ground state.[56]

After the fluorophore has been excited to higher vibrational levels of the first excited singlet state (S_1), excess vibrational energy is rapidly lost to surrounding solvent molecules as the fluorophore slowly relaxes to the lowest vibrational energy level (this occurs in the ps time scale). Solvent molecules assist in stabilizing and further lowering the energy level of the excited state by re-orienting (solvent relaxation) around the excited fluorophore in a slower process that requires between 10 and 100 ps. This has the effect of reducing the energy separation between the ground and excited states, which results in a bathochromic shift of the fluorescence emission. Increasing the solvent polarity produces a correspondingly larger reduction in the energy level of the excited state, while decreasing the solvent polarity reduces the solvent effect on the excited state energy level. The polarity of the fluorophore also determines the sensitivity of the excited state to solvent effects. Polar and charged fluorophores exhibit a far stronger effect than non-polar fluorophores. The solvent also has an effect on the quantum yields of all the other compounds. With **5**, **6** and **3** the fluorescence quantum yield increases on going to a polar solvent, whereas with **4** and **7** there is a decrease on going to a polar solvent (Figure 3.7).

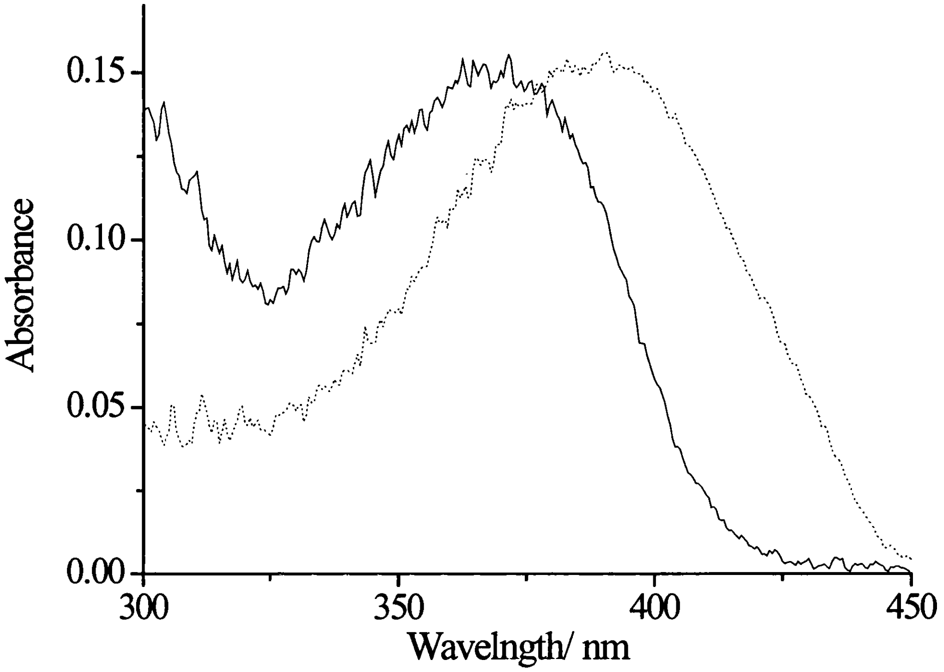

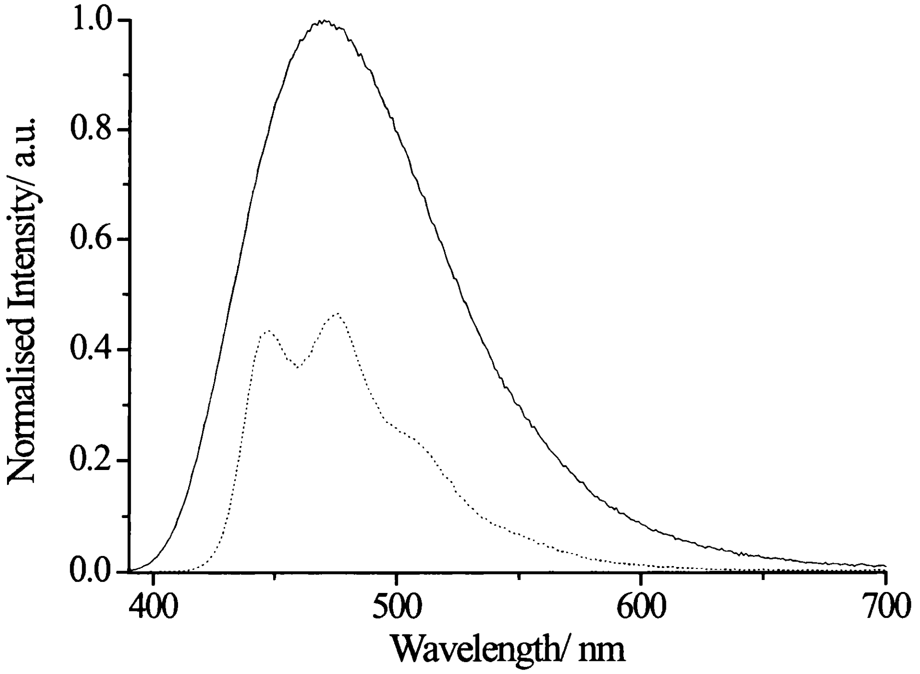

Figure 3.7 a) The absorption spectra of both **6** in isopropanol (solid line) and the α-4-oligothiophene reference (dotted line) in ethanol, both samples have the same absorption value. b) The corresponding fluorescence spectra of the same samples run under identical conditions.

In the case of **9** and **8** the fluorescence is quenched in polar solvents. In general the lowest excited state in the TAAs has π, π* character, however when the nitro group is present in the para position on the stilbene group there is also a very close lying charge transfer state. This charge transfer state becomes the lowest excited state on going to polar solvents, relaxation from this state is via non-radiative processes, and thus the fluorescence is 'quenched'. In order to examine this further emission from **9** and **8** in cyclohexane/isopropanol and cyclohexane/acetonitrile was studied. The results are summarised in Table 3.3, and typical spectra obtained are shown in Figure 3.8.

Table 3.3 Quenching effects due to solvent polarity.

Compound	Volume of isopropanol added to achieve quenching of fluorescence/ μl	Volume of acetonitrile added to achieve quenching of fluorescence/ μl
8	2000	1600
9	100	40

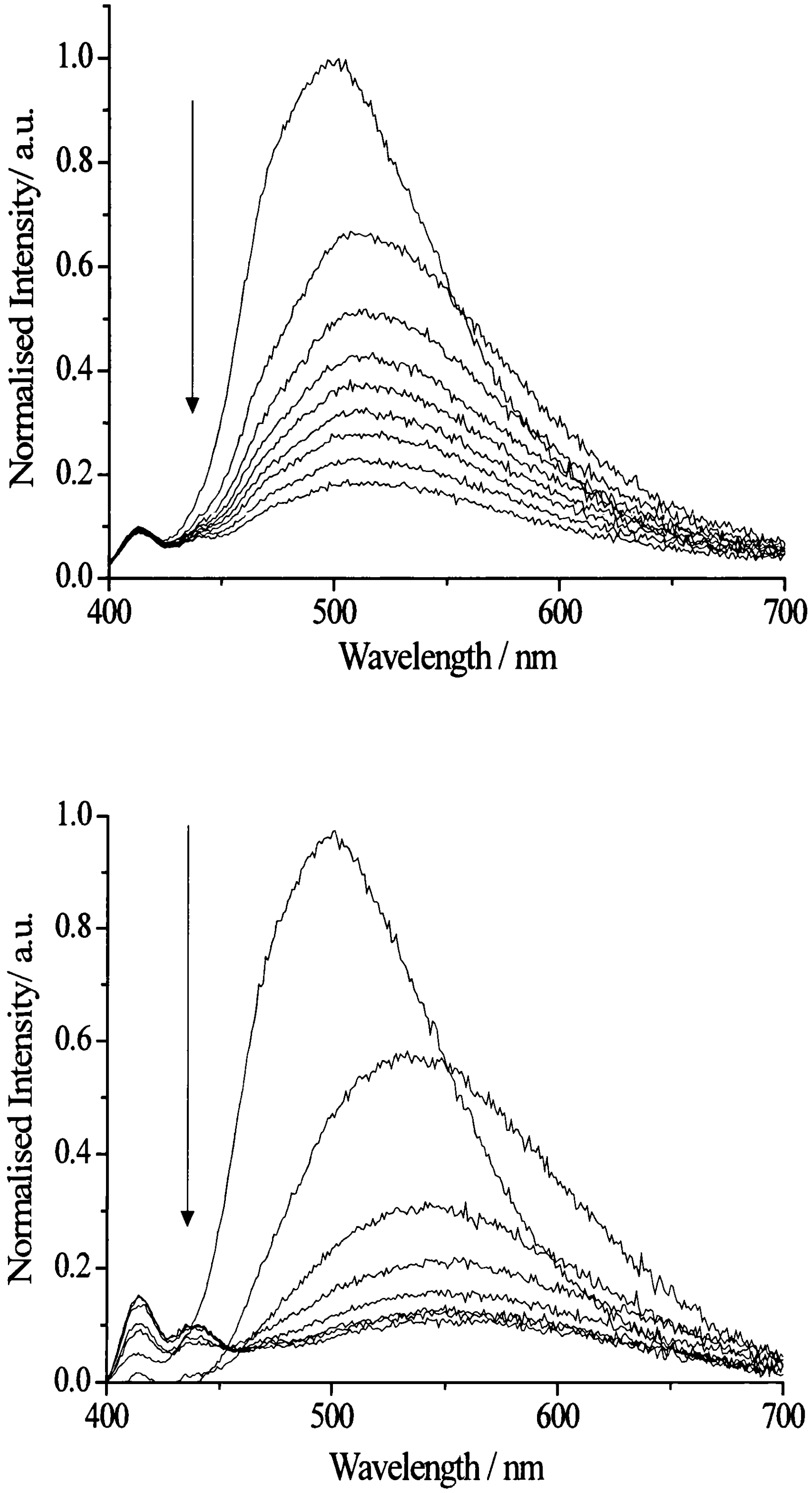

Figure 3.8 Polarity effects on **9**. a) The addition of isopropanol to a solution of **9** in cyclohexane. b) The addition of acetonitrile to a solution of **9** in cyclohexane.

While this does not give quantitative information on the polarity affects of any great accuracy it does show that **9** is affected by the polar solvent by a much greater amount. It also confirms that the quenching is due to the polarity of the solvent due to the fact that quenching occurs with less volume of the more polar acetonitrile than with the isopropanol. **9** is affected more so by the polarity of the solvent due to the fact that the electron withdrawing $-NO_2$ group is closer in proximity to the lone pair of electrons on the central nitrogen. It is closer due to **9** not having the stilbene group.

3.3.3 Comparison of absorption and excited state results for similar TAA in this study

3.3.3.1 Compounds 5 and 6

The absorption and emission characteristics of **5** and **6** are very similar, this is expected as the only difference between the two compounds is the presence of the -OCH_3 group in the para position with respect to the central nitrogen in the case of **6**. In polar solvents **5** exhibits slightly higher extinction coefficients and fluorescence quantum yields. However the differences are very slight and thus **5** and **6** behave essentially the same.

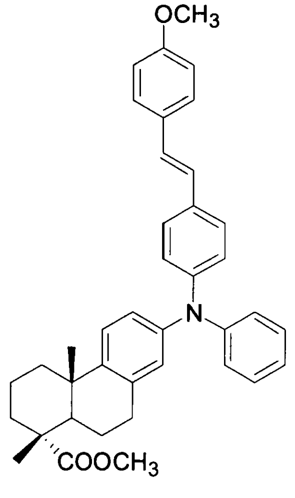

5

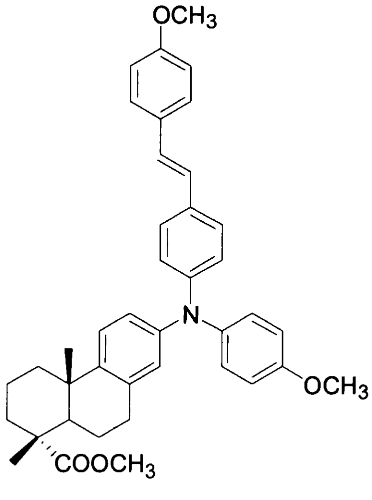

6

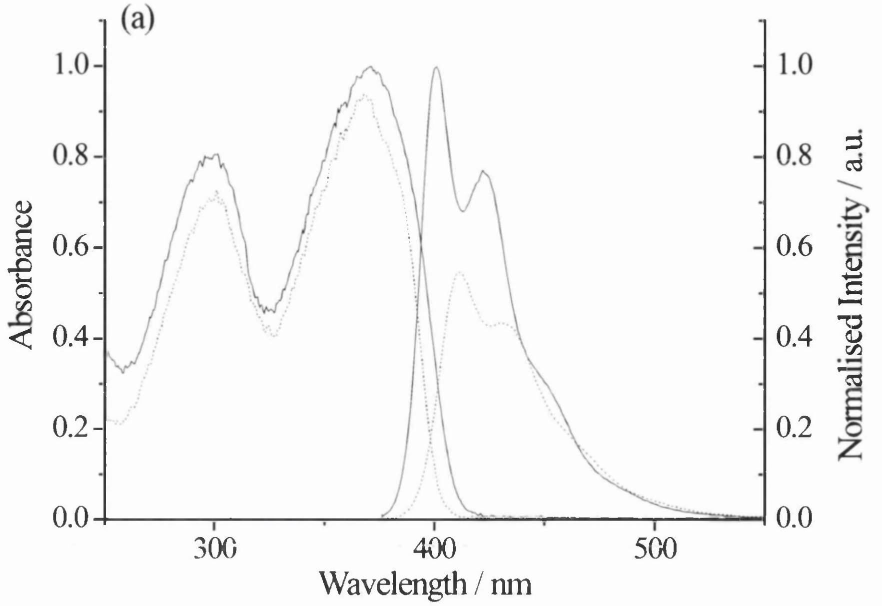

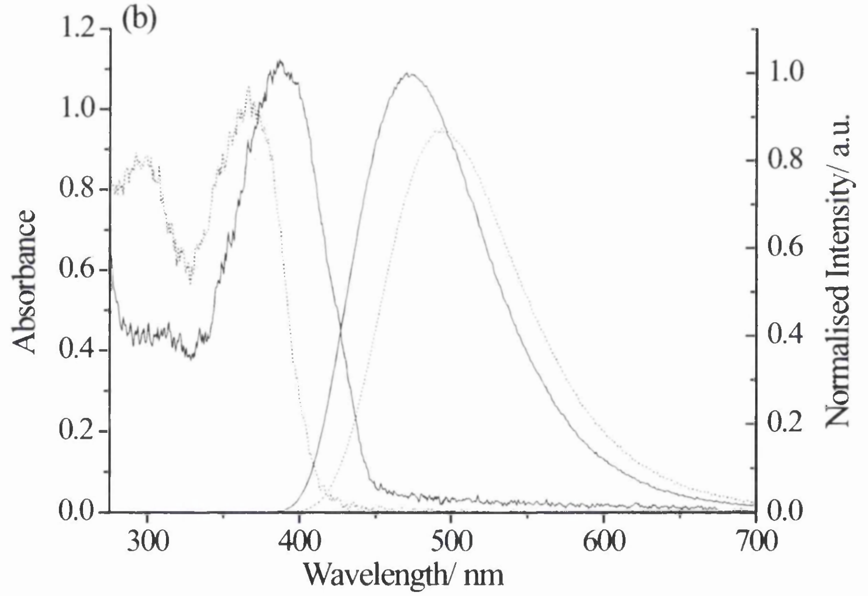

Figure 3.9 a) Absorption (left) and emission (right) spectra of **5** (solid line) and **6** (dotted line) in cyclohexane. b) Absorption (left) and emission (right) spectra of **5** (solid line) and **6** (dotted line) in acetonitrile.

*3.3.3.2 Compounds **3** and **4***

The difference between these two compounds is the presence of a $-OCH_3$ group in the para position on the TAA group in the case of **4**. Both **3** and **4** have the para position of the stilbene group unsubstituted. In this case the presence of the $-OCH_3$ group in the case of **4** does markedly change the absorption characteristics. Molar extinction coefficients are generally higher in the case of **4**. The emission maximum of **4** is at a longer wavelength than that of **3**. **4** also undergoes a more significant bathochromic shift on going to polar solvents, with the emission maximum shifted *ca.* 100 nm on going from cyclohexane to acetonitrile. **4** has higher fluorescence quantum yield than **3** in non polar cyclohexane; however this trend is reversed on going to polar solvents as can be seen in Figure 3.10.

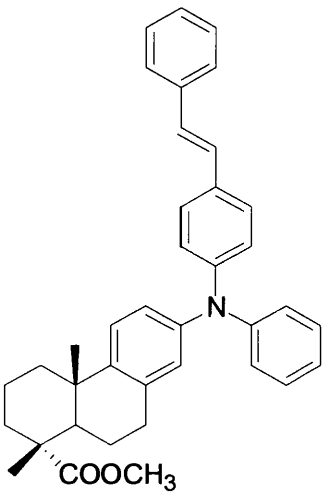

3

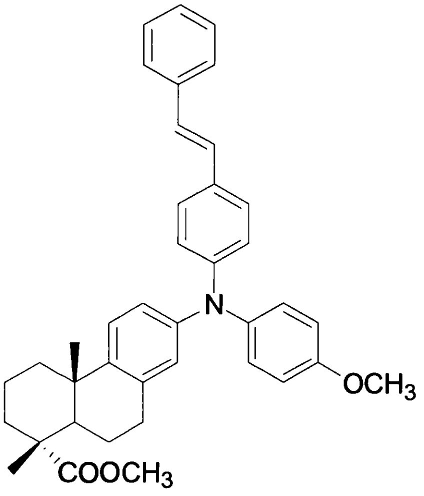

4

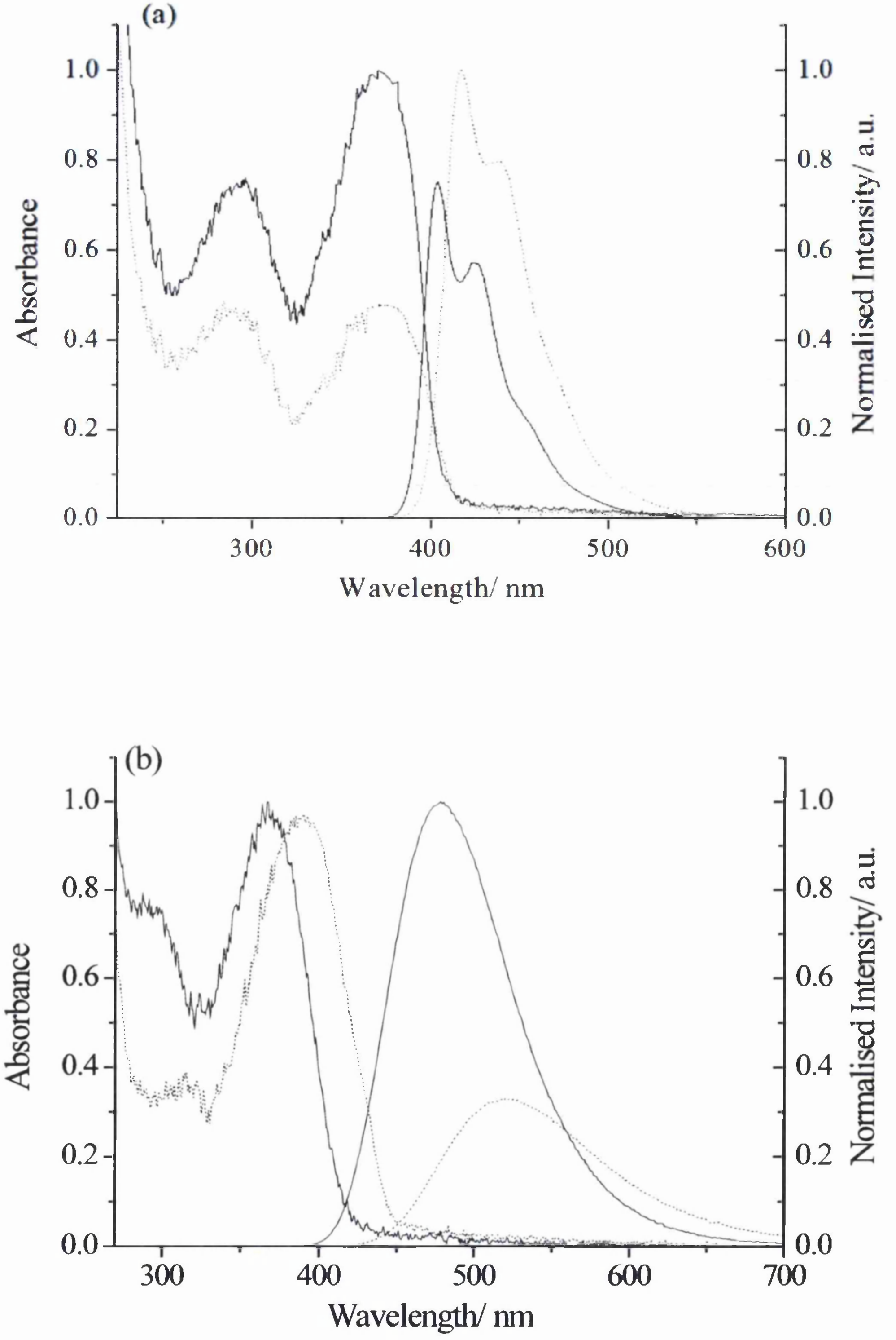

Figure 3.10 a) The absorption (left) and emission (right) spectra of **3** (solid line) and **4** (dotted line) in cyclohexane. b) The absorption (left) and emission (right) spectra of **3** (solid line) and **4** (dotted line) in acetonitrile.

*3.3.3.3 Compounds **8** and **9***

The difference between the two compounds is the presence of the stilbene group in the case of **8**; this causes a significant difference between the two compounds. Substantial bathochromic shifts in absorbance maxima are seen with the presence of the stilbene group; shifts are in the range of 30-44 nm depending on the solvent, there are also large increases in molar extinction coefficient values as shown in Figure 3.11. The stilbene group causes the molar extinction coefficient values to increase by as much as 2×10^4 M^{-1} cm^{-1} (Table 3.1). These differences are due to the stilbene group increasing the conjugation of the molecule. There is also small hyposochromic shift in the fluorescence spectra. The inclusion of the stilbene group in the compound also increases the fluorescence quantum yield in cyclohexane; however the fluorescence of both compounds is quenched by polar solvents (Figure 3.11).

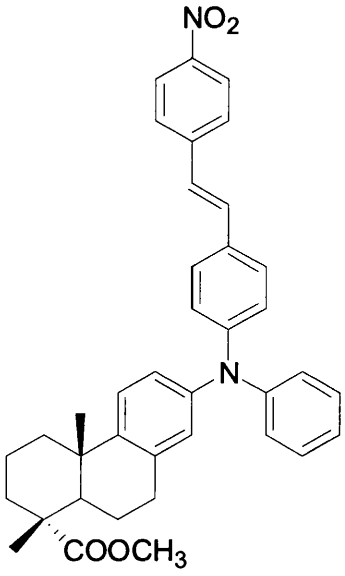

8

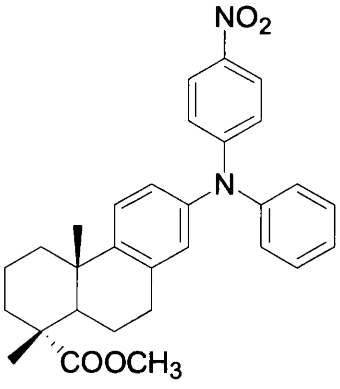

9

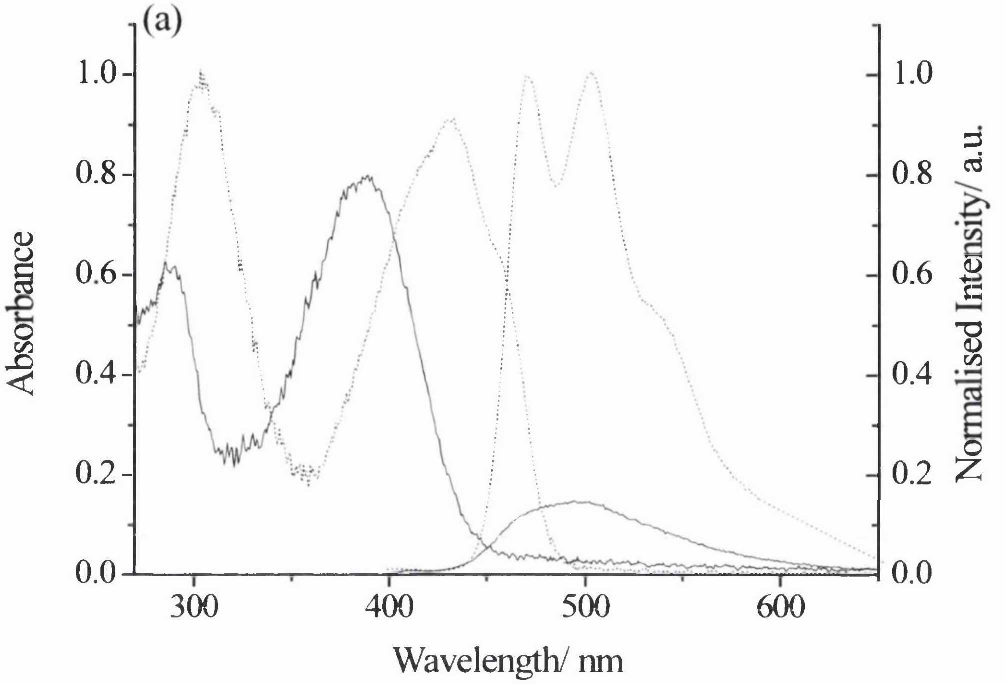

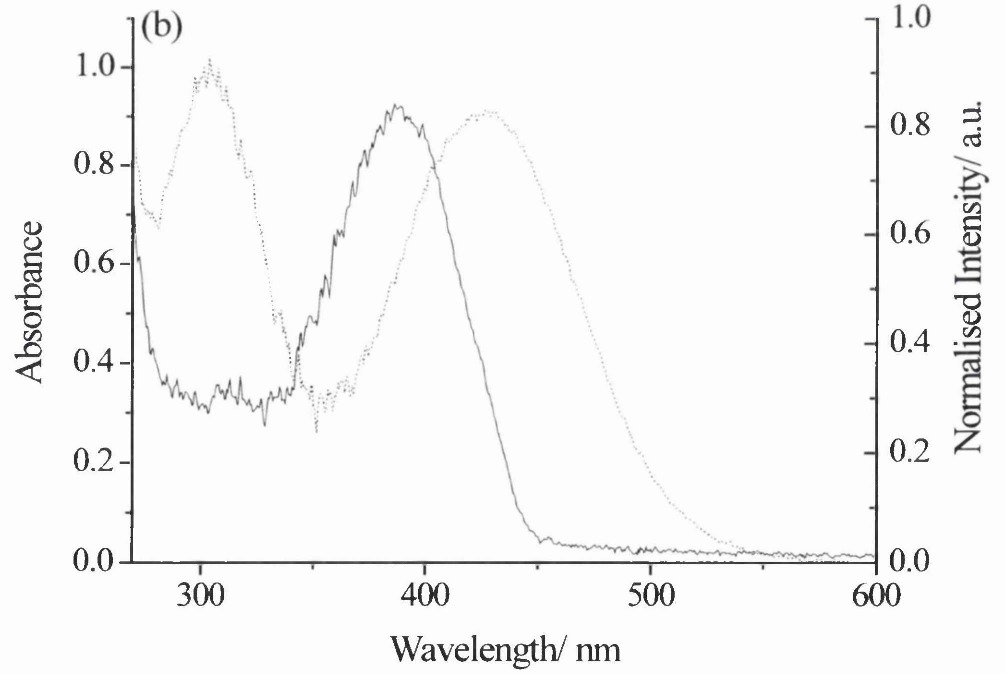

Figure 3.11 a) The absorption (left) and emission (right) spectra of **9** (solid line) and **8** (dotted line) in cyclohexane. b) The absorption (left) and emission (right) spectra of **9** (solid line) and **8** (dotted line) in acetonitrile.

3.3.3.4 Compounds 3 and 8

The difference between these two compounds is the presence of the $-NO_2$ group in the para position on the stilbene group in the case of **8**. This $-NO_2$ group is electron withdrawing and causes a significant bathochromic shift in absorption maximum. The effect of the electron withdrawing $-NO_2$ group is amplified due to the close proximity of the highly conjugated stilbene group. This results in a general increase in molar extinction coefficients in non-polar or moderately polar solvents (cyclohexane and isopropanol). However in acetonitrile (strongly polar) the molar extinction coefficients of both compounds are similar. This may be due to the polar acetonitrile further enhancing the electron withdrawing ability of the $-NO_2$ group which acts in stabilizing a charge transfer band lower in energy than that of the π, π^* absorption band. There is a large bathochromic shift (~80 nm) in the fluorescence spectra on going from **3** to **8** in cyclohexane. The fluorescence quantum yield for **8** (0.57) is also higher than that of **3** (0.34) in cyclohexane. The fluorescence of **8** is quenched in polar solvents (isopropanol and acetonitrile).

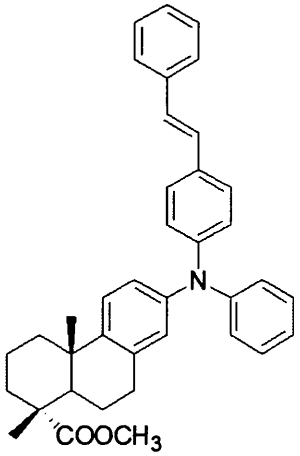

3

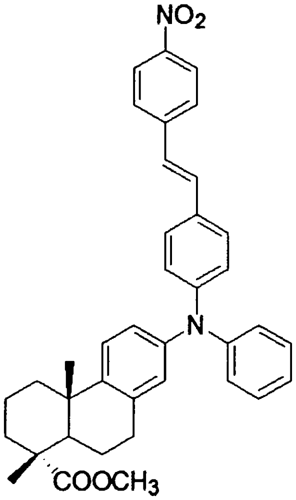

8

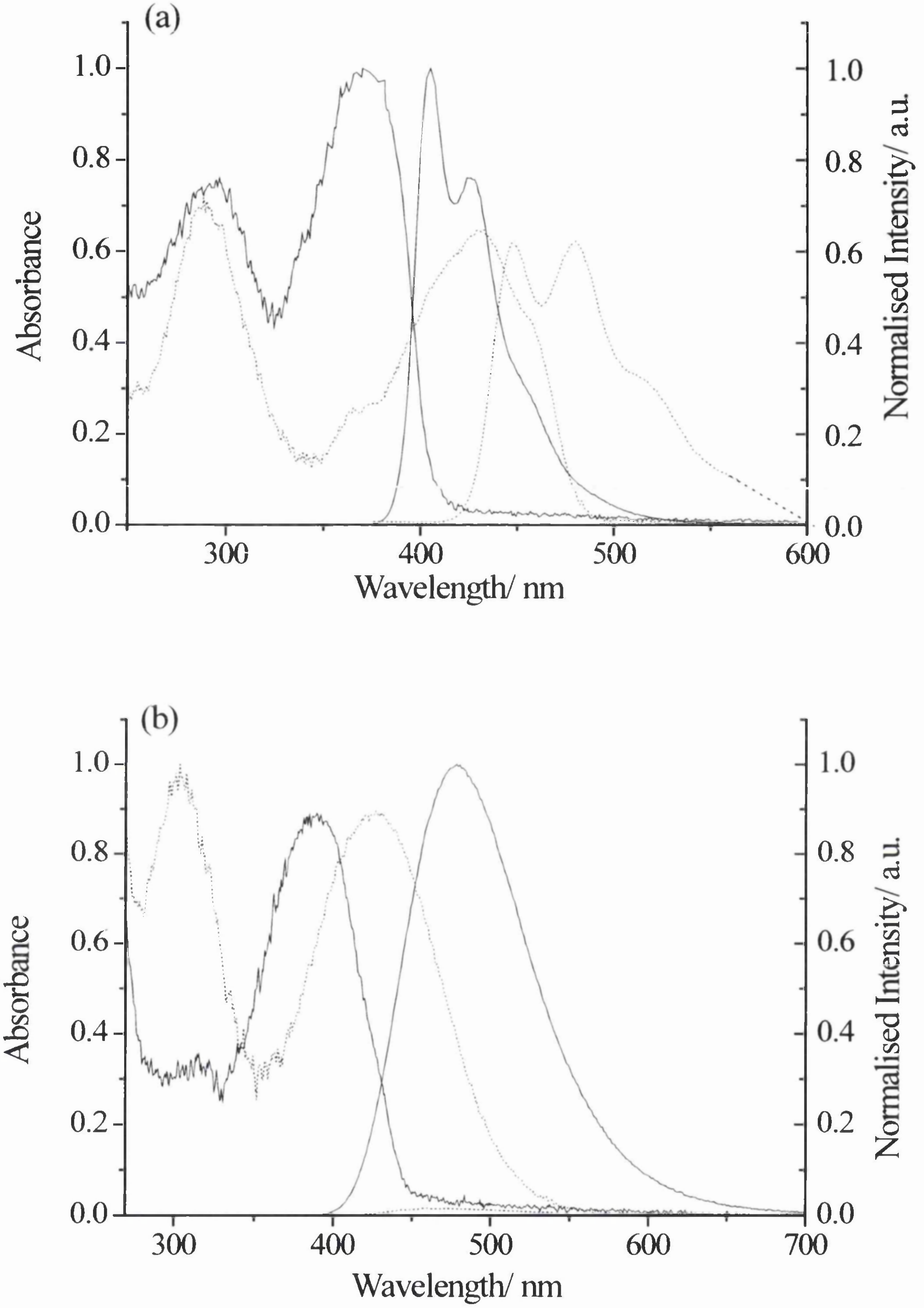

Figure 3.12 a) The absorption (left) and emission (right) spectra of **3** (dotted line) and **8** (solid line) in cyclohexane. b) The absorption (left) and emission (right) spectra of **3** (dotted line) and **8** (solid line) in acetonitrile.

3.3.3.5 Compounds 3 and 7

The difference between the two compounds is that **7** contains a $-N(CH_3)_2$ group at the para position on the stilbene group. The presence of this group has a substantial effect on the absorption characteristics, causing bathochromic shifts in absorption maxima and a sizeable increase in molar absorption coefficients. This leads to **7** having the largest molar extinction coefficients of all the compounds. This is most likely due to the $-N(CH_3)_2$ group further increasing the conjugation of the molecule and in combination with the already highly conjugated stilbene group produces very high molar extinction coefficient values. **7** has the higher fluorescence quantum yield in cyclohexane but the quantum yield values drop significantly on going to isopropanol and acetonitrile whereas for **3** the quantum yields increase significantly on going to the polar solvents.

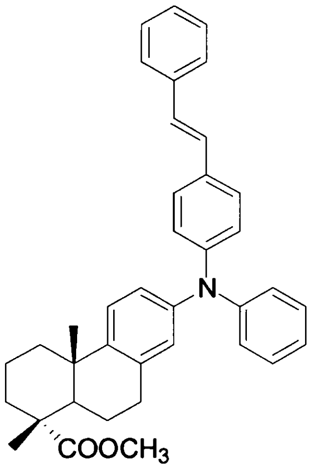

3

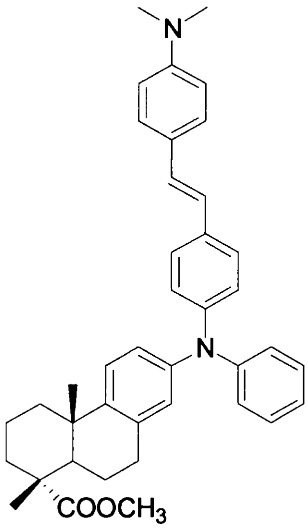

7

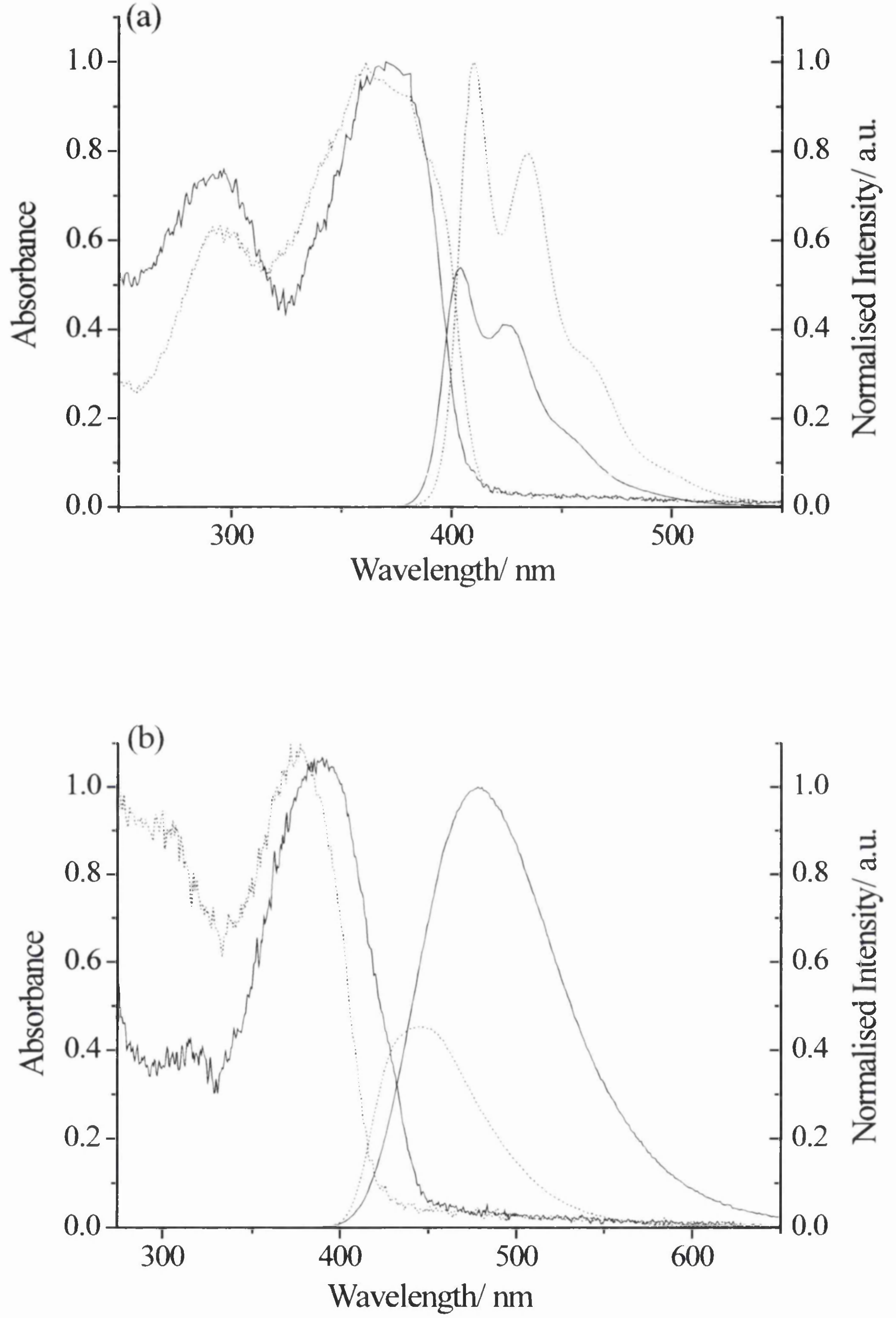

Figure 3.13 a) The absorption (left) and emission (right) spectra of **3** (solid line) and **7** (dotted line) in cyclohexane. b) The absorption (left) and emission (right) spectra of **3** (solid line) and **7** (dotted line) in acetonitrile.

3.3.4 Fluorescence and radiative lifetimes

Radiative lifetimes for **3-9** in cyclohexane were obtained by both comparison of measured lifetimes and quantum yields, and by calculation from the absorption and emission bands using the Strickler-Berg (SB) relationship (Equation 3.1).[57,58]

$$(\tau)^{-1} = 2.88x10^{-9} n^{2} \left[< \nu_f^{-3} > \right]^{-1} \left[\int \left(\frac{\varepsilon(\nu_a)}{\nu_a} \right) d\nu \right] \qquad [3.1]$$

Where n is the solvent refractive index; ε is the molar absorption coefficient and the integration of this term is only over the lowest energy absorption band; ν is the frequency of the transition in cm^{-1}. The term ν_f^{-3} was determined from the integral of the emission spectrum, in terms of corrected intensities in units of relative numbers of quanta at each frequency, divided by the integral of the emission spectrum at ν^{-3} multiplied by this value. The results are summarised in Table 3.4. The radiative lifetimes calculated from the SB relationship are generally slightly lower than those obtained from fluorescence quantum yields and lifetimes. The long wavelength absorption band corresponds to various overlapping electronic transitions, both from different conformation and excited states, and a likely explanation for the differences in experimental and calculated radiative lifetimes is that the lowest energy ($S_0 \rightarrow S_1$) transition is a weak band buried in the more intense absorption around 370 nm, such that the molar absorption coefficients used in the Strickler-Berg calculation are too high and thus give an underestimation of the radiative lifetime. This again suggests the presence of a forbidden transition (likely to be of n, π* origin) as the lowest lying transition in the case of compound **9**, whereas for all the other TAAs studied the allowed transition (of π, π* origin in view of the τ_F (SB) values in Table 3.4) is responsible for the $S_0 \rightarrow S_1$ transition. As is discussed at a later point in this chapter, further clarification on the origin of the nature of this lowest lying excited state can be drawn from fluorescence anisotropy studies of the excitation spectra of these compounds in a rigid media.

Table 3.4 Fluorescence quantum yields, lifetimes and radiative lifetimes for **3**-**9** in cyclohexane.

Compound	Φ_f[a]	τ_f ($\pm$0.05) / ns	Radiative Lifetime[b] ($\pm$ 0.10) / ns	Calculated radiative lifetime[c] / ns
3	0.34	1.60	4.71	1.74
4	0.43	1.96	4.56	2.21
5	0.39	1.29	3.31	2.08
6	0.35	1.58	4.51	1.83
7	0.50	1.26	2.52	1.87
8	0.57	2.38	4.18	1.59
9	0.50	1.05	2.10	8.19

a) In cyclohexane solution with α-4-oligothiophene as reference.

b) Calculated from quantum yield (Φ_f) and lifetime (τ_{exp}) using $\tau_{rad} = \tau_{exp}/\Phi_f$.

c) Calculated from the Strickler-Berg relationship, as discussed in the text.

The radiative lifetimes (both c and d in Table 3.4) reflect the fact that compounds with higher extinction coefficients have shorter radiative lifetimes. Although the agreement between values calculated by the two method is only moderate all the values are consistent with the assignment of π, π* character to the lowest excited state. All the radiative lifetimes are, however, short and thus the emission process in all of the compounds will compete favourably with other processes. Experimental results from a typical single photon counting experiment are shown in Figure 3.14.

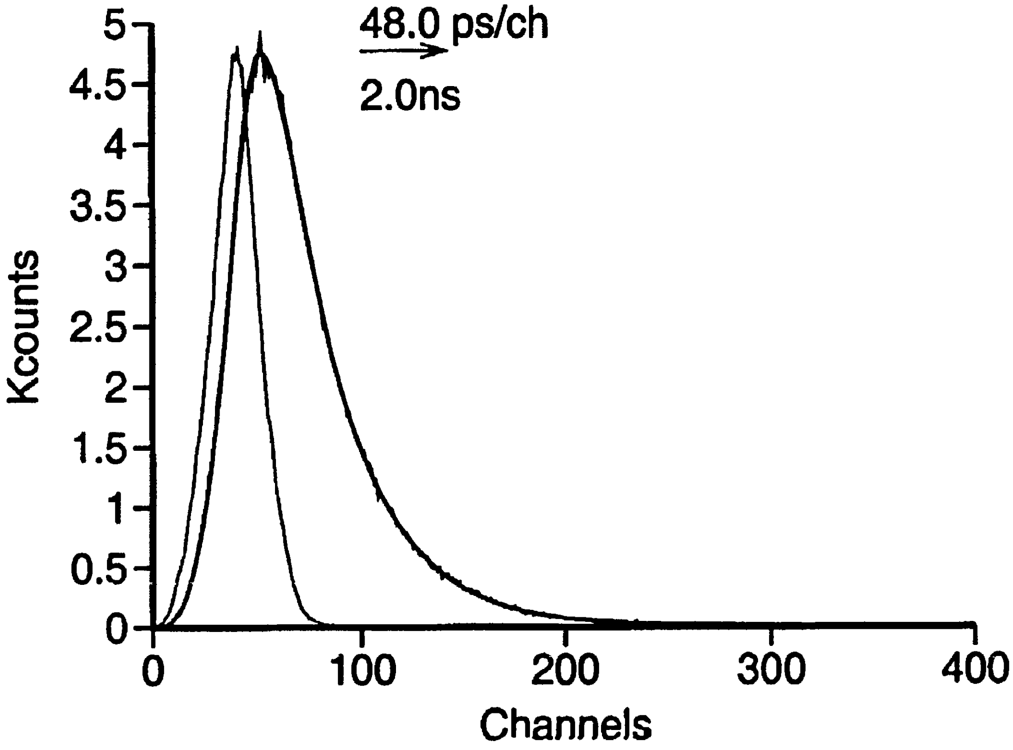

Figure 3.14 Fluorescence decay of **3** in cyclohexane.

3.3.5 Low temperature fluorescence

Fluorescence spectra were also measured in a methylcyclohexane glass at liquid nitrogen temperature, and data are compared with room temperature measurements in Table 3.5. Fluorescence quantum yields are much higher in the 77 K glass, in some cases approaching unity, and there are some slight shifts in emission maxima. Typical spectra obtained are shown in Figure 3.15.

Table 3.5 Summary of the low temperature results; compared with the results at room temperature.

Compound	Room Temperature		Low Temperature	
	λ_{emax}/ nm	Φ_f	λ_{emax}/ nm	Φ_f
3	404	0.34	408	0.67
4	418	0.43	418	0.75
5	400	0.39	403	0.72
6	411	0.35	413	0.95
7	410	0.50	416	0.80
8	483	0.57	484	0.68
9	495	0.50	510	0.93

At room temperature, solvent shell relaxation around the excited state can occur, and emission will be from an equilibrium excited state to a twisted ground state. However, at 77 K in a rigid matrix environment solvent shell relaxation cannot occur and emission is from a Frank-Condon excited state to a planar ground state.

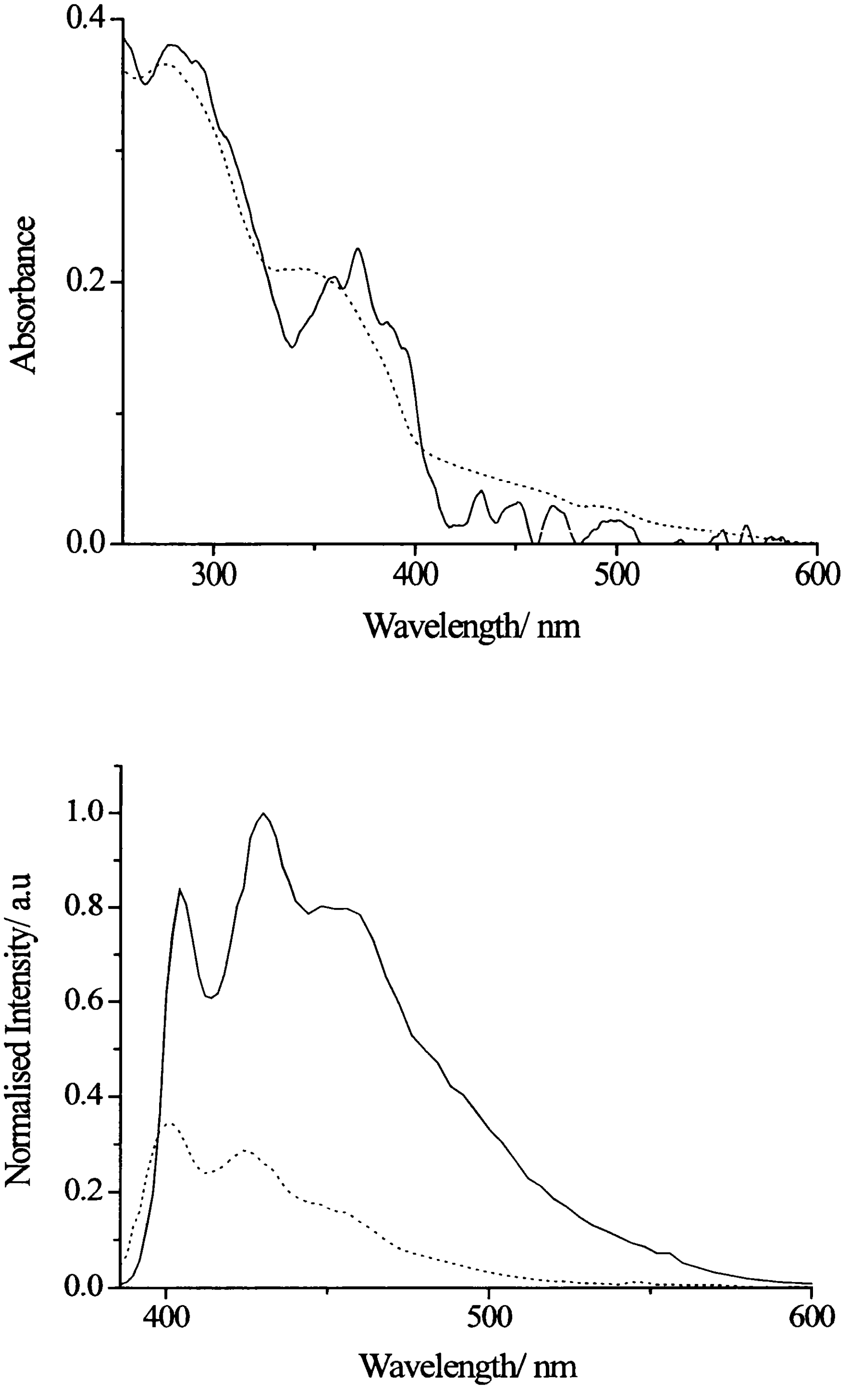

Figure 3.15 Low temperature spectra for **5**. a) Absorption: 77 K (solid line); RT (dotted line). b) Fluorescence: 77 K (solid line); RT (dotted line).

In the low temperature rigid matrix there is a decrease in the probability of internal conversion and intersystem crossing, probably because of the lack of molecular flexibility, which leads to an increase in the fluorescence quantum yield. It is likely that rotation around the N-aromatic bonds is responsible for the importance of the radiationless channel at 293 K ("the loose bolt effect"[59]); at 77 K this deactivation channel vanishes due to the rigidity imposed to the system. Such effects of increased rigidity will also be present in thin films used in electro-optic devices and are likely to favour application of these materials in OLEDs.

The low temperature spectra of **9** and **8** were recorded at 77 K in a mixture of methanol and ethanol (4:1 ratio) in order to determine if the fluorescence is quenched at low temperature by polar solvents since fluorescence from both compounds is quenched at room temperature in polar solvents. At 77 K quenching is not observed, and in both cases the fluorescence quantum yield are very high (0.83 and 0.85 for **9** and **8** respectively). This is most likely to be due to the fact that at 77 K the compounds cannot undergo molecular torsion, i.e. at 77 K emission is from a Frank-Condon excited state to a planar ground state whereas at room temperature deactivation is predominantly nonradiative *via* a twisted excited state. A similar pattern has been described for oligo and polythiophene derivatives. [60,61]

3.3.6 Fluorescence anisotropy

9 was dissolved in diisodecyl phthalate (DIDP), which is a very viscous solvent,[62] and the anisotropy of **9** was then monitored upon the addition of the polar and relatively non-viscous polyethylene glycol 2000 (PEG).

Table 3.6 Fluorescence anisotropy data for **9**

Sample	Solvent	Anisotropy value
9[a)]	Methylcyclohexane	0.56
9	DIDP	0.23
9	DIDP + 5ul PEG	0.19
9	DIDP + 15ul PEG	0.18
9	DIDP + 30ul PEG	0.15
9	DIDP + 100ul PEG	0.07

a) Carried out at 77 K, all other samples were at room temperature.

The observed value for methylcyclohexane at 77 K is above the theoretical maximum anisotropy (0.4), probably due to problems with light scattering, and should be taken as showing that there is no depolarisation during the fluorescence lifetime of **9**. The other results show, as expected, that frozen in a 'glass' or in a highly viscous solution **9** has a relatively high anisotropy value. The anisotropy value then decreases with a decrease in viscosity as it becomes easier for the molecule to undergo molecular torsion.

3.3.7 Chemical oxidation studies

Radical cations of the TAAs were generated by chemical oxidation by cerium (IV) ammonium nitrate in chloroform/acetonitrile. With the exceptions of **6** and **4** this leads to formation of new species with an absorption in the 700-800 nm region. Absorption maxima of TAA radical cations have been reported to lie in the range 640-840nm in acetonitrile solution.[63,64]

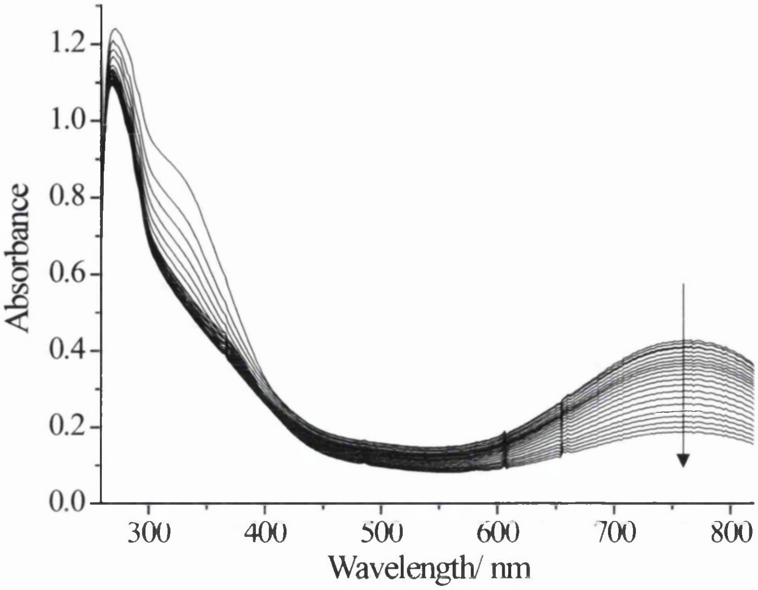

Figure 3.16 (a) Absorption spectrum of **5** after chemical oxidation via the addition of excess Ce(IV). The radical cation formed has a peak in the 700-800 nm region which decays with time, arrow represents increasing time.

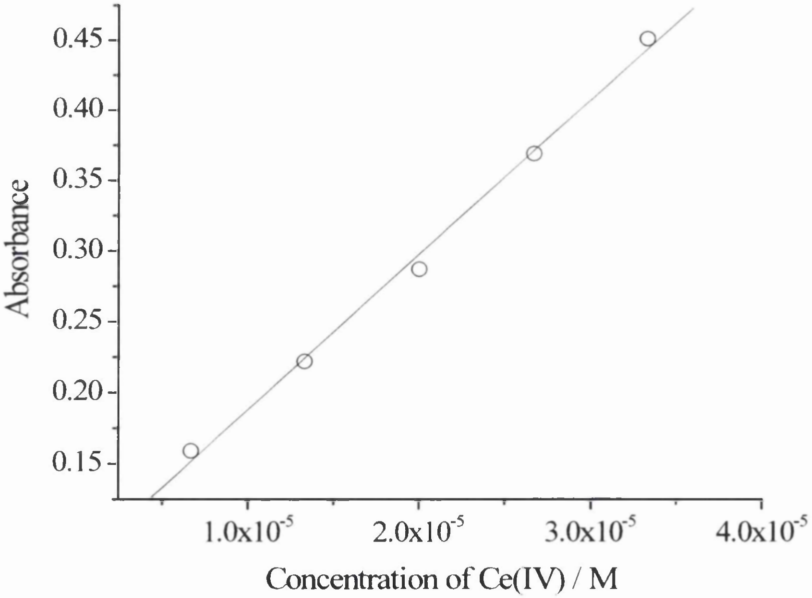

Figure 3.17 Absorption against Ce(IV) concentration, this yields the extinction coefficient of the radical cation of **9**.

Since Ce(IV) is a much stronger oxidizing agent than the amine radical cation, oxidation can be assumed to go quantitatively, such that under the experimental conditions used (excess oxidant), the initial radical cation concentration is identical to the change in concentration of Ce(IV). The plots of initial absorbance against cerium ion concentration are linear, (Figure 3.17), and from the slopes absorption coefficients (ε) of the radical cations can be calculated, these are given Table 3.7. The values are comparable to those reported for other TAA radical cations (typically 7 – 20×10^3 M^{-1}cm^{-1}).[63,64]

Table 3.7 Absorption maxima, extinction coefficients and rate constants of all TAA radical cations formed.

Sample	**λ_{max} / nm**	**ε_{max} / $M^{-1}cm^{-1}$ /× 10^3**	**K_2 / $M^{-1}s^{-1}$**
3	755	20.9	362
5	766	25.5	223
7	748	14.0	495
8	768	11.0	80.4
9	740	12.5	253

6 and **4** did not form a radical cation upon chemical oxidation this is probably due to the stabilising effect of the methoxy group in the para-position on the benzene ring with respect to the central nitrogen.

3.3.8 Thermal properties

3.3.8.1 Hot stage microscopy

Hot stage microscopy (HSM) was carried out on compounds **3-9**. Figure 3.19 shows typical HSM curves both in terms of transmitted light intensity and in terms of DSC counts for both the heating and cooling cycles, pictures taken of the heating and cooling process are shown in Figure 3.20.

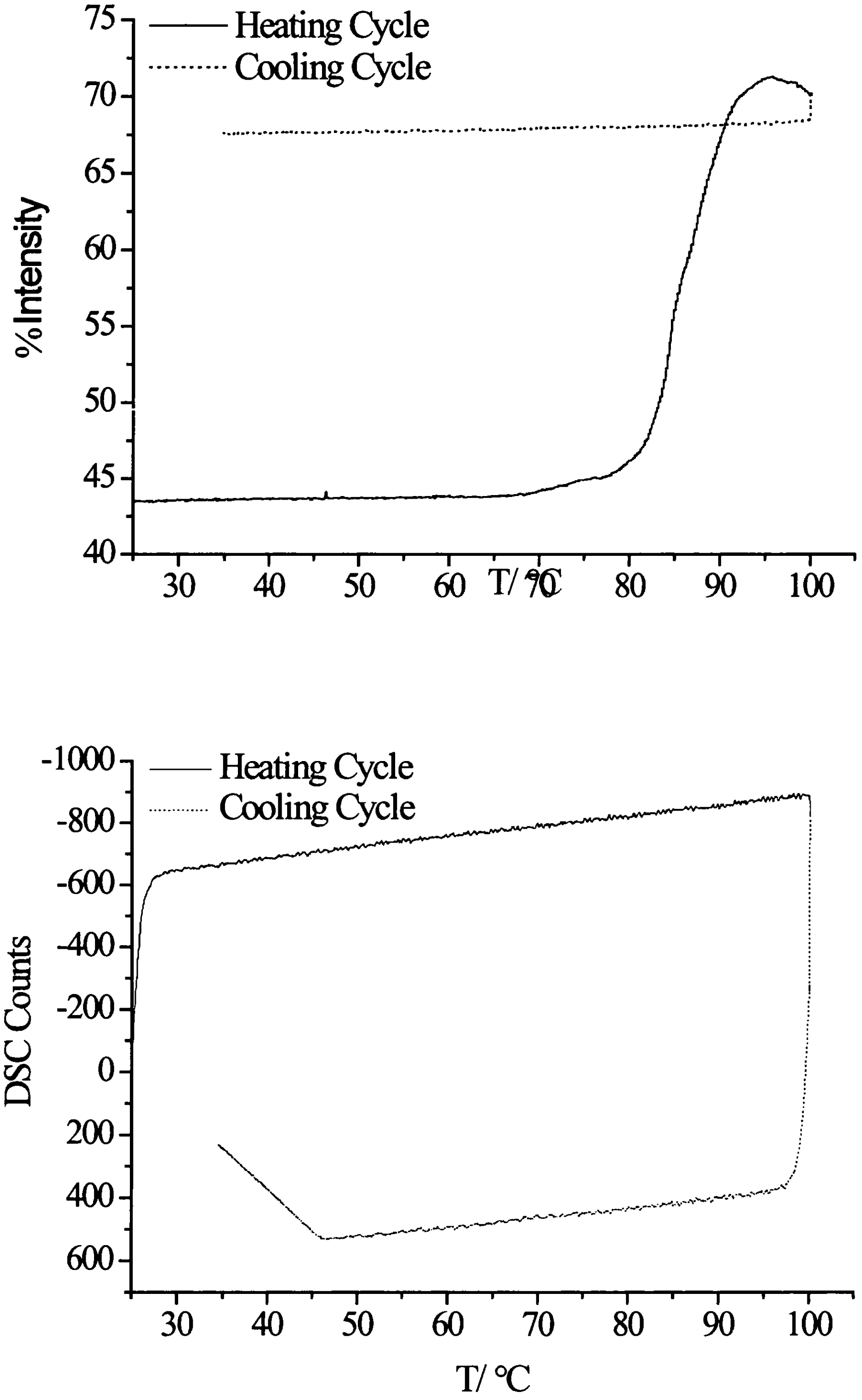

Figure 3.19 Changes in intensity (top graph) and DSC counts (bottom graph) of **9** for both heating (solid line) and cooling cycles (dotted line). Heating rate was 5 °C/minute.

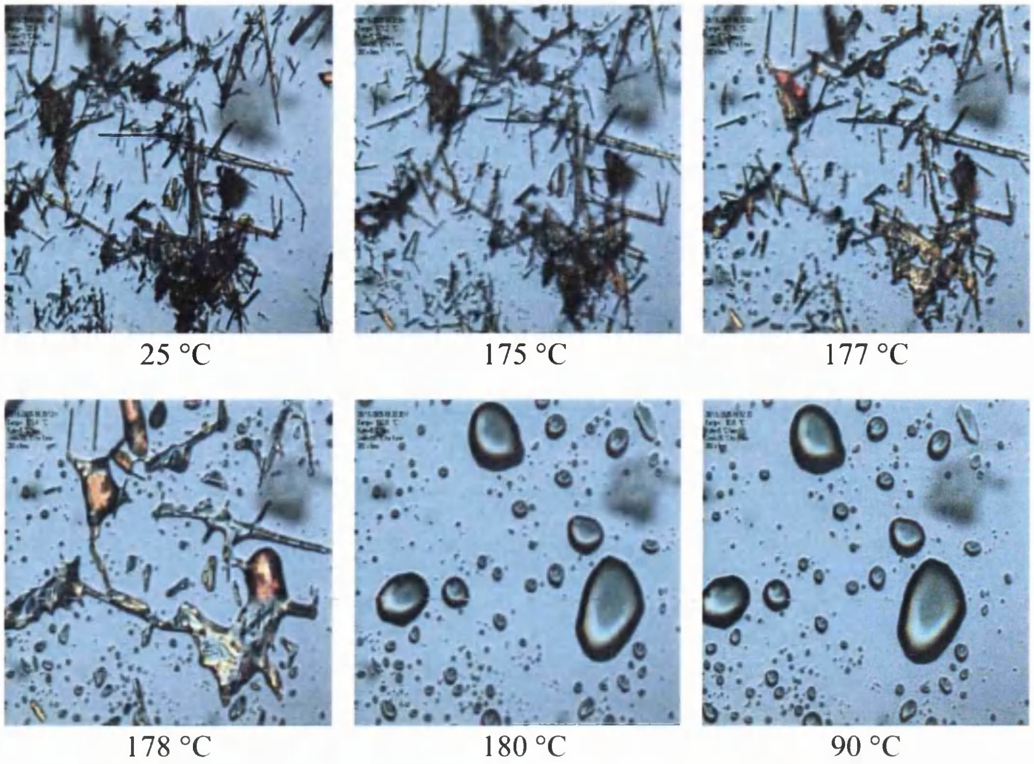

25 °C 175 °C 177 °C

178 °C 180 °C 90 °C

Figure 3.20 Photographs of heating and cooling of **3,** confirming melting but lack of crystallisation upon cooling, observed by thermomicroscopy.

Table 3.8 and Figure 3.21, shows the onset of melting temperature and the melting point ranges.

Table 3.8 HSM results summary showing the onset temperature along with the melting point range of all the compounds.

Compound	Onset Temperature / °C	Melting point range / °C
3	176.0	176-178
4	92.6	98-102
5	106.8	113-117
6	86.1	100-108
7	175.7	177-180
8	182.5	182-185
9	80.0	85-93

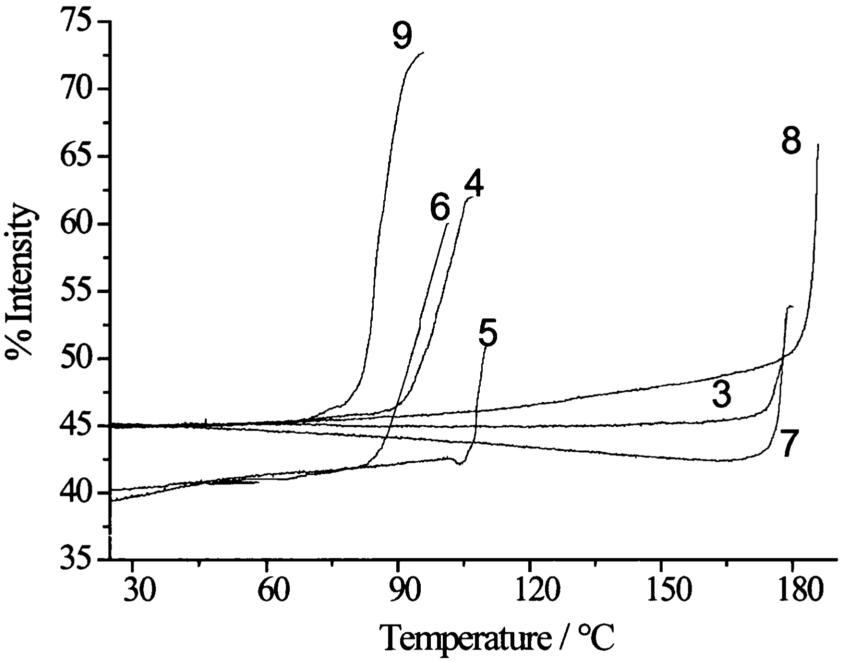

Figure 3.21 HSM heating curves as a function of intensity for all TAA samples, all samples were heated at a rate of 5°C/min.

The differences between the onset of melting temperature and the melting point range arise due to the fact that the onset of melting temperature is the value calculated from the extrapolation of the intensity curves whereas the melting point range is the actual observed value. The HSM shows that these compounds do not crystallize readily; the compounds have also been kept in a small volume solution for a time period greater than a year with no crystallization.

3.3.8.2 Thermogravimetric analysis

Thermogravimetric analysis (TGA) was also carried out on **3-9** in order to determine the thermal properties and in particular the degradation temperatures of the compounds. TGA showed that all compounds were stable in nitrogen up to temperatures of 300 °C (Table 3.9). A typical TGA curve obtained is shown in Figure 3.22. It is important that the thermal degradation temperatures are above 300 °C in order to be well above operating temperatures of relevant devices and also so that the compounds can be applied using vacuum deposition techniques. Also a high thermal degradation temperature means a wider temperature range in which the compounds could be used, possibly leading to a wider range of applications.

Table 3.9 Thermal decomposition temperatures (T_d) for **3-9**.

Compound	T_d / °C (+/- 5°C)
3	357
4	361
5	302
6	323
7	367
8	313
9	300

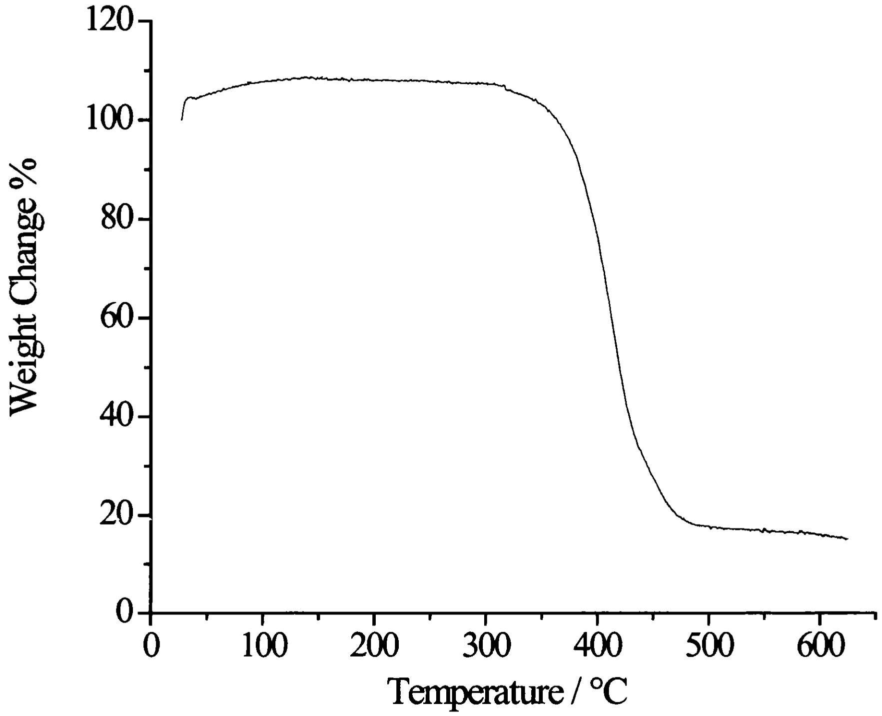

Figure 3.22 TG curve of compound **7** (typical of all samples). Decomposition of the sample occurs above 300 °C.

During thermogravimetric analysis it was also found that some of the compounds sublime. This was confirmed by recording a UV/VIS spectrum of the sublimate and comparing it to the spectrum of that compound. Only two compounds out of the seven (compounds **8** and **9**) did not sublime.

3.4 Conclusions

The photophysical characteristics of seven novel dehydroabietic based TAAs have been investigated. The presence of the bulky dehydroabietic acid moiety has been shown to produce thermally stable, soluble and vacuum sublimable materials without adversely affecting their electrochemical, optical or photophysical properties. These compounds do not crystallise readily and in some cases the presence of the bulky groups seems to enhance their fluorescence emission properties. These properties make the compounds attractive materials for a variety of applications in molecular electronics. Fluorescence quantum yields were greater than 0.3 for all compounds in cyclohexane which indicates that good internal quantum efficiencies could be achieved if they were to be used in molecular electronic devices. However, in polar solvents compounds **9** and **8** which contain the strongly electron withdrawing $-NO_2$ show unusual behaviour. Emission changes significantly with solvent polarity being shifted to the 'red' with complete loss of structure. This can be understood in the terms of a close lying twisted charge transfer band, the position of which is solvent dependent. Quenching by polar solvents does not occur at low temperatures due to the fact that the compounds cannot undergo molecular torsion. The data suggests that room temperature emission is from a twisted excited state to a twisted ground state, whereas at low temperatures emission is from a relatively planar excited state to a planar ground state. High molar extinction coefficients of the magnitude of $3.0\text{-}4.0(\pm0.50)\times10^4$ $M^{-1}cm^{-1}$ were obtained for most compounds, and relatively short radiative lifetimes were observed. High molar extinction coefficients coupled with short radiative lifetimes means that emission will compete very favourably with other competing processes. All compounds show significant solvachromatism in their fluorescence spectra. The absorption and emission properties of **4** in particular alter significantly on going to a polar solvent as thus could find potential use as a polarity probe.

The characteristics suggest that the compounds may find application as blue emitters in OLEDs. Their suitability for electro-optic devices is further enhanced by thermal decomposition temperatures of greater than 300°C, and for certain compounds this is enhanced further by the occurrence of sublimation when heated in a nitrogen atmosphere.

3.5 References

1. M. Stolka, J. F.Yanus and D. M. Pai, *J. Phys. Chem.*, **1984**, *88*, 4707.
2. H. D. Burrows, R. A. E. Castro, M. A. Esteves, B. Gigante, M. L. P. Leitão and A. C. Pauleta, *Mater. Sci. Forum*, **2006**, *8*, 514-516.
3. Y. Shirota, *J. Mater. Chem.*, **2000**, *10*, 1.
4. U. Mitschke and P. Bauerle, *J. Mater. Chem.*, **2000**, *10*, 1471.
5. M. Thelakkat, *Macromol. Mater. Eng.*, **2002**, *287*, 442.
6. Y. Shirota, *J. Mater. Chem.*, **2005**, *15*, 75.
7. K. R. J. Thomas, J. T. Lian, C. M. Tsai and H. C. Lin, *Tetrahedron*, **2006**, *62*, 3517.
8. S. Amthor, B. Noller, C. Lambert, *J. Chem. Phys.*, **2005**, *316*, 141-152.
9. K. L. Tong, S. K. So, H. F. Ng, L. M. Leung, M. Y. Yeung and C. F. Lo, *Synth. Met.*, **2002**, *147*, 199.
10. M. A. Esteves, N. Narender, M. J. Marcelo-Curto and B. Gigante, *J. Nat. Prod.*, **2001**, *64*, 760.
11. K. D. Belfield, M. V. Bondar, O. V. Przhonska and K. J. Schafer, *J. Flu.*, **2002**, *12*, 449.
12. R. Stahl, C. Lambert, C. Kaiser, R. Wortmann and R. Jakober, *Chem. Eur. J.* **2006**.
13. M. Thelakkat, C. Schmitz, C. Hohle, P. Strohriegl, H. W. Schnidt, U. Hofmann, S. Schloter and D. Haarer, *Phys.Chem.Chem.Phys.*, **1999**, *1*, 1693.
14. I. K. Yakushchenko, M. G. Kaplunov, O. N Efimove, M. Yu. Belov and S. N. Shamaev, *Phys.Chem.Chem.Phys.*, **1999**, *1*, 1783.
15. K. Strzelec, N. Tsukamoto, H. J. Kook and H. Sato, *Polym. Int.*, **2001**, *50*, 1228.
16. X. Jiang, S. Liu, M. S. Liu, P. Herguth, A. K. Y. Jen, H. Fong and M. Sarikaya: *Adv. Funct. Mater.* **2002**, *12*, 745.
17. P. Strohriegl and J. V. Grazulevicius, *Adv. Mater.* **2002**, *14*, 1439.

18. J. Yamamoto, A. Uchikawa, A. Kawato, A. Shibata, T. Mizutani and R. Nakashima, *J. Chem. Soc. Jpn., Chem. Ind. Chem.*, **1992**, 874.
19. K. Naito and A. Miura, *J. Phys. Chem.*, **1993**, *97*, 6240.
20. D. E. Loy, B. E. Koene and M. E. Thompson, *Adv. Funct. Mater.*, **2002**, *12*, 245.
21. C. H. Yanga, F. J. Liub, L. R. Huangc, T. L. Wanga, W. C. Lind, M. Satob, C. Chenc and C. C. Chang. *J. ElectroChem.*, **2008**, *617*, 101–110.
22. S. Lengvinaite, J. V. Grazulevicius, S. Grigalevicius, B. Zhang, J. Yang, Z. Xie, L. Wang. *Synthetic Metals*, **2008**, *158*, 213-218.
23. C. W. Tang and S. A. VanSlyke, *Appl. Phys. Lett.*, **1987**, *51*, 913.
24. J. H. Burroughes, D. D. C. Bradley, A. R. Brown, R. N. Marks, K. Mackay, R. H. Friend, P. L. Burns and A. B. Holmes, *Nature*, **1990**, *347*, 539.
25. H. Zhao, C. Tanjutco and S. Thayumanavan, *Tetrahedron Lett.*, **2001**, *42*, 4421.
26. T. Miteva, A. Meisel, W. Knoll, H. G. Nothofer, U. Scherf, D. C. Müller, K. Meerholz, A. Yasuda and D. Neher, *Adv. Mater.*, **2001**, *13*, 565.
27. H. Xiao, B. Leng and H. Tian, *Polymer*, **2005**, *46*, 5707.
28. H. Tanaka, S. Tokito, Y. Taga and A. Okada, *Chem. Commun.*, **1996**, 2175.
29. G. E. Jabbour, S. E. Shaheen, M. M. Morrell, J. D. Anderson, P. Lee, S. Thayumanavan, S. Barlow, E. Bellman, R. H.Grubbs, B. Kippelen, S. Marder, N. R. Armstrong and N. Peyghambarian, *IEEE J. Quantum Electron.*, **2000**, *36*, 12.
30. J. P. Chen, H. Tanabe, X. C. Li, T. Thoms, Y. Okamura and K. Ueno, *Synth. Met.*, **2005**, *132*, 173.
31. E. M. Han, L. M. Do, Y. Niidome and M. Fujihira, *Chem. Lett.*, **1994**, 969.
32. J. Morgado, L. Alcácer, M. A. Esteves, N. Pires and B. Gigante, *Thin Solid Films*, **2007**, *515*, 7697.
33. H. D. Burrows, S. M. Fonseca, B. Gigante, M. A. Esteves, A. M. Guerreiro, *J.Fluorescence*, **2006**, *16*, 227.
34. C. W. Tang, S. A. van Slyke and C. H. Chen, *J. Appl. Phys.*, **1989**, *65*, 3610.
35. Howard, E. Webster, *Scientific American*, **2004**, *290*, 76.
36. J. Kovac, L. Peternai, O. Lengyel. *Thin Solid Films*, **2003**, *433*, 22-26.

37. J. Kalinowski. *J. Phys. D: Appl. Phys.* **32** (1999), p. 179.

38. H. Yersin, D. Donges, *Top. Curr. Chem.*, **2001**, *214*, 81.

39. W. Finkenzeller, H. Yersin, *Chem. Phys. Lett.,* **2003**, *377*, 299.

40. W. Finkenzeller, P. Stoessel, H. Yersin, *Chem. Phys. Lett.,* **2004**, *397*, 289.

41. W. BrÄutting, S. Berleb, and A. G. MÄuckl, *Org. Electr.*, **2001,** *2,* 1.

42. J. H. Kim, E. J. Nam, S. Y. Hong, B. O. Kim, S. M. Kim, S. S. Yoon, J. H. Suh, Y. Ha and Y. K. Kim, *Materials Science and Engineering,* **2004**, *24*, 167-171.

43. M. Yahiro, D. Zou and T. Tsutsui, *Syn. Metals,* **2000**, *111-112*, 245-247.

44. S. Tokito, H. Tanaka, K. Noda, A. Okada and Y. Taga, *Appl. Phys. Lett.*, **1929**, *70.*

45. B. E. Koene, D. E. Loy and M. E. Thompson, *Chem. Mater.*, **1998**, *10*, 2235.

46. H. F. M. Schoo and R. J. C. E. Demandt, *Phillips J. Res.*, **1998**, *51*, 527.

47. P. Calvert, *Chem. Matter.*, **2001**, *13,* 3299.

48. J. S. Yang, S. Y. Chiou and K. L. Liau, *J. Am. Chem. Soc.*, **2002**, *124*, 2518

49. T. Yamamoto, M. Nishiyama, Y. Koie, *Tetrahedron Lett.*, **1998**, *39*, 2367

50. NCMC Solvent Database, SOLV-DB®.

51. R.S. Becker, J. Seixas de Melo, A.L. Macanita and F. Elisei. *J.Phys.Chem*, **1996**, *100*, 18683 - 18685.

52. J. Seixas de Melo, L. M. Silva and M. Kuroda, *J.Chem.Phys.*, **2001**, *115,* 5625.

53. G. Stricker, V. Subramanian, C. A. M. Seidel and A. Volkmer, *J. Phys. Chem. B*, **1999**, *103*, 8612.

54. H. D. Burrows, N. Chattopadhyay, M. A. Esteves, M. Fernandes and B. Gigante, *J. Fluorescence*, **2007**, *17*, 701.

55. J. S. Yang, S. Y. Chiou and K. L. Liau, *J. Am. Chem. Soc.*, **2002**, *124*, 2518; H.-C. Li, Y.-P. Lin, P.-T. Chou, Y.-M. Cheng and R.-S. Liu, *Adv. Funct. Mater.*, **2007**, *17*, 520.
56. N. S. Bayliss and E. G. McRae, *J. Phys. Chem.*, **1954**, *58*, 1002-1006.
57. S. J. Strickler and R. A. Berg, *J. Chem. Phys.,* **1962**, *37*, 814.
58. R.V. Bensasson, E.J. Land and T.G.Truscott, *Excited States and Free Radicals in Biology and Medicine*, Oxford University Press, Oxford, **1993**, pp. 90.
59. N. J. Turro, *Modern Molecular Photochemistry*, University Science Books, Saulsalito, California, **1991**, pp.170-172.
60. R. S. Becker, J. Seixas de Melo, A. L. Maçanita and F. Elisei, *J. Phys. Chem.,* **1996,** *100*, 18683.
61. J. Seixas de Melo, H. D. Burrows, M. Svensson, M. R. Andersson and A. P. Monkman, *J.Chem.Phys.*, **2003**, *118*, 1550.
62. F. J. P. Caetano, J. M. N. A. Fareleira, C. M. B. P. Oliveira dn W. A. Wakeham, *J.Chem.Eng.Data*, **2005**, *50*, 1875.
63. H. D. Burrows, D. Greatorex and T. J. Kemp, *J. Phys. Chem.*, **1972**, *76.* 20.
64. R. I. Walter, *J. Am. Chem. Soc.*, **1966**, *88*, 1923.

Chapter 4

Cationic Conjugated Polyelectrolytes: Aggregation, Energy Transfer and Photophysical Properties

4.1 Introduction

A polymer is a macromolecule that contains N_P covalently bound elementary chemical repeat units. Polymers are synthesised by condensation or by free radical reactions that usually produce a range of molecular sizes. This is called the polydispersity and is often expressed in terms of the ratio between the number-average and weight-average molecular weights, M_n/M_w.[1] When some or all of the repeat units of the polymer are charged the polymer is called a polyion. Together with the polyion there are oppositely charged counter-ions that neutralise all the charges in the chain. The polyion and its counter-ions constitute a polyelectrolyte. Conjugated polyelectrolytes (CPEs) are polymers that contain both a π-conjugated backbone and functional groups that ionize in high dielectric media.[2] This structure is represented in Figure 4.1.

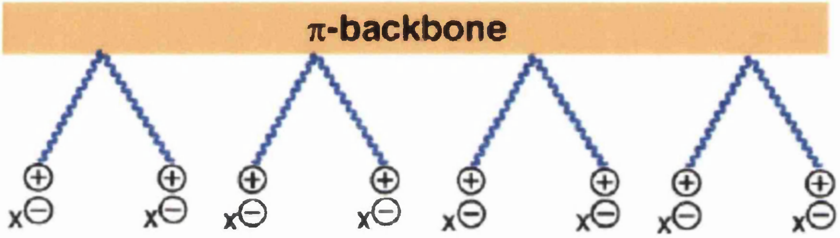

Figure 4.1 Schematic representation of the structure of a conjugated polyelectrolyte.

CPEs are currently the subject of intense research interest due to their exceptional optical, electronic and mechanical properties.[3-9] Cationic conjugated polyelectrolytes (CCPs) tend to be highly sensitive to changes in their physical and chemical environment[10-12] and, hence, one of the major potential uses of CCPs is in biological and chemical sensors.[4,12-14] This is discussed in further detail in Chapter 6. They have the advantage of high sensitivity with short luminescent lifetimes and the possibility of amplified fluorescence energy transfer or quenching processes.[13] Recent research on the application of CPEs in biological and chemical sensors has led to a greater structural diversity and new synthetic protocols for their preparation.[15]

Neutral conjugated polymers are important technological materials with uses in optoelectronic devices, such as polymer light emitting diodes (PLEDs)[16] and solar cells.[17] Part of the interest stems from the possibility of implementing solution-based deposition methods as part of the device fabrication process. Incorporation of ionic side groups increases solubility in polar organic solvents and water, which can potentially provide more environmentally friendly manufacturing processes. Current interest in solar cells based on conjugated stems from the promise of low cost fabrication.[17]

Research into cationic conjugated polymers (CCPs) has recently been mainly focussed in sequence specific DNA assays, designed by utilising the electrostatic interactions between cationic conjugated polymers and negatively charged DNA. [5,18-22] These assays commonly exploit the ability of CCPs for efficient excitation energy transfer using, for example, protein nucleic acids (PNA) and Förster resonance energy transfer (FRET).[9,22-25] Although CCPs have already been used in biosensors[24,25] there is still a great deal of research needed to optimise their use. Two of the main areas in which a greater understanding is required are the aggregation properties and energy transfer processes of CCPs.[26] Their solubility in water is normally limited by the hydrophobicity of the conjugated backbones and interactions between adjacent polymer chains, which lead to aggregation and cluster formation.[27]

4.1.1 Electronic structure of a conjugated polymer

Conjugated polymers are polymers with conjugated double bonds in the main polymer chain which results in extensively conjugated system with strong delocalization of electrons along the polymer chain. The low energy π occupied orbitals, form a valence band, while the higher energy π^* (antibonding) orbitals forms an unoccupied conduction band. The band gap between valence and conduction band gives the polymer semi-conducting behaviour

4.1.2 Polyfluorenes

Polyfluorene (PF) based CPEs are among the most common CPEs used for these applications. Fluorene (Figure 4.2) based conjugated polymers emit in the blue spectral region, and have high efficiencies in both photoluminescence and electroluminescence.[28-31] PFs also possess high charge carrier mobility, good processability, excellent thermal stability and high stability against oxidants.[2] PFs are relatively wide band-gap materials (the band-gap between valence and conduction band) and thus the emission colour can be tuned via energy transfer to smaller band-gap chromophores which can be incorporation into the polymer as co-monomers or substituents. PFs are, in fact, the only family of conjugated polymers found to-date that, with inserting the appropriate group, can emit colours spanning the entire visible range with high efficiency and low operating voltage.[32]

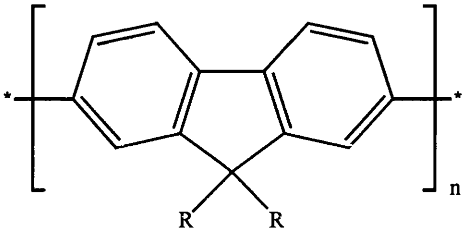

Figure 4.2 Structure of fluorene monomer.

4.1.3 Synthesis of polyfluorenes used in this study

In this study we examined the absorption and emission properties of three water soluble fluorescent cationic conjugated polymers (CCPs), poly {9,9-bis[*N*,*N*,*N*-(trimethylammonium)hexyl] fluorene-*co*-1,4-phenylene} of varying chain lengths (given in Table 4.1) which we will refer to as CCP-S (short), CCP-M (medium) and CCP-L (long). All three polymers were synthesised via the same synthetic route first developed by *Bazan* and co-workers[33] and were synthesised by our collaborators. CCP-S and CCP-M were synthesised by Professor Ullrich Scherf (Bergische Universität, Wuppertal) and CCP-L was synthesised by Dr Ricardo Mallavia (Universidad Miguel Hernández, Alicante, Spain). Here is presented just a summary of the synthesis for the benefit of the reader. The synthetic pathway is shown in Figure 4.3. Synthesis of 2,7-dibromo-9,9-bis(6-bromohexyl) fluorene (**2**) monomer started from the commercially available 2,7-dibromofluorene (**1**) which was alkylated with 1,6-dibromohexane/sodium hydroxide. (**2**) was converted to 9,9-bis[6-(N, N-dimethylamino)hexyl]fluorene (3) with dimethylamine in THF at -78 °C. (**3**) was subjected to a Suzuki-type cross-coupling reaction with 1,4-phenylene-diboronic acid using a palladium catalyst (5 mol %) in THF as solvent, to produce **(4)**. Quarterisation of **(4)** by methyl iodide or methyl bromide in a mixture of DMF and TMF gave poly {9,9-bis[*N,N,N*-(trimethylammonium)hexyl] fluorene-*co*-l,4-phenylene} **(5)**. The number average molecular weight (M_n) along with the degree of polymerisation of all the CCPs was calculated by gel permeation chromatography (GPC) and is given in Table 4.1. The determination of molecular weights of these polymers is difficult and all polymers have a polydispersity of about 2.

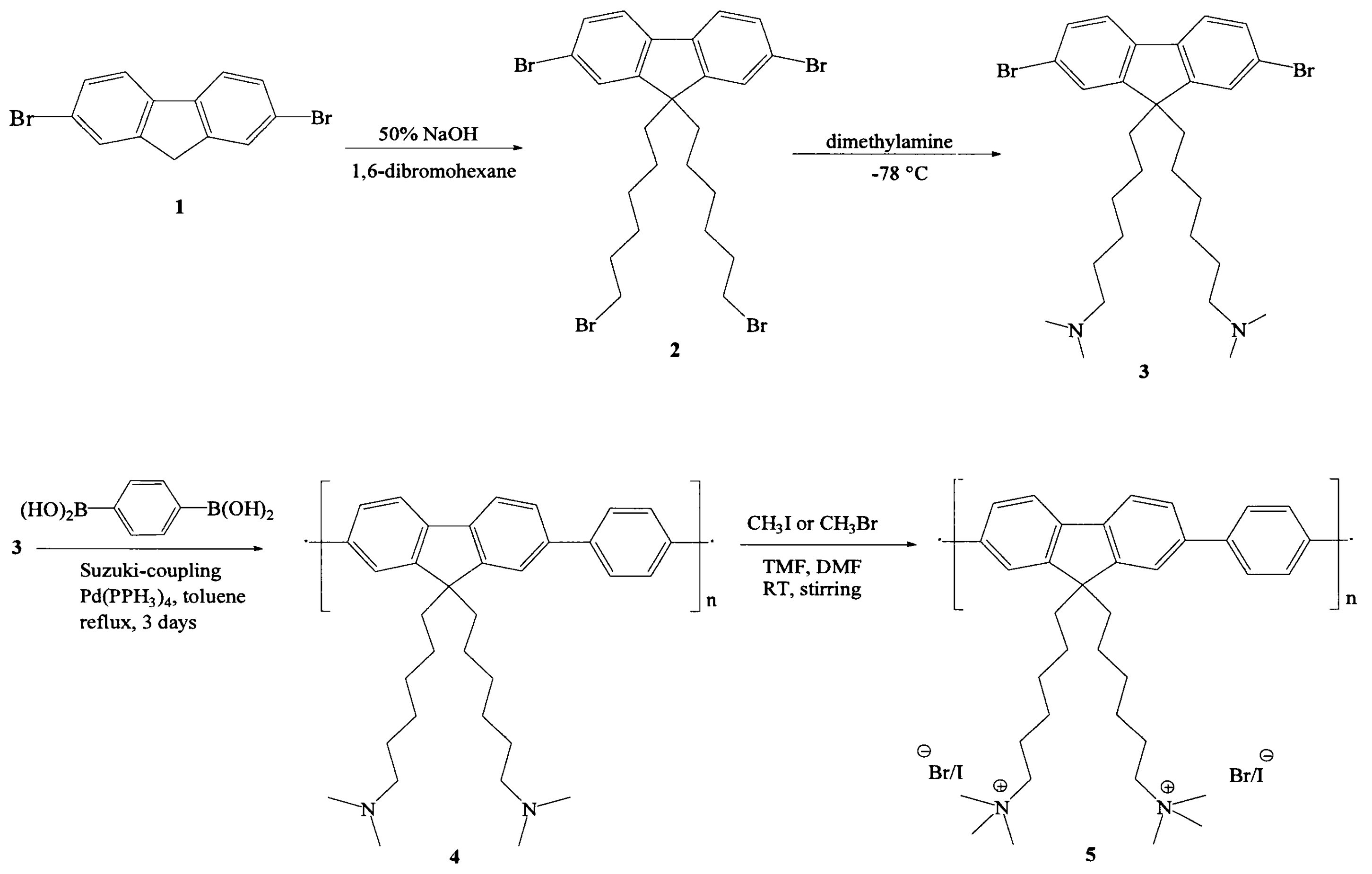

Figure 4.3 Synthetic route for CCPs used in this work.

Table 4.1 Characteristics of CCPs used in this study.

Polymer	Counter Ion	Number average molar mass M_n / Kg/mol	Average number of monomers per chain
CCP-S	Br^-	3.5	5.7
CCP-M	I^-	6.5	12.4
CCP-L	Br^-	52.0	99.1

4.1.4 Aggregation of polyelectrolytes

Conjugated polyelectrolytes tend to aggregate in solution due, in part, to the hydrophobicity of the backbone. This causes a decrease in the emission through aggregate quenching.[10,34] Various methods have been used to try and overcome this problem, including the incorporation of linear and branched polymer side chains and the use of surfactants.[35-40] Minimising aggregation and obtaining the highest quantum yield possible is vital for the use of CCPs in 'FRET' type sensors and displays. Thus knowledge of the aggregation properties of CCPs and possible solutions to breaking up these aggregates is vital for material and sensor applications.

4.1.5 Exciton dynamics of polyelectrolytes

Exciton dynamics are also of great importance for the application of CCPs to sensors and light-emitting and photovoltaic devices.[39-42] A conjugated polymer chain can be thought of as a series of linked chromophores with a distribution of conjugation lengths which arise due to both a distribution of polymer sizes and the fact that, within a polymer, twists and bends of the chain can lead to breaks in conjugation.[43] Upon excitation, excitons move rapidly along the polymer chains and excitation may migrate from the absorbing molecular unit over a considerable number of other units by FRET before deactivation occurs by fluorescence or another process. [43-44] Such energy transfer cannot be recognised from the fluorescence spectra; however, it does lead to a decrease in the fluorescence anisotropy of the system.[45,46] Exciton migration will be influenced by aggregation since this provides the possibility of both interchain FRET and the formation of aggregation "traps".

4.1.6 Aims of this study

For application in electronic devices (such as PLEDs) and in possible sensor applications there is the need for a photochemical and photophysical characterisation, and this chapter describes the characterisation of three CCPs (CCP-S, CCP-M and CCP-L), with emphasis on aggregation and energy transfer characterisation. The aim is understanding and minimising the aggregation of the CCPs in solution. This also led to modelling of the excited-state decay kinetics in aggregated CCP systems in terms of energy transfer migration and trapping using a programme (known herein as ProgClusters) for simulating the movement of excitation energy between excited donor sites, ground state donors and energy traps in 1-D.

4.2 Experimental

4.2.1 Materials

CCP-S and CCP-M were a gift from Professor Ullrich Scherf (Bergische Universität, Wuppertal) and CCP-L was a gift from Dr. Ricardo Mallavia (Universidad Miguel Hernández) and all were used as received. All other chemicals were purchased from Sigma-Aldrich. Acetonitrile and ethanol were of spectroscopic or equivalent grade. All experiments were performed using Millipore Milli-Q deionised water.

4.2.2 Equipment and Methods

4.2.2.1 Aggregation studies

A 5.2×10^{-5} M (in terms of the repeat unit of the polymer) stock solution of CCP was prepared in water and stirred for 24 hours. 200 μl aliquots of the stock solution were then added, individually, to 5 ml volumetric flasks using a micro–pipette and made up to 5 ml with 1, 5, 10, 15, 20, 25 or 30% acetonitrile/water (v/v). (The 200 μl aliquots of the stock solution were also weighed to ensure the weights were within ± 0.0001 g). Absorption measurements were made using a Shimadzu UV-2100 spectrophotometer and steady-state luminescence studies were carried out using the Jobin Yvon-Spex Fluorolog 3-22 spectrometer described in Section 2.3.1. Excitation and emission slits were 4.0 nm. Fluorescence spectra were corrected for the spectral response of the light source and detector.

4.2.2.2 Anisotropy studies

Anisotropies were measured for CCP-S in 25:75 acetonitrile:water (v/v) across the CCP-S concentration range 2.15×10^{-6} to 2.15×10^{-5} M (in terms of repeat units). Anisotropy values are those from the emission weighted averages across the emission band, i.e. from the integrated emission curves. Steady-state fluorescence anisotropy experiments were carried out using a Jobin-Yvon Fluoromax-3 spectrometer (as described in Section 2.3.3) with right angle geometry and excitation and emission slits of 5.0 nm.

4.2.2.3 Modelling studies

ProgClusters had been previously designed by Alastair Douglas to model energy transfer between nearest neighbour Ln^{3+} pairs within a silicate structure, AV-20.[47] However it is not specific to this system and may be applied to any system involving energy transfer in 1, 2 or mixed 1-2D. The program sets up an array of linear repeat units interspersed with inert end group units in a statistical (random) manner, such that the distribution of polymer chain lengths corresponds to the experimental number average molar mass with statistical (random) polymerisation. Link or traps units are then introduced between polymer chains. They are distributed statistically (randomly) according to probabilities entered by the programmer. It is assumed all repeat units have equal chance of excitation. Every repeat unit is initially excited and the total energy remaining after each "step" of a series of energy transfer processes is calculated. In each "step" a specified fraction of the energy remaining at each repeat unit is transferred to adjacent units, links and traps, and energy entering a trap is lost from the array. Superimposed on this loss by trapping is an exponential decay corresponding to a presumed exponential decay of the excited repeat unit when isolated from any traps. We have typically been examining an array containing 500,000 repeat units, over a series of 200,000 steps in each one of which 25% of the energy in a repeat unit is transferred to any adjacent repeat unit, link or trap. Typical arrays are shown in Figure 4.11.

4.3 Results

4.3.1 Aggregation of CCPs

4.3.1.1 Steady-state absorption and fluorescence

Considerable research has been carried out on CCP-surfactant interactions and the breaking of CCP aggregates using non-ionic surfactants.[4,10,36-38] The use of non-ionic surfactant has previously been reported to increase the photoluminescence of a CCP similar to CCP-S by a factor of 8, from a quantum yield of 0.03 in pure water to a quantum yield of 0.23.[10] Organic co-solvents are also known to break up conjugated polyelectrolyte aggregates.[48,49] In the work described here we investigated the effect of ethanol and acetonitrile on the absorption and emission of CCPs. It was found that the use of acetonitrile resulted in a higher fluorescence quantum yield than did ethanol, and therefore acetonitrile was used as a co-solvent for all subsequent experiments. The change in the absorption and emission of CCP-S at various acetonitrile concentrations is shown in Figure 4.4.

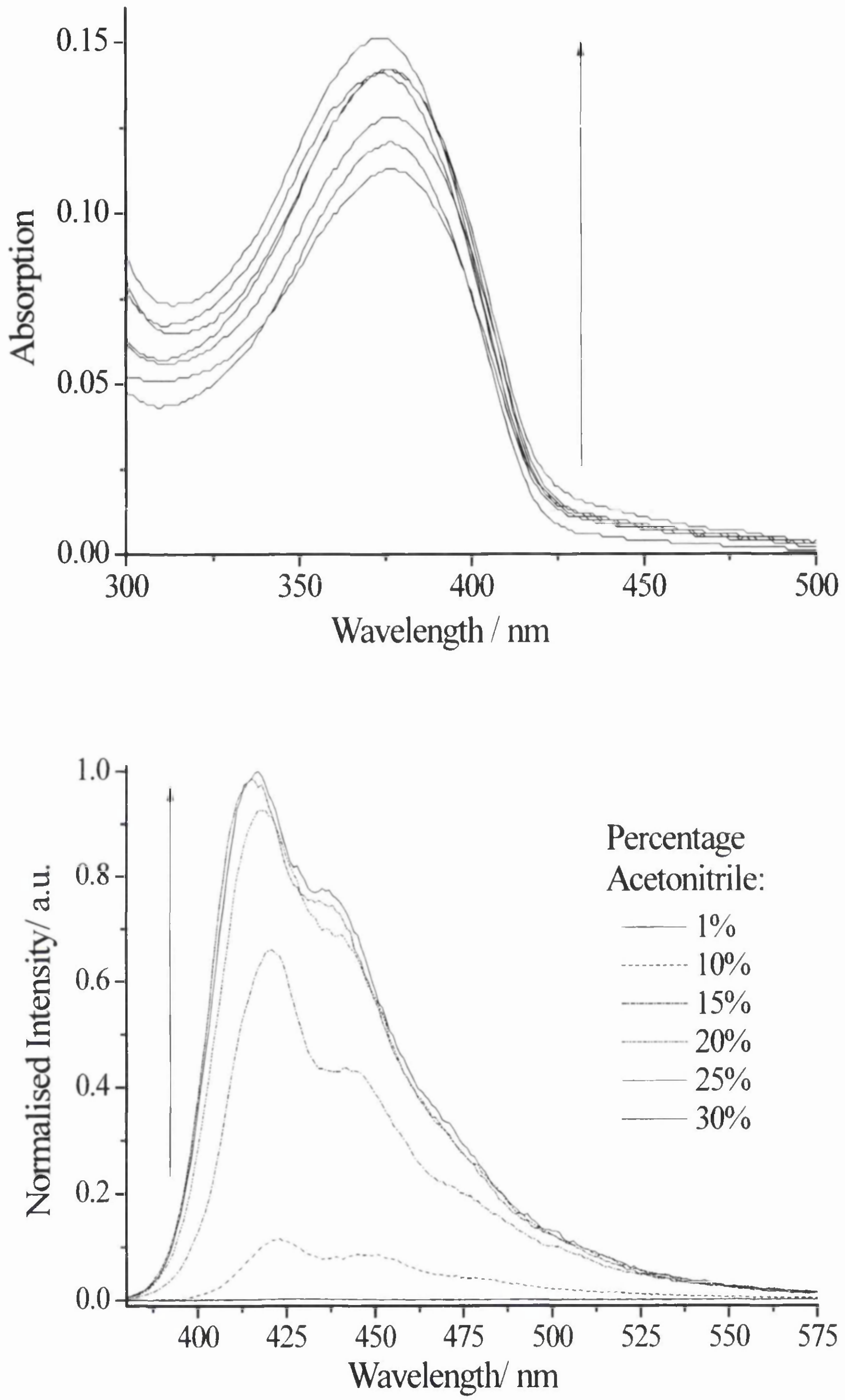

Figure 4.4 Change in absorption and fluorescence spectra of CCP-S with acetonitrile concentration (1, 10, 15, 20, 25, 30% acetonitrile in water). The direction of the arrows indicates increasing acetonitrile concentration.

All CCPs in 25% acetonitrile show broad absorption and emission bands (Figure 4.4) with maxima in the 375 nm and 420 nm regions respectively. Both the absorption (ε_{max}) and the emission intensity (Φ_f) of CCPs increase with acetonitrile percentage until 25 %; after this they essentially remains constant, before decreasing at the highest acetonitrile concentrations. We attribute both the increase in Φ_f and increase in ε_{max} to the break up of polymer aggregates, although it is thought that all the CCPs are still aggregated to some extent even in 25:75 acetonitrile. The increase in absorption and emission with acetonitrile concentration is accompanied by a slight hypsochromic wavelength shift i.e. the more aggregated polymer systems lead to longer wavelength of maximum absorption. Also, increased aggregation causes increased absorption around ~425 nm. The quantum yield of CCP-S in 25/75 acetonitrile/water is 0.28 (±0.01), close to, but slightly higher, than the value 0.23 reported for the same polymer de-aggregated by surfactants.[10] Although caution is needed, because of solvent effects on non-radiative decay pathways, acetonitrile may be more efficient at breaking up CCP aggregates than the non-ionic surfactant pentaethylene glycol monododecyl ether ($C_{12}E_5$) used in that study. The absorption and emission characteristics of the CCPs are given in Table 4.2. Φ_f and ε_{max} increase with increasing chain length. The fluorescence of the CCPs is increased by the conjugation and thus CCP-L has a higher Φ_f than CCP-S. However, the increase in Φ_f is not proportional to the increase in chain length as defects and twists in the polymer chains limit the conjugation. As can be seen in Table 4.2 on increasing the chain length of the CCPs there is a decrease in the Stokes shift. It is not immediately obvious why this should be the case, the effect of the solvent can be neglected since all the CCPs are in the same solvent, however, Stoke's shifts are also affected by complex formation and/ or energy transfer.

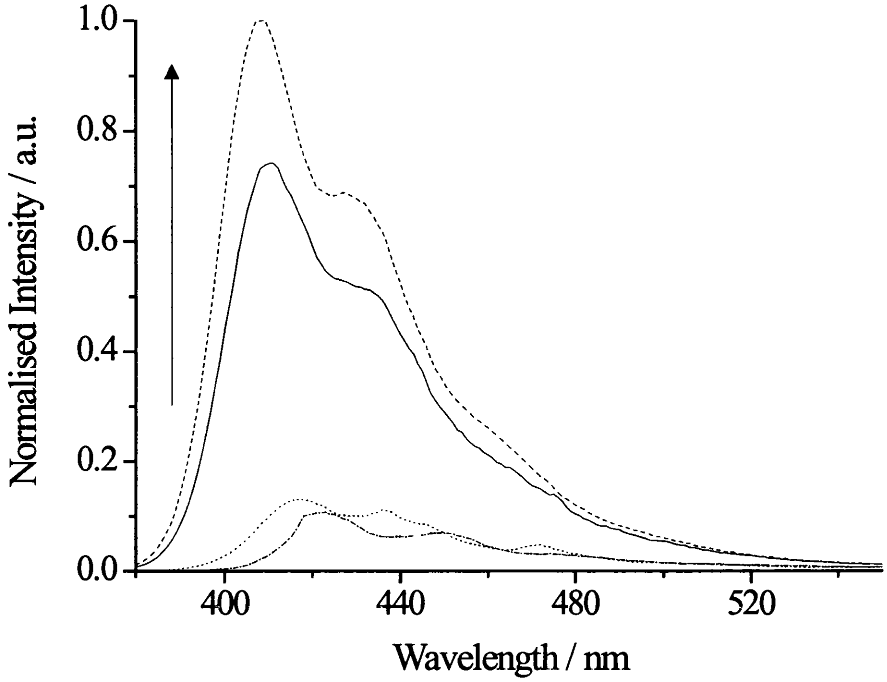

Figure 4.5 Change in emission of CCP-L with acetonitrile concentration. The direction of the arrow indicates increasing acetonitrile concentration. Emission in 25:75 acetonitrile/water is shown by the solid black line.

Table 4.2 General photochemical characteristics of CCPs.

Polymer	λ_{max} / nm	$\varepsilon_{max}{}^{a}/10^4$ M^{-1} cm^{-1}	λ_{emax} / nm	$(\Phi_f)^b$
CCP-S	375	3.7	416	0.28
CCP-M	375	3.8	414	0.34
CCP-L	382	4.2	410	0.36

[a] ε values are precise to $\pm 0.5\times10^4$ M^{-1} cm^{-1}

[b] The error in the quantum yields is ± 5%

4.3.1.2 Pico-second time-resolved emission

Time resolved studies were undertaken in order to gain a greater understanding of the aggregation of CCPs. Figure 4.6, which shows emission decay curves for CCP-S in 10/90 and 30/70 acetonitrile/water mixtures is representative of all CCPs decay curves. In all cases three exponential decay functions were required to obtain a good fit to the measured data ($\chi \approx 1$). Table 4.3 collects kinetic data from analysis using Equation 4.1,

$$I(t) = \sum_{i=1}^{3} a_i \exp(-t/\tau_i) \qquad [4.1]$$

Where a_i represent the amplitudes of the components at $t = 0$, and τ_i is the decay time of the component i. Fractional contributions are calculated from Equation 4.2

$$f_i = \frac{a_i\tau_i}{\sum_j a_j\tau_j} \qquad [4.2]$$

(Where the sum runs over the number of exponential terms. The terms a_i and τ_i are the proportional area under the decay curve for each decay time.), and the fractional density of each component from Equation 4.3:

$$\alpha_i = \frac{a_i}{\sum_j a_j} \qquad [4.3]$$

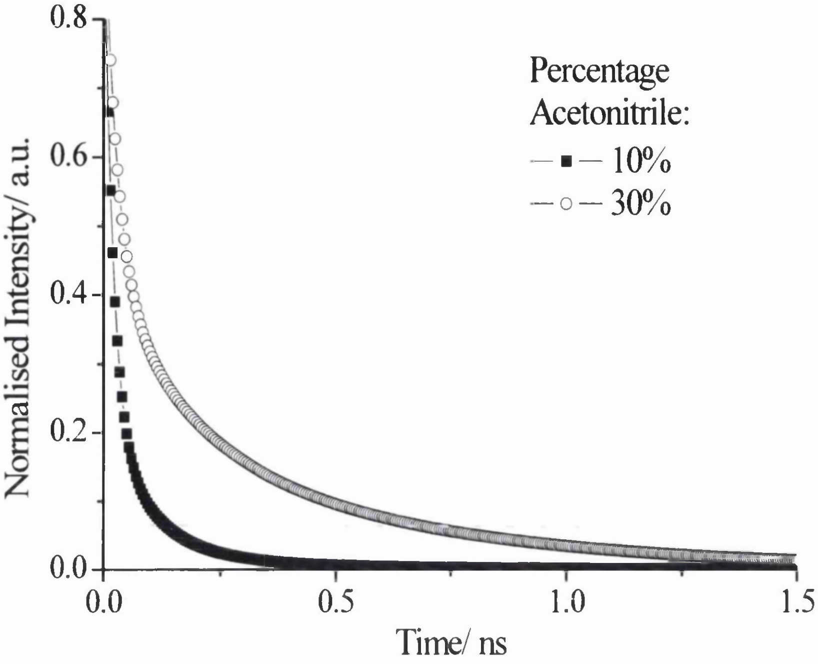

Figure 4.6 Normalised decay curves for CCP-S in 10/90 (solid squares) and 30/70 (open circles) acetonitrile/water mixtures.

For all three polymers of the three lifetimes, those for the fast (~30 ps) and slow decays (~500 ps) are reasonably constant across all solvent mixtures between 15/85 to 30/70 acetonitrile/water, whereas the lifetime of the middle lifetime component decreases significantly with decreasing acetonitrile content and hence increasing aggregation. Furthermore, the fractional contribution of the longest lifetime, which we assume is emission from isolated single chains of polymer[19] increases significantly for all CCPs with increasing acetonitrile concentration. It is possible that the two shorter lifetimes are due to aggregated species and clusters and thus this would suggest that even at optimum co-solvent concentrations there is some aggregation. Although in 25% acetonitrile the fractional contributions to the aggregated CCPs are high, *ca.* 0.79 for CCP-S, this has little impact on the steady state intensity because the single chain products with longer lifetime contribute very strongly to the steady state intensity. The decrease in aggregation with increasing co-solvent is also highlighted by an increase in the average lifetime which is, in essence, a reflection of the steady state intensity. Figure 4.7 shows the change in the fractional contribution of the longest lifetime of the three polymers, with increasing acetonitrile concentration. We assume this reflects an increase in the concentration of repeat units on isolated chains in solution with increasing acetonitrile concentration.

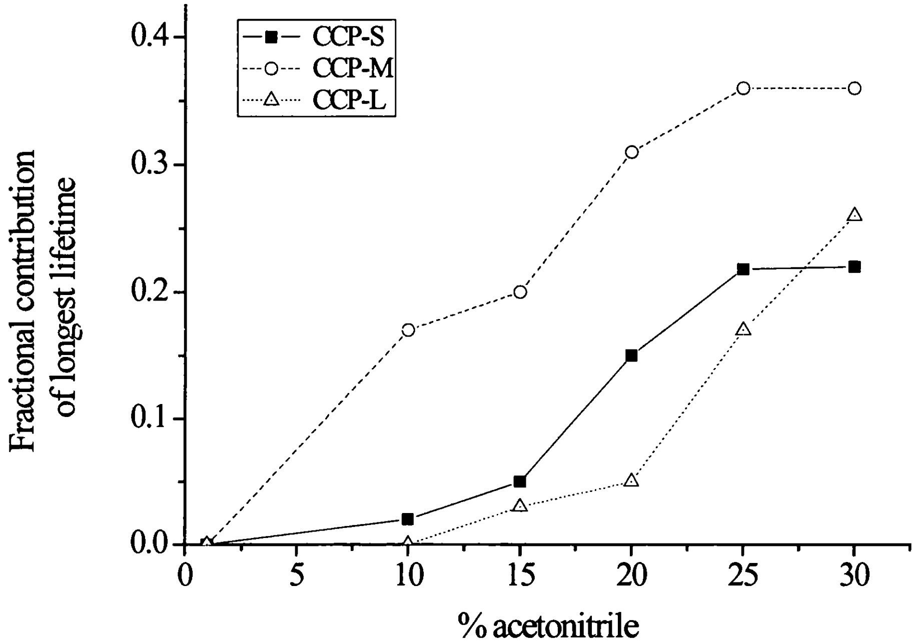

Figure 4.7 Fractional contribution of the longest lifetime with increasing acetonitrile concentration.

Table 4.3 Time resolved data for CCPs in different acetonitrile/ water mixtures.

% acetonitrile	CCP-S							CCP-M							CCP-L						
	a_1	τ_1/ ps	a_2	τ_2/ ps	a_3	τ_3/ ps	$<\tau>$/ ps	a_1	τ_1/ ps	a_2	τ_2/ ps	a_3	τ_3/ ps	$<\tau>$/ ps	a_1	τ_1/ ps	a_2	τ_2/ ps	a_3	τ_3/ ps	$<\tau>$/ ps
10	0.77	19	0.22	93	0.02	459	134	0.62	26	0.21	143	0.17	587	461	0.86	24	0.13	66	0.01	357	52
15	0.66	26	0.29	103	0.05	524	245	0.60	30	0.21	145	0.20	561	420	0.83	23	0.15	81	0.03	379	124
20	0.61	27	0.24	124	0.15	539	377	0.46	34	0.23	175	0.31	555	423	0.54	23	0.41	123	0.05	387	213
25	0.56	27	0.23	142	0.21	539	410	0.40	35	0.24	189	0.36	553	454	0.61	30	0.22	150	0.17	408	283
30	0.55	27	0.23	153	0.22	536	410	0.36	34	0.26	193	0.38	550	459	0.49	31	0.25	156	0.26	404	306

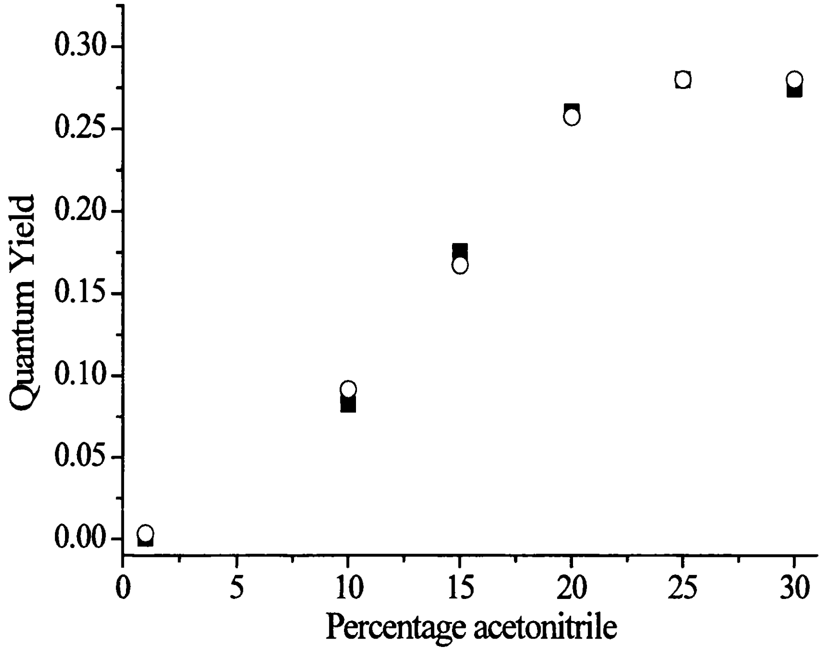

Figure 4.8 Comparison of quantum yield changes from steady state (solid squares) and normalised time-resolved emission values (open circles) for CCP-S.

Figure 4.8 compares quantum yields from steady-state measurements with those calculated from normalised emission decay curves for CCP-S. The quantum yields from the normalised decay curves were calculated from the changes in the area under the normalised curves, given that the quantum yield in 25% acetonitrile is 0.28. These data show that the decrease in quantum yield with acetonitrile is not due to static quenching i.e. there are no other additional decay components occurring faster than the time resolution of the instrument.

4.3.2 Modelling CCP aggregation and energy transfer

4.3.2.1 Polydispersity distributions of CCPs

The values of polymer lengths with statistical (random) polymerisation for all CCPs was modelled using excel software, the distribution of probabilities of a chain of various monomer lengths was calculated by

$$P_m = \frac{P_{site}{}^{m} P_{endgroup}}{P_{site}} \qquad [4.4]$$

where P_m is the probability of a polymer chain of a particular length in terms of repeat units, P_{site} is the probability of a site that isn't an end group of the polymer, m is the number of monomers in the particular polymer chain and $P_{end\ group}$ is the probability of an end group. P_{site} is the known average number of monomers per CCP chain. The probabilities of the length of the three polymers, CCP-S, CCP-M and CCP-L are shown in Figure 4.9. These values of polymer lengths with statistical (random) polymerisation were used in the modelling of CCP aggregation in Section 4.4.2.

4.3.2.2 Energy transfer in aggregated CCP systems

We use a model in which energy transfer from monomer to monomer and monomer to aggregate trap is random walk. Energy transfer occurs in 1D, along the linear polymer chains, and is trapped at the aggregate trap links between polymer chains.

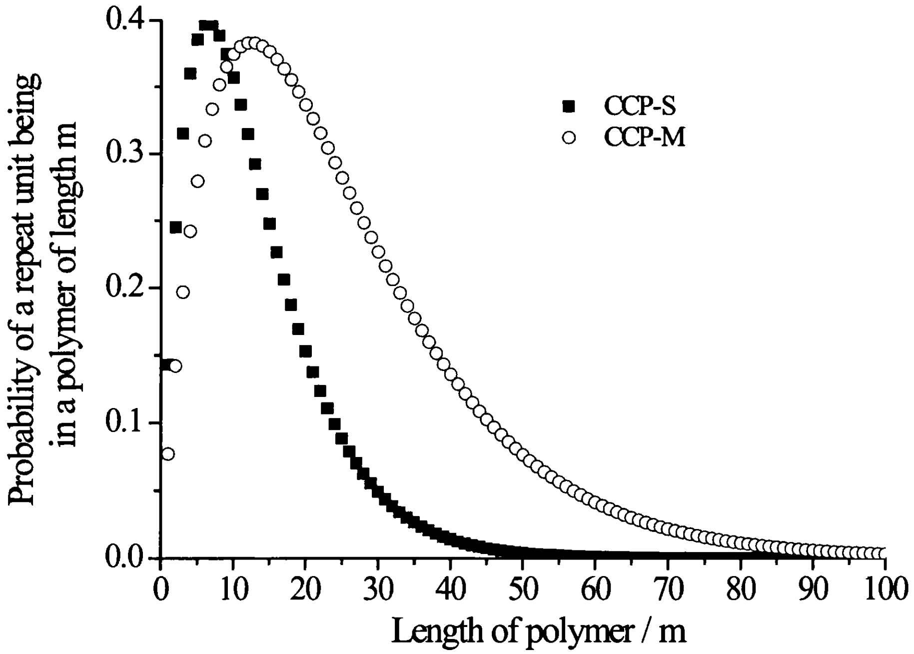

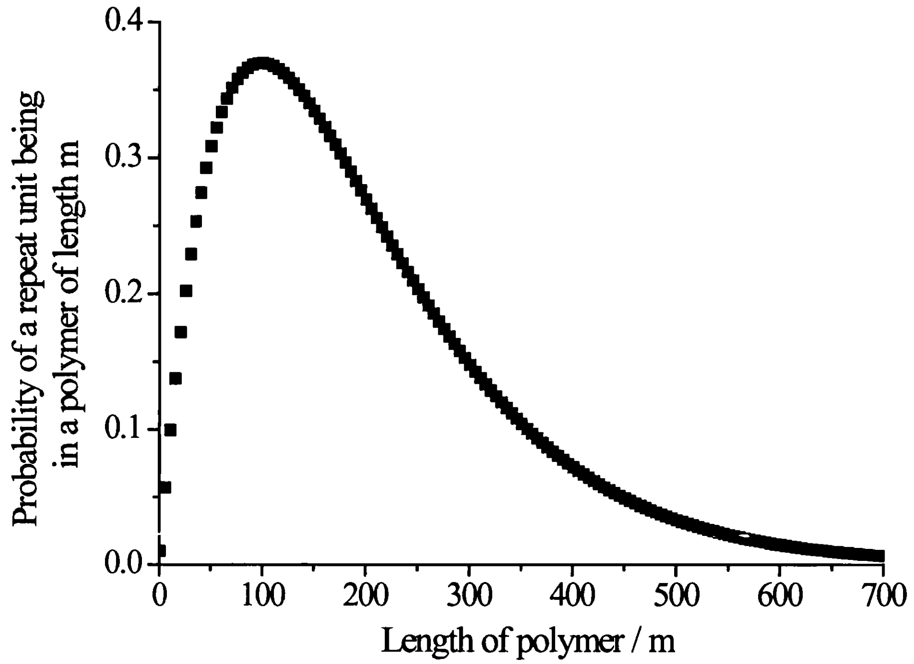

Figure 4.9 Polydispersities of all CCPs used in this study, CCP-S and CCP-M (top graph) and CCP-L (bottom graph), based on random polymerisation.

4.3.2.3 ProgClusters for modelling energy transfer

ProgClusters allows the possibility of varying several programme parameters

1) Array size:

The maximum array size permitted by the programme is height × width <1,000,000,000 sites. However, working with very large arrays significantly increases the computation time. The optimum working array size, in which sufficient numbers of energy "steps" are permitted to enable decay of the system without energy leaking to the array edges was 100 × 10000. The array shape was chosen to be rectangular with the top and bottom edges (100) smaller than the length of the array (10000) as to minimise the energy "reflection" which occurs at the top and bottom of the array. For each sample, curve fits were performed using three simulations, which gave an indication of the variation from run to run and therefore the error associated with the fits. Because the array is made up alternating strips of polymer chains and block sites, an array of this size typically contains *ca.* 500,000 repeat units. As well as providing numerical information about the energy transfer dynamics, ProgClusters also provides a graphical representation (although this is limited to a maximum array size of 400 × 400) which is useful to visualise the dynamics of the loss of excitation energy with time. An example of this is given in Figure 4.11 which shows the loss of excitation energy with increasing number of energy transfer steps for CCP-M.

2) Amount of energy transferred:

The maximum upper limit fraction of energy that may be transferred from any one site to neighbouring sites is limited by the programme to 0.25. This allows for the fact that there may be some clusters within the layer where an energy trap has as many as four nearest excited neighbours. Consequently, if there is one neighbour 0.25 is transferred, if there are two neighbours 0.5 is transferred and so on. In all modelling runs the fraction of energy transferred was fixed at 0.25.

3) Fraction of traps and links between polymer chains:

The fraction of links and energy traps is set by the programmer. In this case the fraction of links is equal to the fraction of energy traps. The fraction of links between polymer chains was calculated from a calibration graph obtained by running ProgClusters with different fractions of links for each polymer and noting the fraction of isolated polymer (which was not in contact by energy migration with any aggregate trap) that remained at the end of the simulation. This produced a calibration graph where the fraction of free polymer from model values is plotted against the fraction of links between polymer chains (set by the user), e.g. Figure 4.10. The fraction of isolated chains from the time resolved data can then be use to estimate the fraction of links between polymer chains in the system. The estimated fraction of links between CCP-M polymer chains in different acetonitrile/water solvent mixtures is given in Table 4.4.

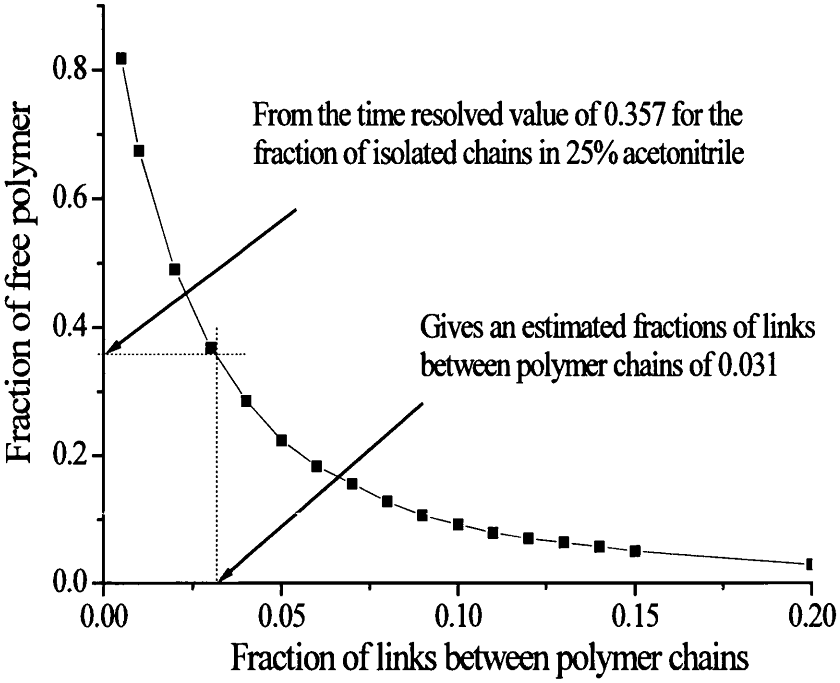

Figure 4.10 Calibration graph created using ProgClusters giving the correlation between the fraction of free polymer chains (isolated) and the fraction of links between polymer chains.

Table 4.4 Estimated fraction of links between CCP-M polymer chains as calculated using ProgClusters.

% Acetonitrile	Fraction of isolated chains from time resolved data	Estimated fraction of links between polymer chains
10	0.174	0.063
15	0.195	0.057
20	0.312	0.037
25	0.357	0.031

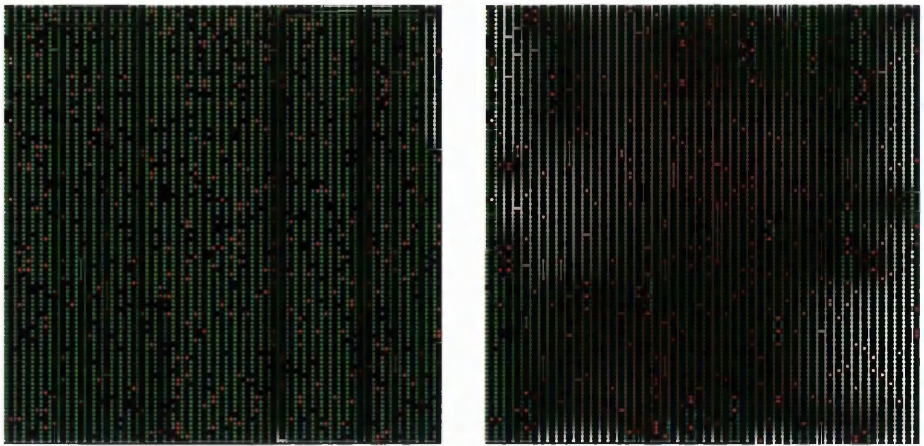

Initial array 5 energy transfer steps

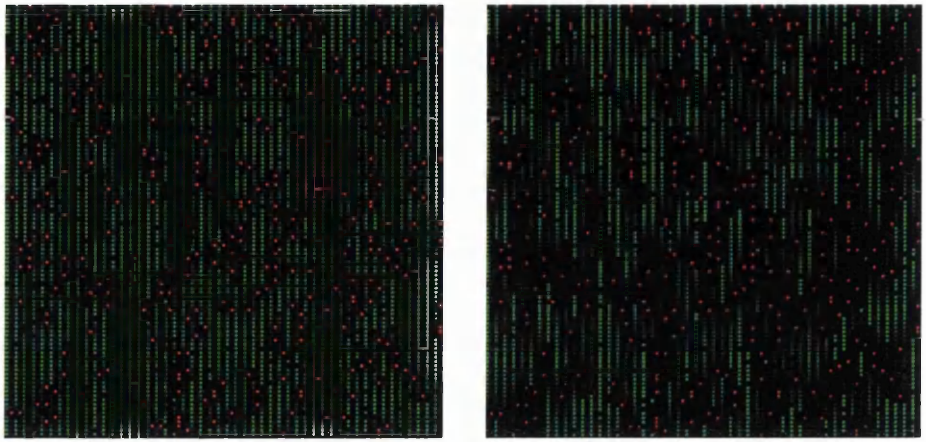

15 energy transfer steps 65 energy transfer steps

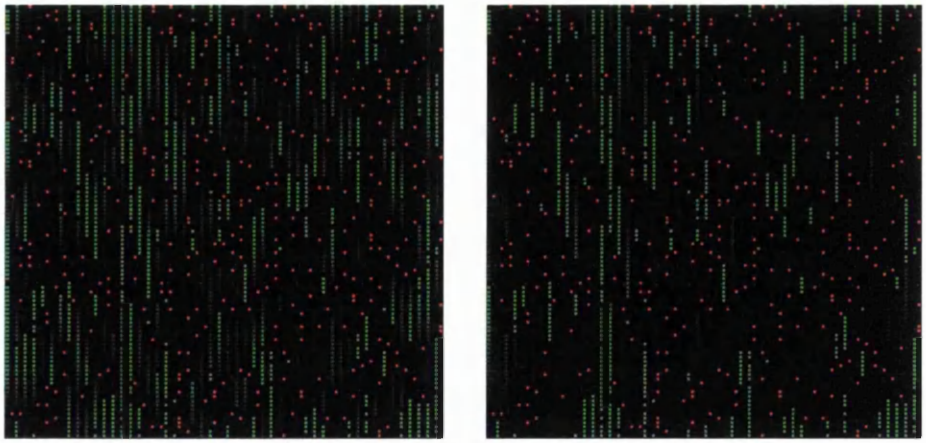

165 energy transfer steps 665 energy transfer steps

Figure 4.11 Energy transfer and loss of excitation energy for CCP-M with increasing number of energy transfer steps. The number of energy transfer steps is given below each array. The red squares represent quencher sites, the green squares represent polymer monomer units and the black is inert space.

From the estimated fraction of links of CCP-M in different acetonitrile concentration solvents the rate of fluorescence decay was modelled and compared to the experimental CCP-M fluorescence decays from time-resolved (Figure 4.12). As can be seen the fit from the model is in excellent agreement with the experimental data and is capable of generating the general curve shape and the general kinetic features associated with aggregation. The rate constant for unquenched decay is 1.9×10^{9} s^{-1} and the rate constant for both energy transfer between repeat units and from repeat units to traps is 2.4×10^{12} s^{-1}. Modelling of CCP-L aggregation was also carried out and the rate constant for unquenched decay is 2.0×10^{9} s^{-1} and the rate constant for both energy transfer between monomers and from monomers to link-traps is 5.2×10^{12} s^{-1} (Figure 4.12). The rate constants generated from ProgClusters will be referred to as k_{PC}.

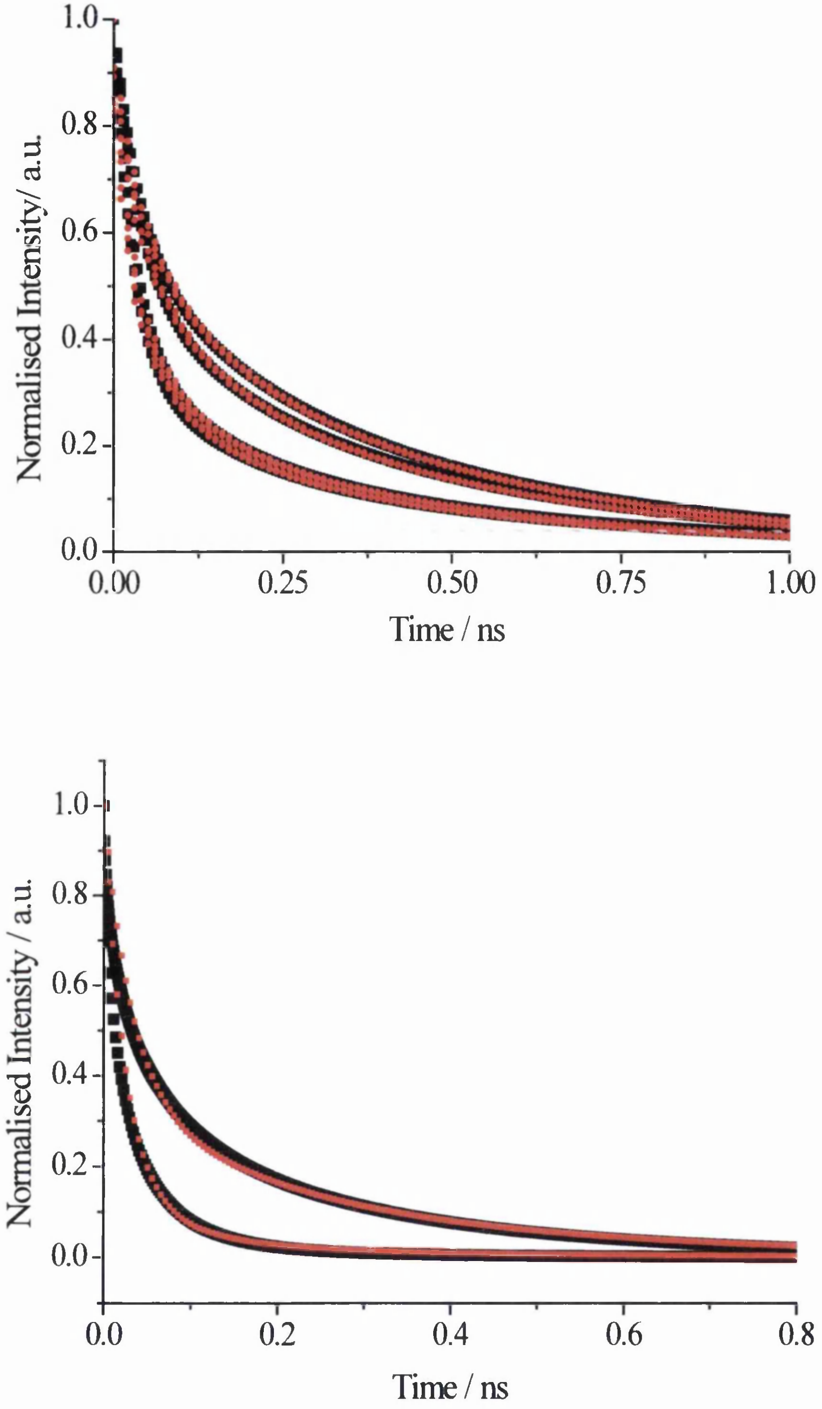

Figure 4.12 Time resolved decays curves for CCP-M (top) and CCP-L (bottom) with different acetonitrile concentrations (black) and modelled decay curves (red).

4.3.3 Anisotropy of CCP-S

The steady-state polarized spectra for CCP-S in a solution of 25/75 acetonitrile/water (v/v) is shown in Figure 4.13. The anisotropy varies little across the emission band, with an average anisotropy of 0.14, which can be compared with theoretical values of 0.4 for zero depolarisation, and 0, for full depolarisation.

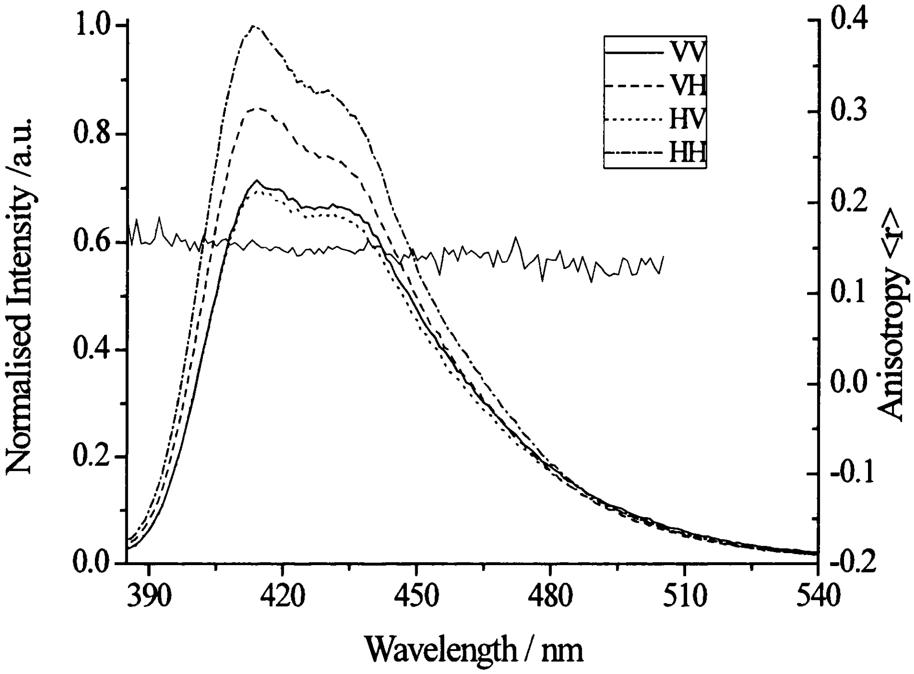

Figure 4.13 Normalised polarized emission of CCP-S in acetonitrile:water (25:75 v/v) the inset in the figure gives the alignment of the polarisers for the relevant spectrum. The anisotropy value is shown by the solid line across the band.

It was found that the fluorescence anisotropy decreased with increasing CCP concentration, Figure 4.14. We interpret this depolarization as due to resonance energy transfer along and between polymer chains, since increasing the concentration of CCP increases aggregation and thus facilitates interchain energy transfer.

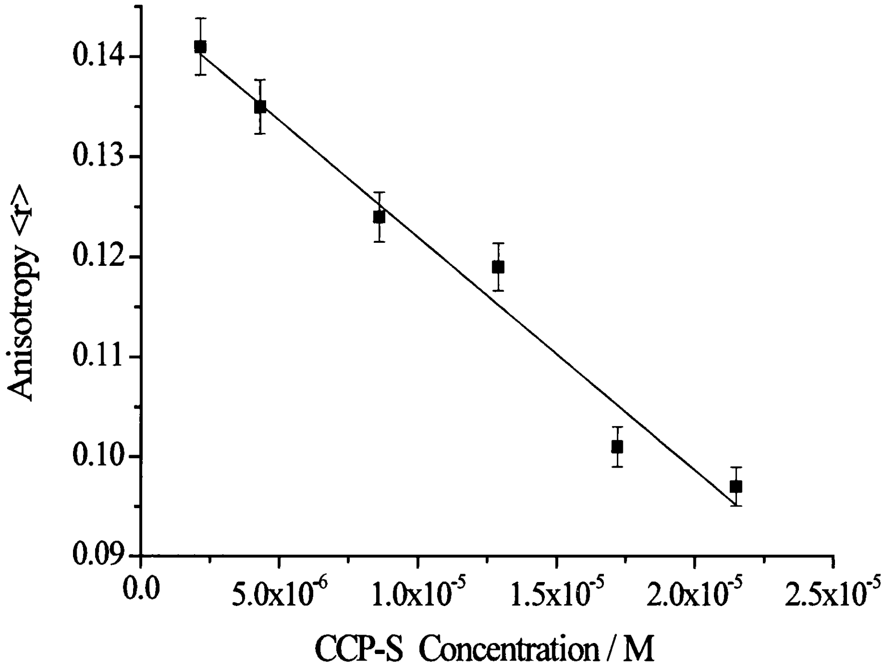

Figure 4.14 Average anisotropy as a function of CCP concentration.

The anisotropy of CCP-S was also measured in various acetonitrile/water mixtures. As expected the anisotropy of CCP-S decreases substantially with a decrease in the percentage acetonitrile, again presumably due to energy transfer as a consequence of increased aggregation.

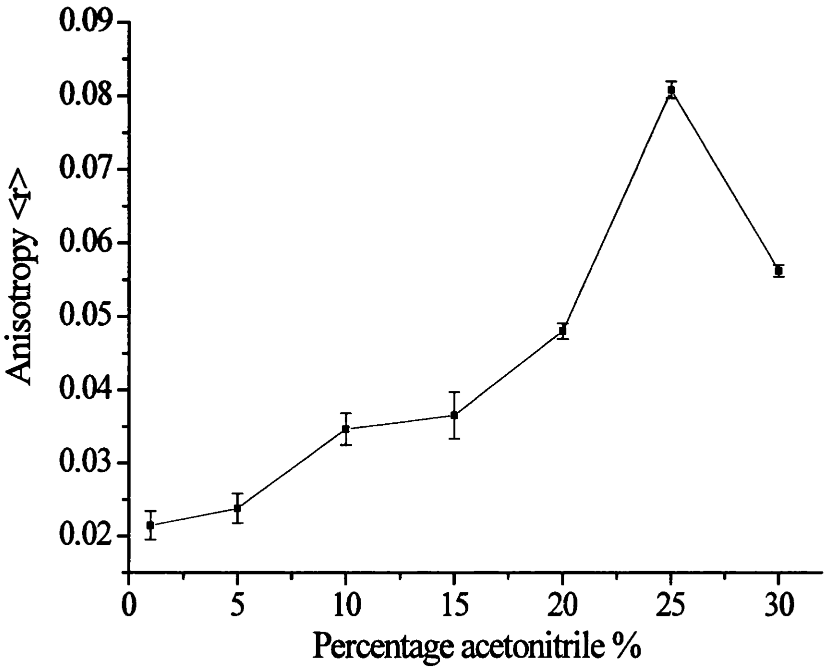

Figure 4.15 Change in anisotropy of CCP-S with various fractions of the co-solvent acetonitrile in acetonitrile/water mixtures.

The anisotropy results agree with the previous conclusion that 25% acetonitrile as a co-solvent is optimum for decreasing aggregation. The change in anisotropy with solvent composition highlights not only the effect of the co-solvent on the degree of aggregation but also provides further evidence that interchain energy transfer is the dominant mechanism for depolarization since an increase in aggregation significantly increases the probability of neighbouring monomers being close enough for FRET. Thus the large degree of aggregation due to changes in solvent composition increases interchain FRET causing a significant decrease in depolarization. In the case of FRET between chemically identical molecules fluorescence anisotropy can be resolved into two terms: depolarisation by rotation and depolarisation by energy transfer, Equation 4.5

$$r=r_0 W_R W_T \qquad [4.5]$$

Where W_R is the depolarization factor due to rotations, W_T is the depolarization factor related to FRET, r is the measured anisotropy and r_0 is the fundamental anisotropy (i.e. the anisotropy observed in the absence of other depolarizing processes such as rotational diffusion or energy transfer). In the case of these polymers, depolarization is believed to be due only to energy transfer, as the polymer is essentially static over the fluorescence lifetime.[50] The absorption and emission of all CCPs have good spectral overlap as highlighted by Figure 4.16. The rate constant for Förster energy transfer between a donor and an acceptor at a distance, R, is given by Equation 4.6

$$k_T = \frac{1}{\tau_D^0}\left[\frac{R_0}{R}\right]^6 \qquad [4.6]$$

Where the Förster radius, R_0, at which half of the donor excited-states will undergo FRET, can be calculated by: -

$$R_0 = 0.211\left[Q_D k^2 n^{-4} J\right]^{1/6} \qquad [4.7]$$

Where Q_D is the fluorescence quantum yield, k^2 is the orientation factor, which for this case can be taken as 0.476, n is the refractive index of the solvent (which is 1.34) [51] and J is the spectral overlap integral. The overlap integral, J, expresses the degree of spectral overlap between the donor emission and the acceptor absorption and is given by

$$J(\lambda) = \int_0^\infty F_D(\lambda)\varepsilon_A(\lambda)\lambda^4 d\lambda \qquad [4.8]$$

$F_D(\lambda)$ is dimensionless, and in all cases presented here $\varepsilon_A(\lambda)$ is expressed in units of $M^{-1}cm^{-1}$ and the wavelength, λ, is in nanometers and thus $J(\lambda)$ is in units of M^{-1} cm^{-1} nm^4. For values of $F_D(\lambda)$ corrected emission spectra with an area normalised to unity were used, the spectral overlap of all CCPs in shown in Figure 4.16. The calculated rate constant for CCP-S for energy transfer, k_T, from repeat unit to repeat unit is 3.9×10^{12} s^{-1}, with a Förster distance of 2.78 nm, (in good agreement with a reported value for a related fluorene-phenylene polymer, PFP, of 2.95 nm[34]). The Förster distances are around 3 nm which can be compared to the repeat unit separation of 0.840 nm. Table 4.5 collects FRET data for all CCPs, which highlights the extremely fast energy transfer possible along and between polymer chains.

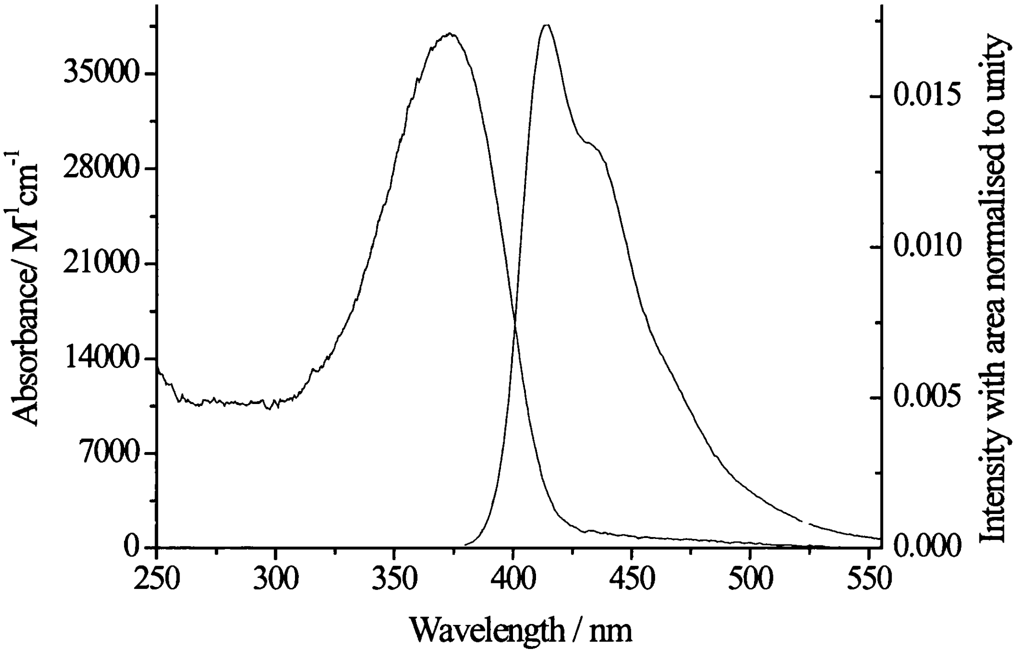

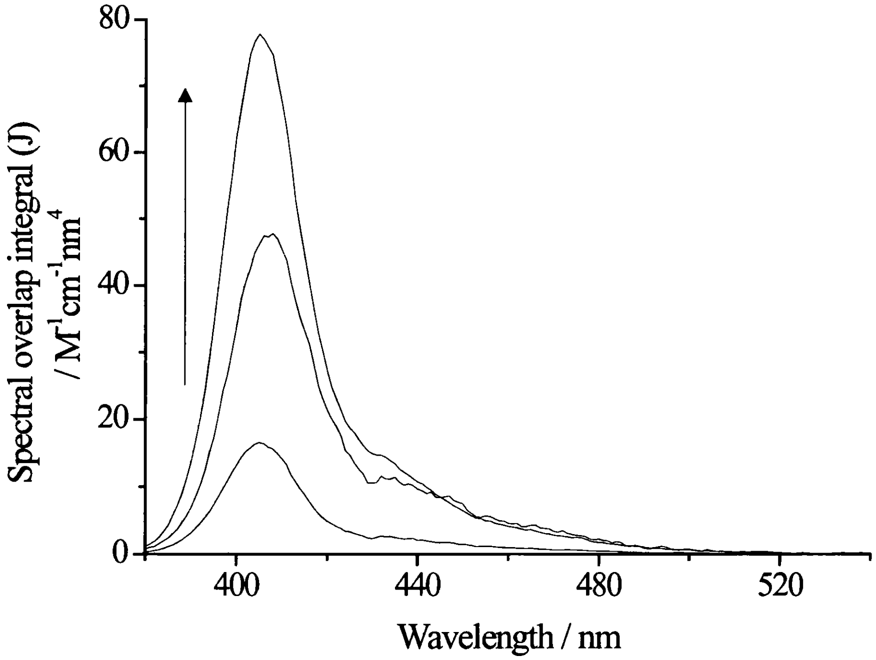

Figure 4.16 Typical absorption and emission spectra of CCP (top) from which the spectral overlap is evident. Spectral overlap integral of all CCPs (bottom), the arrow indicates increases polymer length.

Table 4.5 Förster energy distance and the rate constants of repeat unit to repeat unit energy transfer for the CCPs, and the rate constants of repeat unit to repeat unit and repeat unit to trap from ProgClusters.

Polymer	Förster distance / nm	k_T / s^{-1}	k_{PC} / s^{-1}
CCP-S	2.78	3.9×10^{12}	-
CCP-M	3.01	6.2×10^{12}	2.4×10^{12}
CCP-L	3.08	7.3×10^{12}	5.2×10^{12}

Differences arise due to increasing Φ_f and ε_{max} with increasing chain length along with decreases in Stokes shift with increasing chain length which results in higher spectral overlap. The rate constants are close to, but slightly higher, than those calculated from the curve fit of ProgClusters data, the difference may be due to the fact that energy transfer into an aggregate trap is slower than from repeat unit to repeat unit.

4.4 Conclusions

Addition of acetonitrile as co-solvent breaks up aggregates of CCPs formed in water. This is reflected by a ~10 fold increase in fluorescence quantum yield, a *ca.* twofold increase in absorption extinction coefficient, an increase in the fractional contribution to the lifetime of isolated chains in time resolved measurements for all CCPs and, for CCP-S, a ~4 fold increase in the fluorescence anisotropy. However, even at optimum acetonitrile/water mixtures of *ca.* 25:75 there are hints that there may still be aggregation. If the two shorter lifetimes of the CCPs from time resolved analysis are due to aggregated species and clusters this would confirm that even at optimum co-solvent concentrations there is a degree of aggregation.

Steady state fluorescence anisotropy of CCP-S decreases with increasing aggregation. This decrease in anisotropy is attributed to increased fluorescence depolarisation by interchain energy transfer in aggregate CCP-S complexes. Energy migration along the CCP chains is probably via a FRET mechanism since the calculated rate constants for energy transfer from repeat unit to repeat unit are very high in all cases (*ca.* 10^{12}-10^{13} s^{-1}) and the Förster distances are around 3 nm which can be compared to the repeat unit separation of 0.840 nm. The time resolved emission decay curves for CCP-M and CCP-L in different acetonitrile/water mixtures giving different degrees of aggregation, have been successfully modelled in terms of a series of energy transfer steps where energy is quenched at an aggregate trap (link between polymer chains). Rate constants of *ca.* 2×10^{9} s^{-1} were calculated for the natural decay of an isolated repeat unit while the rate constant of repeat unit to repeat unit or aggregate trap energy transfer was found to be 2.4×10^{12} s^{-1} and 5.2×10^{12} s^{-1} for CCP-M and CCP-L respectively. These values are in good agreement with those calculated for FRET of 6.2×10^{12} and 7.3×10^{12} for CCP-M and CCP-L respectively.

All CCPs studied have high fluorescence quantum yields and molar extinction coefficients in optimum acetonitrile/water mixtures; properties which are advantageous for the use of the CCPs in optoelectronics or materials applications. The chemical structure of these CCPs may be useful as the responsive basis for biological and chemical detection designs based on optical properties since it allows for effective electronic coupling and fast intra- and interchain energy transfer, thus the polymer chain can act as a path for the transfer of excitation energy to energy acceptors and quenchers.

4.5 References.

1. L. H. Sperling, *Introduction to Physical Polymer Science,* 4th Edition, Wiley-Interscience, New Jersey, USA, **2006**.
2. C. V. Hoven, A. Garcia, G. C. Bazan and T. Q. Nguyen, *Adv. Mater.* **2008**, *20*, 3793–3810.
3. B. Liu and G. C. Bazan, *Chem. Mater.,* **2004**, *16*, 4467-4476.
4. H. D. Burrows, V. M. M. Lobo, J. Pina, M. L. Ramos, J. Seixas de Melo, A. J. M. Valente, M. J. Tapia, S. Pradhan and U. Scherf, *Macromolecules,* **2004**, *37*, 7425-7427.
5. B. S. Gaylord, A. J. Heeger and G. C. Bazan, *J. Am. Chem. Soc.,* **2003**, *125*, 896-900.
6. S. Wang, B. Liu, B. S. Gaylord and G. C. Bazan, *Adv. Funct. Mater.,* **2003**, *13*, 463-467.
7. B. S. Gaylord, S. Wang, A. J. Heeger and G. C. Bazan, *J. Am. Chem. Soc.*, **2001**, *123*, 6417-6418.
8. M. R. Pinto and K. S. Schanze, *Synthesis-Stuttgart,* **2002**, *9*, 1293-1309.
9. C. V. Hoven, A. Garcia, G. C. Bazan and T.-Q Nguyen, *Adv. Mater.*, **2008**, *20*, 3793-3810.
10. H. A. Al Attar and A. P. Monkman., *J. Phys. Chem. B,* **2007**, *111,* 12418-12426.

11. M. Leclere, *Adv. Mater.*, **1999**, *11*, 1491.
12. D. T. McQuade, A. E. Pullen and T. M. Swager, *Chem. Rev.*, **2000**, *100*, 2537.
13. S. W. Thomas, G. D. Joly and T. M. Swager, *Chem. Rev.,* **2007**, *107*, 1339-1386.
14. K. E. Achyuthan, T. S. Bergstedt, L. Chen, R. M. Jones, S. Kumaraswamy, S. A. Kushon, K. D. Ley, L. Lu, D. McBranch, H. Mukundan, F. Rininsland, X. Shi, W. Xia and D. G. Whitten, *J. Mater. Chem.,* **2005**, *15*, 2648-2656.
15. R. N. Brookins, K. S. Schanze, J. R. Reynolds, *Macromolecules*, **2007**, *40*, 3524.
16. R. H. Friend, R. W. Gymer, A. B. Holmes, J. H. Burroughes, R. N. Marks, C. Taliani, D. D. C. Bradley, D. A. Dos Santos, J. L. Bredas, M. Logdlund, W. R. Salaneck, *Nature,* **1999**, *397*, 121.
17. K. M. Coakley, M. D. McGehee, *Chem. Mater.*, **2004**, *16*, 4533.
18. C. Fan, K. W. Plaxco and A. J. Heeger, *Trends in Biotechnol.,* **2005**, *23*, 186-192.
19. H. A. Al-Attar and A. P. Monkman, *Adv. Funct. Mater.,* **2008**, *18*, 2498-2509.
20. C. Chi, A. Mikhailovsky and G. C. Bazan, *J. Am. Chem. Soc.,* **2007**, *129*, 11134-11145.
21. K. Y. Pu, S. Y. H. Pan and B. Liu, *J. Phys. Chem. B,* **2008**, *112*, 9295-9300.
22. M. Monteserín, H. D. Burrows, A. J. M. Valente, R. Mallavia, R. E. Di Paolo, A. L. Maçanita and M. J. Tapia, *J. Phys. Chem B,* **2009**, *113*, 1294-1302.
23. D. Anestopoulos, M. Fakis, P. Persephonis, V. Giannetas and J. Mikroyannidis, *Chemical Physics Letters*, **2006**, *421*, 205–209.
24. L. Chen, D. W. McBranch, H. Wang, R. Helgeson, F. Wudl and D. Whitten, *Proc. Natl. Acad. Sci. USA*, **1999**, *96*, 12287.
25. B. S. Gaylord, A. J. Heeger and G. C. Bazan, *Proc. Natl. Acad. Sci. USA,* **2002**, *99*, 10954.
26. H. A. Ho, M. Bera-Aberem and M. Leclerc, *Chem. Eur. J.*, **2005**, *11*, 1718.
27. M. Monteserín, H. D. Burrows, A. J. M. Valente, R. Mallavia, R. E. Di Paolo, A. L. Maçanita, M. J. Tapia, *J. Phys. Chem. B*, **2009**, *113*, 1294–1302.
28. M. Knaapila, B. P. Lyons, K. Kisko, J. P. Foreman, U. Vainio, M. Mihaylova, O. H. Seeck, L. O. Pålsson, R. Serimaa, M. Torkkeli, and A. P. Monkman *J. Phys. Chem. B*, **2003**, *107,* 12425–12430.
29. M. Knaapila, K. Kisko, B. P. Lyons, R. Stepanyan, J. P. Foreman, O. H. Seeck, U.

Vainio, L. O. Pålsson, R. Serimaa, M. Torkkeli, and A. P. Monkman *J. Phys. Chem. B*, **2004,** *108*, 10711–10720.

30. A. W. Grice, D. D. C. Bradley, M. T. Bernius, M. Inbasekaran, W. W. Wu, and E. P. Woo Appl. Phys. Lett. **1998**, *73*, 629.
31. S. Becker, C. Ego, A. C. Grimsdale, E. J. W. List, D. Marsitzky, A. Pogantsch, S. Setayesh, G. Leising, K. Müllen, *Synthetic Metals*, **2001,** *125, 73-80.*
32. M. Leclerc, *J. Polym. Sci. Part A: Polym. Chem.*, **2001,** *39*, 2867-2873.
33. M. Stork, B. S. Gaylord, A. J. Heeger and G. C. Bazan, *Adv.Mater.* **2002**, *14*, 361-366.
34. M. L. Davies, P. Douglas, H. D. Burrows, M. G. Miguel and A. Douglas., *Port.Electrochim.Acta.*, **2009**, *27*, 525 – 531.
35. Y. Wang, B. Erdogan, J. N. Wilson and U. H. F. Bunz, *Chem. Commun.,* **2003**, 1624-1625.
36. L. H. Chen, S. Xu, D. McBranch and D. Whitten, *J. Am. Chem. Soc.,* **2000**, *122*, 9303.
37. J. J. Lavigne, D. L. Broughton, J. N. Wilson, B. Erdogan and U. H. F. Bunz, *Macromolecules,* **2003**, *36*, 7409.
38. H. D. Burrows, V. M. M. Lobo, J. Pina, M. L. Ramos, J. Seixas de Melo, A. J. M. Valente, M. J. Tapia, S. Pradhan, U. Scherf, S. I. Hintschich, C. Rothe and A. P. Monkman, *Colloids Surf. A: Physicochem. Eng. Aspects,* **2005**, *270*, 61.
39. P. Chen, G. Z. Yang, T. X. Liu, T. C. Li, M. Wang and W. Huang, *Polym. Int.,* **2006**, *55*, 473-490.
40. J. L. Bredas, D. Beljonne, V. Coropceanu and J. Cornil, *Chem. Rev.,* **2004**, *104*, 4971-5003.
41. A. Ruseckas, P. Wood, I. D. W. Samuel, G. R. Webster, W. J. Mitchell, P. L. Burn and V. Sundstrom, *Phys. Rev. B,* **2005**, *72,* 115214.
42. D. E. Markov and P. W. M. Blom, *Phys. Rev. B,* **2006**, *74*, 085206.
43. T. Förster, *Ann. Physik.*, **1948**, *437*, 55-75.
44. F. Montilla, L. M. Frutos, C. R. Mateo, and R. Mallavia, *J. Phys. Chem. C,* **2007**, *111,* 18405-18410.
45. T. Förster, *Disc. Farad. Soc.*, **1959**, *27*, 7-17.
46. F. Perrin, *J. Ann. Physique*, **1932**, *17*, 283.

47. R. C. Evans, D. Ananias, A. Douglas, P. Douglas, L. D. Carlos, and J. Rocha, *J. Phys. Chem. C,* **2008**, *112,* 260-268.
48. J. Pina, J. Seixas de Melo, H. D. Burrows, A. L. Maçanita, F. Galbrecht, T. Bünnagel and U. Scherf, *Macromolecules,* **2009**, *42*, 1710.
49. H. D. Burrows, S. M. Fonseca, C. L. Silva, A. A. C. C. Pais, M. J. Tapia, S. Pradhan and U. Scherf, *Phys. Chem. Chem. Phys.,* **2008**, *10*, 4420.
50. I. A. Levitsky, J. Kim and T. M. Swager, *J. Am. Chem. Soc.,* **1999**, *121,* 1466-1472.
51. J. R. Lakowicz, in *Principles of Fluorescence Spectroscopy*, Plenum Press, New York, Springer, 3rd edn., **2006**.

Chapter 5

Imaging and Statistical Image Analysis of CCP-DNA Interactions in Solution and at Surfaces

5.1 Introduction

Many CCPs have charged tetraalkylammonium groups, and as such are closely related to polyamines, such as spermine and spermidine, which are known to induce compaction of DNA.[1-4] Cationic polymers, such as poly(ethylenimine) and poly(l-lysine), also condense DNA effectively.[5] DNA compaction is the subject of intense research activity due to the possibility of biological applications for gene delivery into cells, with the overall goal being to achieve practical and controllable DNA compaction.[6,7,8] Compaction of extended DNA chains into compact 'globule' structures is relevant to both natural cellular processes such as DNA packaging in chromosomes [9,10] and to artificial gene therapy systems [11-14]. DNA is a highly charged polyelectrolyte, and therefore its compaction is non-trivial.[15,16] *In-vitro* condensation of DNA is generally achieved by neutralisation of the negative charges on DNA via electrostatic interactions, and these often involve multivalent species.[17,18] Many compacting agents have been reported in the literature, and a wide range of different types of compounds have been used, such as: polycations [1-4], cationic lipids [4,19], peptides [20,21], surfactants [22-24], and high valent metal ions [4,25].

5.1.1 Deoxyribonucleic acid

Deoxyribonucleic acid (DNA) is a nucleic acid macromolecule responsible for the storage of genetic information. DNA is a polyelectrolyte made from repeating units called nucleotides in a double helix structure.[26,27,28] Nucleotides are made up of three components; a nitrogen containing base, a pentose and a phosphate group. DNA contains two purine bases: adenine (A) and guanine (G); and two pyrimidine bases: cytosine (C), and thymine (T). The four bases of DNA are shown in Figure 5.1.

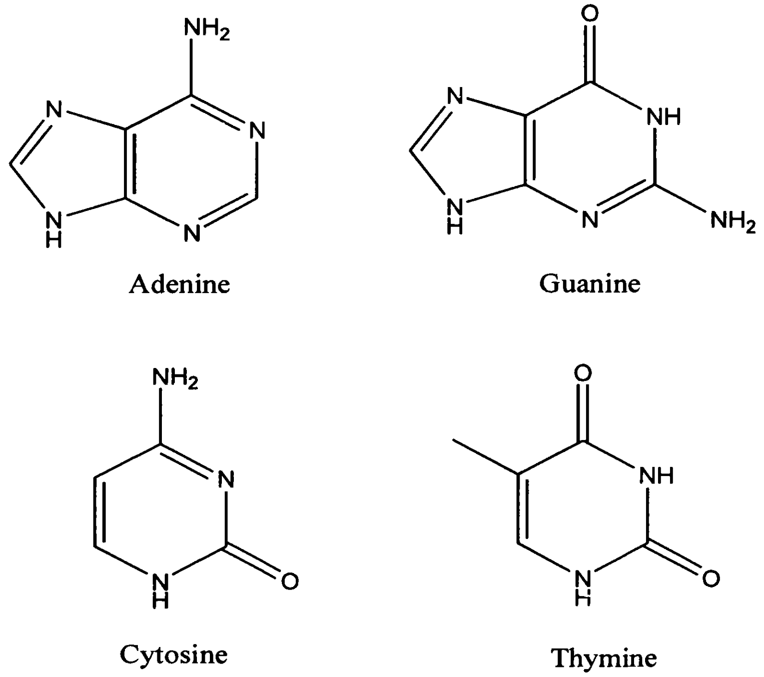

Adenine

Guanine

Cytosine

Thymine

Figure 5.1 Structure of the four DNA bases A, G, C, and T.

Each base binds in a complementary fashion where purines form hydrogen bonds to pyrimidines i.e. A only binds with T and C only binds with G and *vice versa*. This is known as complementary base pairing. This arrangement of two nucleotides binding together across the double helix is called a base pair (bp). The two types of base pairs form different numbers of hydrogen bonds: AT forms two hydrogen bonds, and GC forms three hydrogen bonds (Figure 5.2). The two strands of DNA in the double helix are only held together by these hydrogen bonds between the bases and thus it can be easily denatured by, for example, mechanical force or high temperature.[29] The complementary nature of the bases allows DNA molecules to duplicate themselves, in a process called replication, in which the two halves of the helix separate and a new strand is fabricated to exactly match each half.

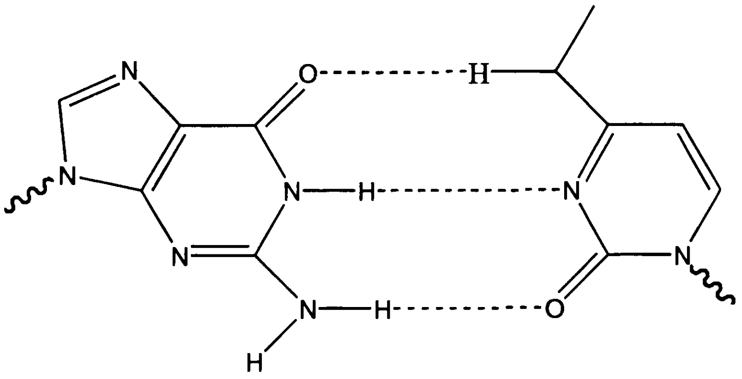

Guanine Cytosine

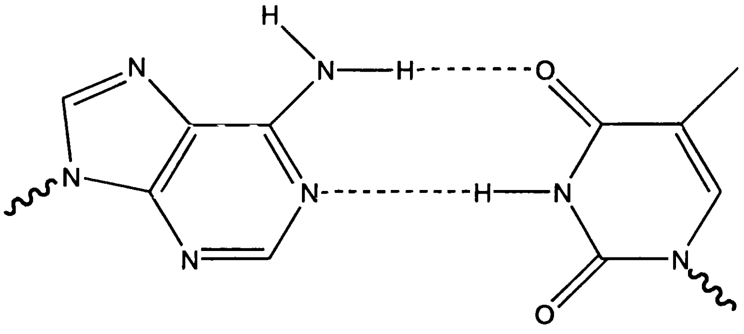

Adenine Thymine

Figure 5.2 Complementary base pairs of DNA. Guanine binds with cytosine through three hydrogen bonds whereas adenine binds to thymine through two hydrogen bonds.

The nucleotide units are covalently bonded via phosphate group bridges by a phosphodiester linkage in the DNA backbone. The backbone of DNA is hydrophilic and the phosphate groups of the DNA backbone have a very low pKa (close to one) and are completely ionised and negatively charged at pH 7 with one charge per base.[30] The DNA chain is 2.2 to 2.6 nm wide, and one nucleotide unit is 3.4 nm long.[31] The strands in the DNA backbone are not directly opposite each other which results in unequally sized grooves. There are two grooves, the major groove is 2.2 nm wide and the other, the minor groove, is 1.2 nm wide.[32] In the major groove the bases are more accessible and species that can bind to the base pairs are more likely to do so in the major groove. For example, proteins like transcription factors that can bind to specific sequences in double-stranded DNA usually make contacts to the sides of the bases exposed in the major groove.[33] The pentose groups (2-deoxyribose) are joined together by the phosphodiester bonds between the third and fifth carbon atoms of adjacent sugar rings (Figure 5.3). These asymmetric bonds mean a strand of DNA has a discernable direction i.e. the strands in the double helix structure of DNA are anti-parallel. The asymmetric ends of DNA strands are called the 5′ and 3′ ends, with the 5′ end having a terminal phosphate group and the 3′ end a terminal hydroxyl group (Figure 5.3).

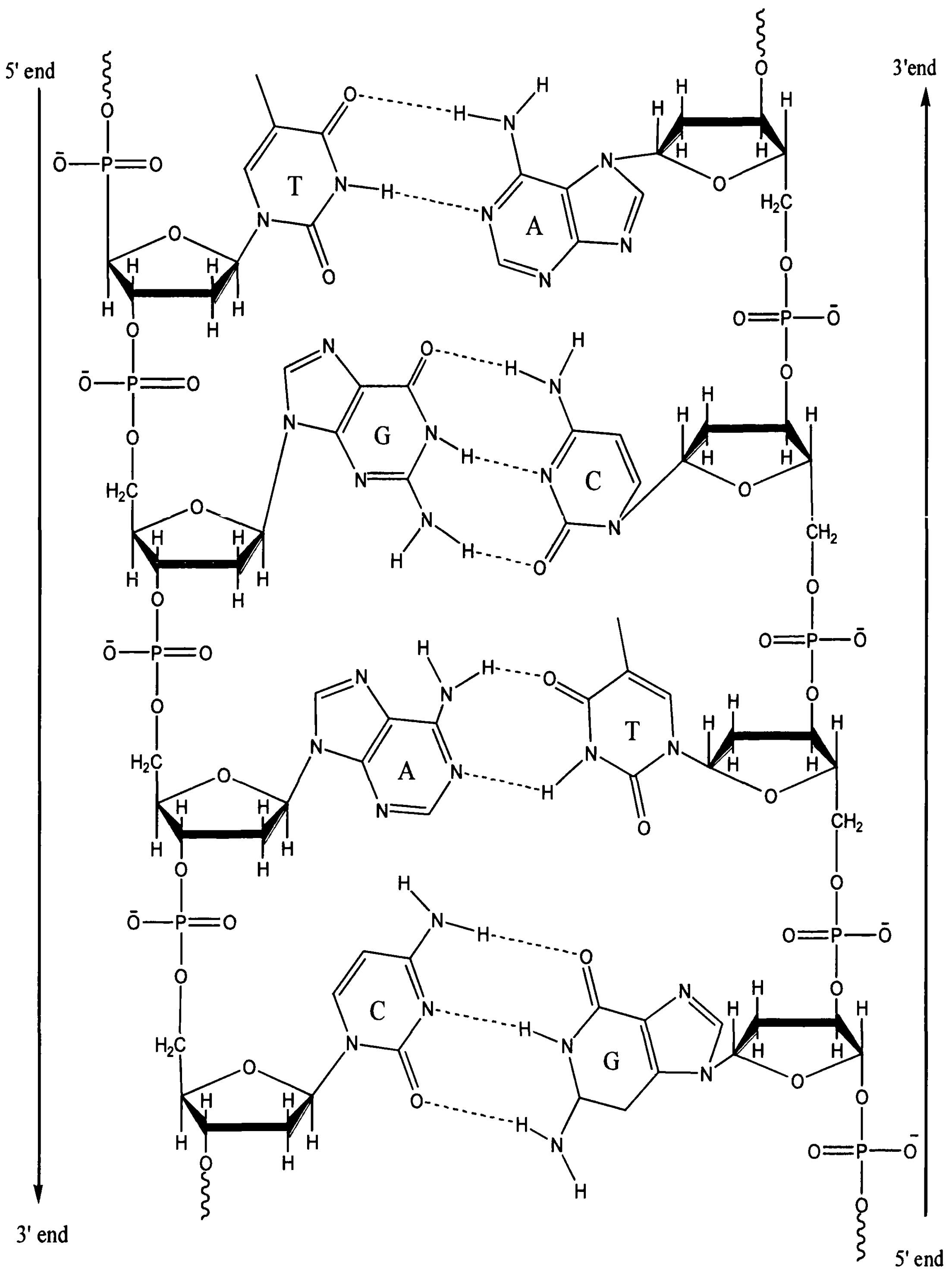

Figure 5.3 Structure of a DNA strand comprising of four base pairs. The base pairing is shown with the letter inside the benzene ring denoting the base. The backbone of the DNA is in an antiparallel direction; in the left hand side the 3′ end is downwards whereas on the right hand right the 3′ end is upwards.

5.1.2 Conformational states of DNA

Double stranded DNA (dsDNA) is a molecule susceptible to conformational changes though alterations in its chemical environment. There are three major DNA conformations: the B-form, A-form and Z-form. Some characteristics of these three forms of DNA are given in Table 5.1. The most common form is the B-form, this is the most stable under physiological conditions and is the form of DNA that has been described this far. The B-DNA helix has a diameter of *ca.* 2.0 nm with 10.5 bp per turn and a helix rise per bp of 0.34 nm. If the relative humidity of B-DNA is reduced to $\leq 75\%$ then it undergoes a reversible conformation transition to A-DNA. A-DNA has 11.6 bp per turn and consequently has helix rise per bp of 0.26 nm. A-DNA has a helical structure with an axial hole as is shown in Figure 5.4; the planes of the base pairs are tilted 20° relative to the helix axis and it is distinguished by a deep major groove and a very shallow minor groove. The A-form is also shorter and wider than the B-form but has a higher charge density. Z-DNA differs from the A- and B- forms of DNA in the fact that it has a left-handed helical structure. It has 12 base pairs per turn resulting in a helix rise per bp of 0.37 nm. Z-DNA has no apparent major groove and presents a deep minor groove. As can been seen in Figure 5.4 the polynucleotide strand is 'zigzagged' and not smooth as in the cases of A- and B-DNA. This is due to the fact that in Z-DNA the nucleotides along the left handed helix alternate between *syn* and *anti* conformations of the bases.[34] The *syn* conformation is more stable for the purine bases than for the pyrimidine bases and thus the Z-form is favoured in nucleotide sequences that have alternations of purines and pyrimidines.[34] DNA with alternating GC sequences are the most favoured for forming Z-DNA.[35] Under physiological conditions B-DNA is more stable than Z-DNA due to the fact that in Z-DNA the phosphate groups are closer together which leads to electronic repulsions.[36,37] The biological importance of Z-DNA still remains unknown. Higher order ternary structures of DNA are also possible e.g. circular DNA and supercoiled structures. The introduction of cationic species can also induce a higher degree of DNA organisation.[38]

Table 5.1 Structural characteristics of the A, B and Z forms of DNA.

DNA Conformation	Helical sense	Diameter / (nm)	No. of bp per helical turn	Helix rise per bp / (nm)	Charge density / (e^- /nm)
A-form	Right handed	~0.26	11.6	0.26	0.077
B-form	Right handed	~0.20	10.5	0.34	0.059
Z-form	Left handed	~0.18	11.6	0.37	0.054

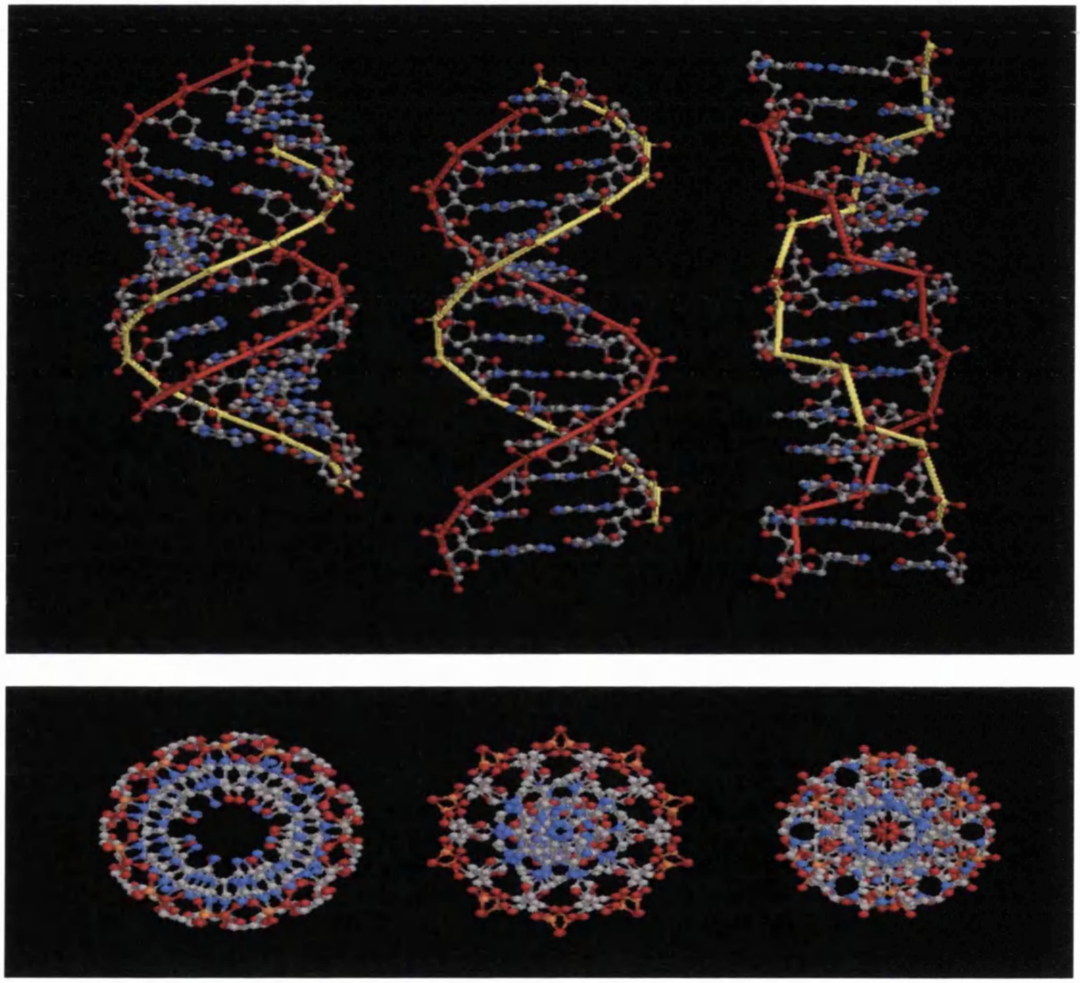

Figure 5.4 "**Ball and stick**" model of DNA secondary structures (all structures are composed of 36 bps), from left to right; A-form, B-form, Z-form. Top pictures show the side on view while the bottom pictures show the top view. Adapted from reference [39].

5.1.3 UV-Vis absorption and solution properties of DNA

All the nucleoside bases absorb UV light. Thus, DNA is characterised by a strong absorption (ε = 6600 $M^{-1}cm^{-1}$) at wavelengths near 260 nm. When a solution of double stranded DNA (dsDNA) is heated above a certain temperature all the hydrogen bonds between the base pairs are broken and the strands separate into two independent molecules (Figure 5.5) i.e. the DNA is denatured into single stranded DNA (ssDNA). The two separate stands then assume a random coil configuration with roughly the same base and charge spacing as dsDNA.[40]

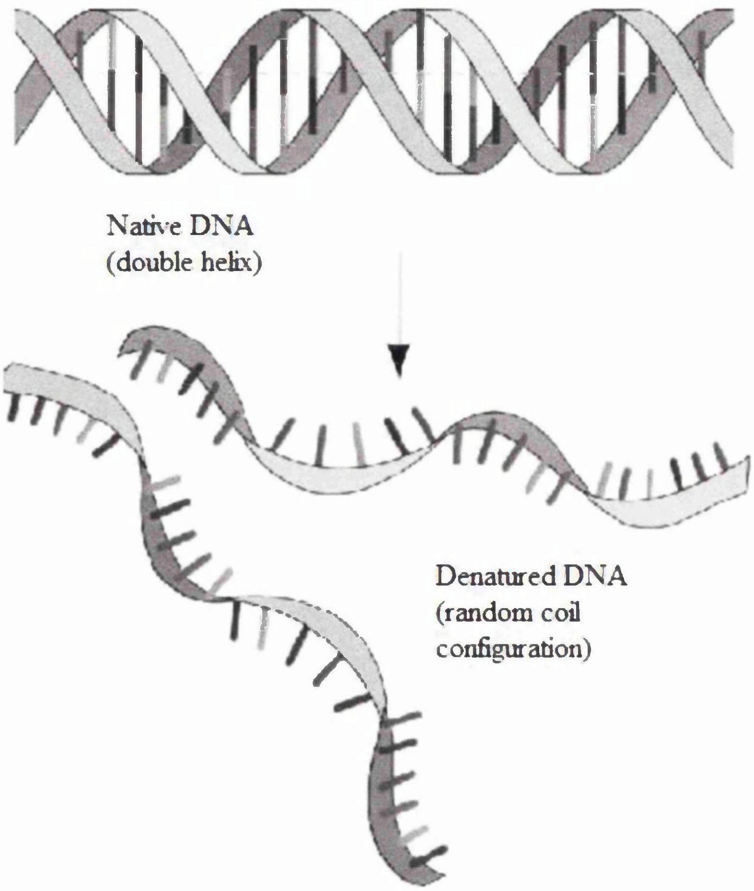

Figure 5.5 Denaturation of DNA. Separation of the double helix structure of dsDNA into the random coil configuration of ssDNA.

Denaturation of DNA can be monitored via the absorption at 260 nm since when DNA is denatured there is a *ca.* 40% in the absorption. The increase in absorption at

260 nm with increasing temperature yields a sigmoidal curve which indicates that denaturation is a cooperative phenomenon. The mid-point of this melting curve is known as the DNA melting temperature, T_m. Typically DNA is completely denatured at temperatures around 90 °C which gives T_m values in the region of 70 °C. Therefore, T_m can be seen as a measure of DNA double helix stability in solution. DNA double helix stability in solution is dependent upon several factors; the nature of the solvent, ionic strength, G-C basepair content and pH. T_m of dsDNA in sodium chloride solution can be calculated by Equation 5.1.[41]

$$T_m = 41.1X_{GC} + 16.6\log[Na^+] + 81.5 \qquad [5.1]$$

Where X_{GC} is the mole fraction of GC base pairs and $[Na^+]$ is the cation concentration in the solution. In salt-free solutions a linear dependency of T_m on DNA concentration itself has also been reported where

$$T_m = 18.3\log[DNA] + 90.2 \qquad [5.2]$$

This behaviour can be explained in terms of counterion condensation whereby counterions are situation closer to the DNA chain in more concentrated regimes. As can be seen from Equation 5.1 the stability of DNA is dependent upon the GC content, i.e. DNA with a high GC content is more stable than DNA with low GC content. There are two ideas relevant to this. The extra stability has been attributed to the presence of the extra hydrogen bond in GC pairs as compared to AT pairs.[34] However, it is also thought that the increased stability is due to the contribution of stacking interactions.[42] It is both the GC content and the overall length of a DNA double helix that determines the strength of the interaction between the two complementary strands of DNA. Long DNA helices with a high GC content have stronger-interacting strands, while short helices with high AT content have weaker-interacting strands.[43] It seems likely that both the presence of the extra hydrogen bond in GC pairs and the stacking interactions have important effects.

5.1.4 Interactions between DNA and oppositely charged species

It is known that DNA interacts with oppositely charged amphiphiles in an associative manner,[44] and great deal of research has focussed around the interactions of cationic conjugated polyelectrolytes and DNA. DNA is negatively charged in solution at neutral pH and thus will interact electrostatically with cationic polyelectrolyte species to form interpolyelectrolyte complexes (IPECs). Cationic polyelectrolytes can induce extremely effective DNA compaction as is discussed further in this chapter. The concentration of counterions is highest in the regions adjacent to the polyelectrolyte and decreases with distance from the polyelectrolyte. General Poisson-Boltzmann (PB) theory models the ionic region around a polyion as a single population described by a continuous distribution of positive and negative ions defined by a Boltzmann factor which is governed by the electrostatic potential of the macroion.[45,46] The PB equation is written as

$$\nabla[\epsilon(r)\nabla\Psi(r)]=-4\pi\rho^{f}(r)-4\pi\sum_{i}c_{i}^{\infty}z_{i}q\lambda(r)\exp[\frac{-z_{i}q\Psi(r)}{k_{B}T}] \qquad [5.3]$$

Where ∇ is the divergence operator, $\epsilon(r)$ represents the position dependent dielectric, $\nabla\Psi(r)$ represents the gradient of the electrostatic potential, pf(r) represents the charge density of the solution, c_{i}^{∞} represents the concentration of the ion i at a distance of infinity from the solute, Z_i is the charge of the ion, q is the charge of a proton, k_B is the Boltzmann constant, T is the temperature and $\lambda(r)$ is a factor for the position dependent accessibility of position r to the ions in solution. The PB equation is, however, extremely difficult to solve for complex systems. A simpler description was described by Manning in what is known as the Manning counterion condensation theory (CC).[47] Manning stated that a cloud of counterions can relieve electrostatic stress by condensing on the surface of an oppositely charged chain.[47] In this approach a macroion chain is treated as an isolated, infinite linear array of fixed charged groups; each of them associated with $q>0$ counterions characterised by a dimensionless charge density parameter ξ.

$$\xi=\frac{z^{2}e^{2}}{\varepsilon_{dielec}kTd} \qquad [5.4]$$

Where z is the valence of the counterion, ε_{dielec} is the solvent dielectric constant and d is the distance between charged sites. The counterion atmosphere around a highly charged polyion is modelled as two distinct populations: condensed counterions which are bound within a well defined volume around the polyion and 'free' counterions, which can be treated as a classical Debye-Huckel ion atmosphere around the weakly charged polyion. Both PB and CC models have been quite successful in describing the interaction of small counterions with rodlike polyions and has provided useful insights into the energetics of such interactions.[48,49]

5.1.5 DNA compaction

The average human cell has around two metres of DNA within its nucleus. The DNA is hierarchically packed in the nucleus with the aid of proteins to form a complex called chromatin. Compaction of DNA in cells is achieved by a mixture of proteins (mainly histones).[50] Each nucleosome normally contains an octamer of core histones (H2A, H2B, H3 and H4) around which is wrapped approximately 160 base pairs of DNA and a single molecule of histone H1 that constrains the linker DNA between adjacent nucleosomes.[51] In the interphase nucleus, in which transcription and replication are going on, this DNA is packaged into nucleosomes that are variably compacted through association with H1 into larger 30nm fibres. In fact, the average nucleus most likely contains DNA with a continuum of chromatin configurations, ranging from highly open 10 nm fibres, through to 30 nm fibres and fibres that are even more tightly packed together (Figure 5.1). The formation of these very large fibres is probably facilitated by interaction between both the H1 linker histone and the tails of the core histones. These DNA-protein complexes are the templates for a number of essential cell processes including transcription and replication. As such, these processes depend on the precise structure of the chromatin fibres. The role of chromatin's higher order structure in transcriptional control has recently been the focus of scientific interest as loss of this regulation may underlie many disease processes.[52,53] It is believed that understanding the role of chromatin structure in gene regulation would help in the development of therapeutic agents for some of the biggest killers of modern time, including HIV and cancer. Thus controllable compaction and decompaction is an extremely important area of research.[6,54,55] In order to allow transcription and replication to occur, chromatin has to unfold to expose the template upon which these processes occur. The double helix thus has several possible structural configurations; it can be opened up in order to access information or conversely can be tightly compacted for storage.

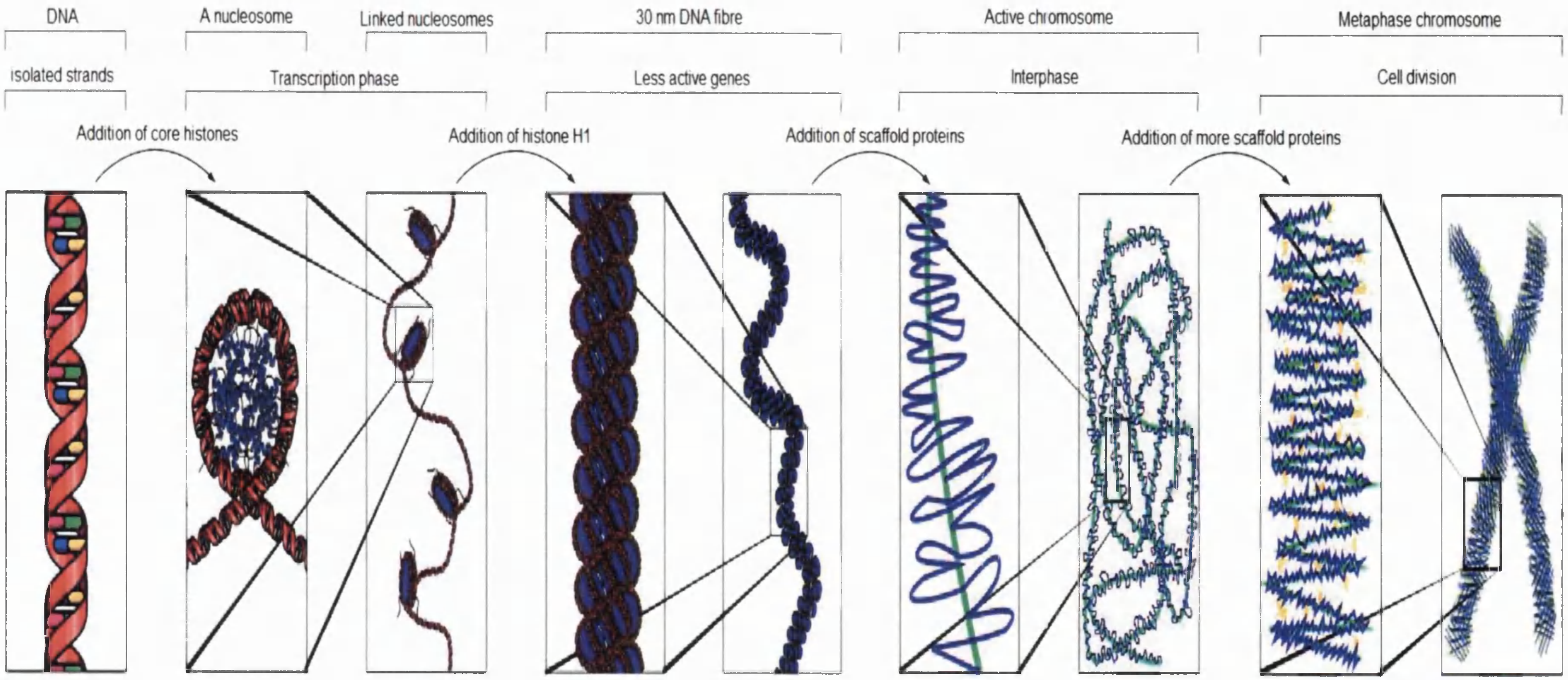

Figure 5.2 Schematic representation of DNA compaction in chromatin in the eukaryotic nucleus.[56]

5.1.6 Fluorescence microscopy of DNA

Fluorescence microscopy has become one of the most important and common techniques used for studying DNA compaction, since it enables the direct visualisation of the motion and conformational changes of individual DNA molecules in solution. It has been used as the principal technique in a large number of studies on the interaction between DNA and different compacting agents.[57-60] Generally, observations are consistent with three stages of compaction upon the addition of a compacting agent. Firstly, in the absence of, or at low concentrations of, the compacting agent, the DNA macromolecule displays an extended conformation exhibiting a slow worm-like or Brownian motion (coil). For intermediate concentrations of the agent, coils and compact structures (globules) coexist in solution. For higher concentrations, only globules are visible and, thus, this is termed total compaction.[58] However, the resolution of FM is usually diffraction-limited to *ca.* 200 nm, and other techniques are needed to obtain more detailed information.

5.1.7 Atomic force microscopy of DNA

Recently, a great deal of research has been focused on the application of atomic force microscopy (AFM) towards biological and polymeric systems, and in particular the imaging of DNA at the nanometre scale.[59-65] A valuable asset of the technique is that if biological molecules are deposited on an ultra-flat surface they can be imaged without the use of contrast enhancement techniques.[66] Mica is the most common substrate for imaging DNA since, when freshly cleaved, it has a very flat, smooth and clean surface.[67] The major problem in obtaining reliable images of immobilized DNA molecules appears to be tip damage or displacement due to adhesive forces. When the DNA is imaged under alcohols the adhesive forces can be eliminated and reliable and reproducible images are acquired. Tapping mode provides an alternative method of eliminating adhesive forces and allows imaging of DNA in air.[68] Tapping mode (TM-AFM) has often been used to study polymeric systems and soft surfaces as it provides information on surface topography, and, perhaps more importantly for polymer characterization, the mechanical properties of the surface.[60,69-71] In TM-AFM the probe (tip) vibrates up and down as the surface is scanned and thus is only intermittently in contact with the surface. This results in decreased lateral frictional forces and less surface damage, and is more suitable for imaging soft materials than contact mode AFM where the tip is constantly in contact with the surface.

Measurement of the phase angle between the free oscillation, at the end of the cantilever, and the imposed driving vibration also provides a map of phase angle across a surface. Phase angle data are captured simultaneously in TM-AFM with those of surface morphology, and can be used to qualitatively distinguish different materials on the surfaces of heterogeneous samples.[72] The interaction of DNA with spermidine has been investigated and visualised using transmission electron microscopy, which shows DNA adopts a compacted toroidal configuration,[73] and the compaction of DNA by protamine has been imaged on a mica surface using AFM.[74]

5.1.8 Aims of this work

In this study we report the use of the fluorescent conjugated cationic polymer, CCP-S, as a compacting agent. The aim is to gain useful information on the physical factors that govern compaction and folding of DNA, and direct high resolution visualization of the compaction of DNA and the formation of supermolecular structures between DNA and CCP-S in aqueous media. The CCP has a rigid rod backbone, and the study of its interaction with DNA is relevant to the current interest in polyelectrolyte condensation and compaction induced by oppositely charged linear counterions.[75,76] In addition the chemical structure of this CCP is useful as the responsive basis for biological and chemical detection designs based on optical properties since it allows for effective electronic coupling and thus fast intra- and interchain energy transfer. This is important because the polymer chain can act as a path for the transfer of excitation energy to a nearby energy acceptor or electron transfer quencher.[77]

5.2 Experimental

5.2.1 Materials

Bacteriophage T4 DNA (165.6 kilobase pairs, contour length of 57 μm) was purchased from Wako Nippon Gene. The fluorescent dye, 4,6-diamidino-2-phenylindole (DAPI) (excitation/emission = 360/460 nm), the antioxidant, 2-mercaptoethanol (ME), and the buffer salt, tris-HCl base, were purchased from Sigma. Salmon testes DNA (~2000 base pairs) was purchased from Sigma-Aldrich and used as received. Mica sheets (1" x 1" x 0.006") were purchased from Agar Scientific Limited and were cleaved before any sample was deposited on the surface. The conjugated cationic polyelectrolyte {9,9-bis[N,N-(trimethylammonium)hexyl] fluorene-*co*-1,4-phenylene} iodide (CCP-S), was a kind gift from Professor Ullrich Scherf (Bergische Universität, Wuppertal). It has an average molecular weight, $\overline{M_n}$ of *ca.* 3 kg mol^{-1} and a polydispersity of ~2, which corresponds to an average number of 5 repeat units and an average chain length of about 6.3 nm. This corresponds to the length of ~20 base pairs of DNA. All experiments were performed using Millipore Milli-Q deionized water.

5.2.2 Sample preparation

5.2.2.1 Fluorescence microscopy

Experiments were carried out at two different DNA concentrations; 1 nM and 500 nM. A T4 DNA stock solution was dissolved in tris-HCl buffer (pH 7.6) and was mixed with solutions of DAPI (0.05 mM), ME (final composition of 4% v/v) and CCP (at the required concentration, and in acetonitrile/water (25:75 v/v) to prevent CCP aggregation). The final concentration ranges were as follows.

a) For 1 nM DNA: DAPI 1nM, 4% (v/v) ME and CCP concentrations of 0, 2.15, 4.31, 8.6, 12.9, 17.2 and 21.5 nM (CCP concentrations given in terms of the monomer repeat unit).

b) For 500 nM DNA: DAPI 500 nM, 4% (v/v) ME and CCP concentrations of 0, 4.31, 8.62, 17.2, 25.8, 34.4 and 43.1 nM.

The behaviour of T4 DNA at 500 nM has been well characterised in previous fluorescence microscopy studies.[78,79] The ratio of DAPI:DNA was kept the same in both experiments so that the binding number of DAPI per base pair (1bp) DNA in aqueous buffer solutions was equal at 0.05, leaving both persistence length (*ca.* 60 nm) and contour length (*ca.* 57 μm), unaltered.[80,81] At the lower concentration of DNA the visualization of individual DNA molecules by fluorescence microscopy was easier, and thus the estimated sizes of DNA at this concentration are the more accurate of the two sets of data.

5.2.2.2 Atomic force microscopy

DNA solutions were prepared by dissolving salmon testes DNA in Millipore water. Shorter stranded salmon testes DNA (2000 bps) was used for AFM studies as the long stranded T4 DNA could produce misleading results due to aggregating, folding and various orientations on the mica surface.[82] The concentration of the DNA solutions were calculated from the absorbance at 260 nm ($\varepsilon = 6600\ cm^{-1}\ M^{-1}$).[83] These solutions were then deposited onto a freshly cleaved mica surface and left for ten minutes before being washed with water and allowed to dry in air. All DNA samples were imaged within 2 hours of being prepared. CCP-S solutions were prepared by dissolving CCP-S in 25:75 acetonitrile:water mixtures with stirring for a period of 24 hours. These were also deposited on fleshly cleaved mica, left for ten minutes and then washed with 25:75 acetonitrile:water and dried in air. For mixed DNA CCP-S samples a small volume of DNA was added to a CCP-S solution and mixed before deposition onto a mica surface. The final concentrations were 1×10^{-4} M DNA (in terms of base pairs) and 2.4×10^{-5} M CCP-S (in terms of monomer units) so that the ratio of CCP-S:DNA was the same as used in the fluorescence microscopy experiments where "beads-on-a-string" structures were first seen.

5.2.3 Experimental Setup

5.2.3.1 Fluorescence microscopy

The instrumentation used is described in Chapter 2. All observations were carried out at 25°C. Special care was taken to clean the glass microscope slides (Marienfeld) and cover-slips with ethanol thoroughly before each observation to prevent DNA degradation and precipitation onto the glass surface.

5.2.3.2 Atomic force microscopy

Samples were imaged in air (20 °C, RH 40.0±5.0 %)), using a Dimension 3100 scanning probe microscope in tapping mode (Digital Instrument Inc. Santa Barbara, CA) in tapping mode (described in Section 2.5.2).

5.2.3.3 Statistical image analysis

Analyses of the fluorescence microscopy images were performed using the public domain Image J 1.31v program (http://rsb.info.nih.gov/ij/). Analysis of the AFM images was performed using the computer programs Cellprofiler[84] and Nanoscope. Cellprofiler was used to calculate the lengths of the structures on the surface and Nanoscope was used to calculate widths and heights. All the image analysis is described in more detail in Section 2.6

5.3 Results

5.3.1 Conformational changes of low concentration isolated DNA molecules

The fluorescence microscopy investigation into the effect of the CCP-S on DNA was first carried out at a DNA concentration of 1 nM. At this very low concentration there is no bundling of DNA and observation of isolated DNA molecules is possible.[72] Figure 6.2 shows fluorescence images of T4 DNA molecules: (a) without CCP, (b) with 8.6 nM CCP and (c) with 21.5 nM CCP. The images show that as the concentration of the CCP is increased, DNA undergoes a transition from a coil structure (a), to a tightly folded compact globular structure (c), via a region of co-existence of both coil and globules (b).

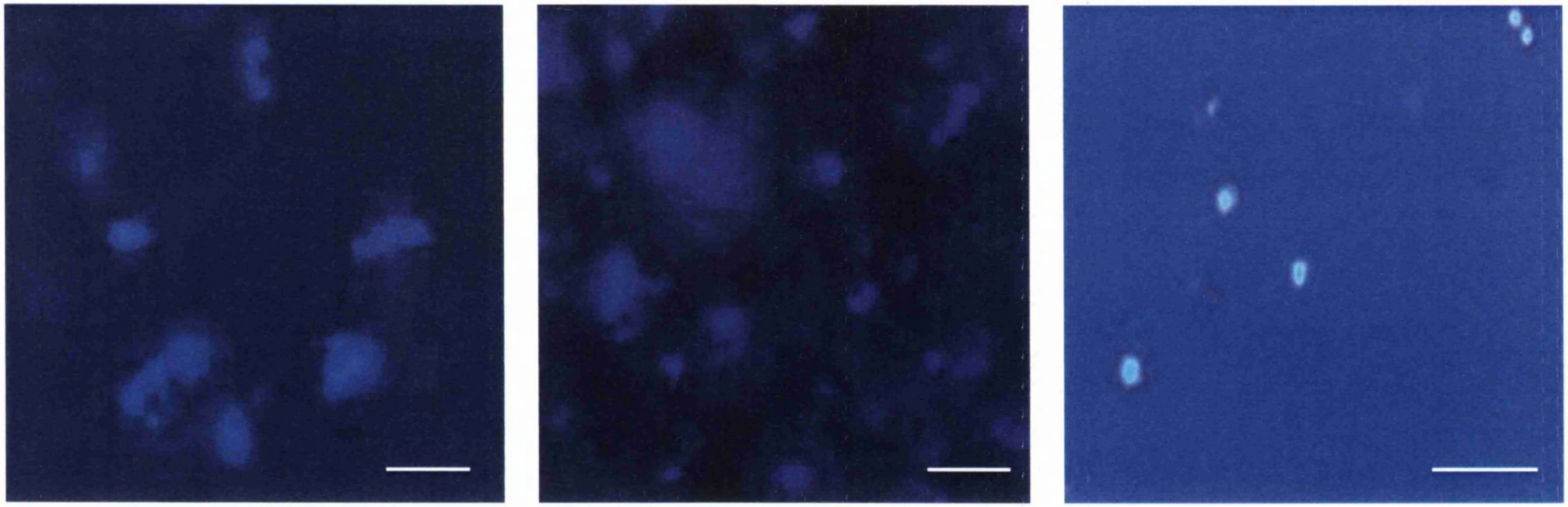

(a) (b) (c)

Figure 5.2 Fluorescence images of T4 DNA molecules moving freely in buffer solution at pH 7.6 for different concentrations of CCP-S: (a) 0 (coils), (b) 8.6 nM (co-existence of coils and globules) and (c) 21.5nM (compaction, globules). The scale bar in the bottom right of the pictures indicates a length of 5 μm.

The distributions of the long axis length L of T4 DNA at different CCP-S concentrations is given in Figure 5.3. In the absence of the CCP (Fig. 5.3(a)) the size distribution lies in the 3-5 μm range with an average length of 3.8 μm; the distribution arises from the polydispersity of the DNA used. At high concentration of CCP-S, where compaction is complete (Figure 5.3 (d)), the average value of L is 0.8 μm with a distribution between 0.5 and 1.2 μm indicating the formation of tightly packed structures. There is also a very small probability at high CCP-S concentration of slightly larger globules with sizes between ~1.5 μm and ~2.5 μm. We can say that these structures are large globules and not small coils because of their shape and the fact that they do not move with the Brownian motion characteristic of DNA coils. These data are in good agreement with previously reported sizes of T4 DNA.[85,86] The histograms show a definite region of co-existence of globules and coils (b,c).

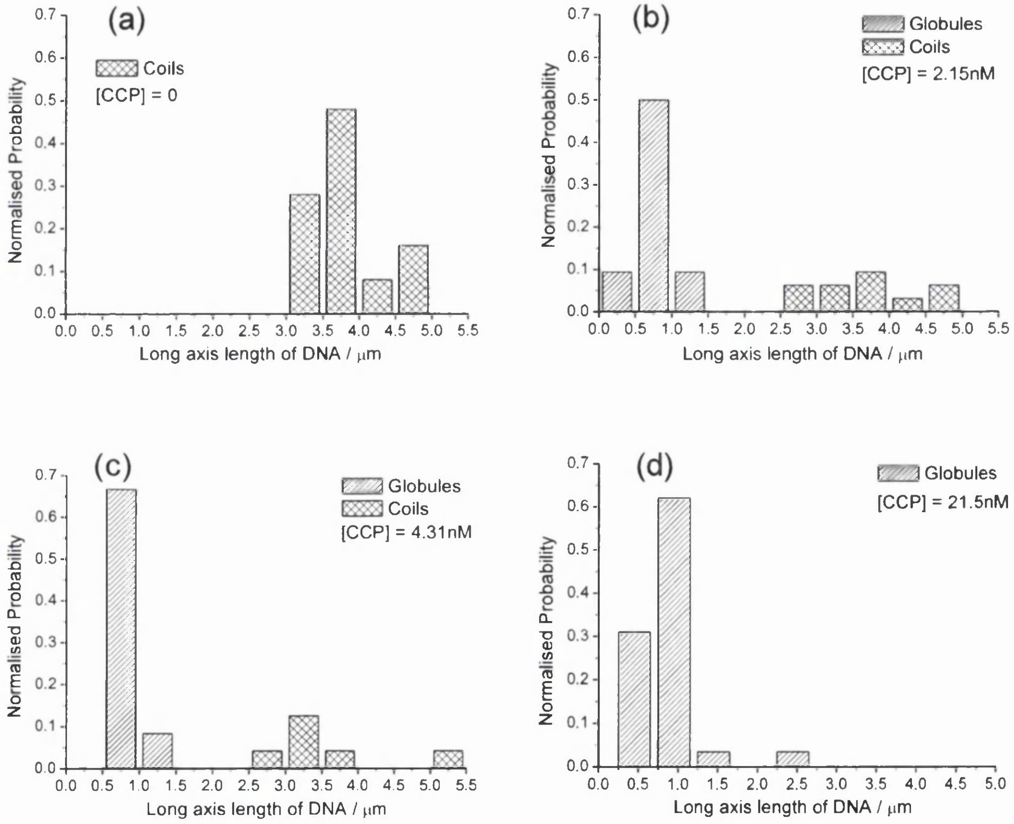

Figure 5.3 Histograms of the distribution of the long-axis length of T4 DNA molecules. The histograms, from left to right, show: coils (a); a state of co-existence, (b,c); and compaction (d). The areas in the histograms are normalized to unity.

The change in size of coils and globules with increasing CCP-S concentration, together with the percentage of compaction at each CCP-S concentration, is shown on Figure 5.4. With an increase in CCP-S concentration the percentage of molecules in the globule conformation increases until, at a CCP-S concentration of 21.5 nM, all the DNA molecules exist as globules. Even at the lowest CCP-S concentration there is over 40% compaction in the sample. The size of the globules remains constant with increasing CCP-S concentration. However the average size of the DNA coils decreases with increasing CCP-S concentration. This may be due to preferential binding of CCP-S to large DNA strands which might be expected on electrostatic grounds, reflected by a general decrease in length across all DNA strands as seen in a few cases such as with divalent cations[85], lysozyme and cationic surfactants[86]. It is important to stress that no intermediate structures are seen.

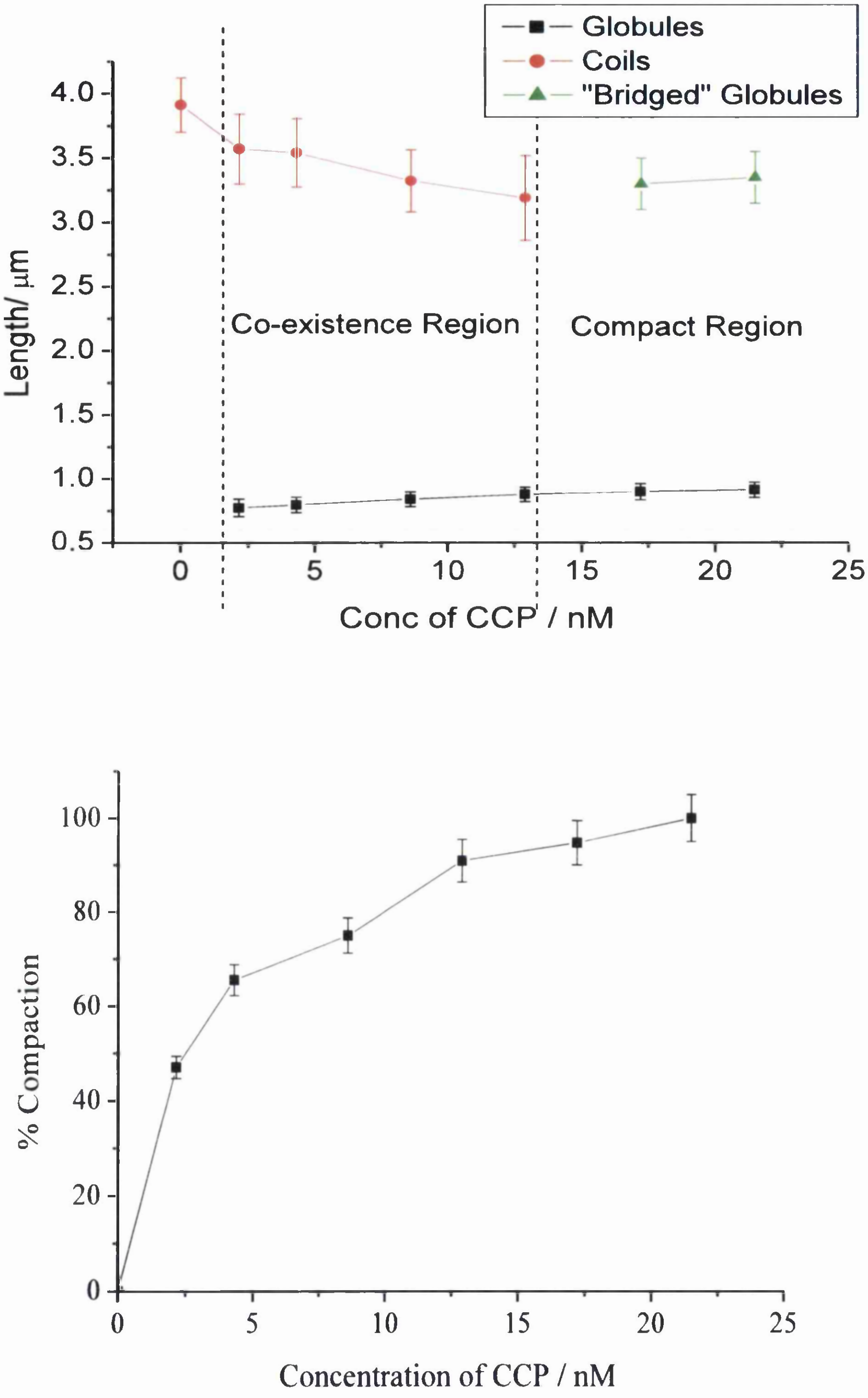

Figure 5.4 (a) Average sizes of coils (red), globules (black), and bridged globules (green) over the CCP-S concentration range studied. (b) Percentage of compaction in the sample over the CCP concentration range.

When DNA is compacted into globules the brightness of the globules appears greater than that of the chains because all of the DAPI molecules bound to DNA, and the CCP associated with DNA, are collected in a small volume. With increasing CCP concentration, the brightness of emission from globules increases, presumably because of an increasing high local concentration of the CCP (although DNA quenches CCP-S fluorescence at the DNA concentrations used for fluorescence microscopy the fluorescence intensity is reduced only by a factor of *ca.* 2). This concentration of fluorophores makes compacted DNA very easy to detect and makes the analysis of the videos much easier. At high CCP-S concentrations globules were seen to be in much closer proximity to each other than at lower CCP-S concentrations and they occasionally moved through the solution as if they were linked. Closer examination showed new structures resembling "beads-on-a-string" with the beads being regions of enhanced luminescence. Examples of these beads-on-a-string structures are shown in Figure 5.5. This is extremely interesting as it may involve bridging between CCP and compacted globules of DNA. Structures of intra-chain segregated T4 DNA, where the DNA is partially compacted at certain points along a single DNA chain, have previously been reported in the literature,[87,88] and are relevant to the emerging field of DNA nanotechnology,[89,90] where DNA is used to template formation of nanostructures in inorganic and organic semiconductors.[91--93] However, visualisation of these structures in free solution has not been too successful due to the small size of the partially segregated DNA coupled with the resolution available with optical microscopy. We believe that we do not have partially segregated individual DNA due to the size of the structures seen and the close proximity of the compacted globules. The structures described here are too big (1 bead ~0.6-0.8 μm) to be consistent with partially segregated DNA. The new structures were free in solution, i.e. not precipitated on the glass, and moved with a similar worm-like Brownian motion to DNA coils. All compacted DNA that appeared to be bridged had the same size distribution as the 'free' globules. It is well known that rigid-backbone polyelectrolytes with flexible side chains such as CCP-S can self assembly to form hierarchical superstructures in aqueous solution,[90] and these beaded structures may arise from compaction of more than one DNA strand in association with such superstructures. In the few cases when these structures were found there was usually three or more compacted globules linked and thus they had similar lengths to that of elongated DNA.

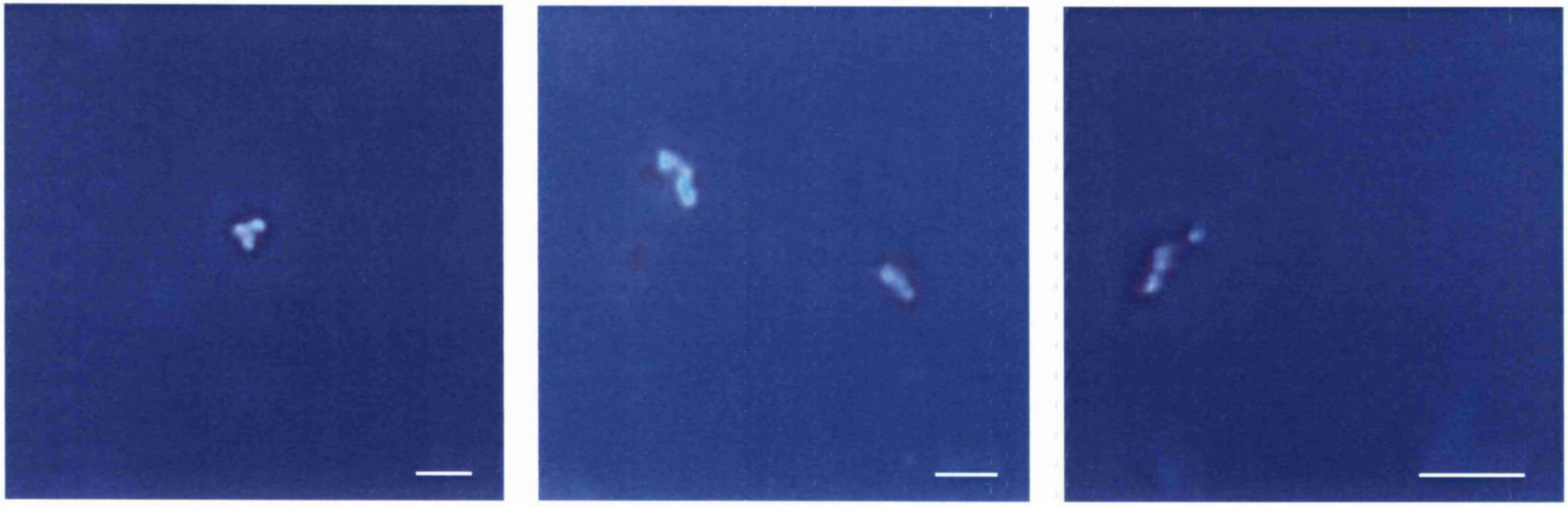

Figure 5.5 Fluorescence microscope images of compacted T4 DNA after the interaction with CCP-S, at a concentration of 21.5 nM, which corresponds to the highest probability of the appearance of bridged structures. The scale bar in the bottom right of the pictures indicates a length of 5 μm.

5.3.2 Conformational changes of isolated DNA molecules at higher DNA concentrations

The interaction of CCP-S with a higher concentration of DNA was also investigated. For this the concentration of DNA was increased from 1 nM to 500 nM and the concentration range of CCP was doubled. Figure 5.6 shows fluorescence images of T4 DNA molecules at a DNA concentration of 500 nM in the presence of different concentrations of the CCP. Again the images show the transition from a coil structure through a region of co-existence to a folded tightly compact structure as the concentration of CCP-S is increased.

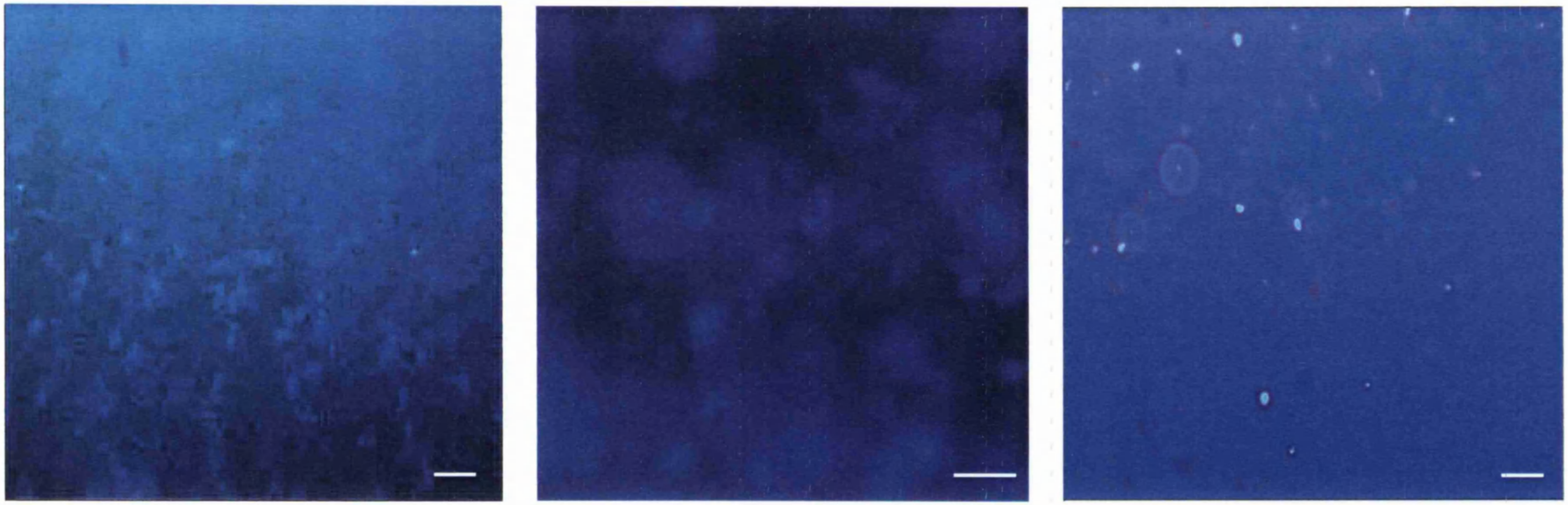

(a) (b) (c)

Figure 5.6 Fluorescence images of T4 DNA molecules moving freely in buffer solution at pH 7.6 for different concentrations of CCP-S: (a) 0 (coils), (b) 17.2 nM (co-existence), and (c) 43.1 nM (compaction). The scale bar in the bottom right of the pictures indicates a length of 5 μm.

This transition through a co-existence region is also shown in Figure 5.7. At this DNA concentration the average long axis length L of elongated DNAs is 3.8 μm with a distribution between 2.5 and 5.4 μm and that of the globules is 0.9 μm with a distribution between 0.6 and 1.5 μm, similar to those observed at lower DNA concentration (Figure 5.3).

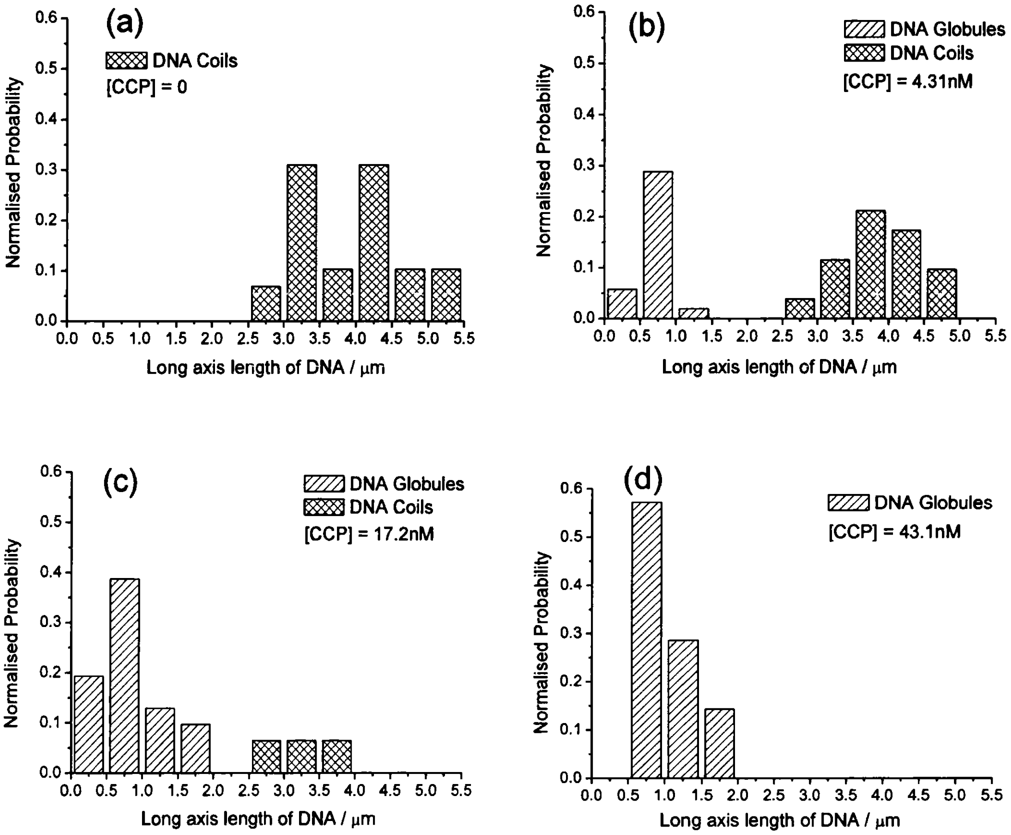

Figure 5.7 Histograms of the distribution of the long-axis length of T4 DNA molecules. The histograms, from left to right, show: coils (a); a state of co-existence, (b,c); to compaction (d). The areas in the histograms are normalized to unity.

The percentage compaction follows the same trend as previously found, with total compaction at high CCP-S concentrations. The size of the coils gradually decreases whereas the size of the globules apparently increases with increasing CCP-S concentration (Fig. 5.8). Again no structures intermediate between elongated and compacted DNA were observed, but "beads-on-a-string" structures were observed at high CCP-S concentrations and were far more common in this system of higher DNA and CCP concentrations.

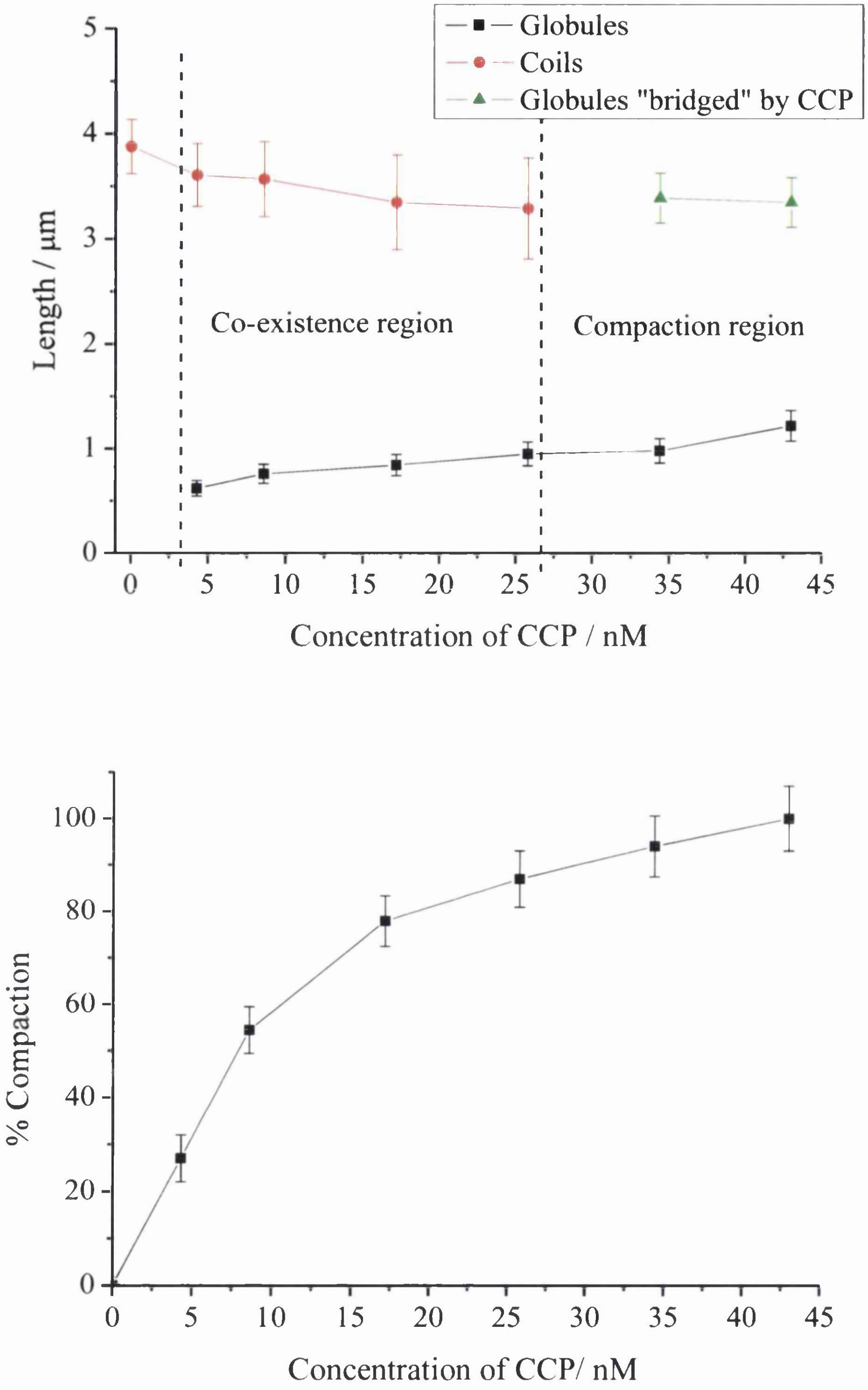

Figure 5.8 (a) Average sizes of coils (red), globules (black), and bridged globules, over the CCP concentration range. (b) Percentage of compaction in the sample over the CCP concentration range.

It is thought that the increase in number of these structures is simply due to the higher concentrations of CCP and DNA in the system. Examples of the structures found are shown in Figure 5.9. These structures have similar lengths to elongated DNA. However, the regions of enhanced luminescence are ~1 μm in diameter and thus the structures are larger than normal DNA coils. It is difficult to determine if the number of these structures further increases with an increase in CCP concentration, because, at higher concentrations of CCP, precipitation onto the glass occurs.

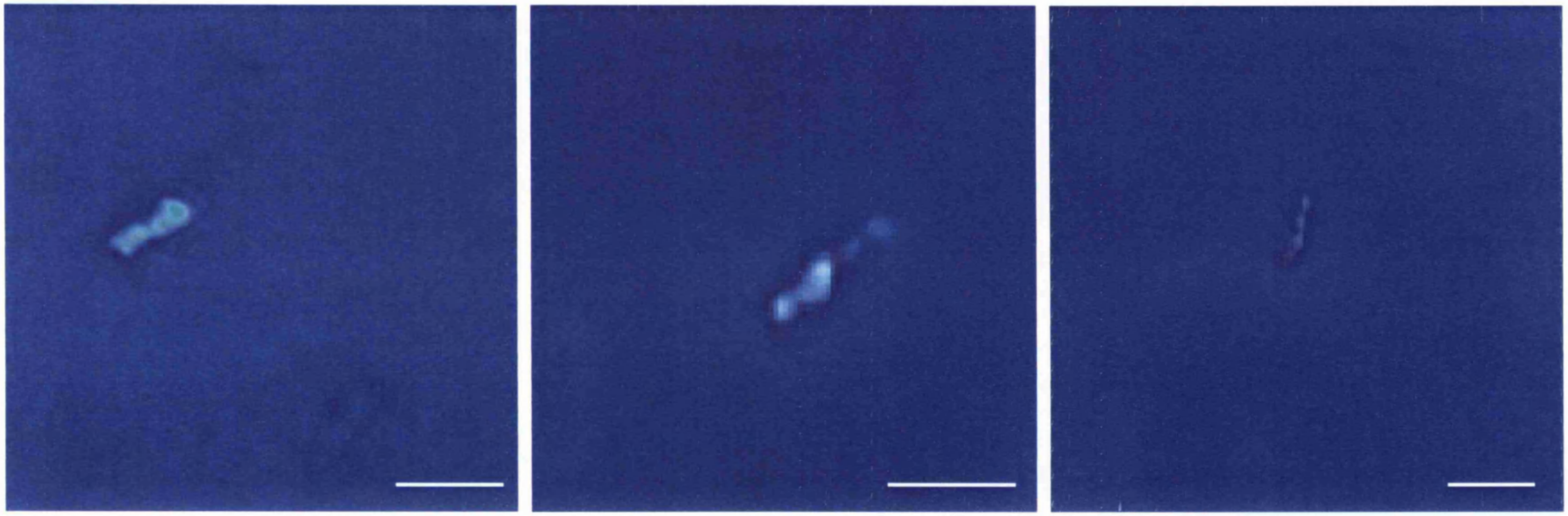

Figure 5.9 Fluorescence microscopic images of compacted T4 DNA after the interaction with CCP-S at a CCP concentration of 43.1 nM, which corresponds to the highest probability of the appearance of bridged structures in this system. The scale bar in the bottom right of the pictures indicates a length of 5 μm.

5.3.3 The effect of spermidine on CCP/DNA systems

To investigate this system further, the effect of spermidine on DNA/CCP systems was studied. Spermidine is a polyamine involved in cellular metabolism and is a widely used DNA compacting agent.[94-96] It was chosen because the quaternary ammonium cationic side chains of the polymer are related closely to polyamines. Spermidine is known to totally compact 500 nM T4DNA at concentrations above 1.4 nM at room temperature.[85] This study was carried out by adding spermidine (at concentrations from 1.0 nM to 5.0 nM) to a sample with a CCP-S concentration of 43.1 nM and a DNA concentration of 500 nM. This was chosen as it was the sample with the highest number of the bridging structures seen. It was found that the spermidine had no effect on the samples, and the "beads-on-a-string" structure remained even at the highest concentration of spermidine. This suggests that the "string" of the "beads-on-a-string" structures is not a free coil of DNA, since we would expect this to be compacted by spermidine. All indications are that, in these structures, the CCP and DNA form DNA-CCP "superstructures" in which linear aggregates of CCP-S molecules act as a bridge between compacted DNA globules.

5.3.4 AFM studies

5.3.4.1 DNA

Typical AFM images obtained from scanning over a small area of the mica surface are shown in Figure 5.10. The DNA is mainly seen as elongated "strands", which is believed to be its solution morphology, with some DNA forming open circles on the surface.

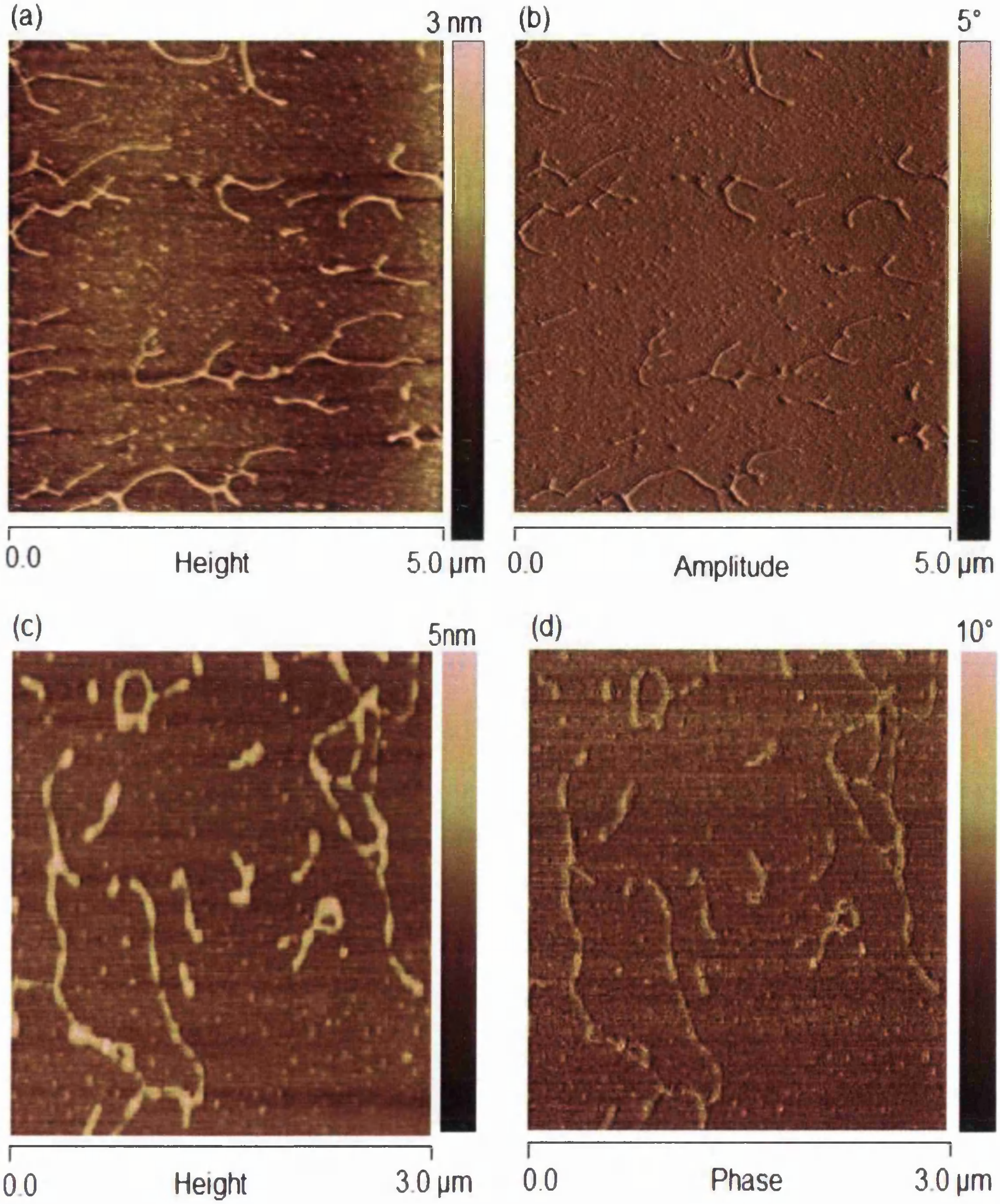

Figure 5.10 DNA on a mica surface. The images are the height (a,c) and corresponding phase images (b,d) on the same area recorded simultaneously.

The average DNA dimensions are: height = 0.95 (± 0.09) nm; width = 21.4 (± 1.44) nm; length 775 (± 82) nm. These are consistent with the native B-form structure in which the length is 0.388 nm per base pair.[97] It is generally thought that the native B-form is the most stable structure under physiological conditions[97] and it has previously been imaged on a mica surface[98]. The polydispersity of the DNA is shown by the length distribution plot, Figure 5.11.

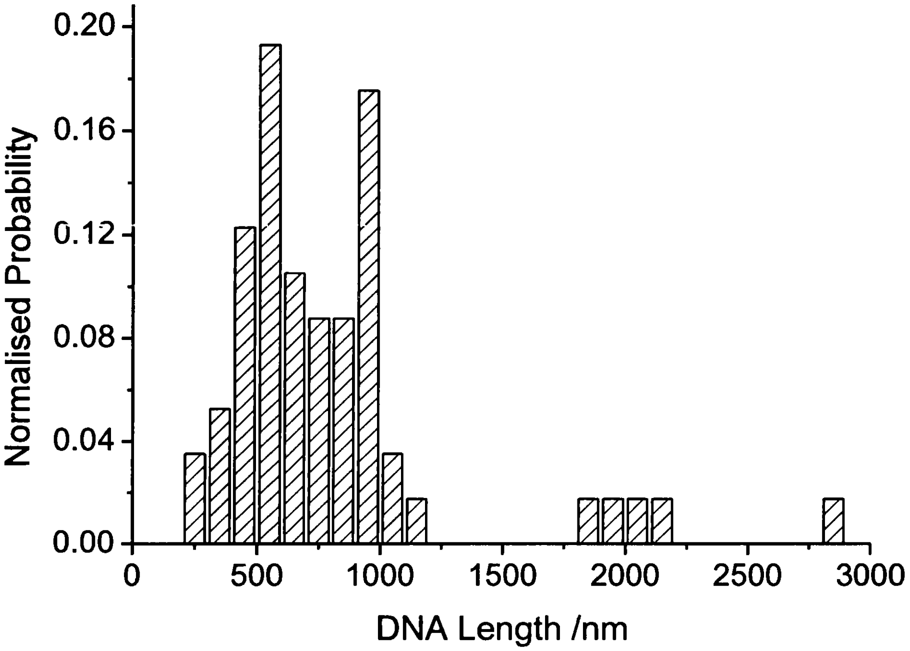

Figure 5.11 Histogram of the distribution of the long-axis length of DNA molecules adsorbed on a mica surface. It is believed that the strands with ~2000 and ~3000 nm length are, in fact, overlapping DNA strands on the surface. The area of the histogram is normalized to unity.

The apparent imaged diameter of the DNA is much larger than expected since the diameter of DNA is actually ~2 nm.[97] It must be remembered that the imaged sizes of DNA, in terms of height and diameter, can be somewhat deceiving. The electrostatic interaction between sample and substrate, along with possible effects from the dehydration of the sample, contributes to the reduction in the measured heights.[99] Also the effect of the finite size of the tip is to overestimate the lateral dimensions i.e. the diameter of the DNA.[98] However, this does not alter the centre-to-centre distance and the relative orientation of the imaged sample.[100] This is due to AFM having better vertical resolution than lateral resolution, typically the vertical resolution is *ca.* ten times better than the lateral resolution,[101] since the lateral resolution approximates the tip curvature and is affected by the shape of the feature imaged due to the tip convolution.[102]

5.3.4.2 CCP-S/DNA interactions

When the polymer is present there are many more linked DNA chains. Furthermore there are now regions of large aggregates of DNA/polymer along the chains; i.e. "beads on a string structures". This is in agreement with the fluorescence microscopy (FM) results, where similar structures were observed, albeit at much lower spatial resolution. While the DNA used here is much shorter than that used in the FM studies (2000 bp for AFM and 166,000 bp for FM studies), and therefore direct comparisons of sizes etc. cannot be made, the similarity of structures observed, both on the mica surface and in solution, is striking.

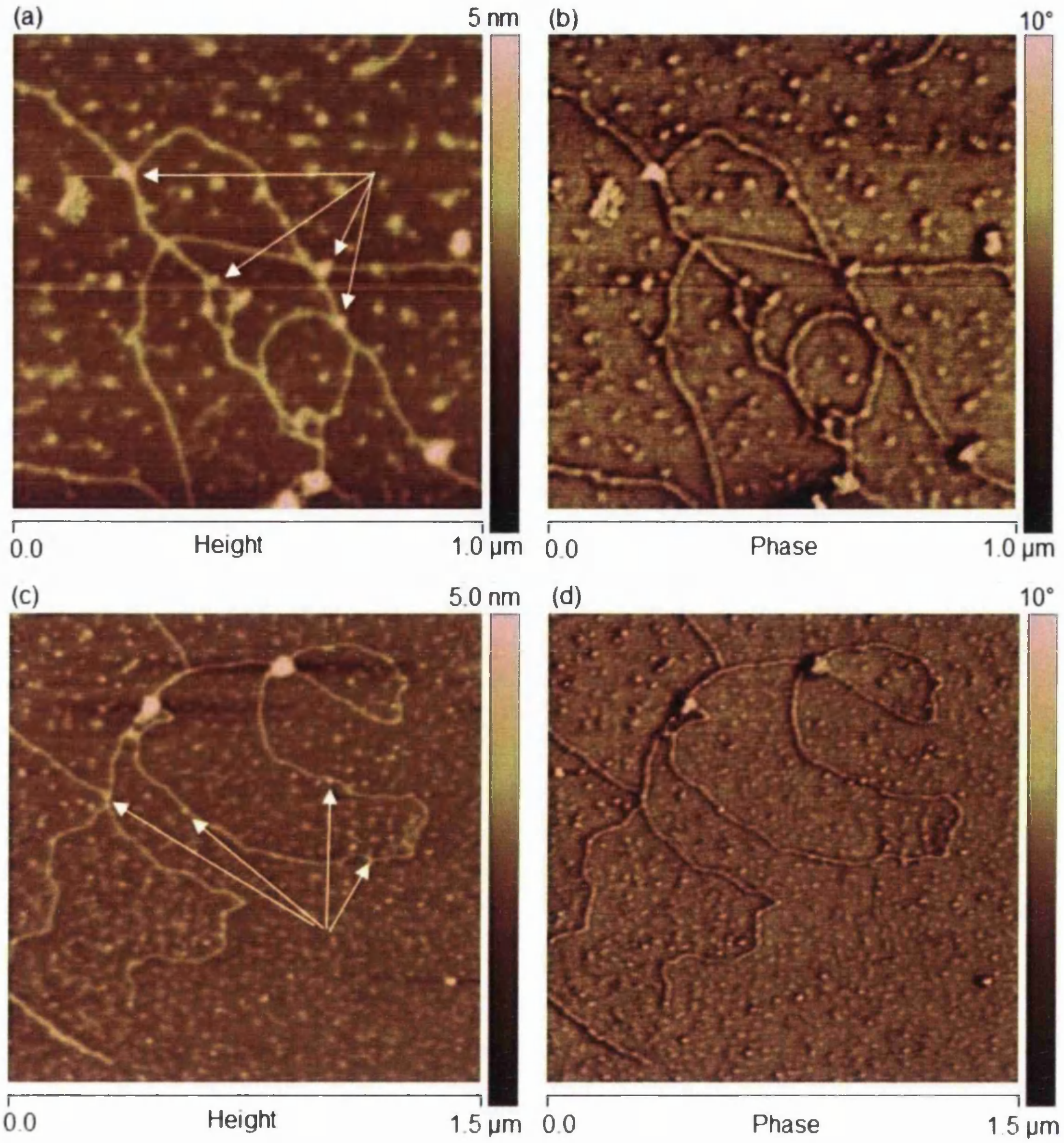

Figure 5.12 Images of the interaction of CCP-S with DNA on a mica surface. The images are the height (a,c) and corresponding phase images on the same area recorded simultaneously (b,d).

The AFM images show compelling evidence for a strong interaction between CCP-S and DNA. The apparent length of the DNA increases to an average of 4050 (± 800) nm, presumably due to several DNA strands being linked together as a consequence of polymer-DNA association, and there are large aggregates, “beads”, along these linked DNA chains. There are also larger aggregates present. The average heights and diameters of the various structures present in the AFM images are given in Table 5.1.

Graphs of typical surface topography across regions of polymer, DNA, and across large aggregates, have been generated using the Nanoscope program and are shown in Figure 5.13.

Table 5.1 Average image heights and widths for structures imaged after mixing CCP-S with DNA.

Subject	Height / nm	Width / nm
DNA only	0.95 (±0.09)	21.4 (±1.47)
CCP-S only	0.67 (±0.02)	27.5 (±0.61)
DNA (in DNA/CCP-S sample)	0.95 (±0.10)	21.1 (±2.50)
Beads on DNA/CCP-S	1.98 (±0.11)	46.2 (±2.13)
Large aggregates	4.47 (±0.14)	70.5 (±5.13)

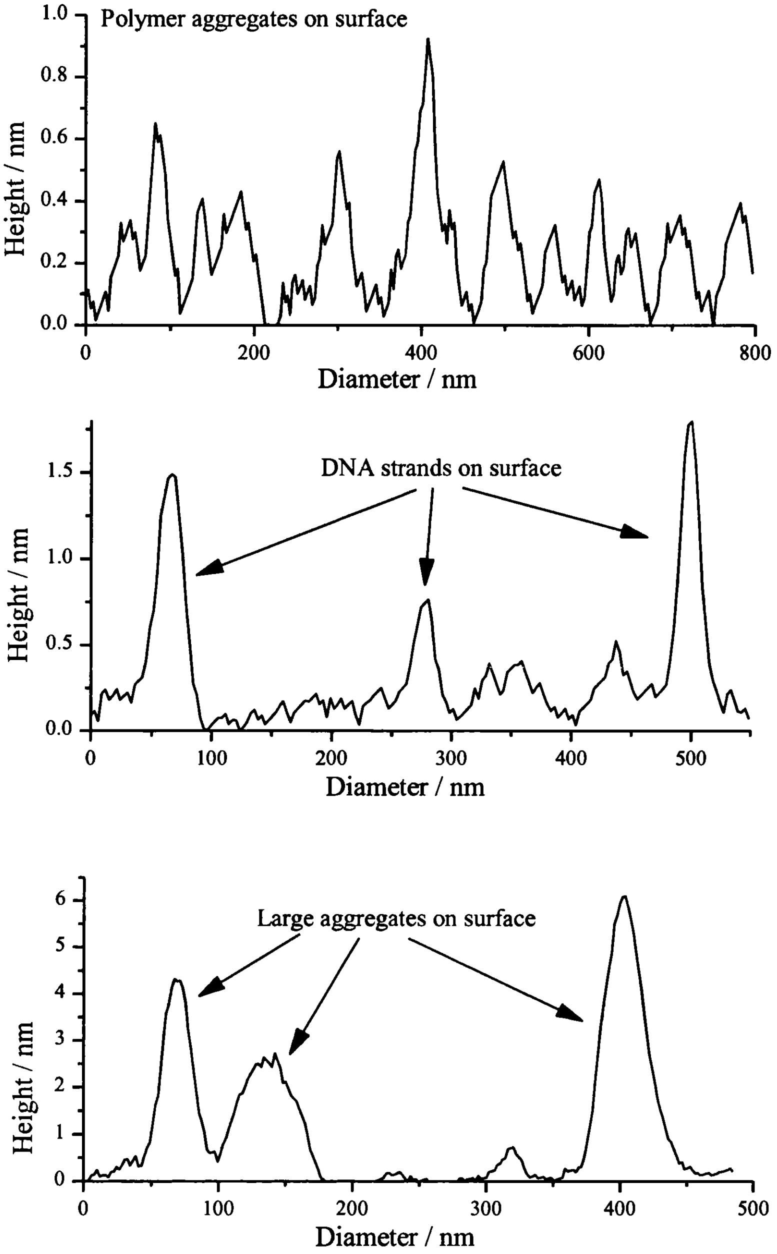

Figure 5.13 Surface topography showing both the height and width of: CCP-S alone (a); DNA strands (b); and large aggregates of compacted DNA/CCP-S (c).

The average height and width of DNA in the absence of CCP-S are 0.95 (±0.09) and 21.4 (±1.47) nm respectively. When CCP-S is present the height and width for many DNA strands remain relatively unaltered (0.95 (±0.10) and 21.1 (±2.50) nm); but at those points along the chain where polymer/DNA aggregate beads are formed (some of which are indicated by the arrows in Figure 13) the average height and widths are increased significantly being: 1.98 (±0.11) and 46 (±2.13) nm respectively. The large aggregates, that are thought to be compacted DNA/CCP-S, have heights and widths of 4.47 (±0.14) and 70.5 (±5.13) nm respectively. The majority of the surface of the mica is covered in what is thought to be isolated CCP-S, which will be attracted to the slightly negative mica surface. All these results indicate that when mixed in solution and then deposited on a mica surface DNA and CCP-S form supramolecular structures in which electrostatic interactions between DNA and polymer result in both compaction and linking of DNA strands, as well as larger aggregate structures.

5.4 Conclusions

Fluorescence microscopy studies have confirmed that CCP-S is very efficient in compacting DNA and that DNA collapse is a discrete transition for isolated DNA chains. Even though DNA quenches CCP-S fluorescence, reducing it by as much as a factor of 2 at the concentrations used for fluorescence microscopy studies, the compaction of DNA by the CCP results in very bright globules, brighter than those obtained with non-luminescent compacting agents (where it is DAPI that makes the visualisation possible) making the compacted DNA more distinguishable from the rest of the sample. This makes counting and measuring DNA globules much easier and more accurate. CCP-S and DNA have been shown to form "bead-on-a-string" "superstructures". These structures are still present after the addition of spermidine at a concentration high enough to induce total compaction of any free DNA in the system, suggesting that they are compacted DNA linked by linear aggregates of CCP-S rather than by strands of DNA.

ds ST DNA (2000 base pairs) has been successfully and reproducibly imaged on a mica surface using tapping mode atomic force microscopy. Images obtained following deposition onto mica of material from mixtures of DNA and CCP-S in acetonitrile/water (75:25) show both the efficient compaction of DNA induced by the polymer and linking and bridging of DNA/polymer aggregates. This results in the formation of DNA/CCP-S networks across the mica surface in which several strands of DNA are linked with aggregated polymer/DNA structures at various points along these chains. The formation of these structures on the mica surface is unequivocal evidence for the formation of the DNA/CCP-S superstructures also seen in FM studies. Formation of such structures may well be of interest for designing functional self-assembled DNA structures for materials applications.[89,90,103]

5.5 References.

1. J. P. Behr, *Acc. Chem. Res.,* **1993**, *26*, 274-278.
2. M. X. Tang, F. C. Szoka, *Gene Ther.,* **1997**, *4*, 823-832.
3. G. Krishnamoorthy, G. Duportail, Y. Mely, *Biochemistry,* **2002**, *41*, 15277-15287.
4. A. D. Miller, *Angew. Chem. Int. Ed.,* **1998**, *37*, 1768-1785.
5. E. Vuorimaa, A. Urtti, R. Seppänen, H. Lemmetyinen, M. Yliperttula, *J. Am. Chem. Soc.,* **2008**, *130*, 11695-11700.
6. S. Danielsen, S. Strand, C. L. Davies, B. T. Stokke, *Biochimica et Biophysica Acta,* **2005**, *1721*, 44-54.
7. H. Q. Mao, K. W. Leong, *Advances in Genetics,* **2005**, *53*, 275-306.
8. W. Sajomsang, U. Ruktanonchai, P. Gonil, V. Mayen, P. Opanasopit, *Carbohydrate Polymers*, 2009, *78*, 743-752.
9. C. R. Calladine, H. R. Drew, B. F. Luisi, A. A. Travers, *Understanding DNA: The Molecule & How It Works*; Elsevier:Amsterdam, 3nd edition, **2004**; p 139-172.
10. G. Arents, E. N. Moudrianakis, *Proc. Natl. Acad. Sci. USA,* **1993**, *90*, 10489-10493.
11. D. Goula, C. Benoist, S. Mantero, S. Merlo, G. Levi, B. A. Demeneix, *Gene Ther.,* **1998**, *5*, 1291-1295.
12. A. Aris, A. Villaverde, *Trends Biotechnol.,* **2004**, *22*, 371-377.
13. H. Petry, C. Goldmann, O. Ast, W. Luke, *Curr. Opin. Mol. Ther.,* **2003**, *5*, 524-528.
14. A. El Aneed, *J. Control Release,* **2004**, *94*, 1-14.
15. K. Minagawa, Y. Matsuzawa, K. Yoshikawa, A. R. Khokhlov, M. Doi, *Biopolymers,* **1994**, *34*, 555-558.
16. V. A. Bloomfield, *Curr. Opin. Struct. Biol.,* **1996**, *6*, 334-341.
17. M. O. Khan, S. M. Mel´nikov, B. Jönsson, *Macromolecules,* **1999**, *32*, 8836-8840.
18. J. M. G. Sarraguca, R. S. Dias, A. A. C. C. Pais, *J. Biol. Phys.,* **2006**, *32*, 421-434.
19. Y. S. Tarahovsky, V. A. Rakhmanova, R. M. Epand, R. C. MacDonal, *J. Biophys.,* **2002**, *82*, 264-273.
20. R. S. Dias, B. Lindman, M. G. Miguel, *Prog. Colloid Polym. Sci.,* **2001**, *118*, 163-167.
21. R. S. Dias, B. Lindman, *DNA Interactions with Polymers and Surfactants;* Eds.; John Wiley: New York, **2008**.

22. M. Rosa, M. C. Morán, M. G. Miguel, B. Lindman, *Colloids and Surfaces A: Physicochem. Eng. Aspects,* **2007**, *301*, 361-375.

23. S. M. Mel'nikov, V. G. Sergeyev, Y. S. Melnikova, K. Yoshikawa, *J. Chem. Soc. Faraday Trans.,* **1997**, *93*, 283-288.

24. G. Krishnamoorthy, B. Roques, J. L. Darlix, Y. Mely, *Nucleic Acids Res.,* **2003**, *31*, 5425-5432.

25. P. G. Arscott, C. Ma, J. R. Wenner, V. A. Bloomfield, *Biopolymers,* **1995**, *36*, 345-364.

26. W. Saenger, *Principles of Nucleic Acid Structure.* Springer-Verlag. New York, **1984.**

27. A. Bruce; A. Johnson, J. Lewis, M. Raff, K. Roberts, and P. Walters. *Molecular Biology of the Cell.* 4th edition. New York and London, Garland Science, **2002**.

28. J. M. Butler, *Forensic DNA Typing.* Elsevier. **2001**.

29. H. Clausen-Schaumann, M. Rief, C. Tolksdorf, H. Gaub, *Biophys J.,* **2000**, *78,* 1997–2007.

30. Y. S. Mel'nikova, B. Lindman, *Langmuir*, **2000**, *16*, 5871-5878.

31. M. Mandelkern, J. Elias, D. Eden, D. Crothers (1981). *J Mol Biol.,* **1981**, *152*, 153–161.

32. R. Wing, H. Drew, T. Takano, C. Broka, S. Tanaka, K. Itakura, R. Dickerson, *Nature,* **1980**, *287,* 755–758.

33. C. Pabo, R. Sauer, *Annu Rev Biochem.,* **1984**, *53,* 293–321.

34. R. Dias and B. Lindman, *DNA Interactions with Polymers and Surfactants,* Wiley-Interscience, New Jersey, **2008**.

35. A. Rich, A. Nordheim, A. H. J. Wang, *Anl. Rev. Biochem.,* **1984**, *53*, 791-846.

36. F. M. Pohl, Cold Spring Harb. Symp. Quant. Biol., **1982**, 47, 113-117.

37. M. Gueron, J. P. Demaret, *Proc. Natl. Acad. Sci. USA,* **1992**, *89,* 5740-5743.

38. M. L. Davies, H. D. Burrows, M. C. Morán, M. G. Miguel and P. Douglas, *Biomacromolecules*, **2009**, *10*, 2987–2997.

39. www.biochemistry.ucla.edu/biochem/Faculty/Martinson/Chime/abz_dna/abz_master.html

40. N. Korolev, A. P. Lyubartsev and L. Nordenskiöld, *Biophys. J.,* **1998**, *75,* 3041-3056.

41. J. Marmur, P. Doty, *J. Mol. Biol.*, **1962**, *5,* 109-118.

42. P. Yakovchuk, E. Protozanova, M. D. Frank-Kamenetskii, *Nucleic Acids Res.,* **2006,** *34,* 564–74.
43. T. Chalikian, J. Völker, G. Plum, K. Breslauer, *Proc Natl Acad Sci USA,* **1999**, *96*, 7853–7858.
44. K. Holmberg, B. Jonssön, B. Kronberg, B. Lindman, *Surfactants and Polymers in Aqueos Solution,* 2nd edition, John Wiley and sons ltd, West Sussex, **2003**.
45. F. Fogolari, A. Brigo, H. Molinari, (2002). *J Mol Recognit.,* **2002,** *15,* 377–392.
46. G. L. Gouy, *J. de Phys.*, **1910**, *9*, 457.
47. G. S. Manning, *Q. Rev. Biophys.*, **1978**, *11*, 179-246.
48. M. T. Record, T. M. Lohman, P.L. deHaseth, *J. Mol. Biol.*, **1976,** *107,* 145-158.
49. D. P. Mascotti, T. M. Lohman, *Proc. Natl. Acad. Sci. USA*, **1990**, *87*, 3142-3146.
50. A. P. Wolffe, *J. Exp. Zool.* **1998**, *282*, 239-244.
51. D. Pruss, J. J. Hayes, A. P. Wolffe, *Bioessays,* **1995**, *17*, 161–170.
52. S. Dimitrov, A. P. Wolffe, *Biochimica et Biophysica Acta,* **1995**, *1260*, 1-13.
53. B. Li, M. Carey, J. L. Workman, *Cell*, **2007,** *128,* 707-719.
54. M. Bretona, M. Bessodesa, S. Bouaziza, J. Herscovicib, D. Schermana, N. Mignet, *Biophysical Chemistry*, In Press, Corrected Proof, Available online August **2009**.
55. Y. Gao, Z. Xu, S. Chen, W. Gu, L. Chen, Y. Li, *International Journal of Pharmaceutics*, **2008,** *359,* 241-246.
56. http://en.wikipedia.org/wiki/File:Chromatin_Structures.png.
57. M. Matsumoto, T. Sakaguchi, M. Kimura, K. Doi, K. Mingawa, Y. Matsuzawa, K. Yoshikawa, *J. Polymer Sci. B Polymer Phys.,* **1992**, *30*, 779-783.
58. Y. Yamasaki, K. Yoshikawa, *J. Am. Chem. Soc.,* **1997**, *119*, 10573-10578.
59. Y. Li, U. H. Yildiz, K. Mullen, F. Grohn, *Biomacromolecules*, **2009**, *10*, 530-540.
60. C. Rivetti, M. Guthold, C. Bustamante, *J. Mol. Biol.*, **1996,** *264*, 919-932.
61. C. Volcke, S. Pirotton, C. H. Grandfils, C. Humbert, P. A. Thiry, I. Ydens, P. Dubois, M. Raes, *J. Biotech.* **2006,** *125*, 11-21.
62. J. Zheng, Z. Li, A. Wu, H. Zhou, *Bio. Phys. Chem.*, **2003**, *104*, 37–43.
63. O. L. Vinogradova, O. V. Lebedeva, K. Vasilev, H. F. Gong, J. Garcia- Turiel, B. S. Kim, *Biomacromolecules,* **2005**, *6*, 1495–1502.
64. E. V. Dubrovin, S. N. Staritsyn, S. A. Yakovenko, I. V. Yaminsky, *Biomacromolecules,* **2007**, *8*, 2258–2261.
65. G. Maurstad, B. T. Stokke, *Biopolymers,* **2004**, *74*, 199–213.

66. Y. L. Lyubchenko, S. M. Lindsay, J. A. DeRose, T. Thundat, *J. Vac. Sci. Technol.B.,* **1991,** *9,* 1288-1290.
67. M. Tanigawa, T. Okada, *Anal. Chim. Acta.,* **1998,** *365,* 19–25.
68. V. J. Morris, A. R. Kirby, A.P. Gunning, *Atomic Force Microscopy for Biologists,* Imperial College Press, London, **1999**.
69. S. N. Magonov, J. Cleveland, V. Elings, D. Denley, M. H. Whangbo, *Surf. Sci.,* **1997,** *389,* 201.
70. H. Wang, J. Han, *J. Colloid and Interface Sci.,* **2009,** *333,* 171-179.
71. R. Brandsch, G. Bar, M. H. Whangbo, *Langmuir,* **1997,** *13,* 6349-6353.
72. A. Knoll, R. Magerle, G. Krausch, *Macromolecules,* **2001,** *34,* 4159-4165.
73. H. Petry, C. Goldmann, O. Ast, W. Luke *Curr. Opin. Mol. Ther.,* **2003,** *5,* 524-528.
74. A. El Aneed, *J. Control Release,* **2004,** *94,* 1-14.
75. A. Podestà, M. Indrieri, D. Brogioli, G. S. Manning, P. Milani, R. Guerra, L. Finzi, D. Dunlap, *Biophys. J.,* **2005,** *89,* 2558-2563.
76. C. Guáqueta, E. Luijten, *Phys. Rev. Lett.,* **2007,** *99,* 138302.
77. S. Wang, B. Liu, B. S. Gaylord, G. C. Bazan, *Adv. Funct. Mater.,* **2003,** *13,* 463-467.
78. Y. Yoshikawa, K. Yoshikawa, T. Kanbe, *Biophys. Chem.,* **1996,** *61,* 93-100.
79. N. Yoshinaga, T. Akitaya, K. Yoshikawa, *Bioch. Biophys. Research Comm.,* **2001,** *286,* 264-267.
80. Y. Matsuzawa, K. Minagawa, K. Yoshikawa, M. Matsumoto, M. Doi, *Nucleic Acids Symp. Ser.,* **1991,** *25,* 131-132.
81. Y. Matsuzawa, K. Yoshikawa, *Nucleosides and Nucleotides* **1994,** *13,* 1415-1423.
82. H. G. Hansma, I. Revenko, K. Kim, D. E. Laney, *Nucleic Acids Research,* **1996,** *24,*713–720.
83. G. Cosa, K.S. Focsaneanu, J. R. N. McLean, J. P. McNamee, J. C. Scaiano, *Photochem. Photobiol.,* **2001,** *73,* 585-599.
84. M. R. Lamprecht, D. M. Sabatini, A. E. Carpenter CellProfiler: free, versatile software for automated biological image analysis. *Biotechniques.* **2007,** *42,* 71-75.
85. M. Takahashi, K. Yoshikawa, V. V. Vasilevskaya, A. R. Khokhlov, *J. Phys. Chem. B,* **1997,** *101,* 9396-9401.
86. S. Gawęda, M. C. Morán, A. A. C. C. Pais, R. S. Dias, K. Schillén, B. Lindman, M. G. Miguel, *J. Colloid Interface Sci.,* **2008,** *323,* 75-83.

87. H. A. Al-Attar, A. P. Monkman, *Adv. Funct. Mater.,* **2008**, *18*, 2498-2509.

88. A. A. Zinchenko, V. G. Sergeyev, S. Murata, K. Yoshikawa, *J. Am. Chem. Soc.* **2003**, *125*, 4414-4415.

89. N. C. Seeman, *Nature* **2003**, *421*, 427-431.

90. P. W. K. Rothemund, *Nature* **2006**, *440*, 297-302.

91. D. L. Feldheim, B. E. Eaton, *ACS Nano.,* **2007**, *1*, 154-159.

92. L. Dong, T. Hollis, B. A. Connolly, N. G. Wright, B. R. Horrocks, A. Houlton, *Adv. Mater.,* **2007**, *19*, 1748-1751.

93. F. A. Aldaye, A. L. Palmer, H. F. Sleiman, *Science* **2008**, *321*, 1795-1799.

94. G. Wegner, *Macromol. Chem. Phys.*, **2003**, *204*, 347-357.

95. K. A. Marx, G. C. Ruben, *Nucleic Acids Res.*, **1983**, *11*, 1839-1854.

96. Y. Yoshikawa, T. Mori, N. Magome, K. Hibino, K.Yoshikawa, *Chem. Phys. Let.,* **2008**, *456*, 80-83.

97. D. L. Nelson, M. M. Cox, *Lenhinger. Principles of Biochemistry.* Wroth Publishers, New York, 3rd edition, **2000**.

98. H. G. Hansma, D. E. Laney, M. Bezanilla, R. L. Sinsheimer, P. K. Hansma, *Biophys. J.,* **1995**, *68*, 1672–1677.

99. F. Moreno-Herreroa, P. Herreroa, J. Colcherob, A. M. Baro, F. Morenoa, *FEBS Letters.* **1999**, *459*, 427-432.

100. C. Bustamante, G. Zuccheri, S. H. Leuba, G. Yang, B. Samori, *Methods Enzymol.,* **1997**, *12*, 73–83.

101. A. Engel, C. A. Schoenenberger, D. J. Müller, *Curr. Opin. Struct. Biol.,* **1997**, *7*, 279–284.

102. H. Yokota, D. A. Nickerson, B. J. Trask, G. Engh, M. Hirst, I. Sadowski, R. Aebersold, *Anal. Biochem.,* **1998**, *264*,158–164.

103. X. D. Liu, M. Yamada, M. Matsunaga, *Adv. Polym. Sci.,* **2007**, *209*, 149-178.

Chapter 6

The Interaction of Cationic Conjugated Polyelectrolytes with DNA

6.1 Introduction

Cationic conjugated polyelectrolytes (CCPs) tend to be highly sensitive to changes in their physical and chemical environment[1-3] and their fluorescence can be quenched with remarkable efficiency in the presence of oppositely charged quenchers.[4,5] This ability of oppositely charged species to quench the fluorescence of CCPs with very high efficiency has been termed "amplified quenching" or "superquenching".[6,7] In heterogeneous solution fluorescence quenching is generally discussed quantitatively using the Stern-Volmer equation.[8]

$$\frac{I_0}{I}=1+k_{SV}[Q] \qquad [6.1]$$

Where I and I_0 are the fluorescence intensity with and without the quencher, respectively, [Q] is quencher concentration, and K_{SV} is the Stern-Volmer constant. It is important to note that the Stern-Volmer equation does not contain a variable for the fluorophore concentration i.e. fluorescence quenching is independent of the fluorophore concentration.[8] For diffusion-controlled quenching of small uncharged fluorophores K_{SV} typically ranges from 10^0 to 10^1 M^{-1}, and for fluorophore and oppositely charged quenchers K_{SV} value increase to 10^2-10^3 M^{-1}. By contrast conjugated polyelectrolytes (CPEs) quenched by oppositely charged quenchers have shown quenching constants of the order of 10^6-10^9 M^{-1}.[1,9] Several different interpretations and explanations have been put forward to explain this highly efficient quenching, these are; efficient intrachain exciton diffusion along the polymer chain,[7,10-12] 3-dimensional interchain exciton diffusion in CPE aggregates,[7,13,14] ion-pair complex formation between the polymer and the quencher,[7,13,15] and ultrafast charge/energy transfer between the polymer and the quencher.[7,14] This high sensitivity to quenching by oppositely charged species has led to the suggestion that CCPs may be useful in chemical and biological sensors, and in particular sensors for DNA.[16-18]

6.1.1 CCP based biosensors

A biosensor is a device that detects, records, and transmits information regarding a physiological change or the presence of various chemical or biological materials in the environment. Detection of DNA and methods for the sequence identification of DNA are currently the subject of a great deal of research and are important for new approaches in medical diagnostics, identification of genetic mutations, gene delivery monitoring, and specific genomic techniques.[19-22] CCPs have already found use as DNA biosensors which have been based on the electrostatic interaction with the oppositely charged phosphate groups of the target DNA or polynucleotide.[23] Polythiophene and polyfluorene based CCPs have been implemented in CCP based DNA sensors.[24,25] There have been several proposed methods of DNA sequence detection using CCPs that show promise for highly sensitive DNA detection.[2,26,27] Leclerc and co-workers have been able to detect and distinguish a specific sequence of oligonucletides having a single mismatch and in very low concentration.[2,26] The method used utilised different electrostatic interactions and conformational structures between the CCP, poly(3-alkoxy-4-methylthiophene)s, and single stranded DNA (ssDNA) or hybridized double stranded DNA (dsDNA). Bazan and co-workers have used cationic poly(fluorene-*co*-phenylene)s CCPs, similar to the CCPs used in this study, as Förster resonant energy transfer (FRET) biosensors.[28-30] In these FRET sensors the sensitivity and selectivity of detection arise from the use of fluorescent labels attached to peptide nucleic acids (PNAs) or DNA. Peptide nucleic acids (PNA) are DNA mimics where the nucleotides are attached to a N-(2-aminoethyl)glycine backbone instead of the negatively charged deoxyribose phosphate backbone as is the case in DNA.[31,32] PNA is an extremely good structural mimic of DNA (or RNA), and PNA oligomers are able to form very stable duplex structures with Watson-Crick complementary DNA. This ability to form stable structures with complementary DNA underpins the detection method. Imagine a solution containing nucleotides, ssPNA or ssDNA, which are labelled with a fluorescent dye (C*) and complementary or non-complementary target ssDNA. If the target DNA and nucleotides are complementary they hybridize to make the negatively charged complex DNA/PNA(C*) or DNA/DNA(C*) this is then electrostatically attracted to the CCP and brings the CCP and C* label in close proximity, this enables FRET between the excited CCP donor and the C* acceptor. The hybridized complex is therefore detected by enhanced emission from the PNA-C* or DNA-C* acceptor. This process is summarised in Figure 6.1. Also the emission of the fluorescent label (C*) by FRET from a CCP has been shown to be considerably more intense than that obtained by direct excitation at the absorption maximum of C*.[33] This demonstrates the optical amplification provided by the light-harvesting properties of the CCP.[33,34] When a non-complementary ssDNA is present there is no hybridization with ssDNA-C* and there is competition between the unhybridised strands for sites adjacent to the CCP. FRET is therefore less effective, and thus complementary DNA strands can be distinguished from non-complementary strands by the examination of C* intensity. Thus if the original base sequence is known the base sequence of all complementary DNA can be deduced. There are however a few problems with this method; screening of the non-complementary strand is not complete and therefore a small amount of FRET to the ssDNA-C* occurs.[28] This means that residual emission can limit the ability to discriminate complementary from non-complementary DNA target sequences.[28] The positively charged CCP is also likely to form a complex with the negatively charged free DNA, in which the CCP excited states can be quenched.[1,35] It may also be possible for CCP–CCP quenching to occur when more than one CCP is bound to a DNA or DNA/PNA duplex.

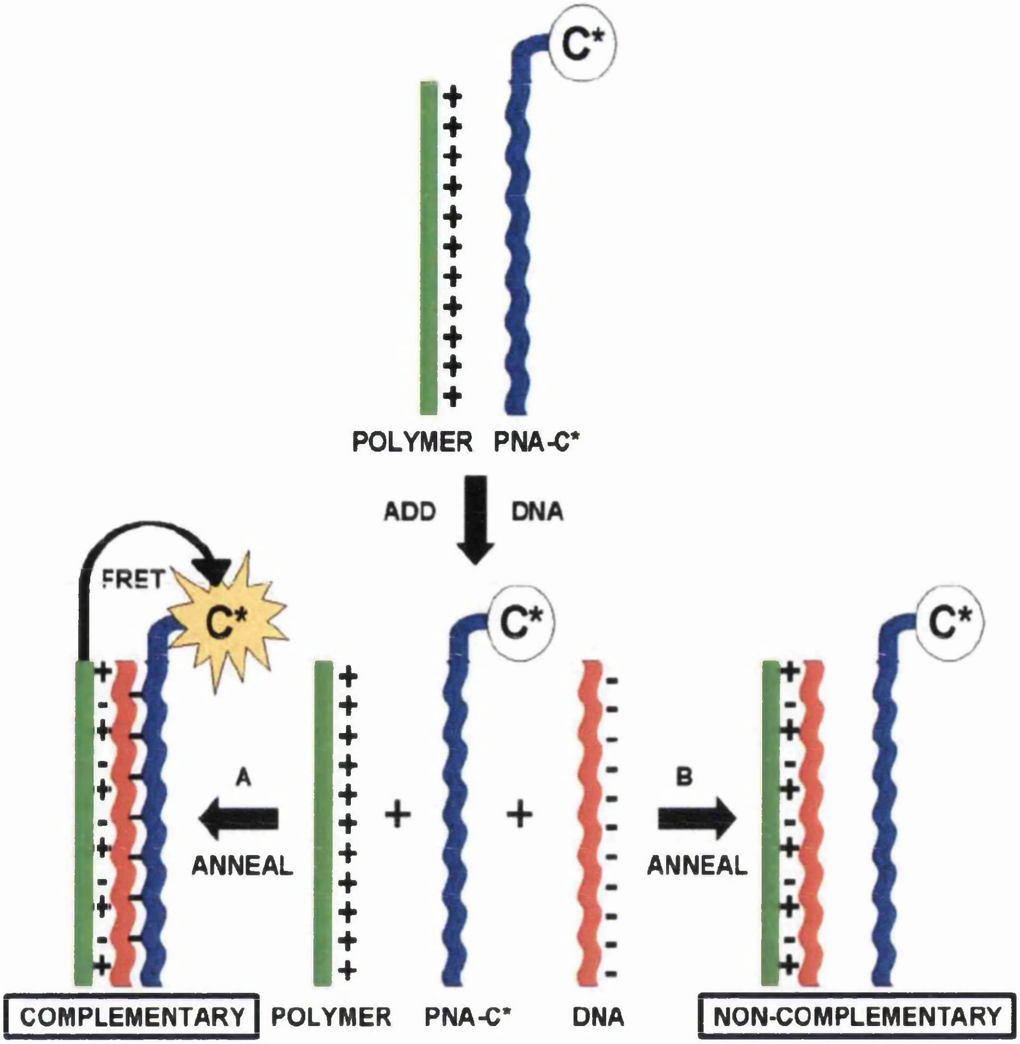

Figure 6.1 Schematic representation of the mechanism by which CCP FRET sensors can be used to detect complementary ssDNA.[5]

For the use of CCPs in FRET based biosensors in DNA detection and sequencing there are three important parameters to consider; (i) maximisation of the quantum yield through minimisation of aggregation, (ii) excitation dynamics and (ii) the interaction of the CCPs with DNA. Studies of aggregation, quantum yields and excitation dynamics have already been described in Chapter 4. In this chapter results from studies of the interaction of the three CCPs (CCP-S, CCP-M and CCP-L) with double stranded DNA (dsDNA) and single stranded DNA (ssDNA), as well as the DNA base guanine, are described and discussed. For use in CCP based biosensors it is important that the interaction, and subsequent quenching mechanism, between CCPs and DNA is well understood. Figures 6.2 and 6.3 show scale sizes of the CCPs and

DNA used in this study. Figure 6.3 highlights the large difference in length of the longest polymer, CCP-L, compared to the DNAs.

6.1.2 Aims of this study

This chapter describes the characterisation of the interaction of the three CCPs (CCP-S, CCP-M and CCP-L) with DNA, and the DNA base guanine, with emphasis on characterisation of the quenching mechanism. The aim is to gain an understanding of the mechanism by which DNA quenches the CCPs and the effect of CCP and DNA chain length on the quenching mechanism. An understanding of quenching is vitally important if the CCPs are going to be used in DNA biosensors. The effect of both CCP length and DNA length on the quenching rate is discussed.

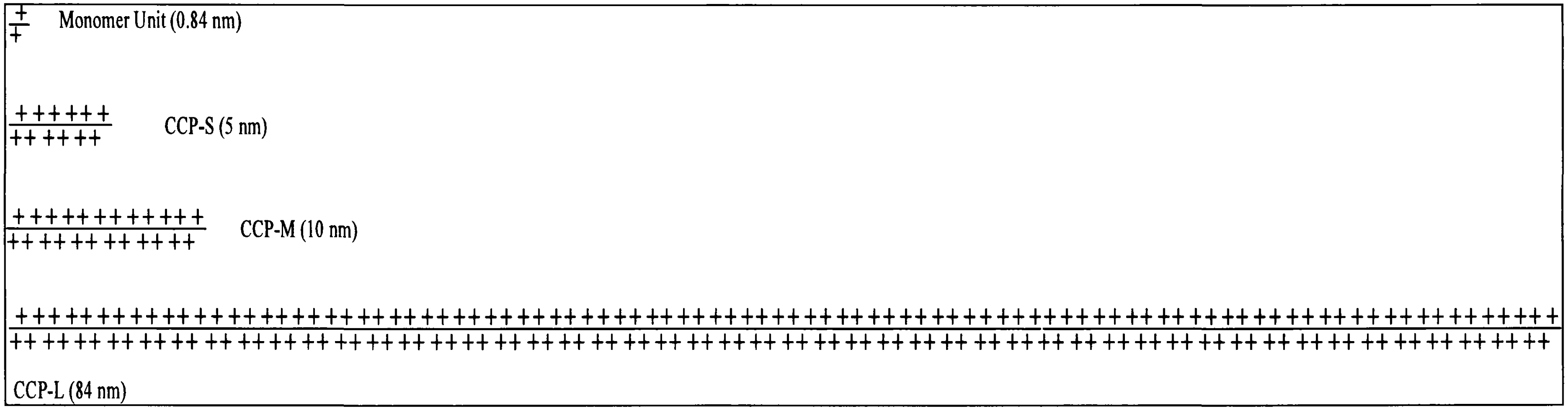

Figure 6.2 Schematic representation of the size of the CCPs used in this study. The approximate length of the CCPs is given in the figure.

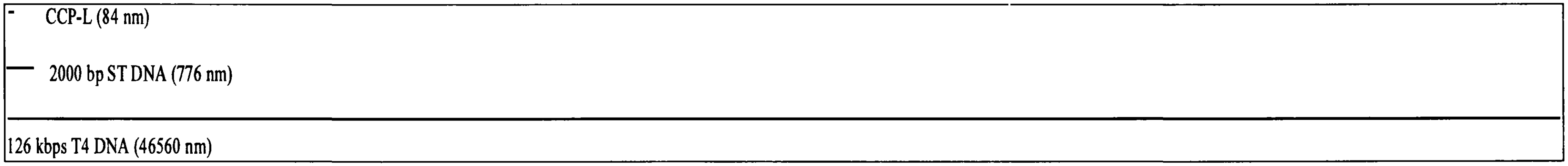

Figure 6.3 Representation of the sizes of the DNA used in this study in comparison with the longest polymer, CCP-L. The sizes of the DNAs are given in the figure and are represented by the solid line.

6.2 Experimental Section

6.2.1 Materials

All CCPs are described in Section 4.2.1 and all CCP samples were dissolved in 25/75 acetonitrile/water (v/v) to minimise aggregation. DNA from salmon testes (ST DNA), having an average molecular weight of 1.3×10^6 (2000 base pairs)[38], was purchased from Sigma Aldrich and used as received. Bacteriophage T4 DNA (165.6 kilobase pairs, contour length of 57 μm) was purchased from Wako Nippon Gene. The buffer salt, tris-HCl base, and the fluorescent dye, 4,6-diamidino-2- phenylindole (DAPI) were also purchased from Sigma. YOYO®-1 iodide, as a 1 mM solution in DMSO, was purchased from Invitrogen™. All other chemicals were purchased from Sigma-Aldrich. Acetonitrile and ethanol were of spectroscopic grade. All experiments were performed using Millipore Milli-Q deionised water.

6.2.2 Equipment and methods

6.2.2.1 Quenching studies with T4 DNA and guanine

T4 DNA solutions were prepared by adding T4 DNA mother solution to tris-HCl base buffer, pH = 7.8, to give the required concentrations; these cover the range 0 - 12.4×10^{-8} M in terms of base pairs. (Unless otherwise stated all DNA concentrations are in terms of base pairs.) The ssDNA solution was prepared by thermal denaturation of the dsDNA solution by heating at 90°C for ten minutes, after which the solution was immersed in an ethanol/ice solution.[39] The UV-Vis absorption spectrum was recorded from 40-90 °C at intervals of 10 °C; a substantial increase in absorption indicates the formation of single stranded DNA. Denaturing the dsDNA solutions means that the concentration of both solutions, dsDNA and ssDNA, were the same in terms of base units. Guanine concentrations were ca. 1/5th of DNA since the guanine content of T4 DNA is known to be ~18%.[40] Stern-Volmer (SV) plots have been corrected for any changes in absorbance associated with change in solvent mixture or with the addition of DNA or guanine. Solvent mixtures are given as v/v. Absorption measurements were made using a Shimadzu UV-2100 spectrophotometer and steady-state luminescence studies were carried out using the Jobin Yvon-Spex Fluorolog 3-22 spectrometer described in Section 2.3. Excitation and emission slits were 4.0 nm. Fluorescence spectra were corrected for the spectral response of the light source (450

W xenon lamp) and detector. Fluorescence decay times with picosecond time resolution were obtained by using a home-built picosecond time correlated single photon counting (TCSPC) apparatus as described in section 2.4.2.

6.2.2.2 Quenching studies with salmon testes DNA (ST DNA)

Quenching studies with ST DNA were first carried out at the same concentrations as T4 DNA, i.e. 0 - 12.4×10^{-8} M in terms of base pairs. Mother solutions of ST DNA were prepared by dissolving the DNA in tris-HCl base buffer, pH = 7.8. The concentrations of the DNA solutions were calculated from the absorbance at 260 nm ($\varepsilon = 6600\ \mathrm{cm^{-1}\ M^{-1}}$).[41] ssDNA was produced by thermal denaturation as described in Section *6.2.2.1*. Quenching studies were also carried out with a higher range of DNA concentrations which were 2.6×10^{-7} to 4.72×10^{-6} M (in terms of base pairs). CCP concentration dependent quenching studies were carried out by keeping the DNA concentration range constant at 2×10^{-7} M to 1.4×10^{-5} M and varying the CCP concentrations. For all CCPs the three CCP concentrations investigated were 3, 6 and 10×10^{-6} M. Table Curve™ 2D version 3 (Jandel Scientific) was used for the equilibrium analysis curve fitting.

6.2.2.3 CCP-S/DNA anisotropy studies

For the change in anisotropy upon the addition of DNA a CCP-S concentration of 2.6×10^{-6} M (polymer chains; 1.5×10^{-5} M repeat units) and DNA concentrations from 3.5×10^{-8} to 2.1×10^{-6} M (in terms of base pairs) were used. Two commercial dyes, DAPI and YoYo-1[42-44] (at concentrations of 3.33×10^{-6} and 4.16×10^{-6} M respectively), were also studied for comparison. Anisotropy values are those from the emission weighted averages across the emission band, i.e. from the integrated emission curves. Steady-state fluorescence anisotropy experiments were carried out using a Jobin-Yvon Fluoromax-3 spectrometer (as described in Section 2.3.3) with right angle geometry and excitation and emission slits of 5.0 nm.

6.3 Results

6.3.1 Quenching of CCPs with long stranded T4 DNA

Fluorescence quenching of the CCPs by DNA or guanine was initially analysed in terms of a Stern-Volmer (SV) relationship. Although, as became subsequently apparent, this is not the best method to describe the quenching it is easy, useful and convenient. Furthermore, since it is the most common method used in the literature, it allows comparison with other work. It also sets the foundation for subsequent discussion of the quenching mechanism.

6.3.2 Steady-state absorption and emission

Quenching by dsDNA and ssDNA of fluorescence of the three CCPs was investigated. The interaction of the CCPs with long chain T4 DNA induces both a decrease in the absorption and a large decrease in the emission intensity; however there are no significant changes in the spectral shape or any notable wavelength shifts. Typical decreases in absorption and emission are shown in Figure 6.4.

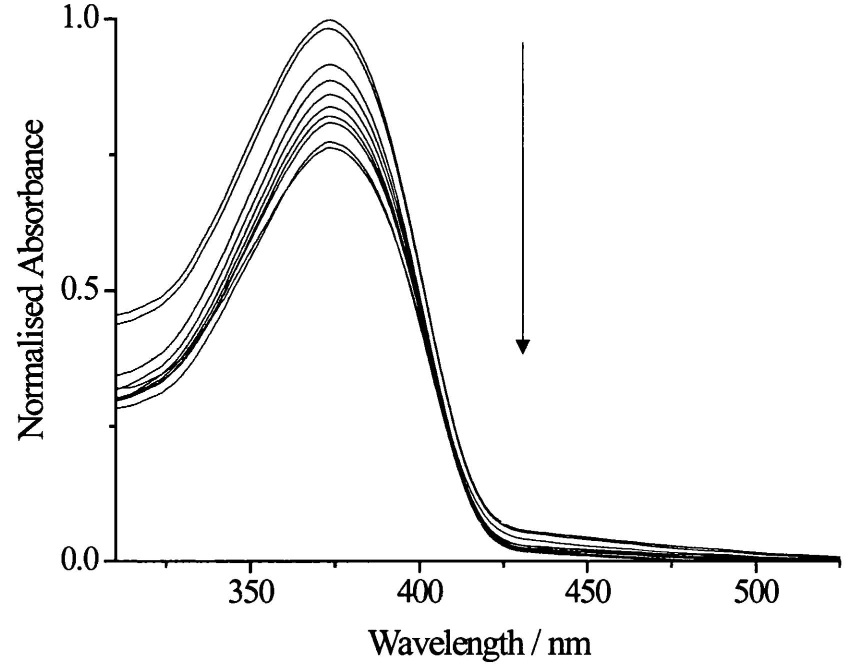

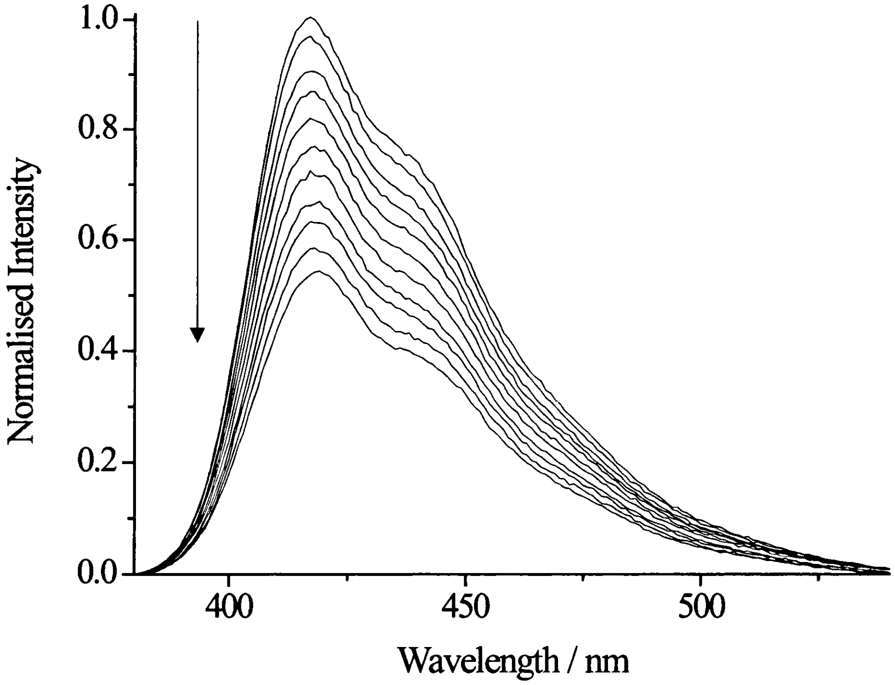

Figure 6.4 Normalised changes in absorption and emission for CCP-M with T4 ds-DNA. The arrows indicate the decrease in absorption and emission with increasing DNA concentration.

Fluorescence quenching was firstly analysed in terms of a SV relationship and the calculated SV plots are given in Figure 6.5. All CCPs are extremely sensitive to DNA quenching, resulting in extremely high SV quenching constants. ssDNA is a better quencher than dsDNA, possibly because in ssDNA the hydrophobic bases are more exposed than in dsDNA which increases the interaction between hydrophobic bases and the CCP chain.

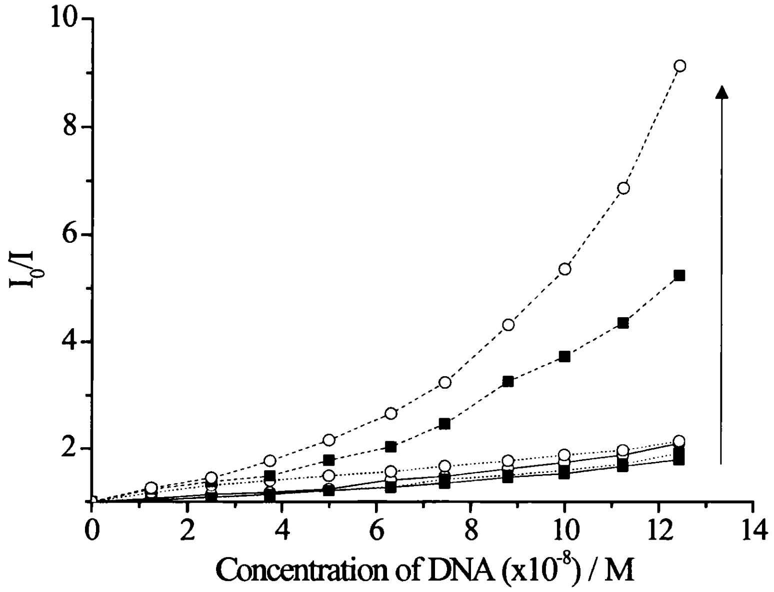

Figure 6.5 SV plots for CCP-S (solid line), CCP-M (dotted line) and CCP-L (dashed line) with dsDNA (solid squares) and ssDNA (open circles) as quenchers. The arrow indicates increasing CCP length.

Table 6.1 SV quenching constants for CCPs with dsDNA and ssDNA, calculated from the initial linear region of the SV plots.

Polymer	Stern-Volmer Constant/ × 10^6 M^{-1} (± 5%)	
	dsDNA	ssDNA
CCP-S	4.72	5.34
CCP-M	6.41	8.56
CCP-L	18.3	29.3

All Stern-Volmer constants, K_{SV}, are calculated from the initial, linear, region of the SV plot. K_{SV} values, and hence sensitivity to DNA, increases with CCP chain length. All the resulting SV plots have an upward curvature. This can be indicative of both static and dynamic quenching processes occurring.[8] However, given the short lifetime of CCP fluorescence, (~500 ps) these quenching constants would give an apparent bimolecular quenching rate constant very much higher than the diffusion controlled limit for dynamic quenching. Fluorescence and atomic force microscopy studies described in Chapter 5 indicate that DNA and CCP-S form structured aggregates in solution, and hence the fluorescence quenching caused by addition of DNA may be explained in terms of the formation of an aggregate complex.[45]

6.3.3 Time-resolved emission

Time-resolved studies were carried out using T4 dsDNA and ssDNA as quenchers. Three exponential decay functions were required to obtain a good fit to the measured data ($\chi \approx 1$) in Table 6.2. Typical normalised emission decay curves are shown in Figure 6.6.

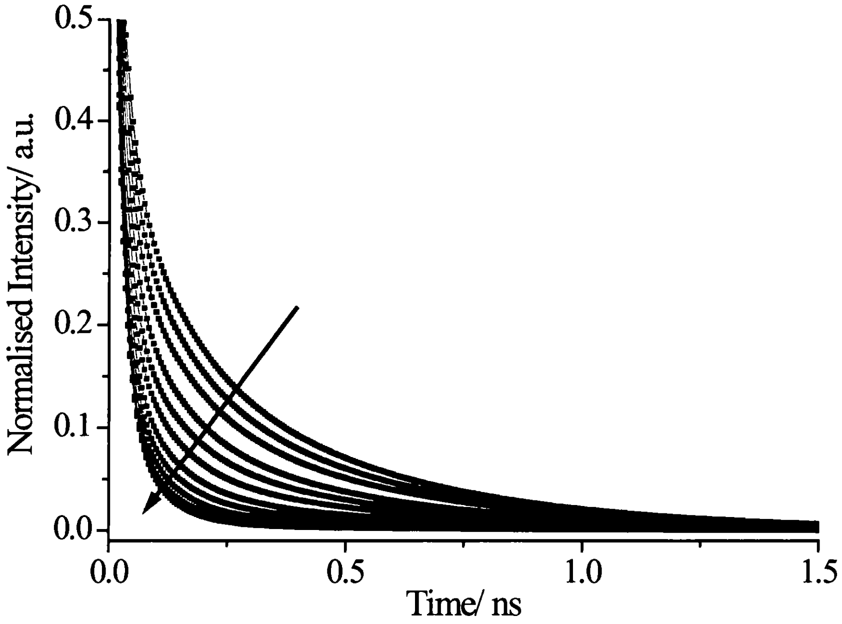

Figure 6.6 Normalised time resolved emission decay curves for CCP-L upon the addition of dsDNA. The arrow indicates increasing DNA concentration.

There is a decrease in the average life time (Table 6.2) with increasing DNA concentration. Of the three lifetimes, those for the fast (~20 ps) and slow decays (~430 ps) are reasonably constant with increasing DNA concentration whereas the lifetime of the middle lifetime component decreases significantly with increasing DNA concentration. This is true for all CCP/T4DNA samples. These results are similar to the lifetime changes associated with changes in acetonitrile concentrations as discussed in Chapter 4. This similarity to aggregate quenching suggests that quenching may involve induced aggregation.

Table 6.2 Time resolved data for CCP-L upon the addition of dsDNA.

[DNA] × 10^{-8} / M	a_1	τ_1/ ps	a_2	τ_2/ ps	a_3	τ_3/ ps	τ_{ave} / ps
0	0.57	23	0.21	119	0.22	427	326
1.25	0.61	23	0.21	117	0.18	428	315
2.50	0.65	22	0.20	114	0.15	431	305
3.74	0.69	22	0.20	104	0.12	428	278
4.99	0.73	21	0.18	102	0.09	432	262
6.23	0.73	19	0.20	86	0.07	428	240
7.48	0.77	19	0.18	84	0.05	429	204
8.72	0.80	19	0.17	81	0.03	434	175
9.96	0.79	18	0.18	72	0.02	428	142
11.20	0.80	18	0.18	67	0.01	424	111
12.44	0.80	18	0.19	64	0.01	425	83

The fractional contribution from the longest lifetime, which we attribute to isolated chains in solution, decreases dramatically with increasing DNA concentration as shown in Figure 6.7.

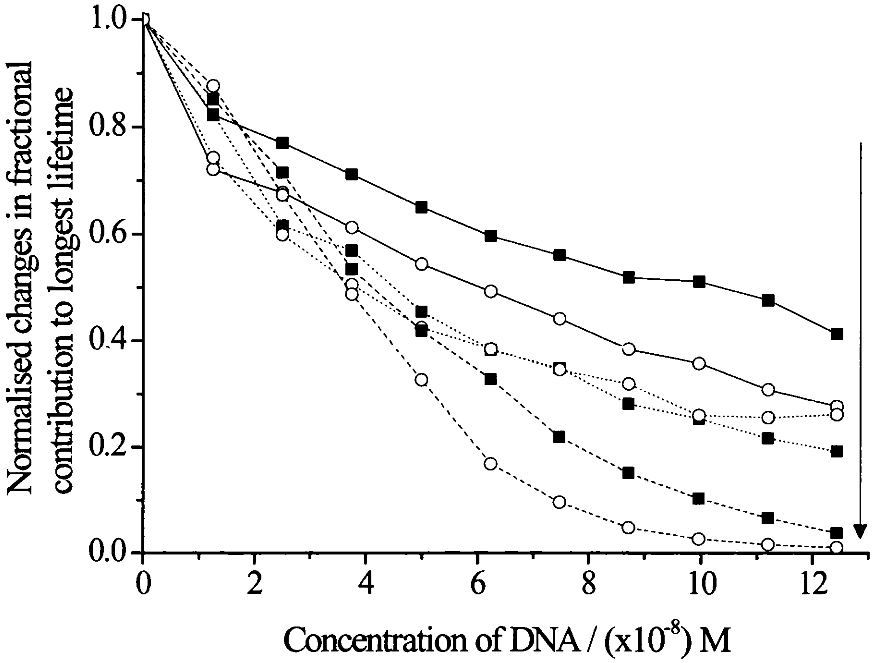

Figure 6.7 Changes in fractional contribution from the longest lifetime for CCP-S (solid line), CCP-M (dotted line) and CCP-L (dashed line) with dsDNA (solid squares) and ssDNA (open circles). The arrow indicates increasing polymer length.

Comparisons of the quenching from time resolved studies and steady state studies on samples of similar CCP concentration can be made. The average lifetime changes are compared with the steady state intensity changes. A SV type plot for changes in the average lifetime with increasing DNA concentration is shown in Figure 6.8. It is similar to the corresponding SV plot for steady state changes in Figure 6.5. At DNA concentrations below *ca.* 8×10^{-8} M^{-1} agreement is quite good, but at higher DNA concentrations steady-state measurements show a greater sensitivity to DNA concentration than the time resolved results, see Figure 6.9.

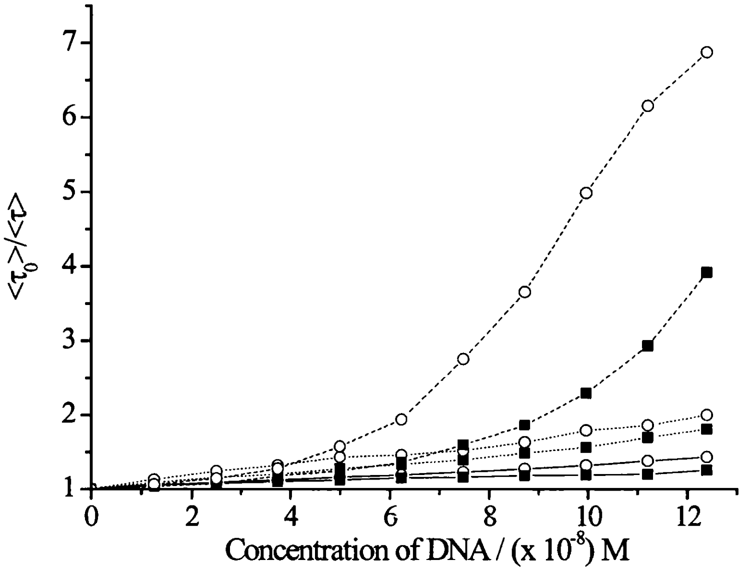

Figure 6.8 Quenching plot from the time resolved data. The change in average lifetime is plotted against the quencher concentration for for CCP-S (solid line), CCP-M (dotted line) and CCP-L (dashed line) with dsDNA (solid squares) and ssDNA (open circles).

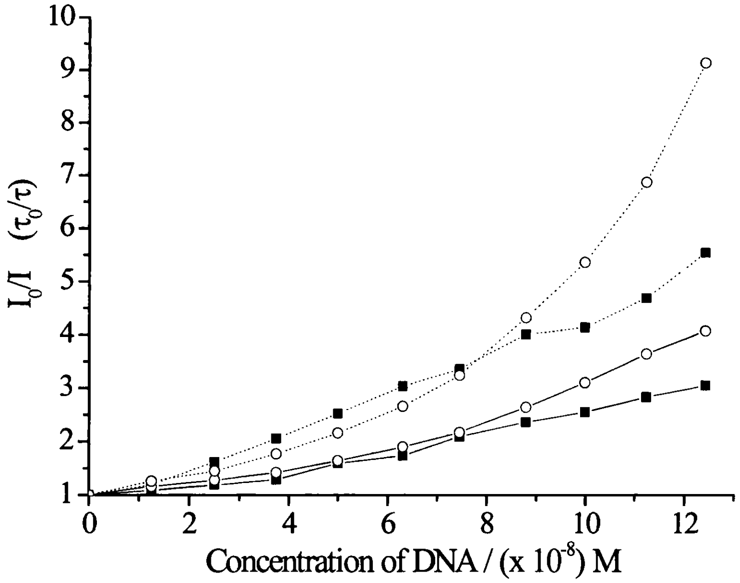

Figure 6.9 Comparison of changes in emission from steady state (open circles) and time resolved values (solid squares) for CCP-S with both dsDNA (solid line) and ssDNA (dotted line).

The most likely explanation is the presence of a kinetic process which is so fast that it occurs within the time resolution of the instrument, i.e. within a few ps, and is therefore lost to the kinetic measurements.

6.3.4 Quenching of CCP fluorescence by guanine

6.3.4.1 Steady state absorption and emission

Guanine has the highest oxidation potential of all the DNA bases (0.81 V) and, because of this, it is thought that if fluorescence quenching occurs via electron transfer, the rate may be dependent on the guanine content of the DNA.[46,47] The guanine content of T4 DNA is known to be 18% and so quenching experiments were carried out at 18% of the concentrations used for quenching with T4 DNA.[39] The interaction of the CCPs with guanine gives similar results to that obtained with T4 DNA. There is both a decrease in the absorption and a large decrease in the emission intensity; again with no significant changes in the spectral shape or any notable wavelength shifts (Figure 6.10), and the CCPs are extremely sensitive to quenching by guanine, as is apparent from the Stern-Volmer plots in Figure 6.11, and the data in Table 6.3.

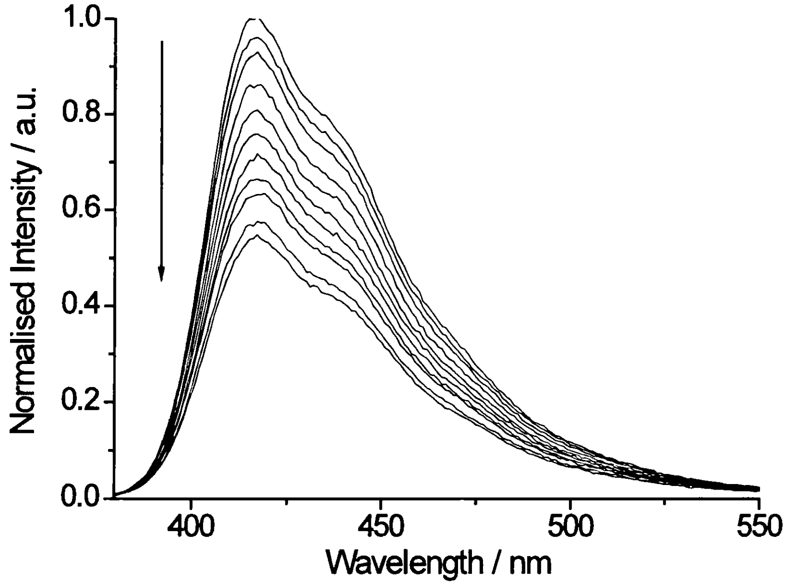

Figure 6.10 Decrease in CCP-M emission upon the addition of guanine (left).

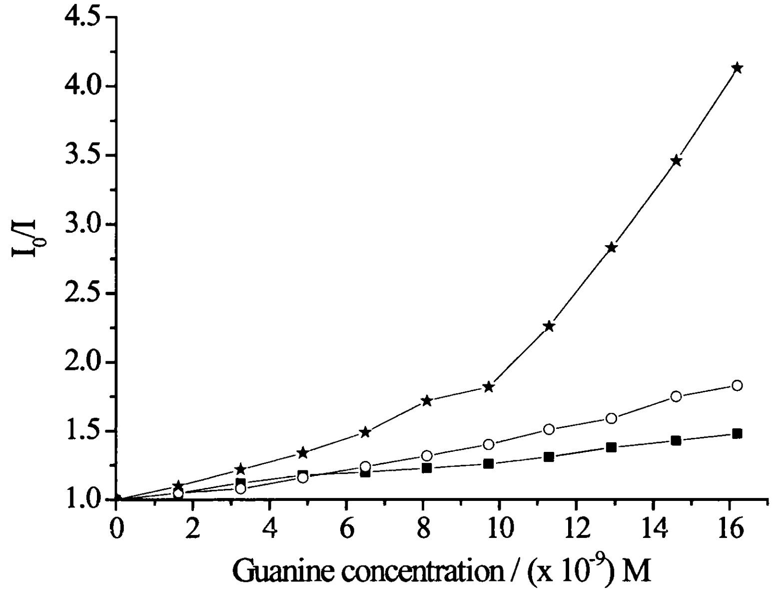

Figure 6.11 SV plots for all CCP-S (solid squares), CCP-M (open circles) and CCP-L (solid stars) with guanine as quencher.

Table 6.3 SV quenching constants for all CCPs with guanine, calculated from the initial linear region of the SV plots.

Polymer	Ksv/ $\times 10^7$ M^{-1} (± 2%)
CCP-S	2.7
CCP-M	4.2
CCP-L	8.8

Sensitivity towards guanine also increases with polymer chain length. However, quenching by guanine alone is not sufficient to account for the efficiency of quenching by T4 DNA. This can be easily seen when the SV data for both dsDNA and ssDNA is given in terms of the guanine concentration, as is shown in Figure 6.12.

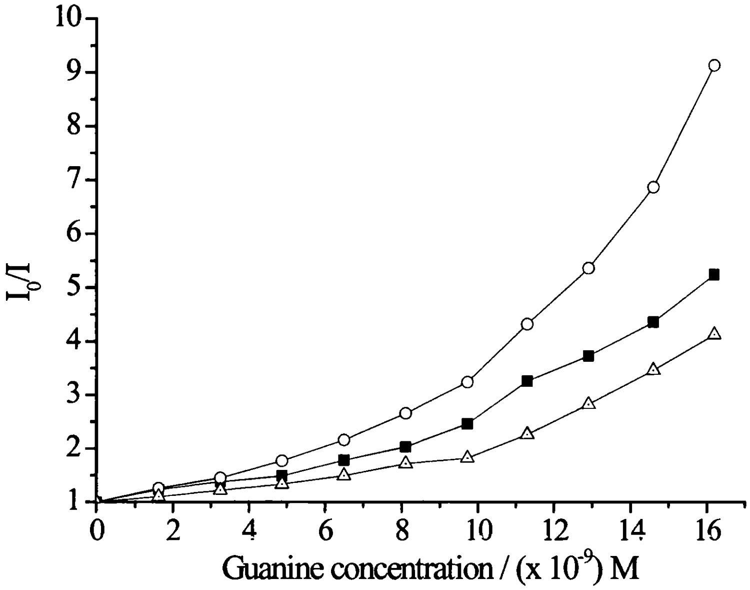

Figure 6.12 Stern-Volmer plots for CCP-L with dsDNA (solid squares), ssDNA (open circles) and guanine (open triangles). (Note that for DNA concentrations are given in terms of guanine present).

For comparison purposes the quenching effect of the other DNA bases, adenine, thymine and cytosine, was studied. For direct comparison with the quenching effect of guanine concentrations of the bases were the same as the guanine concentration range studied. Table 6.4 collects the SV quenching constants of all DNA bases with CCPs; SV plots are given in Figure 6.13. All DNA bases quench CCP-S efficiently, with guanine being the most efficient; presumably this explains the efficiency of DNA as a quencher. Since guanine shows the greatest quenching effect additional experiments into the nature of the quenching mechanism focused on the use of guanine along with dsDNA and ssDNA.

Table 6.4 SV quenching constants for CCP-S with the DNA bases, calculated from the initial linear region of the SV plots.

DNA Base	Ksv/ ×10^7 M^{-1} (± 5%)
Guanine	2.7
Cytosine	0.8
Adenine	1.3
Thymine	1.4

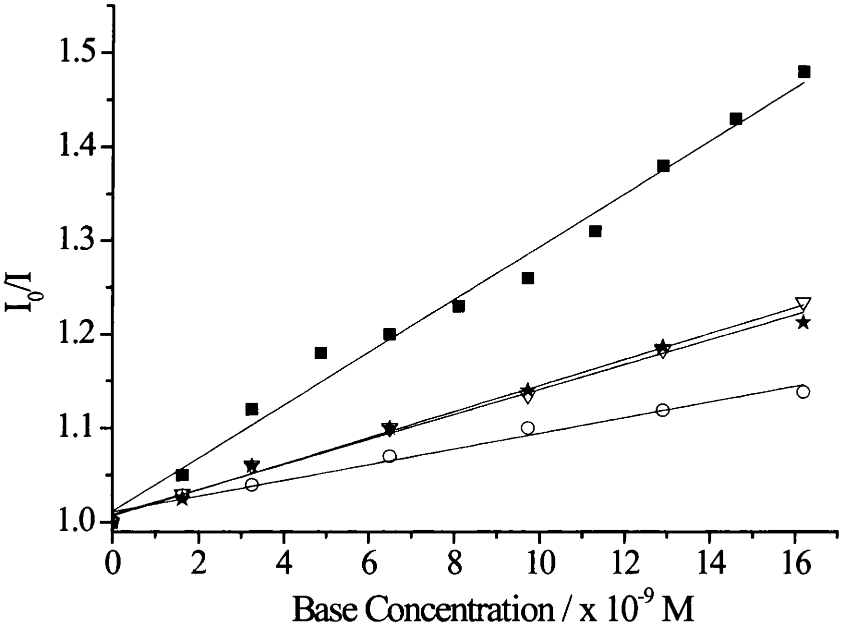

Figure 6.13 SV plots for CCP-S with guanine (solid squares), cytosine (open circles), adenine (open triangles) and thymine (solid stars).

6.3.4.2 Time resolved emission of CCP/guanine systems

Normalised time resolved emission decays with increasing guanine concentration for CCP-L are given in Figure 6.13 with the corresponding data, from fitting to three exponentials, given in Table 6.4. The data show the same trend to that found with T4 DNA as a quencher; i.e. the lifetimes of short and long lifetime components remain relatively constant and that of the middle lifetime component decreases. The fractional contribution to the longest lifetime decreases with increasing guanine concentration; again indicating the removal of isolated polymer chains. All the evidence suggests that guanine and DNA quench via the same mechanism.

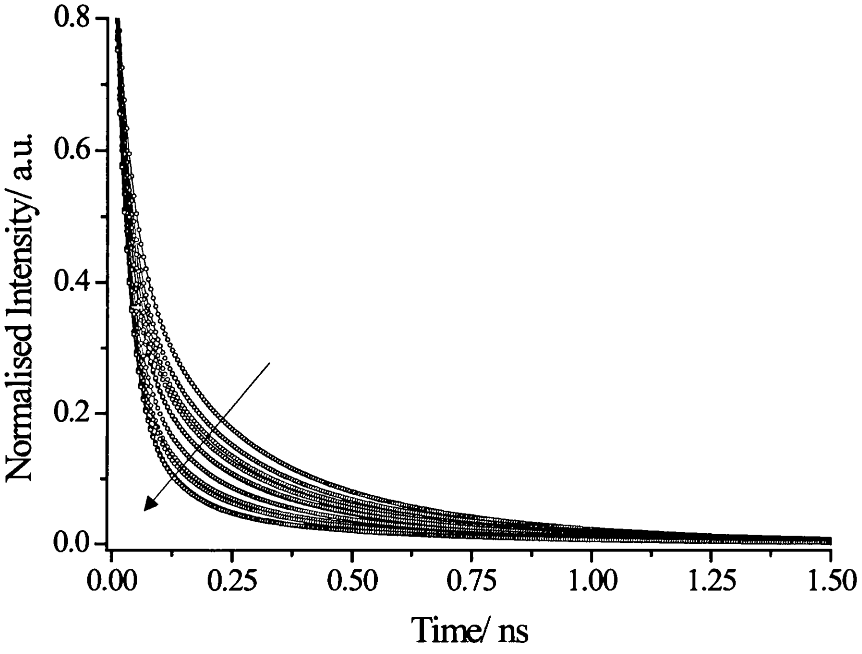

Figure 6.13 Normalised time resolved emission decay curves for CCP-L upon the addition of guanine. The arrow indicates increasing guanine concentration.

Table 6.4 Time resolved data for CCP-L upon the addition of guanine.

Guanine Concentration / × 10^{-9} M	a_1	τ_1/ ps	a_2	τ_2/ ps	a_3	τ_3/ ps	τ_{ave} / ps
0	0.49	32	0.27	139	0.24	421	312
1.62	0.54	31	0.25	133	0.20	420	301
3.25	0.58	31	0.24	131	0.18	421	291
4.87	0.59	30	0.24	126	0.16	420	284
6.49	0.62	29	0.24	120	0.14	420	273
8.10	0.64	31	0.22	124	0.14	425	276
9.72	0.66	28	0.22	111	0.11	423	259
11.34	0.73	29	0.19	112	0.09	427	240
12.95	0.73	29	0.20	105	0.08	431	231
14.56	0.73	28	0.21	92	0.06	430	209
16.17	0.72	27	0.22	88	0.06	432	211

The Stern-Volmer type plots using average lifetimes are shown in Figure 6.14. Again the same trend is seen as the SV data calculated from the steady state results (Figure 6.11). However the results have slightly different quenching rates and as a result of this the data do not sit on top of each other, the only difference between the samples is the concentration of the CCPs.

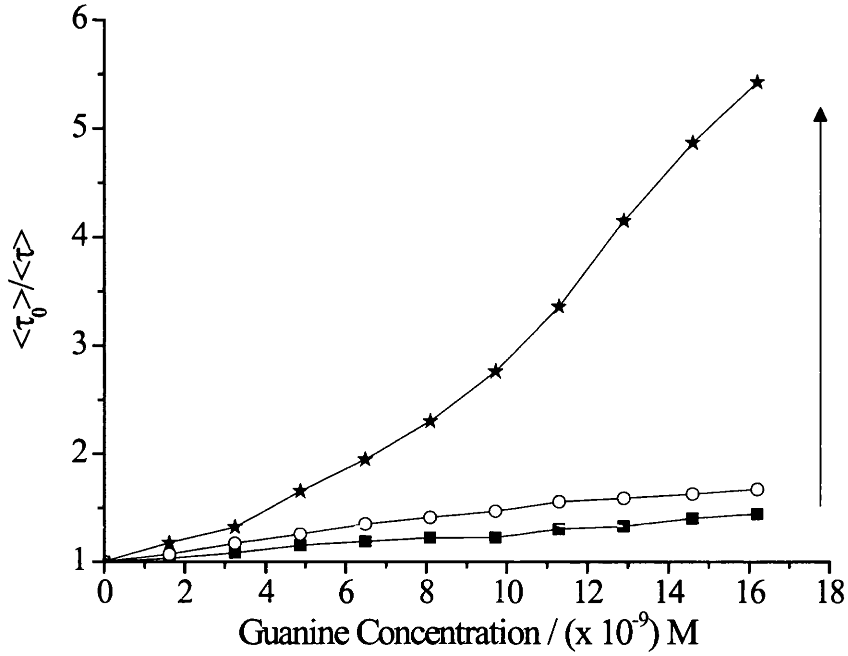

Figure 6.14 Quenching plot from the changes in the time resolved average lifetimes with increasing guanine concentration. The arrow indicates increasing CCP length, the increase in sensitivity to quenching from CCP-S (solid squares) to CCP-L (solid stars) is evident.

6.3.4.3 Modelling guanine quenching of CCP-L

Attempts have been made to model guanine quenching of CCP-L using ProgClusters (described in Chapter 4). Initially the quenching was modelled by adding a number of link traps equal to the concentration of guanine (Figure 6.15). Attempts to model guanine quenching by incorporation of guanine just as additional traps fail. However, as already discussed, time resolved studies suggest that at least one of the quenching mechanisms by which guanine acts involves removing isolated chains (figure 6.15(b)) presumably by an increase in aggregation and thus this increase in aggregation was accounted for by increasing the number of traps in ProgClusters and resulted in the fits shown by Figure 6.16. The increase in the number of traps was calculated from the fractional contribution to the longest lifetime, which we associate with isolated polymer chains, in the time resolved data.

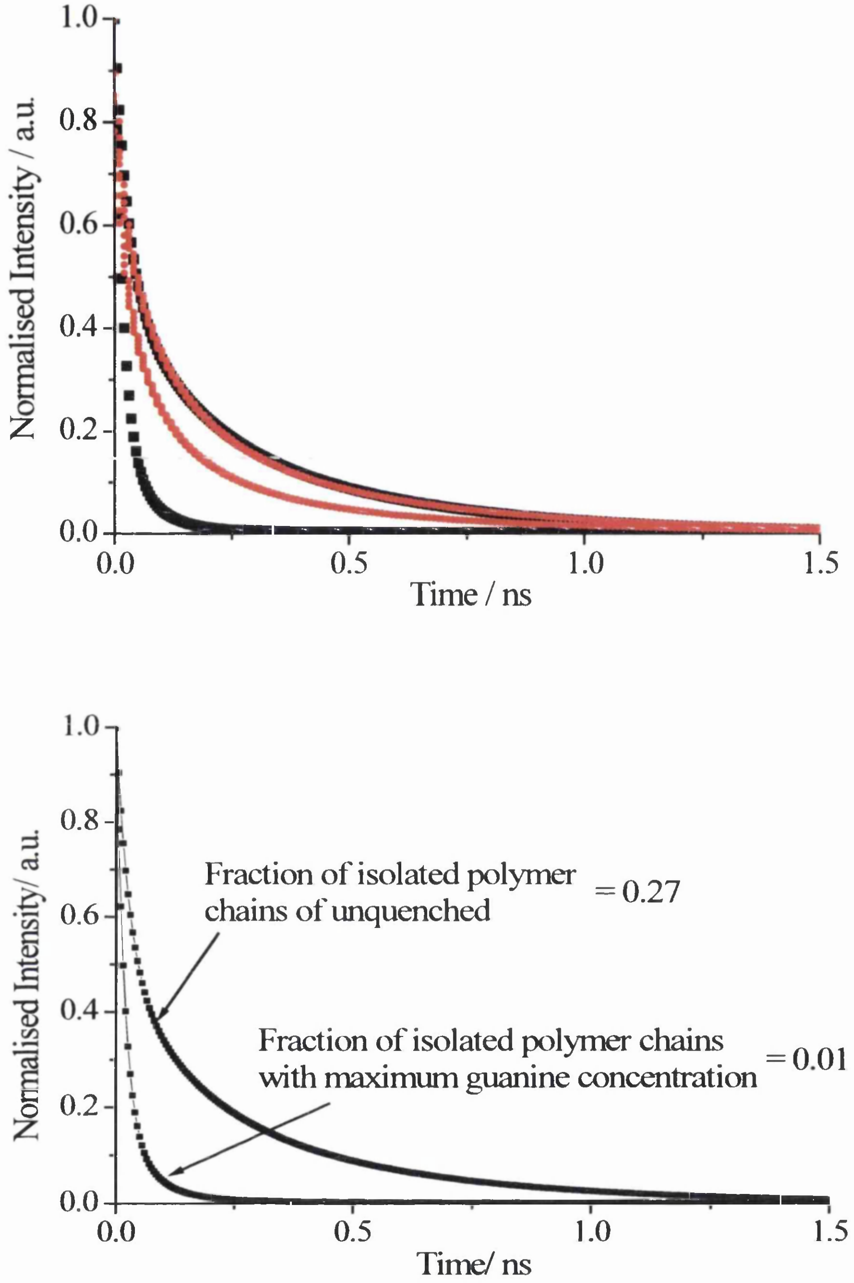

Figure 6.15 (a) Initial modelling of quenching of CCP-L by guanine via the simple addition of link traps equivalent to the guanine concentration where the black data points are experimental values and the red data points are modelled values. (b) Time resolved decays of CCP-L, and of CCP-L in the presence on the maximum guanine concentration studied. The time resolved values indicate that the quenching mechanism involves inducing aggregation in the CCP sample.

Modelling was then carried out on the basis that the role of guanine it to induce aggregation. The degree of aggregation at any guanine concentration was calculated from the fractional contribution of the long lifetime component, in the same way as was used for the aggregation studies as described in Chapter 4.

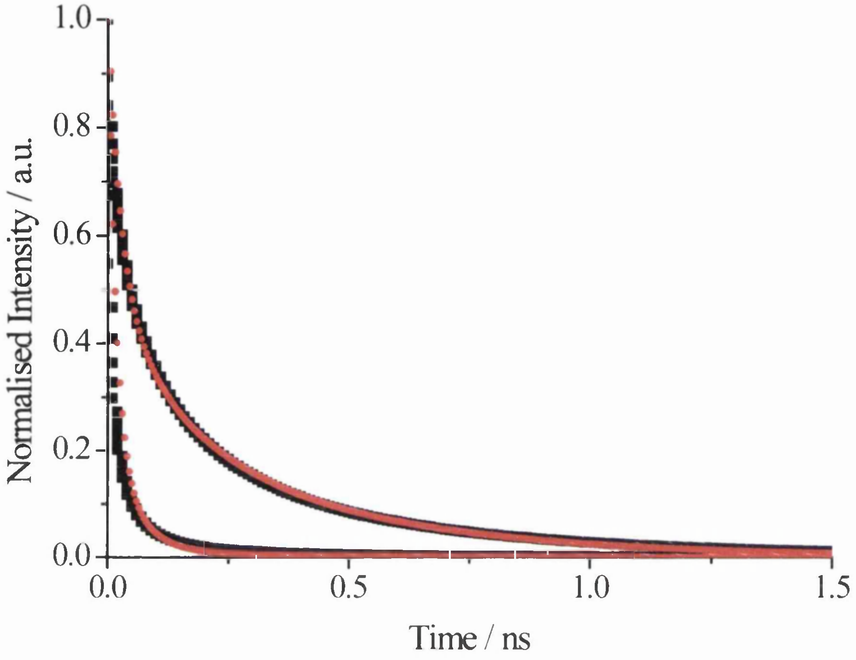

Figure 6.16 Time resolved decays curves for CCP-L with and without guanine (black) and modelled decay curves (red). The fraction of links that were required to be trap sites in order to get a good data fit was 0.75.

This fit results in a rate constant for unquenched decay of 3.0×10^{9} and a rate constant for both energy transfer between monomers and from monomers to link-traps of 1.44×10^{13} s^{-1}. This can be compared to CCP-L with no guanine present where the rate constant for both energy transfer between monomers and from monomers to link-traps is 6.2×10^{12} s^{-1}. This explains the efficiency CCP quenching by guanine, in the presence of guanine the rate of energy transfer from monomer to monomer and from monomer to trap roughly doubles. This increase in the rate of energy into trap sites, as well as the increased number of trap sites due to induced aggregation quenches the system extremely efficiently. Although further systems need to be modelled in order to gain more information of the quenching process, this initial modelling work shows great promise and is capable of generating the general kinetic features of the quenching.

6.3.5 Quenching of CCPs; energy migration into trap sites

It was thought that the curvature of the SV plots may indicate non-competitive quenching i.e. on average each quencher quenches a fixed number of monomer units independent of any other quencher present. This is supported by the linearity of a plot of quantum yield against quencher concentration, an example of which is shown in Figure 6.17.

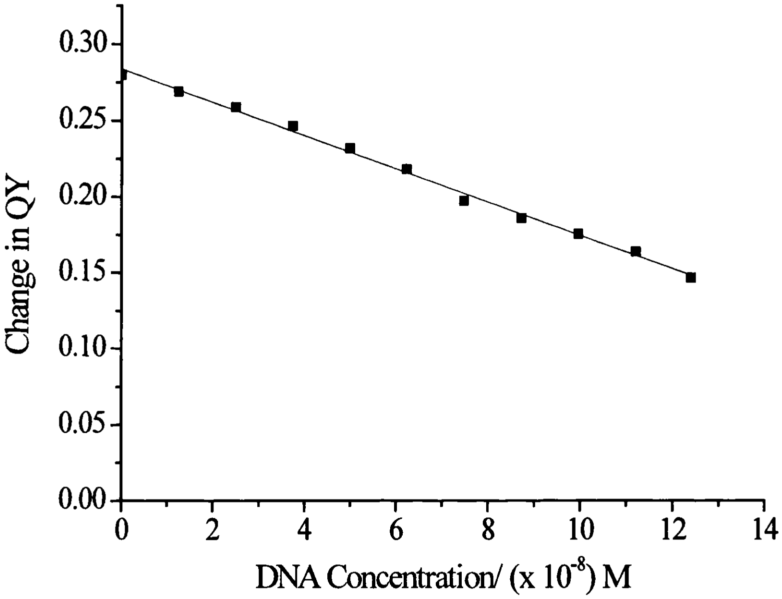

Figure 6.17 Change in quantum yield of CCP-S upon the addition of T4 dsDNA.

The quantum yield can be equated with the number of unquenched monomer units (Equation 6.2).

$$[M_u] = \frac{QY[CCP]}{QY_0} \qquad [6.2]$$

Where $[M_u]$ is the concentration of unquenched monomer, QY is the quantum yield, QY_0 is the quantum yield without any quencher present and [CCP] is the concentration of CCP in terms of monomer units. Using this gives a plot where the slope of the line is equal to the number of monomers quenched by each quencher (examples are shown in figures 6.18 and 6.19).

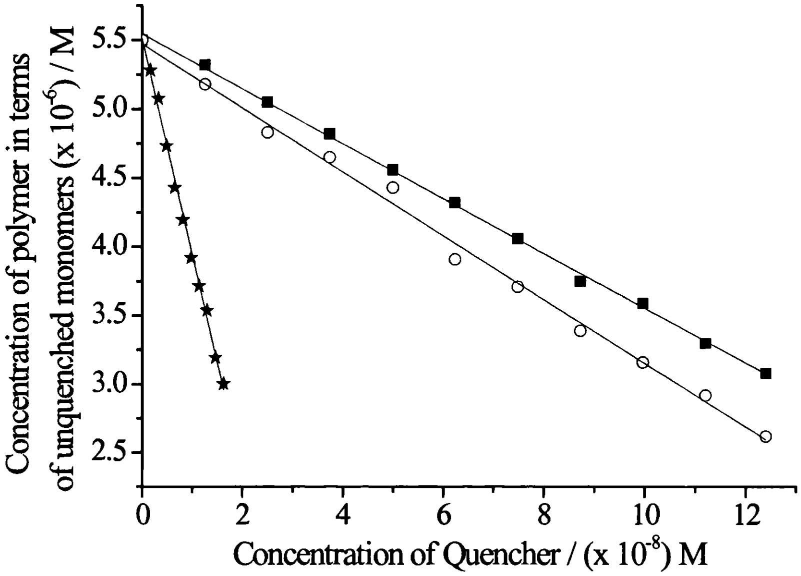

Figure 6.18 Decrease in the number of unquenched monomer units of CCP-M with dsDNA (solid squares), ssDNA (open circles) and guanine (solid stars). The DNA concentration is in terms of base pairs.

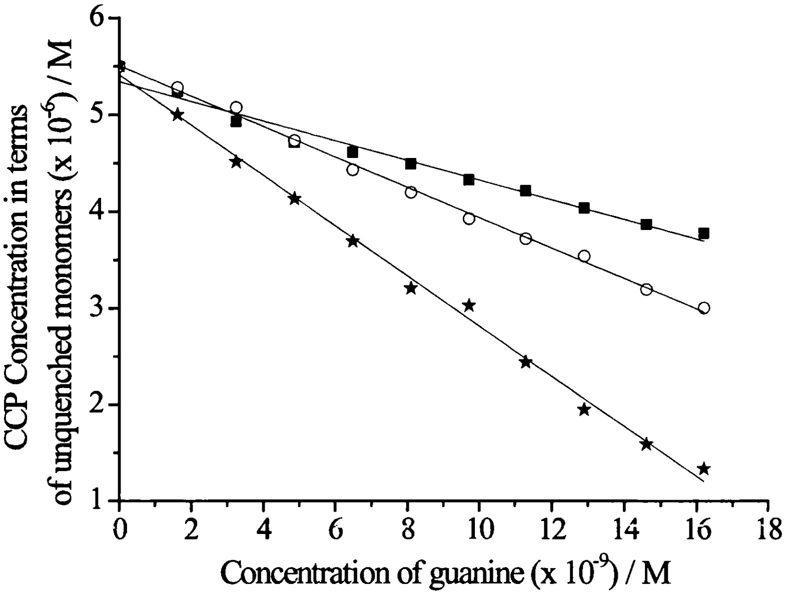

Figure 6.19 Decrease in number of unquenched monomer units for all CCP-S (solid squares), CCP-M (open circles) and CCP-L (solid stars) with guanine.

The number of monomers quenched by each quencher is given in Table 6.5. This increases in the order dsDNA>ssDNA>guanine.

Table 6.5 Number of repeat units quenched by each quencher where the 'quencher unit' refers to a DNA base pair or a guanine molecule.

Polymer	Number of monomers quenched by each 'quencher unit'		
	dsDNA (per base pair)	ssDNA (per base pair)	Guanine
CCP – S	24	31	49
CCP – M	36	37	161
CCP - L	101	117	354

The table shows that each quencher, in particular guanine, has access to a large number of monomers. The results are consistent with the previous results in that ssDNA is a more effective quencher than dsDNA and both are more effective on a per guanine basis than free guanine. There are two processes required to allow each quencher unit access to a large number of repeat units: (i) energy transfer along and between polymer chains (ii) induced aggregation by the quencher. Hence the high SV quenching constants arise from "aggregate energy migration quenching" in which CCP and DNA, or guanine, form an aggregate complex in which excitation energy migrates between and along the polymer chains until it is quenched at an aggregate, or DNA or guanine, "trap".

6.3.6 Quenching of CCPs with ST DNA

In order to determine the effect of DNA chain length on the quenching of the CCPs shorter stranded ST DNA was also used. ST DNA is roughly 60 times shorter than T4 DNA. Stern-Volmer plots resulting from the quenching experiments are again non-linear, with sensitivity to quenching increasing with chain length. The SV quenching constants, along with those for T4 DNA for comparison are given in Table 6.6.

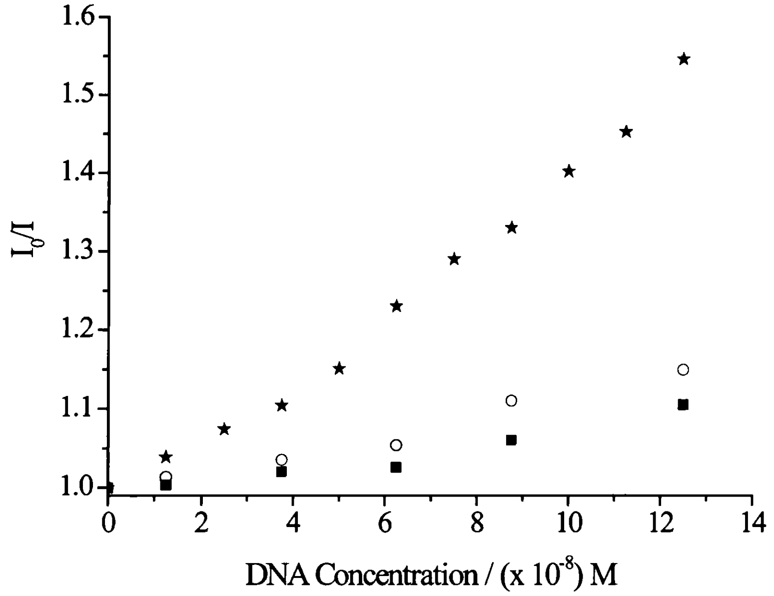

Figure 6.20 SV plots for all CCP-S (solid squares), CCP-M (open circles) and CCP-L (solid stars) with low concentration ST DNA.

Table 6.6 Comparison of SV constants for T4 DNA and ST DNA.

Polymer	Stern-Volmer Constant for T4 DNA / $\times 10^6$ M^{-1}	Stern-Volmer Constant for ST DNA / $\times 10^6$ M^{-1}
CCP-S	4.72	0.8
CCP-M	6.41	1.2
CCP-L	18.3	14.3

As can be seen in Table 6.6 the long chain T4 DNA is more than 5× more efficient quencher than the shorter stranded ST DNA for the shorter polymers (CCP-S and CCP-M) where as the difference is less for the longer CCP-L. This is most likely to be due to electrostatic effects, although the number of charges in the solution and the charge density per unit length of DNA are the same for both types of DNA the number of charges per chain is much higher for T4 DNA. Emission spectra show a broadening and decrease in fluorescence with increasing DNA concentration, along with a gradual slight red shift in the wavelength of maximum emission. Maximum wavelength shifts upon quenching are CCP-S ~ 4 nm, CCP-M ~ 6 nm and CCP-L ~ 10 nm. All of the aggregates irrespective of the polymer length have the same emission maximum whereas the emission maxima for the free polymers for CCP-S, CCP-M and CCP-L are all slightly different.

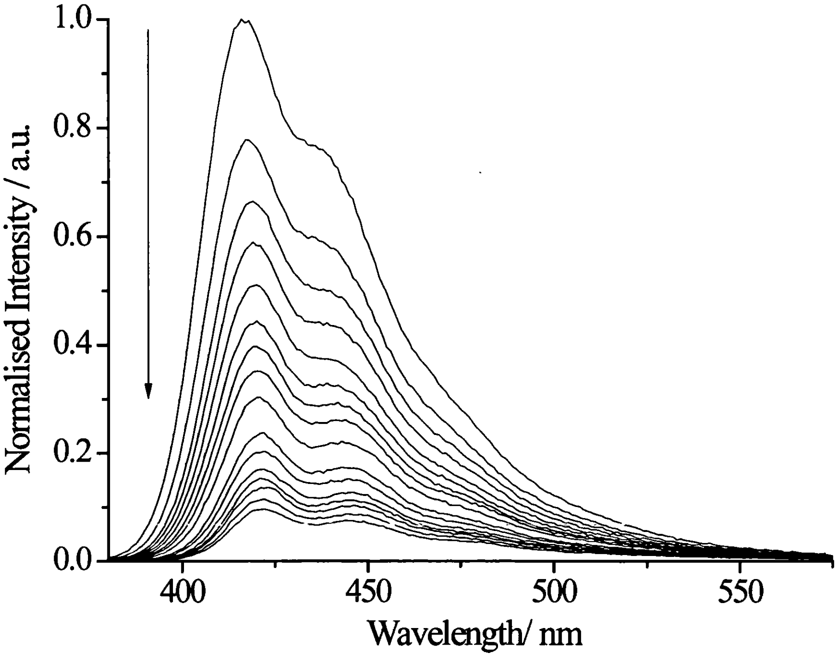

Figure 6.21 Decrease of CCP-S emission upon the addition of ST dsDNA.

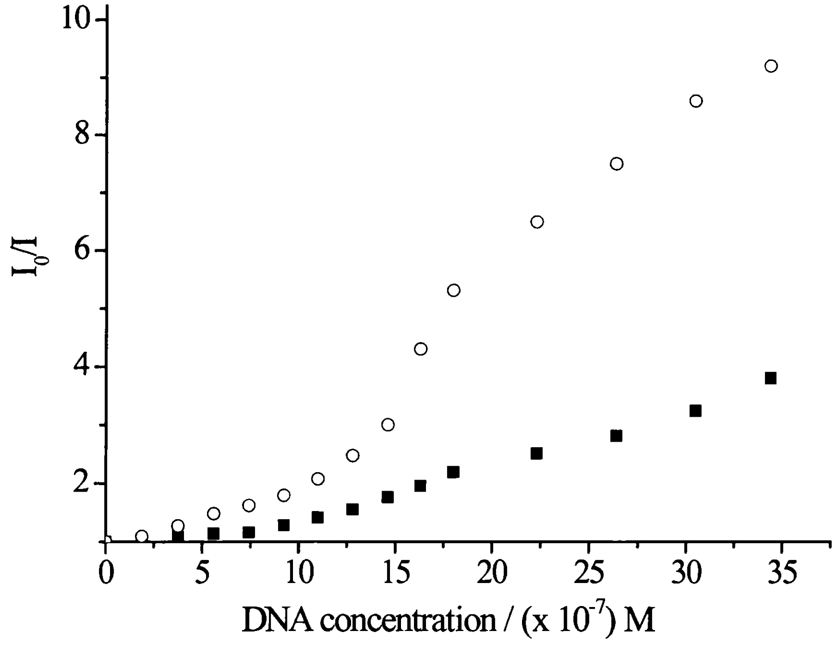

Figure 6.22 SV plots for the quenching of CCP-M fluorescence with both ST dsDNA (solid squares) and ST ssDNA (open circles).

As can be seen in Figure 6.22, as is the case for T4 DNA, ssDNA is a better quencher than dsDNA. .

6.3.6.1 Time resolved emission

The normalised time resolved decays decrease with increasing ST DNA concentration as shown for CCP-L in Figure 6.23, with the corresponding kinetic parameters for a three exponential fit are given in Table 6.7. Again the fractional contribution from the longest lifetime decreases with increasing quencher concentration However there is a difference in the lifetimes upon quenching for ST DNA as compared to T4 DNA, in that for T4 DNA the short and long lifetime components remain relatively constant and the middle lifetime component decreases, whereas for ST DNA all three lifetime gradually decrease on increasing the quencher concentration. Again this is most likely due to electrostatic effects with T4 DNA having few long highly charged chains while for ST DNA there are more shorter, less highly charged chains.

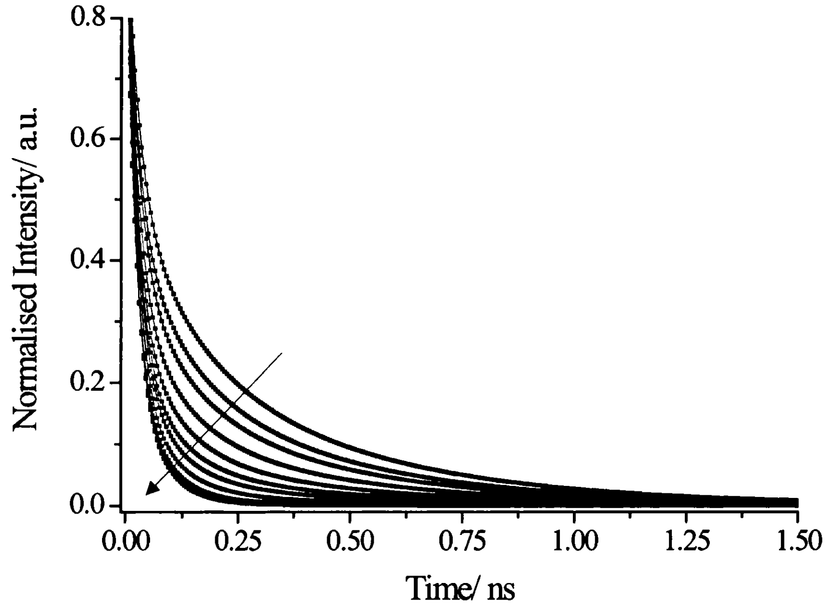

Figure 6.23 Normalised time resolved emission decay curves for CCP-L upon the addition of ST dsDNA. The arrow indicates increasing DNA concentration.

The quenching plots for the time resolved values are also non-linear and appear sigmoidal, with ST ssDNA giving higher quenching constants than ST dsDNA. This is shown in Figure 6.24.

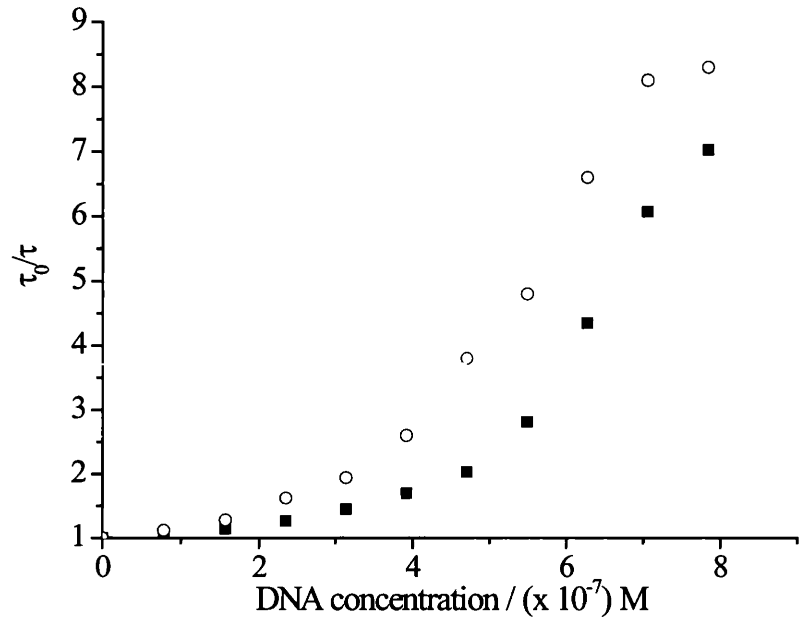

Figure 6.24 Quenching plot from the time resolved data where the change in average lifetime is plotted against the quencher concentration for CCP-L with both dsDNA (solid squares) and ssDNA (open circles).

Table 6.7 Time resolved data for CCP-L upon the addition of ST DNA.

Concentration of ST DNA / × 10^{-7} M	a_1	τ_1/ ps	a_2	τ_2/ ps	a_3	τ_3/ ps	τ_{ave} / ps
0	0.48	29	0.23	138	0.29	424	337
0.78	0.54	27	0.24	133	0.22	422	313
1.57	0.60	28	0.22	131	0.18	419	295
2.35	0.65	26	0.22	116	0.13	413	266
3.14	0.69	24	0.22	102	0.09	408	233
3.92	0.73	25	0.21	98	0.06	408	198
4.70	0.75	24	0.21	90	0.04	405	166
5.49	0.77	23	0.21	82	0.02	402	120
6.27	0.73	20	0.26	66	0.01	383	77
7.06	0.75	21	0.25	63	0.003	396	55
7.84	0.74	20	0.25	61	0.002	367	48

6.3.7 Complexation quenching

The SV plots for all CCPs with ST DNA are sigmoidal rather than linear. SV quenching constants, calculated from the initial linear regions of the plots, are very high and given the short lifetime of the CCPs fluorescence, these quenching constants would give an apparent bimolecular quenching rate constant greater than the diffusion controlled limit for dynamic quenching. It is thought that DNA induces aggregation in CCPs and thus the high quenching constants arise from "energy migration quenching" in which CCP/DNA form an aggregate complex (which, in this case, retains some residual fluorescence) and where excitation energy migrates between and along the polymer chains until it is quenched at an aggregate or DNA "trap". It is commonplace in the literature to analyse the quenching of polyelectrolyte fluorescence by DNA in terms of the Stern-Volmer relationship, as has been done here, however, it seems more appropriate to treat the non-linear Stern-Volmer as a complexation equilibrium. For an equilibrium between lumophore L and quencher Q, forming the complex LQ, for which:

$$L+Q \rightleftharpoons LQ \qquad [6.3]$$

$$K=\frac{LQ_{eq}}{(L_{eq}.Q_{eq})} \qquad [6.4]$$

$$Q_t = Q_{eq} + LQ_{eq} \qquad [6.5]$$

where subscript eq refers to equilibrium concentrations; and t refers to the total concentration added, i.e. the sum of the free and bound concentrations of either lumophore or quencher, then the relationship between the total concentration of quencher, Q_t, and the resulting ratio of emission intensity, I_0/I, where I_0 is the emission intensity in the absence of quencher and I in the presence of quencher, is given by:

$$Q_t = [(\frac{I_0}{I})-1].\frac{1}{K}+L_t-\frac{L_t}{[\frac{I_0}{I}]} \qquad [6.6]$$

For the situation in which the complex formed between the lumophore and quencher (LQ) has an intrinsic fluorescence such that I never reaches zero:

$$Q_t = L_t[\frac{(I_0-I)}{(I_0-I_{LQ})}]+\frac{1}{K}[\frac{(I_0-I)}{(I_0-I_{LQ})}] \qquad [6.7]$$

Rather surprisingly, this analysis fits the data well for quenching by ST DNA, (Fig 6.25) with best fit equilibrium constants for CCP-S, K, of 8.4 (($\pm$1.2)$\times 10^6$ M^{-1} for dsDNA and 8.6 ($\pm$1.7)$\times 10^6$ M^{-1} for ssDNA, and a relative emission for the complex of 6%. Based upon this analysis figure 6.25(c) gives the calculated fractions of free DNA and polymer with increasing total DNA concentration.

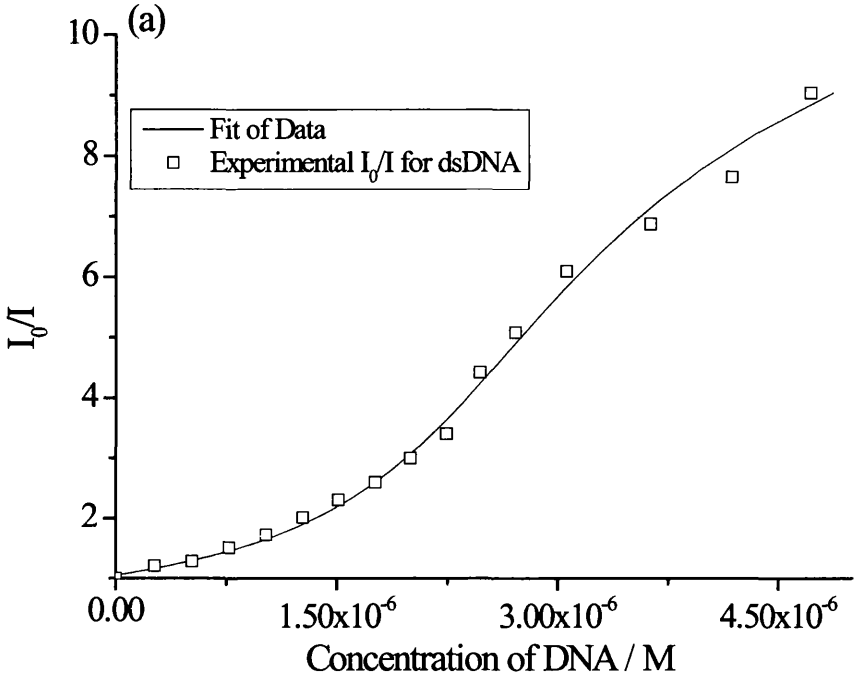
(a)
Fit of Data
Experimental I_0/I for dsDNA
I_0/I
10
8
6
4
2
0.00
$1.50x10^{-6}$
$3.00x10^{-6}$
$4.50x10^{-6}$
Concentration of DNA / M

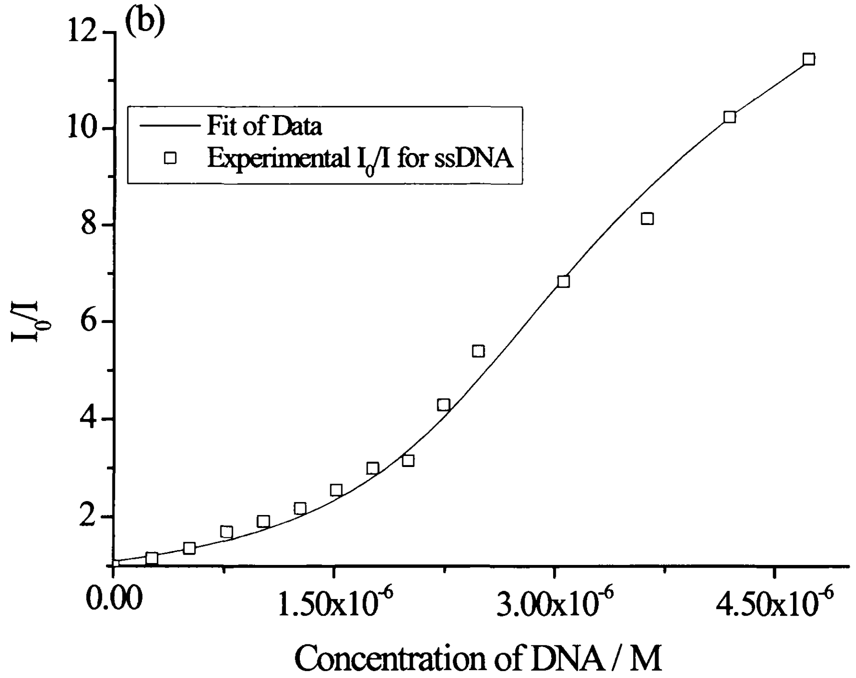
(b)
Fit of Data
Experimental I_0/I for ssDNA
I_0/I
12
10
8
6
4
2
0.00
$1.50x10^{-6}$
$3.00x10^{-6}$
$4.50x10^{-6}$
Concentration of DNA / M

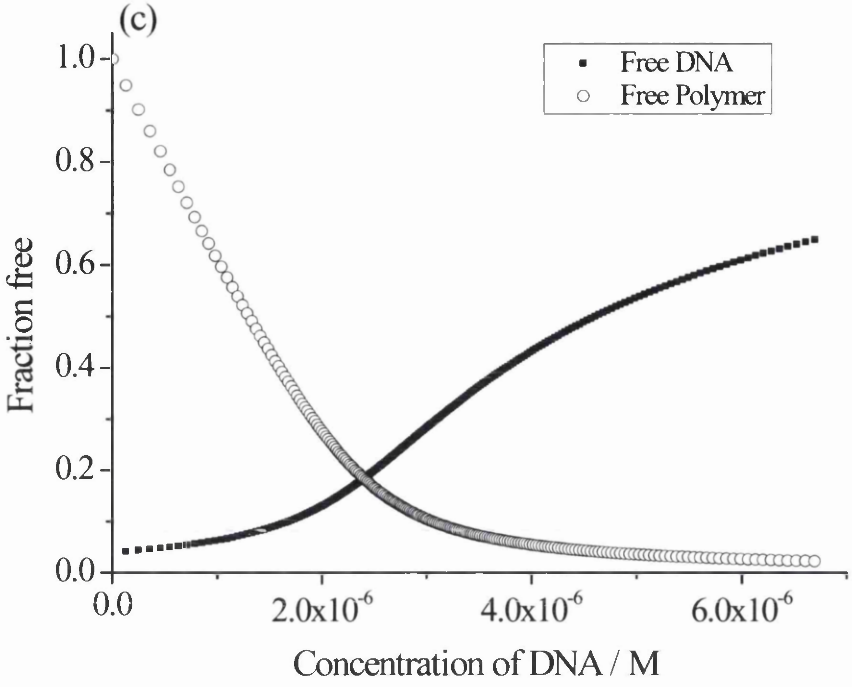

Figure 6.25 Stern-Volmer plots (open circles) for both dsDNA (a) and ssDNA (b) as quenchers with the fit of data treating the quenching as a complexation equilibrium as the solid line for the data set when quencher and lumophore concentrations are comparable. Plots of the change in the fraction of free polymer and free DNA present as a function of increasing total DNA concentration are shown in (c).

In the concentration range where there is a low fraction of free DNA each DNA strand complexes many polymer chains. Under these conditions two quenching mechanisms seem likely: 1) polymer-polymer aggregation quenching as association of polymer with the base pairs of the DNA brings polymer chains together and decreases the distance between adjacent polymers; 2) quenching by nucleic acid bases, particularly guanine. The latter mechanism is supported by the observation of efficient quenching by guanine in solution, although the mechanism for guanine quenching also seems to involve induced aggregation (work presented in Chapter 7 on transient absorption studies suggests that quenching by DNA or guanine is, at least in some aspects different from simple aggregation quenching). The residual emission from the aggregate complex is most likely not a specific product of the CCP/DNA complex but rather CCP emission which is not accessible for energy migration quenching.

6.3.8 Quenching of CCPs - concentration dependent quenching?

The complexation equilibrium treatment of the quenching data fits extremely well. The mechanism implies that quenching efficiency will be dependent on the concentration of CCP. Thus quenching experiments with three different polymer concentrations with fixed quencher concentrations were carried out. Figure 6.23 shows SV plots for the three CCPs at different CCP concentrations across similar DNA concentrations.

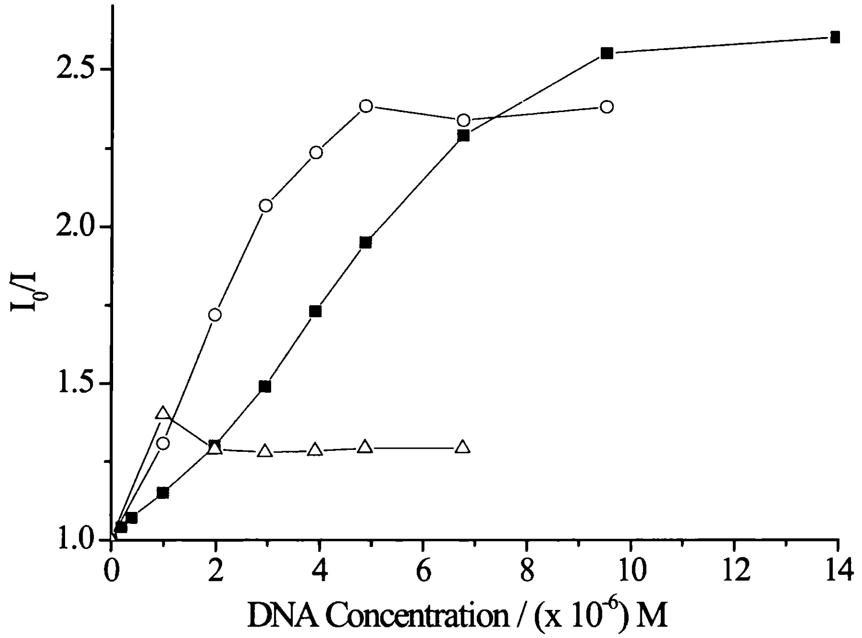

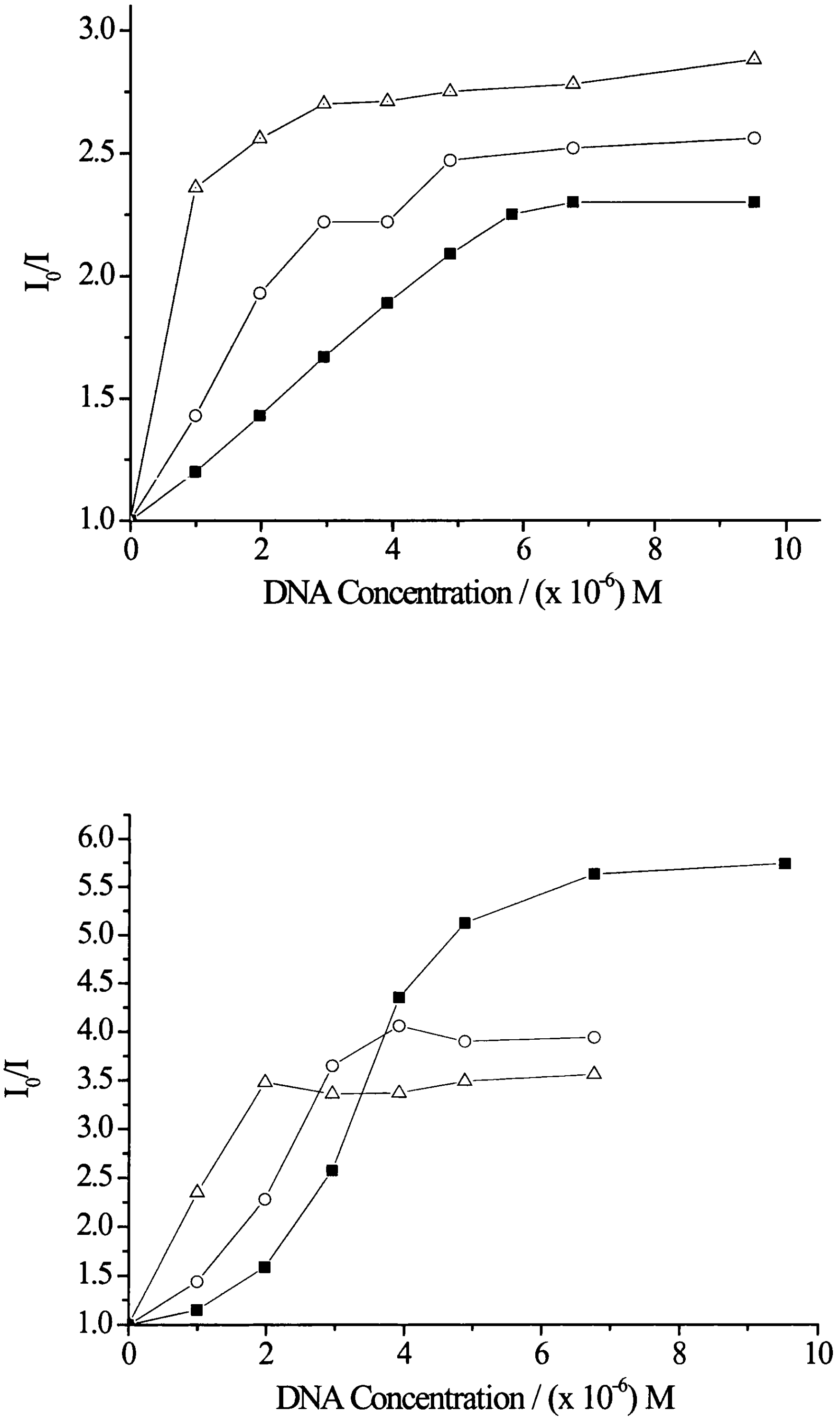

Figure 6.23 Dependence of quenching rates on CCP concentration, for CCP-S (top), CCP-M (middle)) and CCP-L (bottom) at CCP concentrations of 1×10^{-5} M (solid squares), 6×10^{-6} M (open circles) and 3×10^{-6} M (open triangles).

The quenching is clearly dependent on CCP concentration. In all cases the lowest CCP concentration has the highest initial K_{SV} (table 6.8), and at a [CCP] dependent critical concentration of quencher, which we will refer to as the complexation point, there is little change in emission intensity. Since electrostatic attraction between CCP and DNA is almost certainly a major factor in complexation the charge ratio at the complexation point is also tabulated in Table 6.8.

Table 6.8 Initial quenching rates and the charge ratio of the complexation point for all CCPs in this study at the stated CCP concentration.

Polymer	Polymer Concentration / 10^{-6} M	Initial K_{SV}/ M^{-1} (± 5%)	Charge Ratio of DNA/CCP at Complexation Point
CCP-S	3	4.0×10^5	0.15
	6	3.1×10^5	0.91
	10	2.0×10^5	2.88
CCP-M	3	1.4×10^6	0.28
	6	4.3×10^5	0.85
	10	2.0×10^5	2.90
CCP-L	3	1.4×10^6	0.21
	6	4.4×10^5	0.69
	10	2.3×10^5	2.10

The charge ratios at the point of complexation follow the same trend for each CCP. If we ignore the lowest concentration of CCP as this is the most difficult sample to accurately determine the precise complexion point, then CCP-L has the lowest charge ratios for the complexation point. Lower concentrations of DNA are needed to fully complex the CCP. There is no significant difference in these results between CCP-S and CCP-M.

6.3.9 Fluorescence anisotropy of dye/ DNA complexes

The effect of addition of DNA on the anisotropy of CCP-S and also, for comparison, two commercial dyes which bind to DNA, DAPI and YoYo-1 are shown in Figure 6.25.

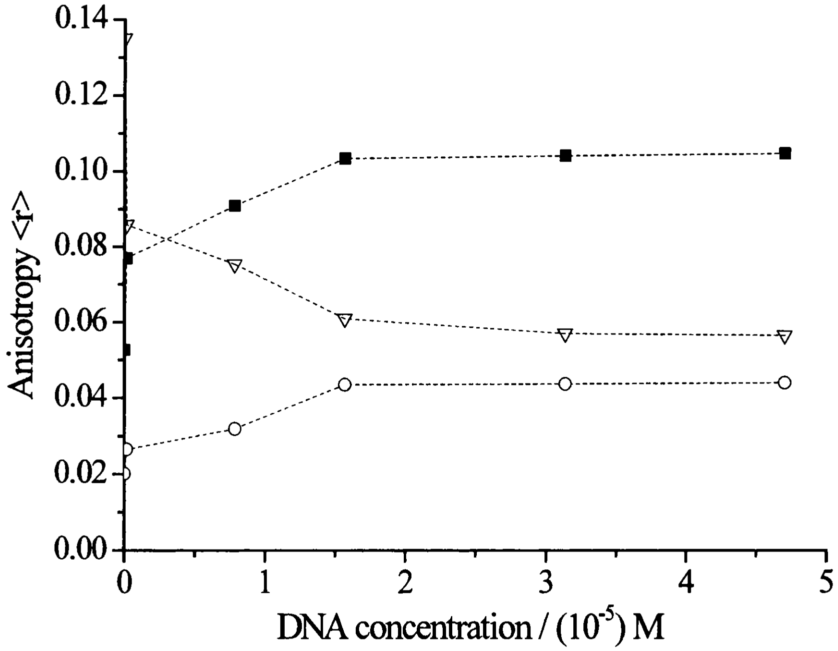

Figure 6.25 Change in anisotropy of DAPI (solid squares), YoYo-1 (open circles) and CCP-S (open triangles) with increasing DNA concentration. The concentrations of DAPI and YoYo-1 were 3.33×10^{-6} M and 4.16×10^{-6} respectively and the concentration of CCP-S was 4.89×10^{-6} M.

As expected, the anisotropy values of both DAPI and YoYo-1 increase as they bind to DNA and thus become incorporated in a large molecular unit with a lower tumbling rate. In contrast, the anisotropy of CCP-S decreases upon binding. This is strong evidence for interchain energy transfer in the CCP-S/DNA aggregate complex.

6.4 Conclusions

The CCPs used in this study are extremely sensitive to fluorescence quenching by dsDNA, ssDNA and guanine. For T4 dsDNA typical initial K_{SV} values are *ca.* 10^6-10^7 M^{-1}. Sensitivity to quenching increases with CCP chain length for example for the CCPs with T4dsDNA K_{SV} values increase from 4.72×10^6 M^{-1} for CCP-S to 1.83×10^7 M^{-1} for CCP-L. ssDNA is a more efficient quencher than dsDNA, this is most apparent in the case of CCP-L where, for T4 ssDNA, the K_{SV} values increases from 1.83×10^7 M^{-1} to 2.9×10^7 M^{-1}. T4 DNA is a more efficient quencher of CCP fluorescence than ST DNA with K_{SV} values being *ca.* 5 fold higher for T4 DNA for polymers CCP-S and CCP-M.

All SV plots for steady-state fluorescence quenching are non-linear and in some cases sigmoidal. Initial K_{SV} values are much higher than expected for the diffusion control limit and quenching is static rather than dynamic. The quenching mechanism is well modelled in terms of a complexation equilibrium in which a CCP/DNA aggregate complex is formed which brings polymer chains into close enough proximity to allow interchain excitation energy migration and quenching at aggregate or DNA base traps. The calculated equilibrium constants for CCP-S are 8.4×10^6 M^{-1} for dsDNA and 8.6×10^6 M^{-1} for ssDNA. The data shows that at low quencher concentrations each active quenching unit acts as an independent centre around which aggregation of the polymer can occur, and that each quenching unit acts as quencher for a large number of monomer repeat units – for CCP-L, which is the most sensitive to quenching typical values are *ca.* 100 monomers

Steady state fluorescence anisotropy of CCP-S decreases with increasing DNA concentration. This decrease in anisotropy is attributed to increased fluorescence depolarisation by interchain energy transfer in aggregate and CCP/DNA complexes. This is consistent with results presented in Chapter 4 where it was suggested that the mechanism for energy transfer through and along CCP chains is via rapid Forster mechanism.

The sensitivity of CCPs to quenching by DNA suggests they could find use as potential DNA sensors. The quenching mechanism has been shown to be well modelled using a complexation equilibrium. This understanding of the interaction and quenching mechanism may be useful in designing CCP based DNA sensors.

6.5 References

1. H. A. Al Attar and A. P. Monkman., *J. Phys. Chem. B,* **2007**, *111,* 12418-12426.
2. M. Leclere, *Adv. Mater.*, **1999**, *11*, 1491.
3. D. T. McQuade, A. E. Pullen and T. M. Swager, *Chem. Rev.*, **2000**, *100*, 2537.
4. J. Wang, D. Wang, E. K. Miller, D. Moses, G. C. Bazan and A. J. Heeger, *Macromolecules*, **2000**, *33*, 5153–5158.
5. S. Brent, A. J. Gaylord, Heeger, and G. C. Bazan, *PNAS,* **2002**, *99*, 1710954–10957.
6. Q. Zhou, T. M. Swager, *J. Am. Chem. Soc.,* **1995**, *117*, 7017–7018.
7. L. H. Chen, D. W. McBranch, H. L. Wang, R. Helgeson, F. Wudl, D. G. Whitten, *Proc. Natl. Acad. Sci. U.S.A.,* **1999**, *96*, 12287– 12292.
8. J. R. Lakowicz, in *Principles of Fluorescence Spectroscopy*, Plenum Press, New York, Springer, 3rd edn., **2006**.
9. X. Zhao, H. Jiang, and K. S. Schanze, *Macromolecules,* **2008**, *41*, 3422-3428.
10. D. L. Wang, J. Wang, D. Moses, G. C. Bazan, A. J. Heeger, *Langmuir,* **2001**, *17*, 1262–1266.
11. B. S. Gaylord, S. J. Wang, A. J. Heeger, G. C. Bazan, *J. Am. Chem. Soc.,* **2001**, *123*, 6417–6418.
12. L. H. Chen, D. McBranch, R. Wang, D. Whitten, *Chem. Phys. Lett.*, **2000**, *330*, 27–33.
13. C. Y. Tan, M. R. Pinto, K. S. Schanze, *Chem. Commun.*, **2002**, 446– 447.
14. C. Y. Tan, E. Alas, J. G. Muller, M. R. Pinto, V. D. Kleiman, K. S. Schanze, *J. Am. Chem. Soc.,* **2004**, *126*, 13685–13694.
15. C. H. Fan, S. Wang, J. W. Hong, G. C. Bazan, K. W. Plaxco, A. Heeger, J. *Proc. Natl. Acad. Sci. U.S.A.,* **2003**, *100*, 6297–6301.
16. D. T. McQuade, A. E. Pullen and T. M. Swager, *Chem. Rev.*, **2000**, *100*, 2537.
17. S. W. Thomas, G. D. Joly and T. M. Swager, *Chem. Rev.,* **2007**, *107*, 1339-1386.
18. K. E. Achyuthan, T. S. Bergstedt, L. Chen, R. M. Jones, S. Kumaraswamy, S. A. Kushon, K. D. Ley, L. Lu, D. McBranch, H. Mukundan, F. Rininsland, X. Shi, W. Xia and D. G. Whitten, *J. Mater. Chem.,* **2005**, *15*, 2648-2656.

19. Balakin, K. V., Korshun, V. A., Mikhalev, I. I., Maleev, G. V., Malakhov, A. D., Prokhorenko, I. A. & Berlin, Y. A. *Biosens. Bioelectron.,***1998**, *13,* 771–778.
20. S. B. Primrose, R. M. Twyman, Principles of Genome Analysis and Genomics, 3rd ed., Blackwell, Malden, MA **2003**, Ch. 1.
21. J. Wang, *Nucl. Acids Res*., **2000**, *28*, 3011.
22. D. Wang, X. Gong, P. S. Heeger, F. Rininsland, G. C. Bazan, A. J. Heeger, Proc. *Natl. Acad. Sci. USA*, **2002**, *99*, 49.
23. H. Peng, C. Soeller, T. Sejdic, *J. Chem. Commun.,* **2006**, 3735-3737.
24. H. A. Ho, K. Dore, M. Boissinot, M. G. Bergeron, R.M. Tanguay, D. Boudreau, M. Leclerc, *J. Am. Chem. Soc.,* **2005**, *127*, 12673-12676.
25. E. S. Baker, J. W. Hong, B. S. Gaylord, G. C. Bazan, M. T. Bowers, *J. Am. Chem. Soc.,* **2006**, *128*, 8484-8492.
26. H. A. Ho, M. Boissinot,M. G. Bergeron, G. Corbeil, D. Boudreau,M. Leclerc, *Angew. Chem. Int. Ed.,* **2002**, 41, 1548.
27. H. A. Ho, K. Dore, M. Boissinot, M. G. Bergeron, R. M. Tanguay, D. Boudreau, M. Leclerc, *J. Am. Chem. Soc.,* **2005**, *127*, 12673.
28. S. Wang, B. S. Gaylord, and G. C. Bazan, *J. Am. Chem. Soc.,* **2004**, *126*, 5446-5451
29. Q. H. Xu, B. S. Gaylord, S. Wang, G. C. Bazan, D. Moses, and A. J. Heeger, *Proc. Natl. Acad. Sci. U.S.A.,* **2004**, *101*, 11634-11639.
30. B. S. Gaylord, M. R. Massie, S. C. Feinstein, and G. C. Bazan, *Proc. Natl. Acad. Sci. U.S.A.,* **2005**, *102*, 34–39.
31. P. E. Nielson, M. Engholm, R. H. Berg, O. Burchardt, *Science*, **1991**, *254*, 1497.
32. M. Engholm, O. Burchardt, P. E. Nielson, R. H. Berg, *J. Am. Chem. Soc*., **1992,** *114,* 1895.
33. D. T. McQuade, A. H. Hegedus, T. M. Swager, *J. Am. Chem. Soc*., **2000**, *122*, 12389.
34. J. S. Yang, T. M. Swager, *J. Am. Chem. Soc.,* **1998**, *120*, 11864.
35. S. A. Kushon, K. Bradford, V. Marin, C. Suhrada, B. A. Armitage, D. McBranch, D. Whitten, *Langmuir,* **2003**, *19*, 6456.
36. S. A. Kushon, K. Ley, K. Bradford, R. M. Jones, D. McBranch, D. Whitten, *Langmuir*, **2002**, *18*, 7245.
37. M. L. Davies, P. Douglas, H. D. Burrows, M. G Miguel and A. Douglas. *Port. Electrochim. Acta*., **2009**, *27*, 525 – 531.

38. H. L. Dong, Z. Z. Qing, Y. Dong, F. Ying and X. Jin-Gou, *Analytica Chimica Acta,* **1999**, *389*, 85-88.
39. D. Freifelder and P. F. Davison, *Biophys. J.,* **1963,** *3*, 49-63
40. K. Yoshikawa, Y. Yoshikawa and T. Kanbe, *Chem. Phys. Lett.,* **2002,** *354*, 354–359.
41. G. Cosa, K. S. Focsaneanu, J. R. N. McLean, J. P. McNamee, J. C. Scaiano, *Photochem. Photobiol.,* **2001,** *73*, 585-599.
42. R. P. Haugland, *Molecular Probes. Handbook of Fluorescent Probes and Research Chemicals,* 5th ed., Molecular Probes, Inc., Eugene, Oregon, **1992.**
43. A. N. Glazer and H. S. Rye, *Nature,* **1992**, *359*, 859-861.
44. I. N. Gadjev, G. T. Deligeorgiev, I. Timcheva and V. Maximova, *Dyes and Pigments*, **2003**, *57*, 161-164.
45. M. L. Davies, H. D. Burrows, M. C. Morán, M. G. Miguel and P. Douglas, *Biomacromolecules*, **2009**, *10*, 2987–2997.
46. M. D. Evans and M. S. Cooke, *Oxidative Damage to Nucleic Acids*, Springer New York, **2007**.
47. H. Xie, D. Yang, A. Heller, and Z. Gao, *Biophys. J.,* **2007**, *92,* 70–L72.

Chapter 7

Flash Photolysis Study of CCP/DNA and CCP/Guanine Interactions

7.1 Introduction

This chapter describes results from a flash photolysis study of the interaction of the three CCPs with dsDNA, ssDNA and guanine. Flash photolysis was developed by Eigen, Norrish and George Porter in 1949 and since then flash photolysis has become one of the principal techniques in detecting short-lived transient species.[1,2] However, it is interesting to note that the triplet states of fluorene based conjugated polymers have generally been studied by pulse radiolysis,[3,4,5] which is a higher energy generally less specific method.[4] This is because ISC in similar systems has been shown to be inefficient and thus direct optical excitation does not generate triplet states in significant yields.[5] In this chapter results from a ns flash photolysis study of CCPs alone and CCPs in the presence of DNA and guanine are presented. The experiments were carried out in order to determine if electron transfer was a possible quenching mechanism and also to see if any radical species, either from the CCPs or from the guanine (both free and in DNA), were produced. Guanine radical species have reported transient absorption bands at 310 and 390 nm.[6] PF radical transient absorption bands occur at 580 and 600 nm for the cationic and anionic forms respectively.[4]

7.1.1 Aims of this study

In order to gain further information on the nature of the quenching mechanism by which DNA and guanine quench CCPs the ns flash photolysis transient absorption of CCPs alone and in the presence of either DNA or guanine was investigated. The kinetic and spectral transient properties of the CCPs are investigated and the effect that DNA and guanine has on transient states is discussed.

7.2 Experimental

7.2.1 Materials

All CCPs are described in Section 4.2.1 and most CCP samples were dissolved in 25/75 acetonitrile/water (v/v) to minimise aggregation. The only exception to this is for CCP-S where the effect of the acetonitrile concentration was also investigated. ST DNA (refer to Section 5.2.1) was purchased from Sigma Aldrich and used as received. Acetonitrile was of spectroscopic grade. All experiments were performed using Millipore Milli-Q deionised water.

7.2.2 Equipment and methods

Nanosecond flash photolysis experiments were carried out using 355 nm radiation from a frequency tripled Nd/YAG laser (Spectra Physics) with an Applied Photophysics Laser Kinetic Spectrometer (as described in Section 2.4.3). Samples were contained in 1 cm square cells and the transmission monitored at 90 degrees to the excitation pulse over the wavelength range 200 to 700 nm. 5 nm slits were used. Table Curve^{TM} 2D version 3 (Jandel Scientific) was used for the kinetic and equilibrium analysis curve fitting.

7.2.2.1 Aggregation studies

A 5.2×10^{-5} M (in terms of the repeat unit of the polymer) stock solution of CCP-S was prepared in water and stirred for 24 hours. 100 μl aliquots of the stock solution were then added, individually, to 5 ml volumetric flasks using a micro–pipette and made up to 5 ml with 1, 5, 10, 15, 20, 25 or 30% acetonitrile/water (v/v). (The 100 μl aliquots of stock solution were also weighed to ensure the weights were within ± 0.0001 g). The transient absorption spectrum was then recorded from 200-700 nm; the sample volume was 2.50 ml in 1 cm quartz cells.

7.2.2.2 Transient absorption of CCPs in the presence of DNA and guanine

ST dsDNA solutions were prepared by adding ST dsDNA mother solution to tris-HCl base buffer, pH = 7.8, to give the required concentrations; these cover the range 0-

7×10^{-6} M in terms of base pairs. (Unless otherwise stated all DNA concentrations are in terms of base pairs.) The ssDNA solution was prepared as described in Chapter 6. Denaturing the dsDNA solutions means that the concentration of both solutions, dsDNA and ssDNA, were the same in terms of base units. Guanine concentrations covered the range 0-1×10^{-6} M. Solvent mixtures are given as v/v. Absorption measurements were made using a Shimadzu UV-2100 spectrophotometer.

7.3 Results

7.3.1 Transient absorption of CCPs

All the CCPs studied show an intense relatively shorted lived (τ~10 ns) transient absorption between 400–500 nm and a broad unstructured relatively long lived (τ *ca.* 0.10 μs) transient absorption across the wavelength range studied (200–700 nm) (Figures 7.1 and 7.2). For convenience these two transients will, from now on, be referred to as **TS$_f$** and **TS$_s$**. The decay of **TS$_f$** is complete within ~70 ns after the laser pulse. It is impossible to say definitively whether **TS$_f$** is a precursor to **TS$_s$**, or whether both are produced simultaneously. However if it is a precursor the absorption of both transients must be very similar across both the 200-380 nm and 520-700 nm ranges which is unlikely, and for this reason we assume the transients to be two independent species which are both formed within the excitation pulse and subsequently decay independently. It is a surprise that there is no transient depletion of absorbance around the abs$_{max}$ of the CCPs at *ca.* 375 nm, although there is generally a minimum in the transient absorption spectra around this wavelength.

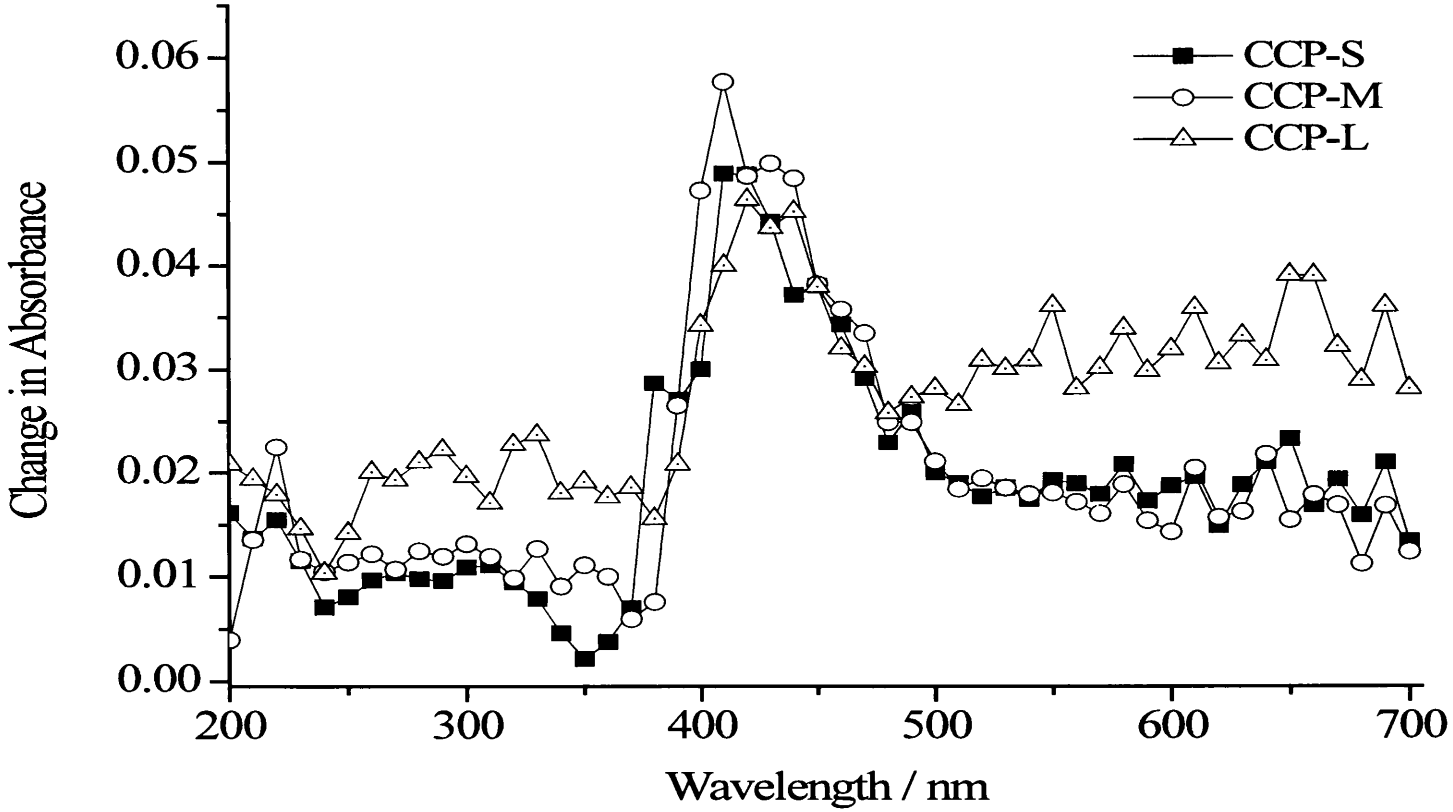

Figure 7.1 Transient absorption spectra of CCP-S (squares), CCP-M (circles) and CCP-L (triangles) at 47 ns after the laser pulse.

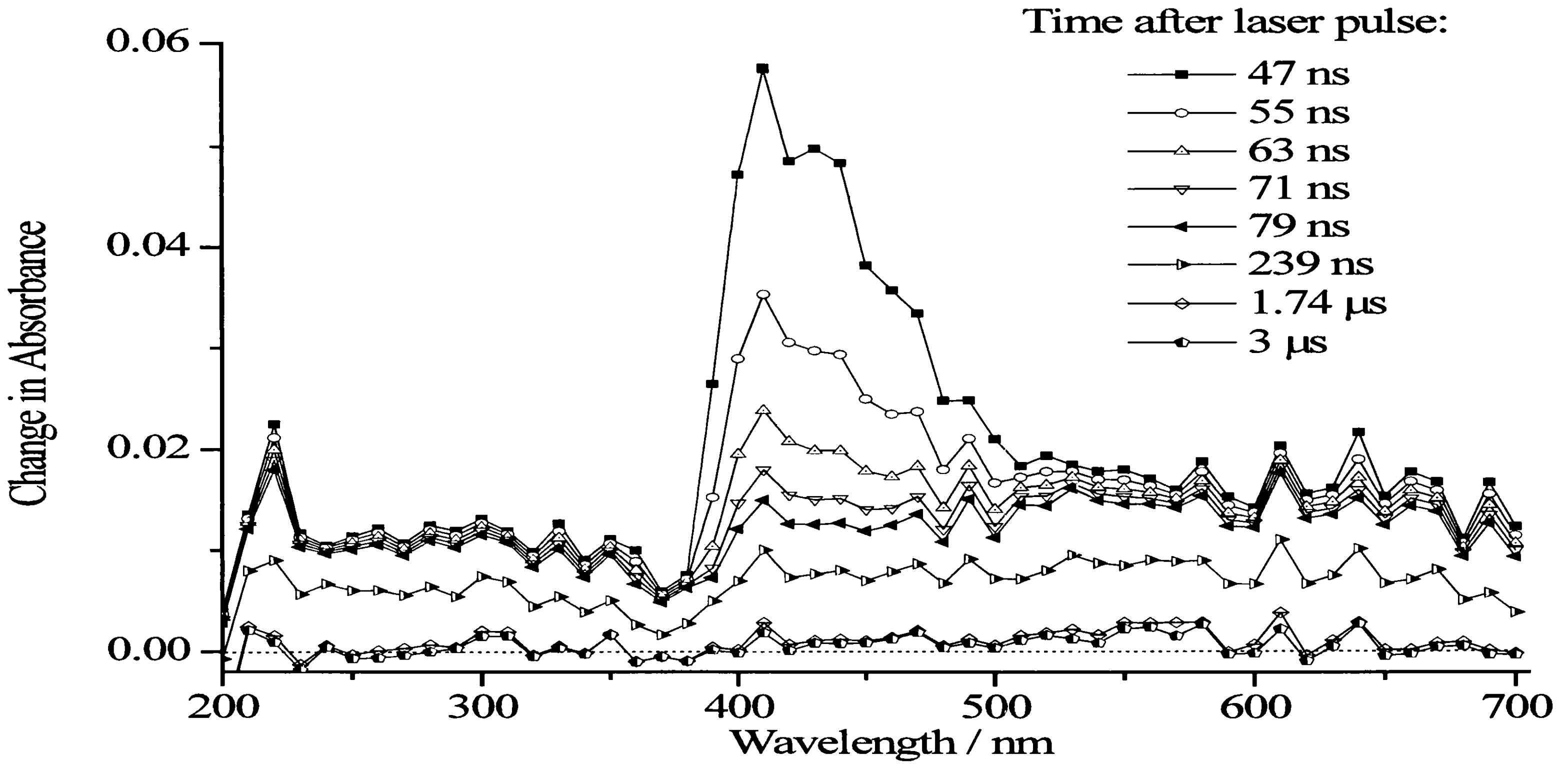

Figure 7.2 Transient absorption spectra of CCP-M at the indicated times after the excitation laser pulse.

The transient absorption spectra of all three CCPs are similar. The effect of acetonitrile concentration, and hence aggregation, on the transient absorption of CCP-S at 600 nm was investigated. There were no significant changes in the either the magnitude or the decay kinetics with variation in acetonitrile concentration.

7.3.2 Kinetics

7.3.2.1 ***TS$_f$***

The decay kinetics for **TS$_f$** are close to the edge of what can be reliably measured with ns flash photolysis. Figure 7.3 shows transient decay at 410 nm for CCP-M where both **TS$_f$** and **TS$_s$** are present, along with a double exponential fit to the data in which the slow component rate constant is fixed to the best single exponential fit for **TS$_s$** (see later). This analysis gives a lifetime for **TS$_f$** of ~10 ns (k ~1×10^8 s^{-1}).

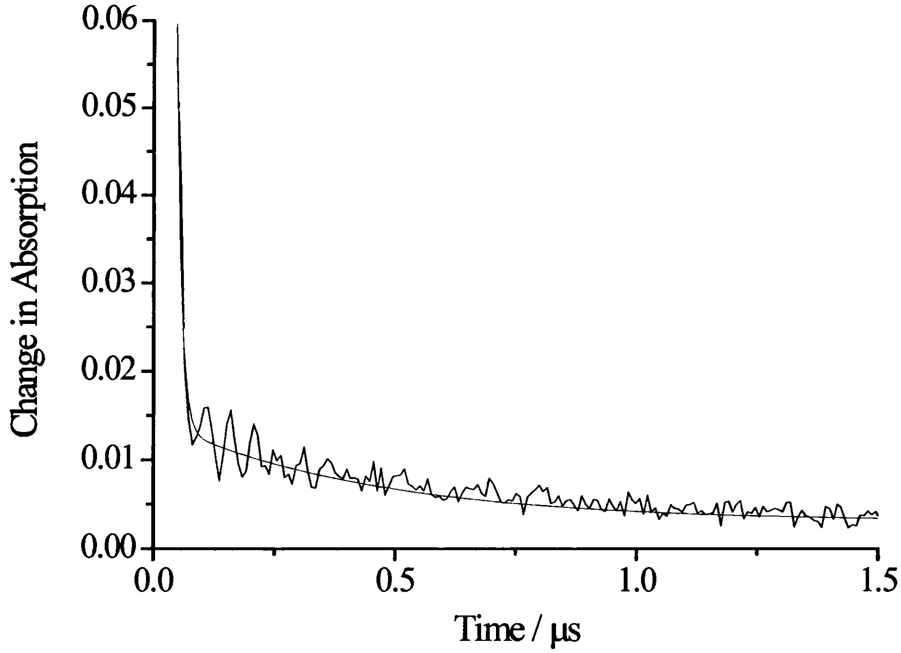

Figure 7.3 Transient decay of CCP-M at 410 nm fitted to a 1+1 exponential with the slower rate constant fixed at 2.5×10^6 s^{-1}.

7.3.2.2 ***TS***

The decay kinetics of $\mathbf{TS_s}$ are independent of wavelength across the full spectral range 200-700 nm. Figure 7.4 compares kinetics of $\mathbf{TS_s}$ measured as 410 nm with those at 600 nm for CCP-M while Figure 7.5 compares kinetics measures at 300 nm and 600 nm for CCP-L.

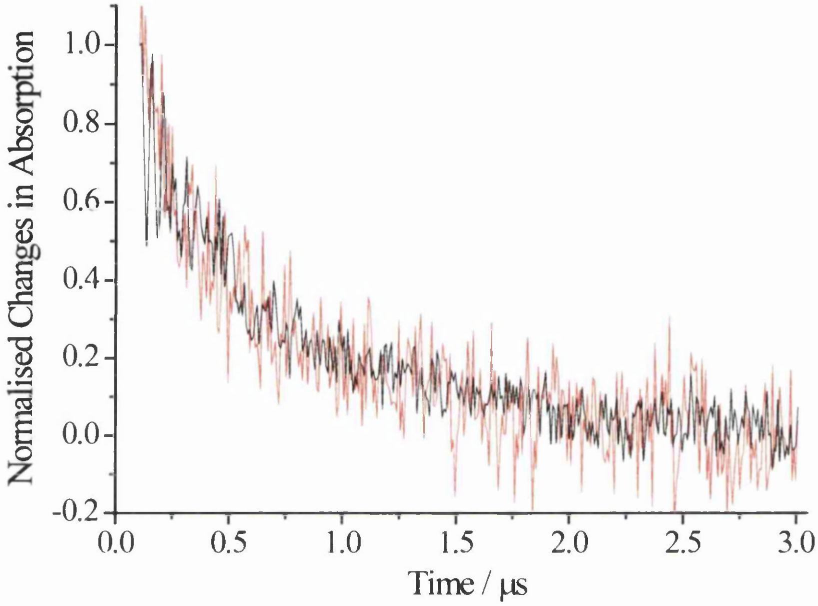

Figure 7.4 Normalised transient absorption decays at 410 nm (red) and 600 nm (black) of CCP-M. The time scale over which the decays are compared is after the complete decay of $\mathbf{TS_f}$.

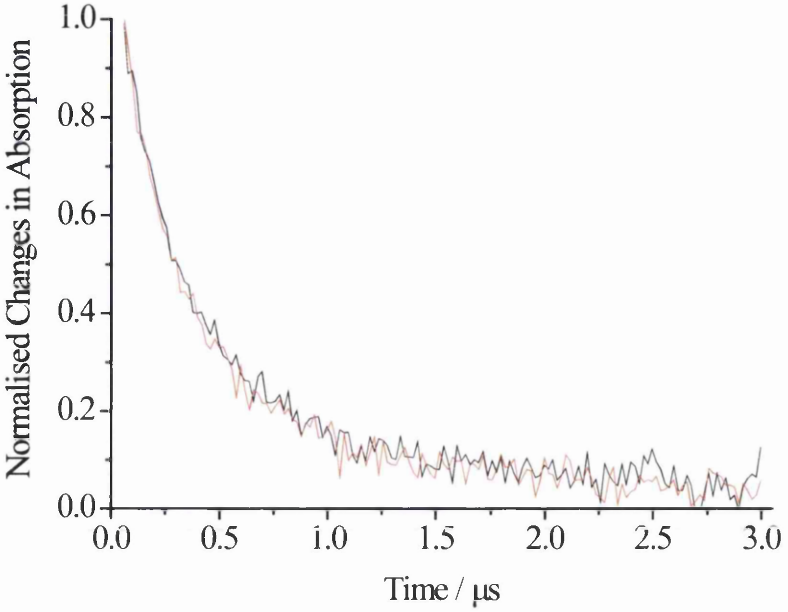

Figure 7.5 Decay kinetics for normalised transient absorption at 300 nm (red) and 600 nm (black) for CCP-L.

Transient decays for $\mathbf{TS_s}$ are fitted best in terms of two parallel first order processes (1+1 exponential decay), Equation 7.1.

$$\Delta A=a+\alpha_1\exp(-k_1t)+\alpha_2\exp(-k_2t) \qquad [7.1]$$

Where ΔA is normalised change in absorbance, a is a small zero offset correction, α_1 the amplitude of component 1 which decays with rate constant k_1 and α_2 is the amplitude of component 1 which decays with rate constant k_2. It is not known if this is a fit of "convenience" to a complex decay, or whether $\mathbf{TS_s}$ is made up of two populations which decay independently. If it is the latter pre-exponential factors can be seen as an indication of the fractional contribution from the different species to the overall rate of decay. A typical fit, and residuals, is shown in Figure 7.5. The results for analysis of all CCPs decays at 300 nm and at 600 nm are given in tables 7.2.

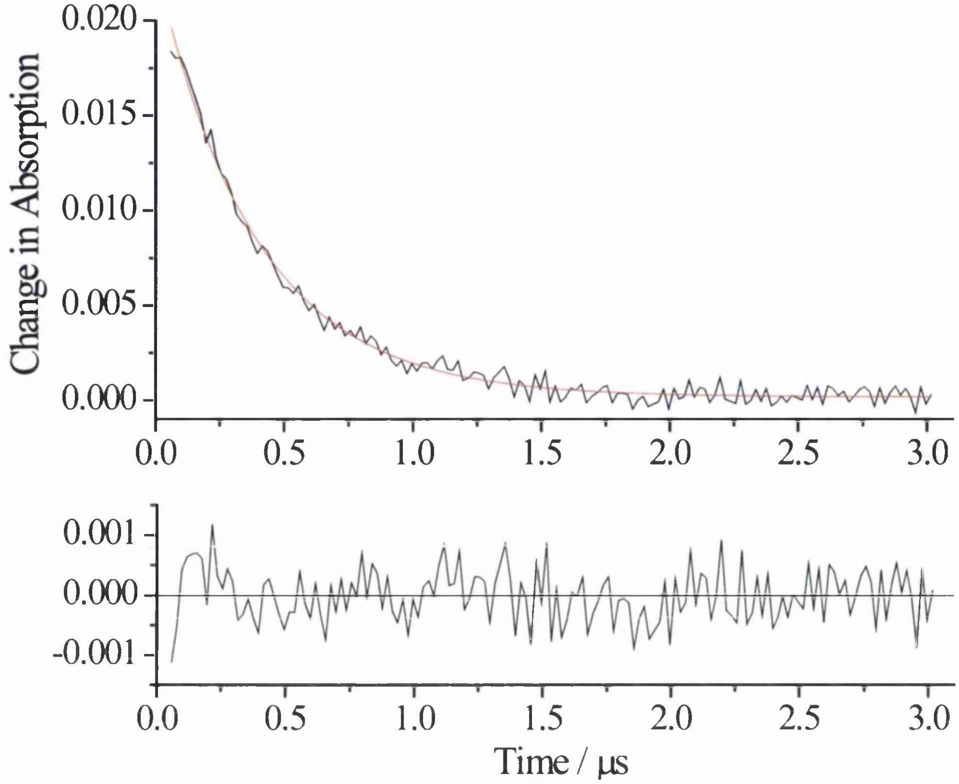

Figure 7.6 1+1 exponential fit (top) and residuals (bottom) for the decay of the transient species from CCP-L at 300 nm.

Table 7.2 Results from the 1+1 exponential decay fit for all CCPs at 300nm

Polymer	α_1	$k_1/ \times 10^6$ M^{-1} ($\pm 7 \times 10^5$)	τ_1 / μs	α_2	$k_2/ \times 10^6$ M^{-1} ($\pm 5 \times 10^5$)	τ_2 / μs	τ_{ave} / μs
CCP-S	0.65	5.35	0.19	0.35	2.45	0.41	0.27
CCP-M	0.73	6.58	0.15	0.27	1.45	0.70	0.29
CCP-L	0.61	16.5	0.06	0.39	2.10	0.48	0.22

Table 7.3 Results from the 1+1 exponential decay fit for all CCPs at 600nm

Polymer	α_1	$k_1 / \times 10^6\ M^{-1}$ (± 1×10^6)	τ_1 / μs	α_2	$k_2 / \times 10^6\ M^{-1}$ (± 5×10^5)	τ_2 / μs	τ_{ave} / μs
CCP-S	0.77	8.40	0.12	0.23	1.35	0.74	0.26
CCP-M	0.67	11.9	0.08	0.33	1.53	0.65	0.28
CCP-L	0.63	30.5	0.03	0.37	1.67	0.60	0.23

From the overlap of the decays at 300 and 600 nm and the subsequent kinetic analysis of the decays it appears that the absorption across the whole spectrum associated with $\mathbf{TS_s}$ is just on species (or a combination of species which decay together), In terms of a 1+1 kinetic analysis, the pre-exponential factors indicate that there are two populations of this species which decay independently with one population contributing *ca.* 2/3 of the decay. We will refer to these populations as the major and minor populations. At both 300 nm and 600 nm the rate constant of the major population increases significantly with CCP chain length resulting in shorter average decay times. The rate constants of the minor population remain roughly constant with increasing chain length.

Comparison with spectral data for triplet CCP, and guanine and CCP radicals shows that neither $\mathbf{TS_s}$ nor $\mathbf{TS_f}$ can be assigned to these species. In addition the lifetime of $\mathbf{TS_s}$ is a factor of 10 lower that the lifetimes reported for PF radicals and a factor of 100 lower than the lifetimes of PF triplet states.[4,7]

7.3.2 Transient absorptions of CCP/DNA systems

For all CCPs the addition of DNA (both ds and ss) and guanine initially causes an increase in the transient absorption either side of the intense transient band (400-500 nm) of $\mathbf{TS_f}$. There is then an increase in transient absorption across the whole spectra range studied loss of $\mathbf{TS_f}$ (this is reflected by a lack of structure in the initial transient spectrum 400-500 nm region, Figure 7.7). Is seems that all the quenchers prevent the formation of $\mathbf{TS_f}$ rather than quench it upon formation. Figure 7.6 shows the decay curves with increasing DNA concentration at 300 nm.

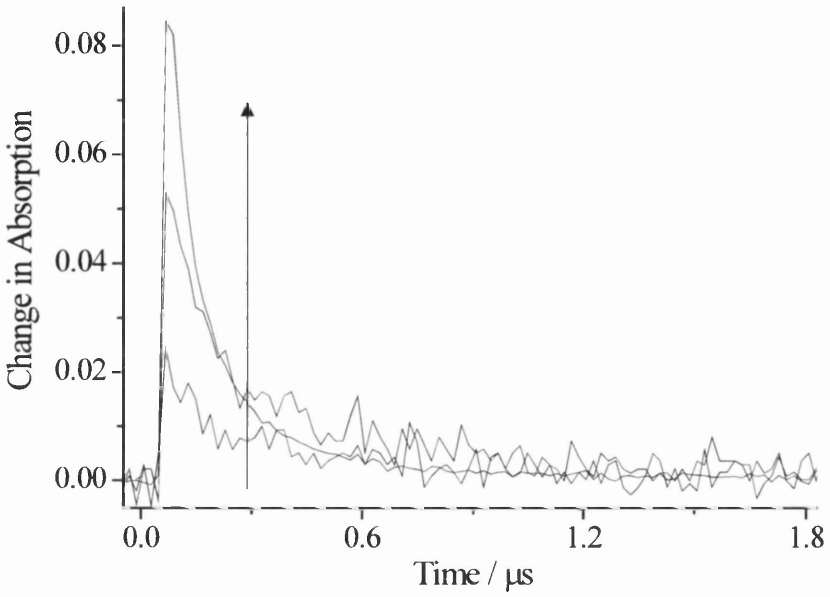

Figure 7.7 Transient absorption of CCP-L at 300 nm with 0, 3.5×10^{-6} and 7×10^{-6} M DNA. The arrow indicates increasing DNA concentration.

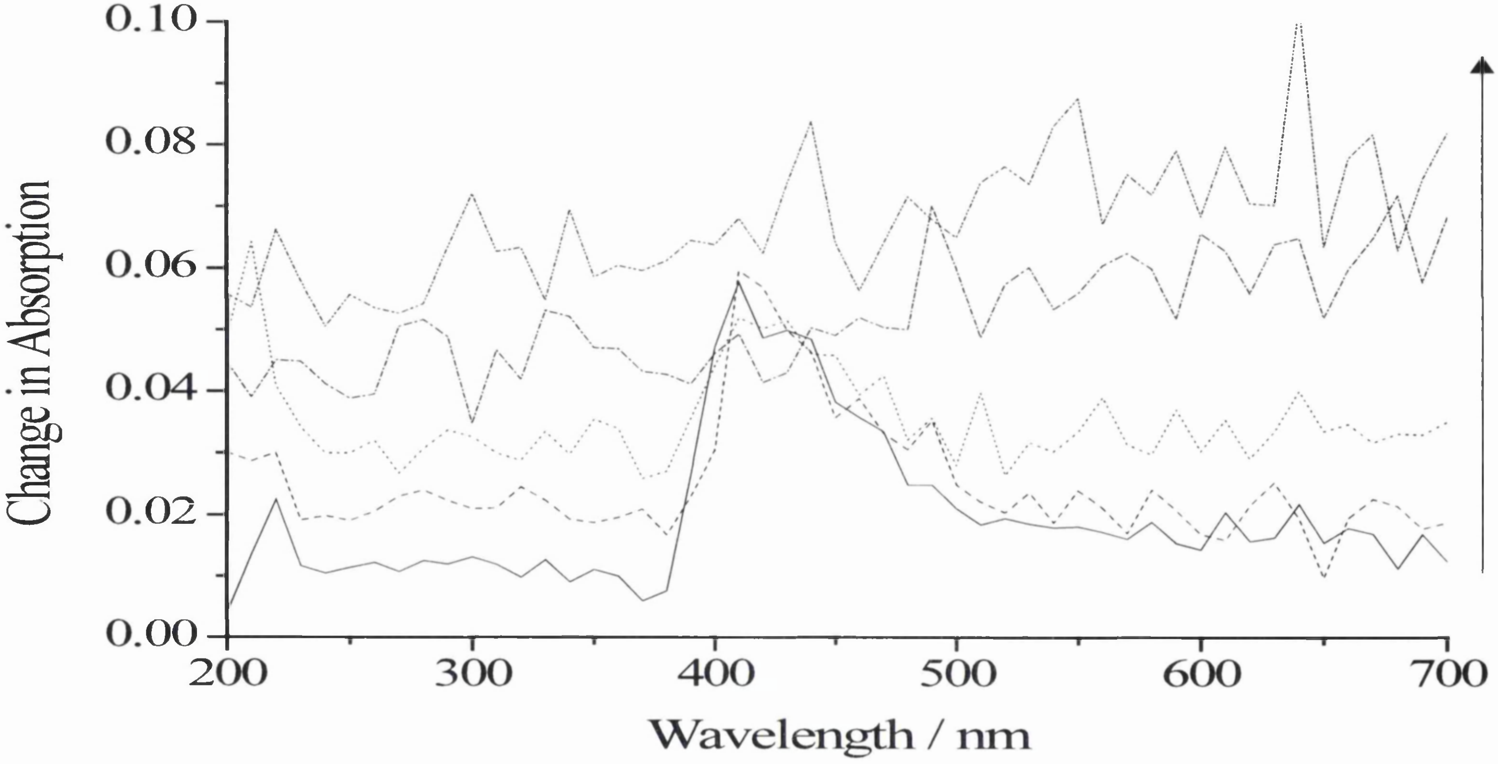

Figure 7.8 Transient absorption of CCP-M with 0, 2.2×10^{-7}, 7.2×10^{-7}, 1.4×10^{-6} and 7×10^{-6} M DNA. The arrow indicates increasing DNA concentration.

7.3.2.1 Transient kinetics in the presence of quencher

The increase in the transient absorption is accompanied by a decrease in the average lifetime of the transient. None of the decays are single exponential but all give reasonable fits to 1+1 exponential which are convenient for the calculation of an average lifetime. Figure 7.9 shows the variation of average lifetime with quencher concentration for CCP-L which shows the biggest sensitivity to the nature of the quencher used.

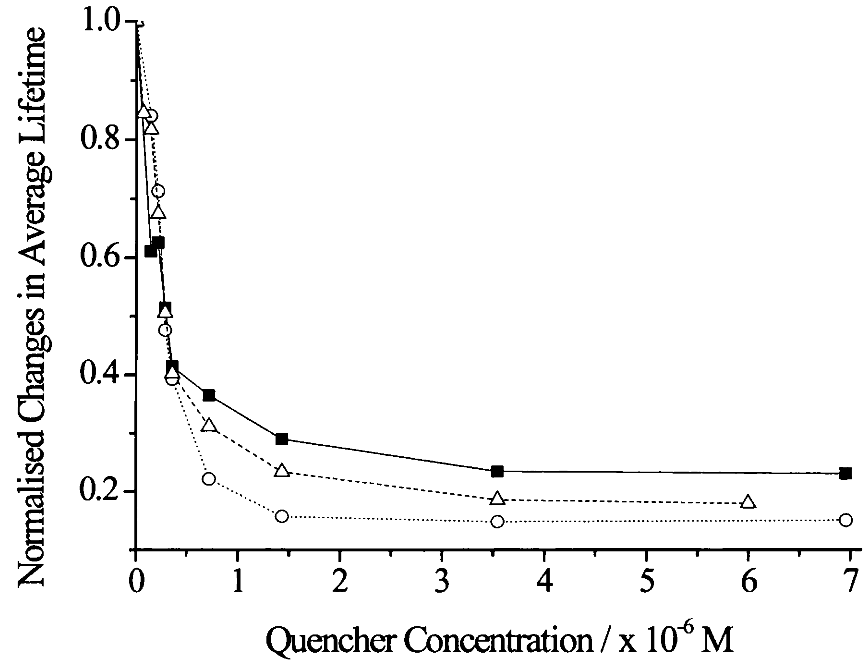

Figure 7.9 Normalised changes in the average lifetime of CCP-L with increasing quencher concentration, dsDNA (solid line, squares), ssDNA (dotted line, open circles) and guanine (dashed line, open triangles).

Table 7.4 gives kinetic parameters for a 1+1 fit to the transient decays of the three CCPs at 300 nm with the highest concentration of dsDNA studied. The decays are given in Figure 7.10. The average lifetimes of the three CCPs decrease *ca.* 50-66% in the presence of dsDNA. The average lifetime of the CCPs in the presence of DNA, (both ds and ss) or guanine decreases with increasing chain length.

Table 7.4 Results from the exponential decay fit for all CCPs at 300nm with the maximum concentration of dsDNA studied (6.95 × 10^{-6} M).

Polymer	α_1	k_1 / × 10^7 M^{-1} (± 5 × 10^5)	τ_1 / μs	α_2	k_2/ × 10^6 M^{-1} (± 1 × 10^5)	τ_2 / μs	τ_{ave} / μs
CCP-S	0.77	1.5	0.07	0.23	3.18	0.31	0.13
CCP-M	0.91	1.3	0.08	0.09	2.09	0.48	0.12
CCP-L	0.88	2.0	0.05	0.12	4.04	0.25	0.07

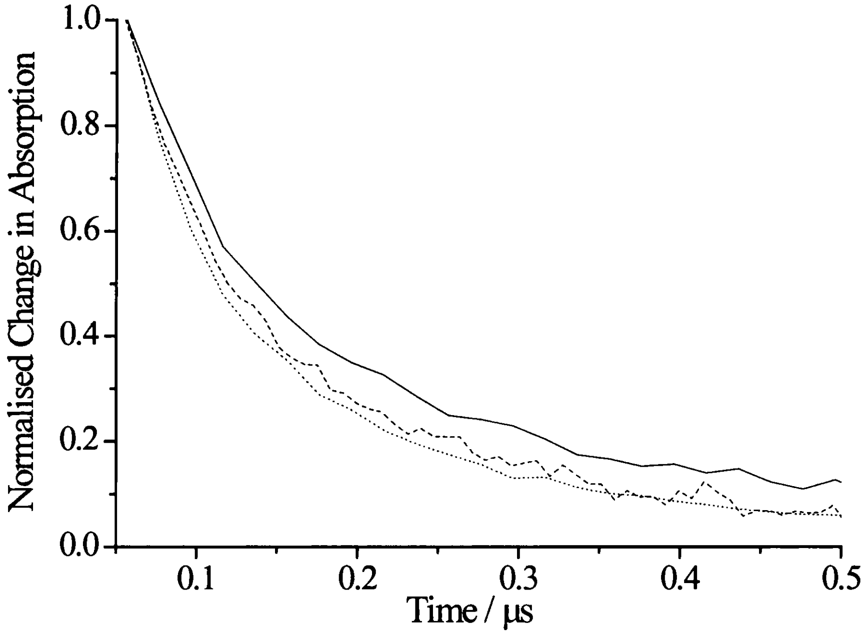

Figure 7.10 Normalised decay curves for CCP-S (solid line) CCP-M (dashed line) and CCP-L (dotted line) with 6.95×10^{-6} M dsDNA at 300 nm.

It was also found that the decay kinetics vary slightly with quencher with the maximum variation for CCP-L. Table 7.5 collects kinetic characteristics for CCP-L in the presence of dsDNA, ssDNA and guanine. Figure 7.11 shows the decay curves. The effect of quencher follow the same pattern as steady state fluorescence quenching in that guanine is less effective than dsDNA which is less effective than ssDNA.

Table 7.5 Results from the exponential decay fit for CCP-L at 300nm with the maximum concentration of dsDNA, ssDNA and guanine.

Quencher	α_1	k_1 / × 10^7 M^{-1} (± 5 × 10^5)	τ_1 / μs	α_2	k_2/ × 10^6 M^{-1} (± 1 × 10^5)	τ_2 / μs	τ_{ave} / μs
dsDNA	0.78	1.93	0.05	0.22	4.62	0.22	0.09
ssDNA	0.91	1.80	0.06	0.09	3.72	0.27	0.076
Guanine	0.88	1.07	0.09	0.12	2.15	0.47	0.13

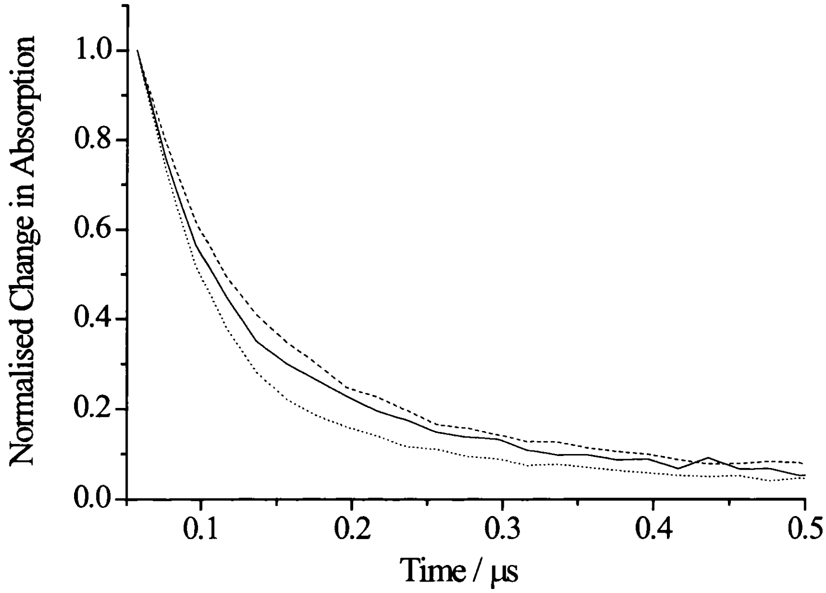

Figure 7.11 Normalised decay curves at 300 nm for CCP-L with (dsDNA (solid line), ssDNA (dotted line) and guanine (dashed line) at the maximum concentrations studied.

7.3.3 CCP/DNA complex formation

The transient absorption increases with DNA concentration and it seems possible that the increase in transient absorption results from complex formation between CCP and

DNA. If so, then relative changes in transient absorption should be comparable to the changes in steady state emission (SV data plots) in Chapter 6. Figure 7.8 shows the changes in transient absorption with quencher concentration.

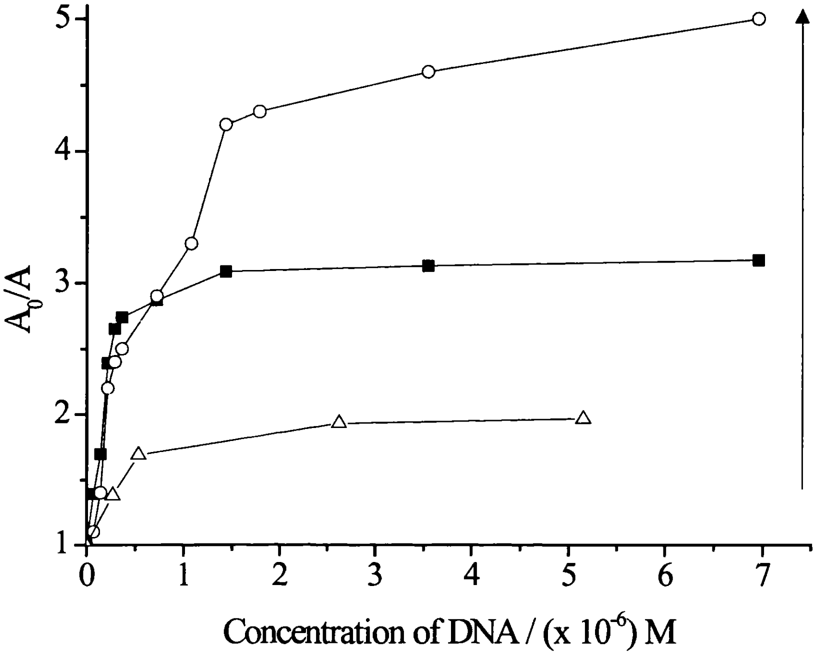

Figure 7.8 Changes in transient absorption at 300 nm with increasing DNA concentration for CCP-S (open triangles), CCP-M (solid squares) and CCP-L (open circles). The arrow indicates the increasing chain length of the CCPs.

Although we do not have fluorescence quenching data for exactly the same polymer and quencher concentrations it is interesting to compare the general behaviour of fluorescence quenching and increase in transient absorption. Figure 7.9 shows the change in transient absorption compared with the changes in steady state emission intensity. The two sets of data are consistent in that the lower the polymer concentration the steeper the initial slope of the plots, and the lower the DNA concentration at which the plateau region is reached i.e. the lower the "complexation point".

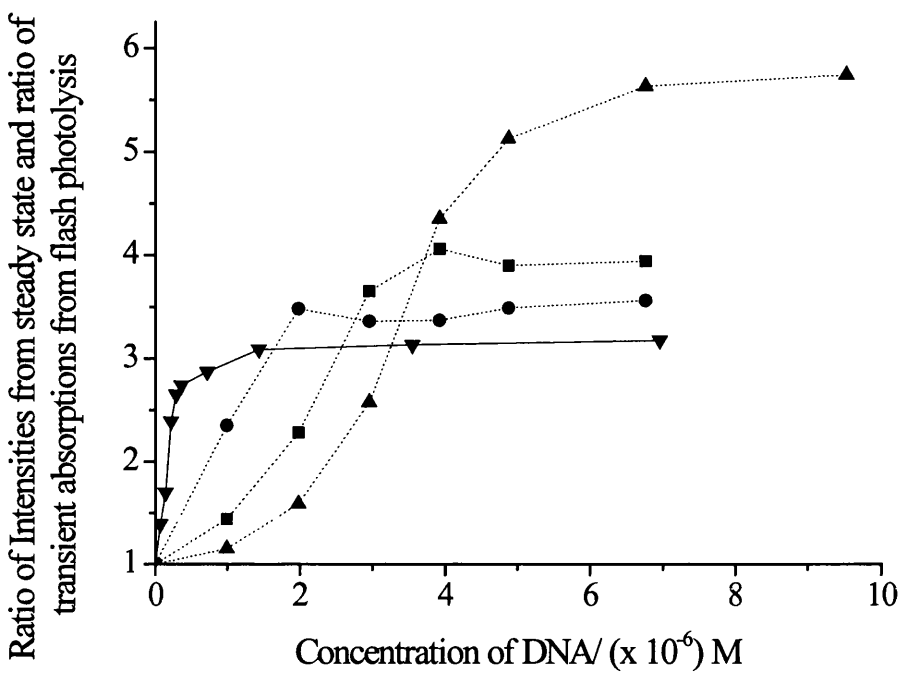

Figure 7.9 Changes in transient absorption of CCP-M at a concentration of 2×10^{-6} M (inverted triangles, solid line) at 300 nm superimposed on Figure 5.23 which shows the dependence of steady state quenching rates on CCP concentration at CCP concentrations of 1×10^{-5} M (solid triangles, dotted line), 6×10^{-6} M (solid squares, dotted line) and 3×10^{-6} M (solid circles, dotted line).

Since it is thought that the increase in transient absorption is due to complex formation between the polymer and DNA the data was treated in terms of two pairs of parallel first order decays in which rate constants and relative amplitudes are fixed; one pair from the 1+1 fits for the polymer when no DNA is present and, one pair from the 1+1 fits from the DNA/CCP complex at the plateau region of Fig. 7.8 i.e. at high quencher concentration. Although complex the normalised fits actually only have one fitting parameter corresponding to the ratio of the contribution from the signal expect for polymer not bound to DNA, and that for polymer bound to DNA. Thus a ratio of the two pairs give the amount of free CCP and the amount of CCP/DNA complex.

$$\Delta A = a + (A(\alpha_1 \exp(-k_1 t)) + (\alpha_2 \exp(-k_2 t))) + (B(\alpha_3 \exp(-k_3 t)) + (\alpha_4 \exp(-k_4 t))) \quad [7.2]$$

Where A and B are the fractions of free CCP and CCP/DNA complex, respectively, α_1 and α_2 are the amplitudes of component 1 which decays with rate constants k_1 and k_2 respectively, when no quencher is present. $\alpha 3$ and α_4 are the amplitudes of component 1 which decays with rate constants k_3 and k_4 respectively, at the maximum quencher concentration. (Figure 7.11 compares the results from a 1+1 fit and a complexation fit to a kinetic decay showing that both fit the data extremely well.)

This treatment of the data allows us to plot the change in the faction of free polymer and the change in the fraction of complexed polymer with DNA as is shown in figure 7.10. The trend that is displayed in Figure 7.10 is representative of all samples; the curves are sigmoidal with the fraction of CCP decreasing upon complex formation with DNA. The curves obtained are comparable with the curves obtained from the equilibrium fitting of the steady state quenching in Chapter 6, suggesting that the increase in transient absorption is from CCP/DNA complex formation.

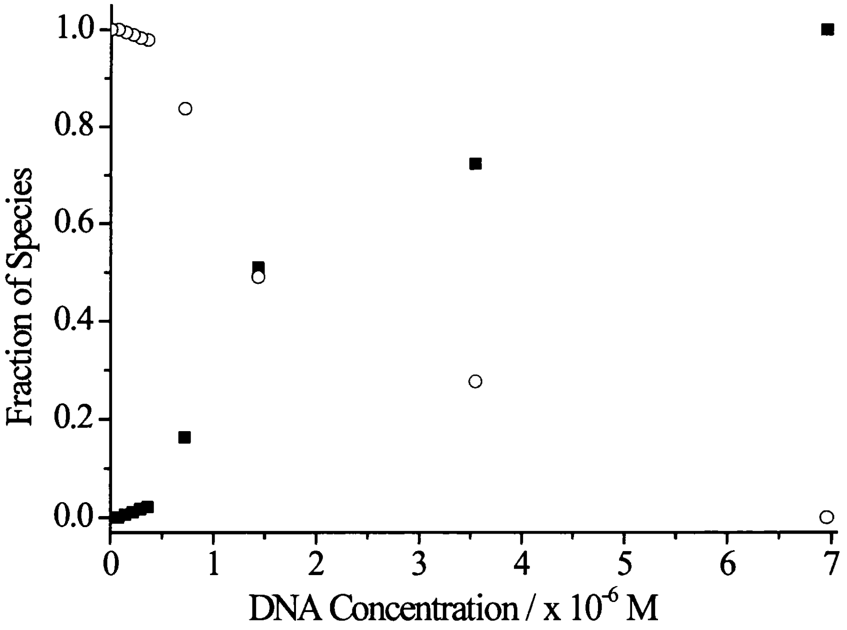

Figure 7.10 Change in the fraction of CCP-M (open circles) and CCP-M/DNA complex (solid squares) with increasing DNA concentration.

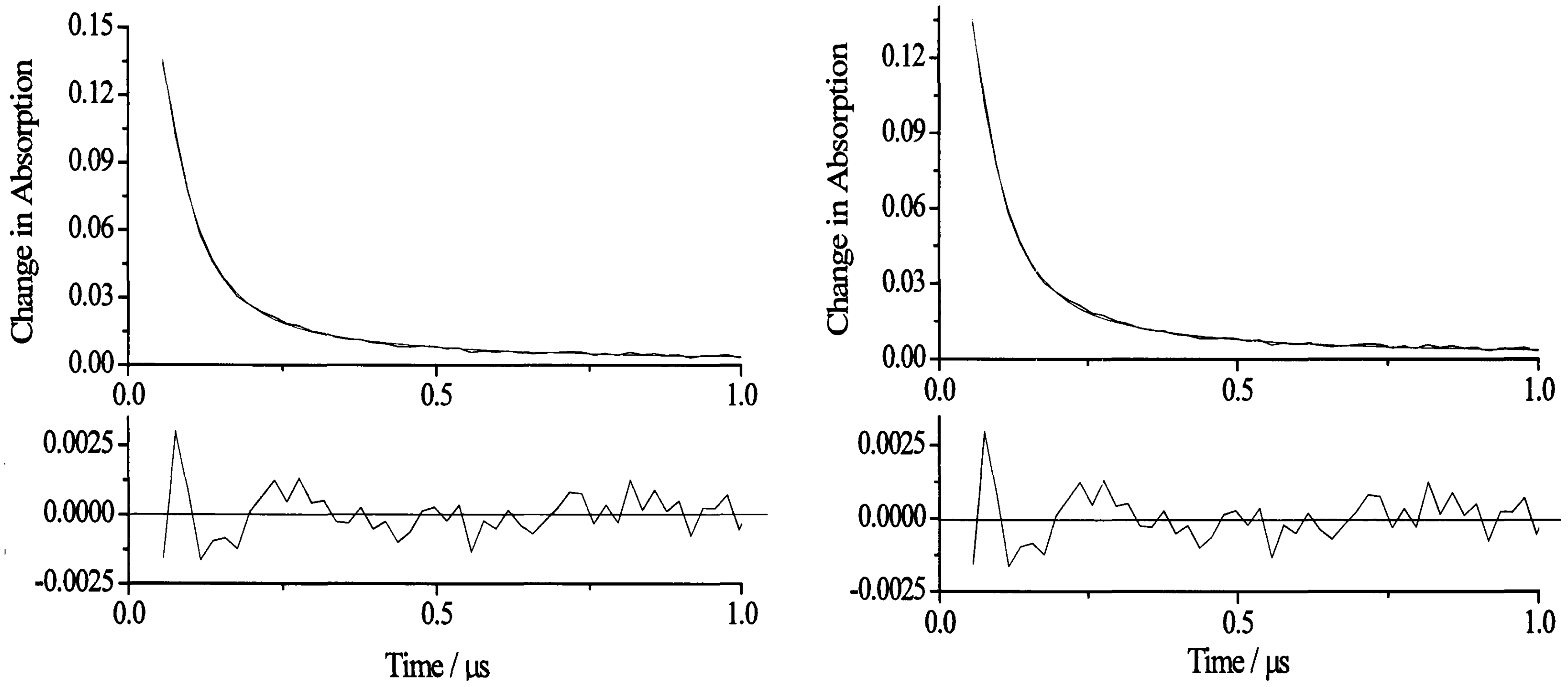

Figure 7.11 Comparison of the exponential decays fits for CCP-L at the maximum DNA concentration studied (7×10^{-6}) at 300 nm. Graph A (left) shows a 1+1 exponential fit whereas graph B shows the fit the derived equation. As can be seen both fit the data extremely well proving that the derived equation is suitable to analyse the data. Residuals are given as an inset in the appropriate graph.

7.3.4 CCP/Guanine complex formation

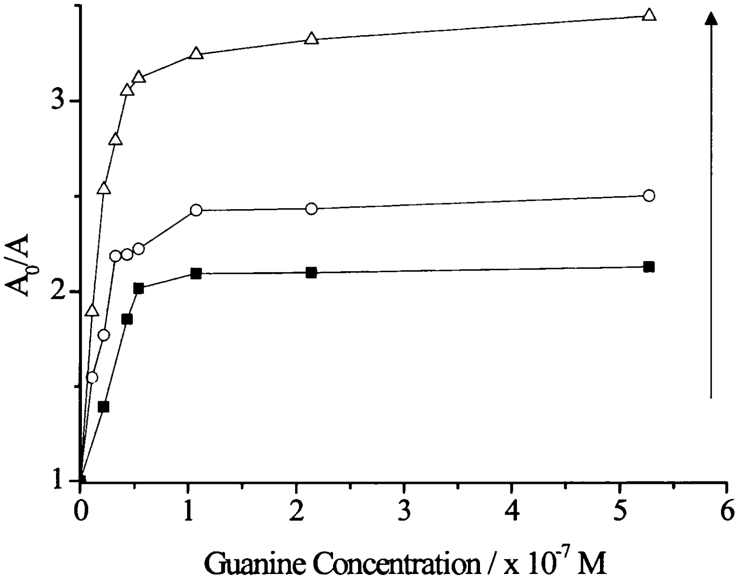

Figure 7.12 Changes in transient absorption with increasing guanine concentration for all CCPs studied. The arrow indicates the increasing chain length of the CCPs.

The behaviour with guanine is very similar and has been analysed in the same way as for DNA complexation.

Table 7.5 Results from the exponential decay fit for all CCPs at 300 nm with the maximum concentration of guanine studied (1×10^{-6} M).

Polymer	α_1	k_1 / × 10^7 M^{-1} (± 5 × 10^5)	τ_1 / μs	α_2	k_2/ × 10^6 M^{-1} (± 1 × 10^5)	τ_2 / μs	τ_{ave} / μs
CCP-S	0.11	1.1	0.09	0.01	2.15	0.47	0.01
CCP-M	0.07	1.0	0.10	0.01	1.82	0.55	0.01
CCP-L	0.11	1.5	0.07	0.03	3.21	0.31	0.02

A typical plot of the change in the fraction of free CCP and the change in the fraction of the CCP/guanine complex with increasing guanine concentration is given in Figure 7.13.

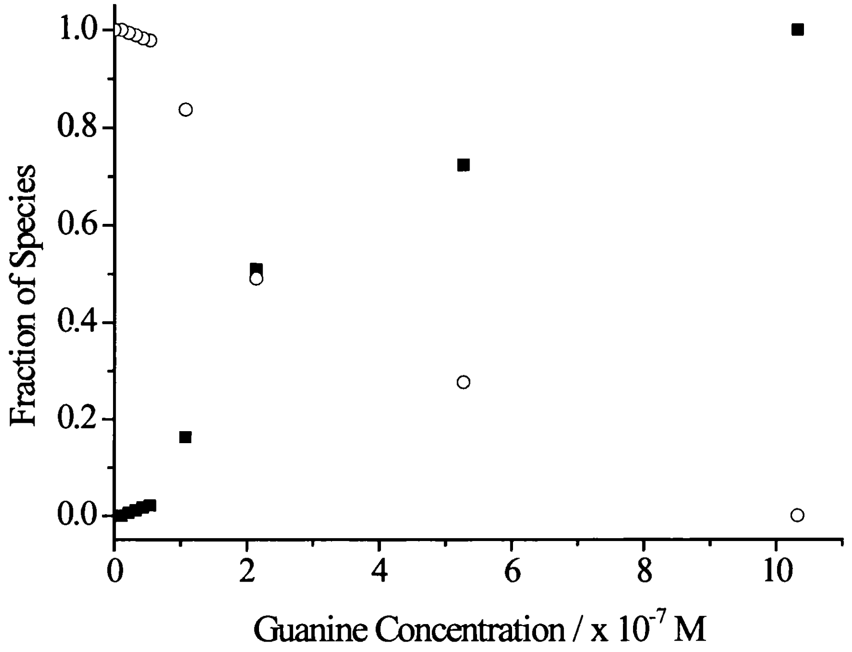

Figure 7.13 Change in the fraction of CCP-L (open circles) and CCP-L/guanine complex (solid squares) with increasing guanine concentration.

7.4 Conclusions

All CCPs studied produce two transient species following excitation at 355 nm; a relatively short lived species, **TS$_f$**, with an intense absorption between 400 and 500 nm, and a longer lived species, **TS$_s$**, that absorbs across the wavelength range 200-700 nm. **TS$_f$** has a lifetime of ~10 ns. The decay of the **TS$_s$** is best fitted in terms of two parallel first order processes. Accepting this approach then the rate constant for decay of the major population increases significantly with CCP chain length; from 5.35×10^6 M^{-1} for CCP-S to 16.5×10^6 M^{-1} for CCP-L (at 300 nm) whereas the rate constant of the minor component remain roughly constant at $\sim2\times10^6$ M^{-1}.

Upon the addition of DNA (both ds and ss) and guanine there is a general increase in the transient absorption corresponding to **TS$_s$** with a loss of the **TS$_f$**. The effect on the transient absorption is independent of the type of quencher used. These changes in transient absorption with quencher concentration follow similar behaviour to the steady-state emission data described in Chapter 6. Although the data support the interpretation of the interaction between CCPs and DNA or guanine in terms of a complexation equilibrium we do not know the nature of the chemical species which give rise to these transients. However, comparison with transient spectra recorded in the literature indicates that they cannot be assigned to either the CCP triplet or CCP or guanine radicals.

7.5 References

1. R. Bonneau, J. Wirz and A. D. Zuberbuhler. *Pure & Appl. Chem.*, **1997**, *69*, 979-992.
2. R. G. Norrish and G. Porter, *Nature,* **1949**, *164*, 658.
3. N. Takeda, S. Asaoka and J. R. Miller, *J. Am. Chem. Soc.*, **2006**, *128*, 16073-16082.
4. S. Asaoka, N. Takeda, T. Iyoda, A. R. Cook and J. R. Miller, *J. Am. Chem. Soc.*, **2008**, *130*, 11912-11920.
5. H. D. Burrows, J. Seixas de Melo, C. Serpa, L. G. Arnaut, M. G. Giguel, A.P. Monkman, I. Hamblett and S. Navaratnam, *J. Chem. Phys*, **2002**, *285*, 3-11.
6. M. D. Evans and M. S. Cooke, *Oxidative Damage to Nucleic Acids*, Springer New York, **2007**.
7. H. D. Burrows, J. Seixas de Melo, M. Forster, R. Guntner, U. Scherf, A. P. Monkman and S. Navaratnam, *Chem. Phys. Lett.*, **2004**, *385*, 105-110.

Chapter 8

Conclusions

8.1 TAA dyes

8.1.1Photophysics of TAAs

In this work seven novel TAA dyes have been investigated with a view to their possible use in optoelectric devices. These dyes have good photophysical properties with quantum yields of great than 0.3 in cyclohexane and generally high molar extinction coefficients (3.0-4.0(±0.50)$\times10^4$ $M^{-1}cm^{-1}$). The molar extinction coefficients are relatively unaffected by solvent polarity. There are, however, significant changes in the emission of TAAs with solvent polarity. For **5**, **6** and **3** the fluorescence quantum yield increases on going to a polar solvent, whereas for **4** and **7** there is a decrease. For **9** and **8** there is a red shift with complete loss of structure of the emission band, and a marked reduction in emission intensity, as solvent polarity is increased. This may be understood in terms of a close lying twisted charge transfer state the position of which is solvent dependent. This is supported by the data from the low temperature emission spectra as this solvent "quenching" does not occur in a rigid glass at low temperatures because the compounds cannot undergo molecular torsion. This suggests that room temperature deactivation in fluid solution is predominantly non-radiative *via* a twisted CT excited state to a twisted ground state, whereas emission in a rigid glass at low temperatures or in a highly viscous environment is emissive from a planar excited state to a planar ground state. In general the lowest excited state of these dyes has π, π* character, however when the nitro group is present in the para position on the stilbene group there is also a very close lying charge transfer state. This charge transfer state becomes the lowest excited state on going to polar solvents, relaxation from this state is via non-radiative processes, and thus for these compounds in polar solvents there is very little fluorescence emission.

8.1.2 Thermal properties of TAAs

All TAAs studied have excellent thermal properties for possible use in devices. They do not crystallise readily and have thermal decomposition temperatures of greater than 300 °C in all cases. Thus, the addition of the bulky dehydroabietic acid moiety has produced thermally stable, soluble materials that do not crystallise, without compromising their electrochemical, optical or photophysical properties. These properties make the compounds attractive materials for a variety of applications in molecular electronics.

8.2 CCPs

8.2.1 Photophysics of CCPs

CCPs aggregate in water, and this causes a reduction in Φ_f. These aggregates can been broken up by the use of acetonitrile as a co-solvent. In optimum acetonitrile/water mixtures the CCPs studied have high fluorescence quantum yields, *ca.* 0.3, molar extinction coefficients of $3.7\text{-}4.2\times10^4$ M^{-1} cm^{-1}, and the fluorescence lifetime of isolate chains is *ca.* 450 ps.. Time resolved decays of CCPs in varying degrees of aggregation have been modelled by ProgClusters in terms of a series of energy transfer steps where energy is quenched at an aggregate trap formed where polymer chains come into close proximity. Rate constants of *ca.* $2\text{x}10^9$ s^{-1} were calculated for the natural decay of an isolated repeat unit while the rate constant for energy transfer between repeat units, or from repeat units to aggregate traps was found to be $2.4\text{x}10^{12}$ s^{-1} and $5.2\text{x}10^{12}$ s^{-1} for CCP-M and CCP-L respectively. Since aggregation quenching results in low photoluminescence quantum efficiencies, this limits the potential applications of CCPs in LED displays or biosensors. Thus knowledge of the aggregation properties of CCPs and solutions to breaking up these aggregates is vital for material and sensor applications.

8.2.2 CCP/quencher interactions

These CCPs are extremely sensitive to quenching by DNA (both ds and ss) and guanine, with quenching constants far in excess of the diffusion controlled limit. Previously, quenching has usually been analysed in terms of a dynamic SV relationship which results in non-linear plots and unreasonably high dynamical quenching rate constants.[1,2,3] It has been shown in this thesis that this unusually efficient quenching may be understood in terms of "energy migration quenching" in which CCP and quencher form an aggregate complex in which excitation energy migrates between and along the polymer chains until it is quenched at an aggregate "trap". The quenching efficiency is dependent on the chain lengths of both CCP and

DNA and also the CCP concentration. This leads to the possibility of tuning sensors for maximum sensitivity at very low quencher concentrations

Both FM and AFM have shown that the CCP compactions DNA and causes DNA to link together resulting in supramolecular structures.[4]

Although the nature of the transient species formed in flash photolysis experiments could not be determined the change in transient absorption on the addition of quencher is also well modelled in terms of a complexation equilibrium.

From all of this data it is proposed that the interaction between CCPs and DNA seems likely to proceed as follows. Electrostatic effects cause the CCP to associate with the DNA backbone, due to physical constraints around the DNA not all CCP repeat units will be accessible for quenching. When the charges on the backbone of DNA are neutralised the DNA compacts, incorporating some CCPs chains, into a tightly packed structure. This understanding of aggregation energy migration quenching of CCPs and CCP/DNA interactions may be important when considering the use of CCPs in sensor materials.

8.3 References

1. Al Attar and A. P. Monkman. *J. Phys. Chem. B* **2007,** *111,* 12418-12426.
2. Q. Zhou, T. M. Swager, *J. Am. Chem. Soc.,* **1995**, *117*, 7017–7018.
3. L. H. Chen, D. W. McBranch, H. L. Wang, R. Helgeson, F. Wudl, D. G. Whitten, *Proc. Natl. Acad. Sci. U.S.A.,* **1999**, *96*, 12287– 12292.
4. M. L. Davies, H. D. Burrows, M. C. Morán, M. G. Miguel and P. Douglas, *Biomacromolecules*, **2009**, *10*, 2987–2997.